IRCCS, Integrated Research Consortium on Chemical Sciences

統合物質創製化学研究推進機構

令和元年度 事業報告書

IRCCS, Integrated Research Consortium on Chemical Sciences

統合物質創製化学研究推進機構

令和元年度 事業報告書

目　次

1

統合物質創製化学研究推進機構について

1-1

本機構の背景

１−１．本機構の背景

革新的な機能性物質の発見と創造が、科学と科学技術に飛躍的な発展をもたらしてきた。その根幹を担ってきたのが、原子・分子レベルで物質を探求し、創造しつづけてきた「ものづくり」の化学、すなわち物質創製化学である。豊かな物質に彩られた現代社会の恒常的発展を維持し、我が国の科学技術立国としての地位を揺るぎないものとするためにも、次世代の飛躍を約束する新たな機能性物質群を創造していかねばならない。特に、緊迫するエネルギー・環境問題の解決や最先端バイオ・情報技術の進展を図り、科学技術全般の国際的競争力を高めるためにも、革新的な機能性物質群の創造と、それらの合理合成法の開拓に向けた新学術基盤の構築が急務である。化学者に課せられた任務は極めて重い。

次世代の機能性物質創製の鍵を握るのが、物質を構成する元素、分子、分子集合体という階層性の理解と制御であると考えられている。元素により特徴づけられる多種類の原子が結合を作ることにより分子が形成され、さらに分子が集積することにより分子集合体へと組織化され、それぞれの階層に特有の性質や機能がある。生体物質の構造に例えると、個々の原子の特性を基礎とし（元素）、その機能を発揮する最小単位となるタンパク質や核酸が構成され（分子）、これらがさらに集積してウイルスや細胞内組織であるミトコンドリア（分子集合体）となる。高度に機能化された革新的な物質を創製するためには、全ての階層における構成単位を創製する術を学び、その機能を解明しなければならない。

本事業に参画する京都大学・名古屋大学・九州大学・北海道大学の４研究組織は、それぞれ「元素」「分子」「集合体」「触媒」をキーワードとした強力な中核的国際研究拠点として認知されている。本事業の前身となる「統合物質創製化学推進事業 − 先導的合成の新学術基盤構築と次世代中核研究者の育成（H22〜27年度）」においては、４研究組織のそれぞれがストロング・ポイントをもつ各物質階層を中心に、個別に蓄積されてきた物質合成における知識と知恵を融合・深化させるとともに、物質合成概念の統合にも取り組んだ。すなわち、古典的な化学反応を利用した「化学的物質合成」ともに、高温超伝導体や発光材料、半導体などの開発に利用されてきた「物理的物質合成」や、生命体が穏和な条件下に日常的に行っている精巧かつ高効率な「生命物質合成」にも学ぶことによって、持続型経済社会を実現する、環境に調和した新たな「物質創製概念」の創出を実践した。「物質階層の統合」と「物質合成概念の統合」を合言葉として、各研究機関の知識と経験を融合・深化させて新たな物質創製化学を遂行した結果、天然窒素還元酵素における機能中心構造の全合成、カーボンナノチューブ構造の化学合成、低環境負荷の鉄触媒による液晶材料の合成、強誘電性と強磁性が共存する

マルチフェロイック物質の開発など、革新的な研究成果が生まれた。さらに、若手研究者に自由闊達な研究環境と、大学の垣根を越えた共同研究や情報交換の機会を与えたことによって、物質創製化学の未来を切り開く力量ある次世代中核研究者の育成を実現した。本事業は、この 4 大学間連携事業をさらに組織化・システム化した「新機構」を設立し、社会のニーズに応える「統合物質創製化学」を推進する。

1-2

本機構の目的

１－２．本機構の目的

新物質創製は、化学結合の形成のための新しい方法論や、機能の発現のための物質構築論などを探求する極めて基礎的な基盤学術である一方、その成果は、新触媒や新材料開発はもちろん、イノベーション創成を通じてエネルギー・資源から環境・創薬に至る極めて広い範囲に適用される。ここでは、基礎と応用が直結し（縦糸）、また化学を中心として物理から生命科学までの多くの研究分野の協力が必須である（横糸）。すなわち、物質と情報そして人が集結することが何より重要な分野と言えよう。しかしながら、我が国の物質創製研究は極めて高い国際競争力をもつにもかかわらず、新物質創製を総合的かつ戦略的に進める機関・組織は、残念ながら我が国には存在しない。基礎と応用を結ぶ縦糸と多様な分野を結ぶ横糸を組み合せ、近年長足の進歩を遂げたナノ計測や計算化学を取り込んだ統合的な研究組織の構築が急務である。その一方で、現在のひっ迫した財政の下では、多くの面積とポストを必要とする新研究所設立のような事業は現実的ではない。物質創製の学術を継承・発展させ、迫りくる環境問題などの重点課

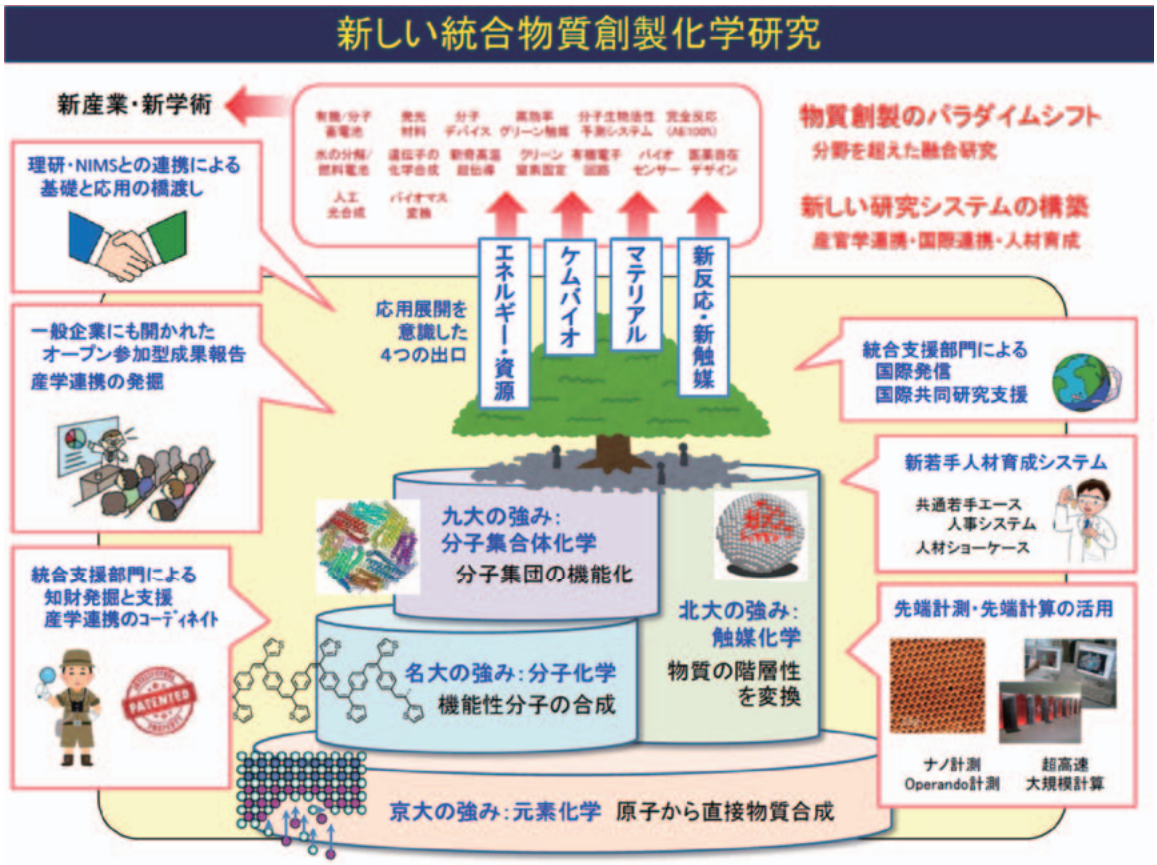

図１

題を解決し、また新産業創出を成すためには、産官学連携や国際連携を前面に出し、責任あるマネージメント体制を持ちながらも、最小限の面積とポストの獲得で遂行できる、大学間連携を基盤とした「統合物質創製化学研究推進機構」は、必要かつタイムリーな事業である。

図１に統合物質創製化学研究推進機構の概念図を示す。本機構事業に参画する名古屋大学・京都大学・九州大学・北海道大学の４研究組織は、「分子」、「元素」、「集合体」、「触媒」の化学研究において、それぞれに特色ある強力な中核的国際研究拠点として認知されているが、以下に示すそれぞれのストロング・ポイントを活かしながら、物質の階層構造を縦断する研究連携を実現する。

名古屋大学：無機化学から有機化学にわたる分子性物質の合成と機能の発現、さらには不斉反応を含む分子触媒の開発研究において卓越した成果をあげてきた。最近では、生物無機化学やナノ炭素科学分野においても世界をリードする。

京都大学：元素の特性の解明と、それに基づく機能創出の化学において先導的な研究成果をあげている。機能性元素科学という新しい研究パラダイムを提唱し、分子性物質から凝縮系物質に至る様々な革新的新物質群の出現を促してきた。

九州大学：複雑な分子集合体・集積体を構築する新概念を提出し、多くの機能性集積体の合成研究を通してナノサイエンス・テクノロジー研究に先鞭をつけた。最近では、核酸ナノマシンやナノハイブリッド材料の創出などで顕著な成果を挙げる。

北海道大学：触媒化学において世界を先導する中核的研究拠点である。触媒元素・分子のナノ・ミクロ集積・集合化学の研究を推進し、資源高度利用触媒、環境触媒、バイオ利用触媒、燃料電池・電極触媒、光触媒などで多くの成果を挙げる。

さらに本研究推進機構では、基礎研究を中心とする一方、「新反応・新触媒」、「マテリアル」、「エネルギー・資源」、「ケムバイオ」という、応用展開を意識した４つの出口を設定して基礎と応用を直結させる。その上で、産官学連携や国際連携を組織的に取り込み、新しい研究システムや研究支援体制、人材育成システムを取り入れた、社会に開かれた新組織である。物質創製における我が国の研究の厚みを継承し、新学術・新産業の創出と後継人材の育成を両立させながら、持続可能な社会の発展を導く。

1-3

本機構の組織

１－３．本機構の組織

本機構事業では、１－２で説明した機構研究の概念を実現するため、全く新しい大学間連携のフレームワークを構築する。一般論だが、これまでの大学間ネットワーク事業が抱える問題点としは、

① 高い大学間の壁
② 出口設定が難しく、研究目標を立てにくい
③ 平等主義によるガバナンス不足
④ 縦割り（大学別）の研究支援と人材育成支援
⑤ 外部意見が反映されにくい
⑥ 連携のメリットがネットワーク内に閉じる

などが挙げられる（図２(a)）。最大の問題点は⑥で、連携のメリットが社会発信されず、また社会の要請による事業という意識も希薄であった。ネットワーク形成のような大学強化事業は、社会からの認知によってはじめて達成されるもので、本研究推進機構事業においては、成果、情報、人材がネットワークの外側に輩出される外部発信型の連携を目指している。研究推進機構の組織図を図３に示すが、以下、運営体制、統括研究部門、研究支援部門についてその概要を説明する。

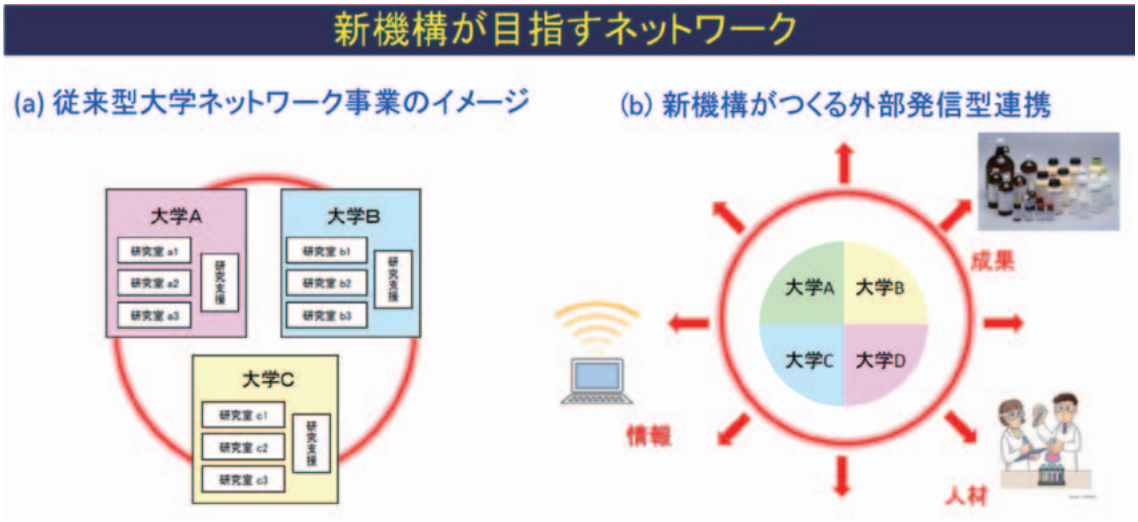

図２

運営体制

本事業推進に全責任を負う機構長を置く。機構長は、国内の学識経験者（4〜6名）や理化学研究所などの連携機関から派遣された委員、本事業の実行委員から構成される運営委員会を組織する。運営委員会は、連携事業計画の策定と成果の取纏めを行う。運営委員会で制定された事業計画は、研究統括部門の研究プラットホーム・リーダーから構成される実行委員会によって遂行される。

統合研究部門

機構長および運営委員会のリーダーシップの下、応用という研究の出口を意識した統合研究部門（新反応・新触媒、マテリアル、エネルギー・資源、ケムバイオの４研究プラットホーム）を設置する。各プラットホームには、連携大学から１研究室ずつ選抜した４研究室と、産官学・海外から招聘した連携客員研究室を設置して共同研究を実施する。各プラットホームにおける研究内容は以下の通りである。

新反応・新触媒研究：連携４大学の固体触媒（北大）、分子触媒（名大）、元素触媒（京大）、分子集合体触媒（九大）の研究チームの共同研究によって、ゼロエミッション・カップリング反応の開発など、必要なものを必要なだけグリーンにつくりだす化学を発展させ、炭素ナノ材料や医薬品の革新的合成に展開する。

マテリアル研究：炭素材料、ナノ粒子、有機物、無機固体、金属錯体、高分子に至る物質群の開発は、機構４大学が世界を先導している分野である。その研究は多岐にわたるが、例えば４大学が開発する新規光機能性分子を超分子化することによって、既存の細胞イメージングから、分子イメージングや更には機能イメージングへと発展させる。

エネルギー・資源研究：エネルギー・資源問題は化学が取り組むべき緊急課題である。金属ナノ粒子・界面の機能化（北大、名大）や革新的ナノカーボン材料開発（名大）を通じて、新しい燃料電池や太陽電池を開発する（北大、京大、九大）。X線吸収スペクトル計測（北大、名大）などによって反応機構を押さえながら、ユビキタス元素が生み出すグリーンエネルギーを創製する。

ケムバイオ研究：人工酵素を実現するための基本設計の確立は、生命科学における主題の一つである。生体分子合成（九大）とナノクラスター導入技術（京大）、ミューテーション技術（名大）を組み合わせ、計算シミュレーション（九大）を道しるべとしながら、機能をつくりこんだ人工酵素の合成にまで発展させる。

各研究プラットホームの構成は以下の通りである。

プラットホーム名	リーダー	コア研究室メンバー
新反応・新触媒	中野環（北大）	唯美津木・伊丹健一郎（名大）、中村正治（京大）、永島英夫・國信洋一郎（九大
マテリアル	島川祐一（京大）	清水研一（北大）、山口茂弘（名大）、高原淳・友岡克彦（九大）
エネルギー・資源	阿波賀邦夫（名大）	福岡淳（北大）、村田靖次郎（京大）、佐藤治（九大）
ケムバイオ	吉澤一成（九大）	長谷川淳也（北大）、阿部洋（名大）、二木史朗（京大）

各プラットホームにグループリーダーを置き、各分野の連携研究の推進に責任をもつ。さらに、各プラットホームでは若手研究者を特任助教や博士研究員として雇用する。これらの若手研究は、共通若手エース人事システムにより採用される。若手研究者の登竜門として機構を位置づけ、切磋琢磨による人材育成によって外部のパーマネント・ポジションに送り出す。

本機構内に限定せず、統合的な共同研究を促進するため、**融合創発研究**を実施する。共同研究提案を行い、運営委員会の審査を経て採択課題を決定し、実施する。また、年度末に研究成果について報告書を作成し、運営委員のレビューを受けるものとする。概ね毎年 10 件程度を実施する。

統括支援部門

名古屋大学物質科学国際研究センター内に設置し、センターに付設の化学測定機器室を用いて本事業の研究を支援するとともに、国際シンポジウム等の開催に必要な外国人研究者招聘に関わる事務手続き、本事業の研究成果の取纏め、ポスターの作成、ホームページの管理などの広報活動を担当する。具体的には、以下の支援を行う。

① **外部発信・国際発信**：機構の研究成果を、HP や種々のメディアなどを通じて国際的に広報する。
② **共同研究コーディネート**：機構研究全体を見渡して、新しい共同研究を萌芽させる。
③ **知財発掘と管理**：機構研究全体を見渡して、知財獲得を支援する。
④ **若手キャリアパス支援**：求職情報を若手に流布し、キャリアパスセミナーを実施する。
⑤ **会議・シンポジウム開催支援**：オープン参加型シンポなどを広報、支援する。

1-4

本機構の特徴

１－４．本機構の特長

社会に開かれた新機構は、以下の５つの特長を持つ。

① 戦略的なガバナンスに基づく融合研究：機構長のリーダーシップの下、応用という研究の出口を意識した統合研究部門（新反応・新触媒、マテリアル、エネルギー・資源、ケムバイオの４研究プラットホーム）を設置し、各プラットホームには、連携大学から１研究室ずつ選抜した４研究室と、産官学・海外から招聘した連携客員研究室を設置して共同研究を実施する。更に融合研究部門を設置し、産官学や国際連携の場とする。大学間の壁を乗り越え、かつ開かれた研究組織を構築する。

② イノベーション創出とグローバル化（図４）：研究部門を横断的に支援するため統括支援部門を設置し、マネージメント教員、プロジェクト支援員などを配置する。共同研究コーディネート、知財獲得、国際発信、若手人材育成などを、大学間の壁を取り払って行う。理化学研究所などを連携機関として加え、イノベーション創出などを活性化する。

③ 外部発信型連携：新しい産官学連携と国際連携のパラダイムを構築する。オープン参加型の成果報告会などを開催することによって、研究成果・研究情報・人材を、産業界、官界、学界、海外に対して外向きに発信・輩出する。

④ 共通若手エース人事システム（図５）：大学院生から若手研究者まで、各階層のニーズに合わせた人材育成を行う。特任助教や研究員の人事ついては、共通若手エース人事システムを採用する。すなわち、連携大学共通の選考委員会を設置して人選する。機構の

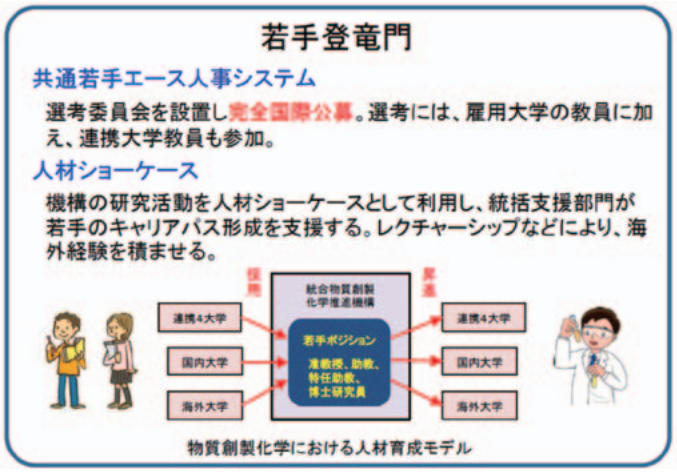

図４

研究活動を人材ショーケースとして利用して若手のキャリアパス形成を支援すると共に、レクチャーシップ派遣や招聘により国際的人脈形成を促す。若手研究者の登竜門として機構を位置づけ、切磋琢磨による人材育成によって外部のパーマネント・ポジションに送り出すことにより、物質創製分野における新たな人材育成モデルを実現する。

⑤ ナノ計測と計算化学の支援：ナノ計測と計算化学の支援の下、合理的な物質創製研究を展開する。

以上、基礎研究を重視しながらも、応用という研究の出口を意識した４テーマに各大学から１研究室を送り込む形で統合研究部門を形成することによって、互いの研究の強みを補完する研究体制を敷く。ガバナンスを効かした機構運営によって招聘される、理化学研究所などからの客員研究室の存在は、産官学との結びつきを強化すると共に、機構組織の流動性を高めるだろう。この上で、大学の壁を越えた統括支援部門による効率的な知財発掘や国際発信によって、新機構のビジビリティは必然的に高まる。このように、社会を意識した機構の研究活動は、院生や若手研究者の人材ショーケースとして作用し、前述した共通若手エース人事システムは人材の流動性を必然的に生み出す。

1-5

事業計画

１－５．事業計画

本事業のロードマップを図６に示す。

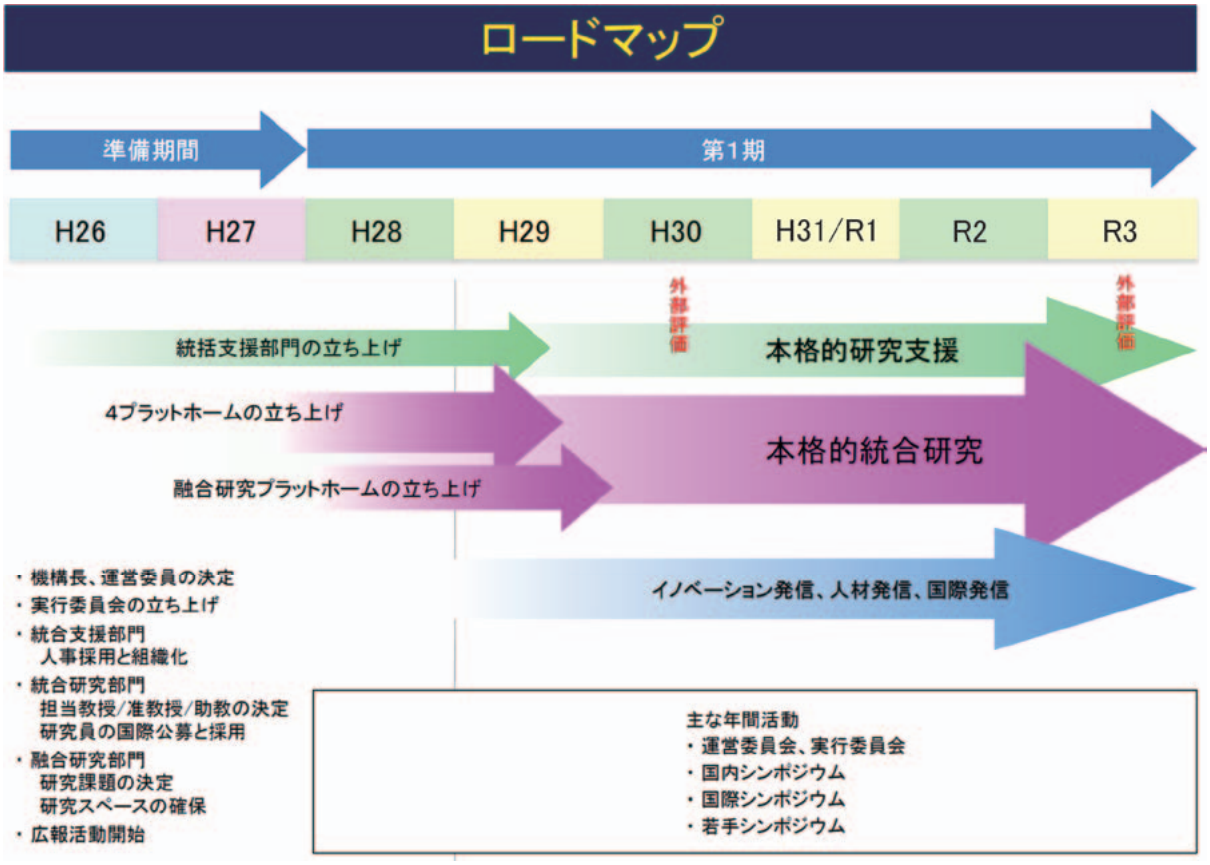

図６

1-6

本機構の期待される成果と波及効果

１－６．本事業の期待される成果と波及効果

１）本事業がめざす物質階層の統合と物質合成概念の統合により、総合的な物質観に基づく多彩な物質創製法が創出される。それらは、生体機能、電子機能、光機能、触媒機能などの有用機能をもつ機能性物質群を創造するための新学術基盤の構築へと展開される。

２）革新的な機能性物質群の創製は、材料科学分野に革新をもたらす。これまでの物質合成では、ナノテクノロジーで多用される熱力学支配による自己組織化が指導原理として用いられてきた。これに対して、本事業では、準安定物質の合成法の開拓により、自己組織化を超えた新規機能性物質群の創製法が開発されるものと期待される。これにより、高圧合成と薄膜技術の融合による非平衡物質群の創製、人工超格子をもつ特異な高次構造体の合成、光磁気特性を示す新規錯体や有機発光素子の開発、酵素反応の解明と生命機能の理解に資する人工酵素の合成などが達成され、最先端のバイオ・情報技術へと応用・展開される。

３）縦糸（基礎と応用）と横糸（多様な分野）が結ばれ、産官学及び国際的に開かれた物質創製化学研究が実施され、物質創製化学の新しい学術基盤が構築される。その結果、環境に優しい新触媒開拓、新規機能電子物質に基づく骨太イノベーション、更には新医薬品や生体活性物質開発が成される。これらは持続可能な文明社会の構築に大きく貢献する。

４）高度な研究機能をもつ国際研究拠点の有機的連携により、多くの若手研究者に広範な学問領域を統合した卓越した研究環境を提供することができる。このような環境は、幅広い知識と複眼的思考力を備えた中核研究者の養成に必要不可欠な要件である。本事業では、若手研究者を統合研究フェローとして処遇し、自由で創造的な研究環境を提供する。これにより、物質創製化学の将来を担う中核研究者を多数育成できるものと期待される。また、国際研究拠点の連携は、我が国の学術的先進性と国際競争力を確保するためにも重要であり、多くの若者に、海外の一流研究者と切磋琢磨する機会を提供し、国際的な研究者として成長するためのインセンティブを与える。

５）本申請が提案する新機構のスキームの有効性は、物質創製化学分野にだけ限定されない。このスキームにより、参加大学の強みを生かして我が国の学術を結集できるほか、大学間連携のメリットが産官学連携や国際連携を通じて外向きに発信されることにより、社会からの支持も得られる。この効果は、新国立研究所の設立にも匹敵する。このような外向きリンクの大学間連携事業のパイロットプログラムとして、他分野への波及効果やインパクトも大きい。

６）事業計画終了後は、新物質創製を総合的かつ戦略的に進める研究システムという枠組みは残しながらも、統括研究部門における研究テーマや参加研究室を全面的に見直し、また現在の連携 4 大学以外からの参加を促してオールジャパン体制をつくり、更に進んだ物質創製最先端研究を進める。

2

メンバー

2-1

コア研究室メンバー、連携研究室メンバー
リサーチフェロー

● 機構長

渡辺芳人
　名古屋大学 名誉教授

● 特別顧問

巽　和行
　名古屋大学 名誉教授

● 北海道大学

新反応・新触媒研究プラットホーム　メンバー一覧

＜コア・連携研究室＞

福岡　淳　教授（基礎研究系・物質変換研究部門）
高橋　保　教授（基礎研究系・分子触媒研究部門）
大谷文章　教授（基礎研究系・光触媒科学研究部門）
朝倉清高　教授（基礎研究系・触媒表面研究部門）
中野　環　教授（基礎研究系・高分子機能科学研究部門）
清水研一　教授（基礎研究系・触媒材料研究部門）
長谷川淳也　教授（基礎研究系・触媒理論研究部門）
西田まゆみ　教授（実用化推進系・研究開発部門）

＜リサーチフェロー＞ …令和２年３月末現在

佐川拓矢　研究員（触媒科学研究所・物質変換研究部門）

● 名古屋大学

エネルギー・資源研究プラットホーム　メンバー一覧

＜コア・連携研究室＞

阿波賀邦夫 教授（物性化学）

山口茂弘 教授（機能有機化学）

伊丹健一郎 教授（有機化学）

唯美津木 教授（無機化学）

阿部洋 教授（生物有機化学）

野依良治 特別教授・斎藤進 教授（分子触媒化学）

田中健太郎 教授（分子組織化学）

菱川明栄 教授（光物理化学）

柳井毅 教授（量子化学）

荘司長三 教授（生物無機化学）

＜リサーチフェロー＞ …令和２年３月末現在

Wu Yang（物性化学）

阿部奈保子（生物有機化学）

王晨光（機能有機化学）

● 京都大学

マテリアル研究プラットホーム　メンバー一覧

＜コア・連携研究室＞

中村 正治 教授（有機分子変換化学・元素科学国際研究センター）

島川 祐一 教授（先端無機固体化学・元素科学国際研究センター）

金光 義彦 教授（光ナノ量子物性化学・元素科学国際研究センター）

村田 靖次郎 教授（構造有機化学・化学研究所）

二木 史朗 教授（生体機能設計化学・化学研究所）

時任 宣博　教授（有機元素化学・化学研究所）

若宮 淳志　教授（分子集合解析・化学研究所）

＜リサーチフェロー＞…令和 2 年 3 月末現在

SHARMA, Akhilesh Kumar 特定研究員（有機分子変換化学・元素科学国際研究センター）

INJAC, Sean Dusan Alexander 研究員（先端無機固体化学・元素科学国際研究センター）

RAFIEH, Alwani Imanah Binti 研究員（分子集合解析・化学研究所）

● 九州大学

ケムバイオ研究プラットホーム　メンバー一覧

＜コア・連携研究室＞

吉澤　一成　教授（反応・物性理論分野・先導物質化学研究所）
佐藤　治　教授（分子物質化学分野・先導物質化学研究所）
國信　洋一郎　教授（機能分子化学分野・先導物質化学研究所）
友岡　克彦　教授（集積分子機能分野・先導物質化学研究所）
永島　英夫　教授（クラスター分子化学分野・先導物質化学研究所）
高原　淳　教授（複合分子システム分野・先導物質化学研究所）

＜リサーチフェロー＞ …令和 2 年 3 月末現在

塩田　淑仁　准教授（反応・物性理論分野・先導物質化学研究所）
金川　慎治　助教（分子物質化学分野・先導物質化学研究所）
SU, Shengqun　特任助教（分子物質化学分野・先導物質化学研究所）
河崎　悠也　特任助教（集積分子機能分野・先導物質化学研究所）

2-2

外部評価委員

● 外部評価委員

岩村 秀
　東京大学 名誉教授

岩澤康裕
　電気通信大学 燃料電池イノベーション研究センター長 特任教授

上村大輔
　神奈川大学 特別招聘教授

江崎信芳
　鳥取環境大学 学長

大峰 巌
　分子科学研究所 名誉教授

新海征治
　九州大学高等研究院 特別主幹教授

玉尾皓平
　豊田理化学研究所 所長

3

令和元年度事業報告

3-1

第３回 統合物質若手の会

統合物質創製化学研究推進機構（IRCCS）

第三回　若手の会

開催日：令和元（2019）年 7 月 12 日（金）~ 13 日（土）
会場：「久山温泉　ホテル夢家」
主催：統合物質創製化学研究推進機構

プログラム

令和元年 7 月 12 日（金）

14:00-14:25　参加登録
14:25-14:30　開会の挨拶

座長　宋 志毅（北海道大学　中野研准教授）
14:30-14:45　OP1　田原 淳士（九州大学　永島研助教）
「イリジウム触媒を用いたアミドのヒドロシラン還元による D-A 型π共役エナミン合成およびその物性評価」
14:45-15:00　OP2　河野 慎一郎（名古屋大学　田中研講師）
「カラムナー液晶および二次元単分子膜を構築するサルフェン型大環状化合物の開発」
15:00-15:15　OP3　後藤 真人（京都大学　島川研助教）
「異常高原子価鉄イオンを含む B サイト層状・無秩序ペロブスカイト酸化物の酸素脱離」

15:15-15:35　休憩

座長　田中 慎二（名古屋大学　北村研助教）
15:35-15:50　OP4　高 敏（北海道大学　長谷川研助教 ）
「Reactivity of Metal Clusters in the Regime of Structural Fluxionality」
15:50-16:05　OP5　井川 和宣（九州大学　友岡研助教）
「キラル分子の新規立体化学制御法「DYASIN」の開発と応用」
16:05-16:20　OP6　河野 健一（京都大学　二木研助教）
「膜曲率誘導によるオクタアルギニンの膜透過促進」

16:20-16:40　休憩

座長　鳥越 尊（九州大学　國信研助教）
16:40-17:30　招待講演 1　植村 卓史　先生（東京大学　教授）
「ナノ空間で高分子を制御する」

18:00-19:00　夕食

20:00-22:00　情報交換会

令和元年 7 月 13 日（土）

座長　行本　万里子（京都大学　時任研助教）

9:00-9:15　OP7　佐川 拓矢（北海道大学　福岡研博士研究員）
「キチン由来糖アルコールの脱水縮合反応」

9:15-9:30　OP8　阿部 司（九州大学　吉澤研特任助教）
「二核銅-酸素錯体の生成に及ぼす配位子効果に関する理論的研究」

9:30-9:45　OP9　有安 真也（名古屋大学　荘司研特任助教）
「シトクロム P450 による高圧条件下ガス状アルカンの直接水酸化」

9:45-10:05　休憩、写真撮影

座長　関根 康平（九州大学　國信研助教）

10:05-10:20　OP10　縣 亮介（京都大学　中村研特定研究員）
「鉄触媒クロスカップリング反応の開発と機能性有機化合物合成への応用」

10:20-10:35　OP11　高島 舞（北海道大学　大谷研助教）
「光触媒酸素発生反応における光強度依存性解析」

10:35-10:50　OP12　藤本 和宏（名古屋大学　柳井研特任准教授）
「励起エネルギー移動理論の開発と応用」

10:50-11:00　休憩

座長　井川 和宣（九州大学　友岡研助教）

11:00-11:50　招待講演 2　内田 竜也　先生（九州大学　准教授）
「効率的酸化反応を目指して」

11:50-12:00　閉会の挨拶
吉澤 一成　先生（九州大学、オブザーバー）

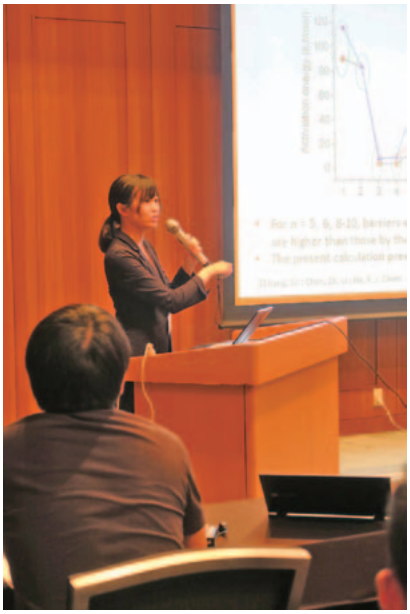


ナノ空間で高分子を制御する

3-2

第５回 統合物質国内シンポジウム

Integrated Research Consortium on Chemical Sciences

統合物質創製化学研究推進機構
第５回国内シンポジウム

物質創製化学のフロンティア

開催日
2019 年 11 月 18 日（月）13:00~18:30
19 日（火） 9:30~15:10

会場
北海道大学　創成科学研究棟　5F 大会議室

特別講演

丸岡 啓二　京都大学大学院薬学研究科　教授
「丸岡触媒®および簡素化丸岡触媒®の創製」

招待講演

井上 克也	広島大学 教授
畠山 琢次	関西学院大学　教授
本倉 健	東京工業大学 准教授

研究報告

北海道大学	福岡　淳	**名古屋大学**	菱川 明栄
	三輪　寛子		Jung Jieun
京都大学	村田 靖次郎	**九州大学**	國信 洋一郎
	河野 健一		金川 慎治

融合創発研究成果報告

名古屋大学	松井 公佑	**九州大学**	河崎 悠也

問い合わせ先
中野　環
北海道大学　触媒科学研究所　高分子機能科学研究部門
Tel: 011-706-9155　Fax: 011-706-9156
tamaki.nakano@cat.hokudai.ac.jp

統合物質創製化学研究推進機構　第５回国内シンポジウム

「物質創製化学のフロンティア」

平成３１年１１月１８日（月）～１９日（火）

（北海道大学　創成科学研究棟　5F　大会議室にて）

１１月１８日（月）

13:00-13:10　開会の辞

13:10-13:40　研究報告（A-1）　名古屋大学　菱川 明栄 教授

「位相制御２色強レーザー場による反応の可視化と制御」（ケムバイオ研究プラットフォーム）

13:40-14:00　研究報告（B-1）　京都大学　河野 健一　助教

「膜曲率誘導による膜透過性ペプチドの細胞内送達促進」（ケムバイオ研究プラットフォーム）

14:00-14:40　招待講演（IL-1）　東京工業大学　本倉 健　准教授

「協奏効果の発現へ向けた機能集積型触媒の開発」

14:40-15:00　休憩

15:00-15:30　研究報告（A-2）　北海道大学　福岡 淳　教授

「触媒によるバイオマス変換：セルロース・キチンから化学品の合成」（マテリアル研究プラットフォーム）

15:30-16:20　特別講演（PL）　京都大学　丸岡 啓二　教授

「丸岡触媒®および簡素化丸岡触媒®の創製」

16:20-16:30　休憩

16:30-17:10　ショートプレゼンテーション

17:10-18:30　ポスターセッション

18:30-20:00　懇親会

１１月１９日（火）

9:30-9:50　研究報告（B-2）　名古屋大学　Jung Jiuen　助教

「A highly efficient iridium photocatalyst for CO_2 reduction as a bi-functional photocatalyst」（新反応・新触媒研究プラットフォーム）

9:50-10:20　研究報告（A-3）　京都大学　村田 靖次郎　教授

「内包フラーレンの有機合成による孤立化学種の実現」（エネルギー・資源研究プラットフォーム）

10:20-10:40　休憩

10:40-11:20　招待講演（IL-2）　関西学院大学　畠山 琢次　教授

「超高色純度熱活性化遅延蛍光材料の開発」

11:20-11:35　融合創発研究成果報告（C-1）　名古屋大学　松井 公佑　助教

「3D-XAFS イメージングによる固体高分子形燃料電池の劣化機構の可視化」

11:35-11:50　融合創発研究成果報告（C-2）　九州大学　河崎 悠也　特任助教

「多分子連結素子 DACN-MMC の開発とペプチド化学への応用」

11:50-13:20　昼食

13:20-13:40　研究報告（B-3）　北海道大学　三輪 寛子　助教

「ミュオンスピン回転法を用いた触媒構造解析」（エネルギー・資源研究プラットフォーム）

13:40-14:10　研究報告（A-4）　九州大学　國信 洋一郎　教授

「非共有結合性相互作用を利用する炭素－水素結合変換反応における位置選択性制御法の開発」（新反応・新触媒研究プラットフォーム）

14:10-14:50　招待講演（IL-3）　広島大学　井上 克也 教授

「キラル物性科学―キラル磁性体の研究を中心に」

14:50-15:10　研究報告（B-4）　九州大学　金川 慎治 助教

「分子内電子移動を起源とする電子焦電性発現に向けた極性結晶構築戦略」（マテリアル研究プラットフォーム）

15:10-　閉会の辞


LOSED


CLOSED


CLOSED


CLOSED

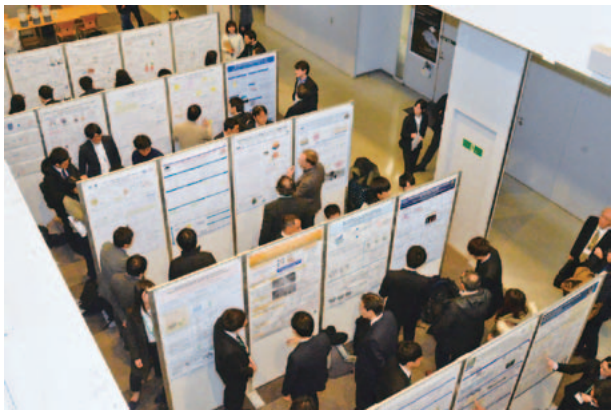


超高色純度熱活性化遅延蛍光材料の
開発


SED

3-3

第３回 統合物質国際シンポジウム

The 3rd IRCCS - The 2nd Reaction Infography Joint International Symposium : "Reaction Imaging Meets Materials Science"

Nagoya University
Noyori Materials Science Laboratory

January 31 - February 1, 2020

January 31

Keynote Lecture *Kaoru Yamanouchi*
François Légaré
Zhi Heng Loh
Jiro Itatani
Hideki Hirori
Shigeki Owada
Mizuho Fushitani
Satoru Takakusagi

February 1

Soo Young Park
Ning Jiao
Iwao Matsuda
Toshiki Sugimoto
Kenichi Shimizu
Takeru Torigoe
Masaharu Nakamura
Hideo Nagashima
Osami Shoji

Hosted by

Integrated Research Consortium on Chemical Sciences (IRCCS)
The World Research Reaction Infography (R-ing)

Contact

Research Center for Materials Science (RCMS) office
kihara@os.rcms.nagoya-u.ac.jp

The 3rd IRCCS - The 2nd Reaction Infography Joint International Symposium: "Reaction Imaging Meets Materials Science"

Nagoya University
Noyori Materials Science Laboratory
January 31 - February 1, 2020

January 31 (Friday)

9:30-9:45 **Opening Remarks**
Yoshihito Watanabe (Nagoya Univ.)
Mizuki Tada (Nagoya Univ.)

Session I
Chair: Akiyoshi Hishikawa

9:45-10:25 François Légaré (INRS-EMT, Canada)
"Probing the insulator to metal phase transition in VO_2 using high harmonic spectroscopy"

10:25-10:55 Jiro Itatani (Univ. Tokyo)
"Intense infrared and mid-infrared sources for attosecond science: new opportunities at higher energies and in solids"

10:55-11:25 Hideki Hirori (Kyoto Univ.)
"Extreme nonlinear optical phenomena caused by strongly driving electronic states in solids"

11:25-12:05 Zhi Heng Loh (Nanyang Tech. Univ., Singapore)
"Ultrafast molecular dynamics of transient ions probed by femtosecond XUV and soft X-ray radiation"

Lunch @ chez Jiroud

Session II
Chair: Mizuki Tada

13:15-13:45 Shigeki Owada (JASRI / RIKEN)
"Current status of SACLA"

13:45-14:15 Mizuho Fushitani (Nagoya Univ.)
"Mapping electron correlations in nonlinear ionization of Xe 4d double-core-hole states by multielectron-ion coincidence spectroscopy"

14:15-14:45 Satoru Takakusagi (Hokkaido Univ.)
"Development of *operando* PTRF-XAFS technique for elucidating 3D structure-activity relationship in heterogeneous catalysis"

Break

Chair: François Légaré
Keynote Lecture
15:05-16:05 Kaoru Yamanouchi (Univ. Tokyo)
"Ultrafast molecular dynamics and ultrahigh resolution spectroscopy using ultrashort intense laser pulses"

Group Photo

Poster Session
16:30-17:30

Banquet
17:45-19:00 @ Restaurant "Hananoki"

Februrary 1 (Saturday)

Session III
Chair: Ryotaro Matsuda
9:00-9:30 Iwao Matsuda (Univ. Tokyo)
"X-ray optospintronics at SACLA"

9:30-10:00 Toshiki Sugimoto (IMS)
"Infrared spectroscopy of water-assisted carrier trapping at TiO_2 photocatalyst surfaces with *distinct* morphologies"

10:00-10:30 Kenichi Shimizu（Hokkaido Univ.）
"Machine learning and DFT calculations for catalysis Informatics"

Break

Session IV
Chair: Susumu Saito
10:50-11:20 Takeru Torigoe (Kyushu Univ.)
"Iridium-catalyzed ortho-selective C–H borylation of thioanisole derivatives using simple bipyridine-type ligand"

11:20-11:50 Masaharu Nakamura (Kyoto Univ.)
"Exploring synthetic opportunities of iron catalysis in sustainable chemistry"

Lunch

Session V

Chair: Shigehiro Yamaguchi

13:10-13:40 Hideo Nagashima (Kyushu Univ.)
"Activation of H-H and H-Si bonds by transition metal-silicon linkage"

13:40-14:10 Osami Shoji (Nagoya Univ.)
"Hydroxylation of nonnative substrates catalyzed by cytochrome P450BM3 exploiting decoy molecules"

14:10-14:50 Soo Young Park (Seoul National Univ., Republic of Korea)
"Luminescent organic semiconductor"

Closing Remarks

Kunio Awaga (Nagoya Univ.)

P01 The first potential and polarization dependent BCLA+BI-XAFS studies on the PtAu model catalyst prepared by APD method
○ HU BING 【 北大 】

P02 A theoretical study of the factors affecting the CO2 and CO adsorption on Cobalt cluster
○ Min Gao, Hirokazu Kobayashi, Atsushi Fukuoka, Jun-ya Hasegawa 【 北大 】

P03 Theoretical Design for efficient intersystem crossing based on exploring minimal energy intersystem crossing point
○ Fuyu Yin, Min Gao, Naoki Nakatani, Akira Nakayama, Jun-ya Hasegawa 【 北大 】

P04 Synthesis and reactions of poly(naphthalene-1,4-diyl) as a precusor of tailor-made graphenes
○ Shiyi Song, Ka Son, Tamaki Nakano 【 北大 】

P05 Synthesis and chirality of hyperbranched polyphenylenes
○Yuting Wang, Zhiyi Song, Tamaki Nakano 【 北大 】

P06 Unexpected structural defects found in fluorene-based conjugated copolymers synthesized through Suzuki-Miyaura coupling
○ Yuehui Yuan, Zhiyi Song, Tamaki Nakano 【 北大 】

P07 A theoretical and spectroscopic study of In-CHA zeolite for activation of light alkanes
Shunsaku Yasumura, Chong Liu, Takashi Toyao, Zen Maeno, ○ Ken-ichi Shimizu 【 北大 】

P08 Applivation of Machine Learning to Discover New Heterogeneous Catalysts: A Case Study on Oxidative Coupling of Methane.
○ Motoshi Takao, Takashi Toyao, Zen Maeno, Satoru Takakusagi, Ichigaku Takigawa, Kenichi Shimizu 【 北大 】

P09 Role of Mesoporosity for Low Temperature Ethylene Oxidation over Hydrophobic Pt/Silica
○ Shazia Sharmin Satter, Kiyotaka Nakajima, Atsushi Fukuoka 【 北大 】

P10 Carbon Catalyzed Hydrolysis of Cellulose to Cello-oligosaccharides in a Semi-flow Reactor
○ Pengru Chen, Abhijit Shrotri, Atsushi Fukuoka 【 北大 】

P11 Single Atom Rh Promoted In2O3 for CO2 Hydrogenation to Methanol
○Shaikh Nazmul Hasan Mohammad Dostagir, Abhijit Shrotri, Atsushi Fukuoka 【 北大 】

P12 Production of hexitols from a real biomass molasses using a sponge Ni catalyst
○ Cheng Yang, Hirokazu Kobayashi, Atsushi Fukuoka 【 北大 】

P13 Travelling of carbon atoms in organic molecules.
○ Masayoshi Bando, Kiyohiko Nakajima, Zhiyi Song, Tamotsu Takahashi 【 北大 】

P14 Cation-distribution-tuned ferrimagnetism and perpendicular magnetic anisotropy in NiCo2O4 epitaxial films

○ Yufan Shen, Zhenhong Tan, Daisuke Kan, Yuichi Shimakawa 【京大】

P15 Synthesis of π-Conjugated Polymers Containing Benzodithiophene and Benzotriazole Units via Highly Selective Direct Arylation Polymerization (DArP): Effects of Homocoupling Defects on Photovoltaic Performance

○ Masayuki Wakioka, Naohiro Torii, Fumiyuki Ozawa 【京大】

P16 Artificial curvature inducing peptide triggering cellular endocytic uptake

○ Toshihiro Masuda, Shiroh Futaki 【京大】

P17 Programmable RNA methylation and demethylation using PUF RNA binding proteins

○ Miki Imanishi, Kouki Shinoda, Akiyo Suda, Shiroh Futaki 【京大】

P18 Development of a Method for Large Scale Synthesis of H2O@C60 Using a Triazine Derivative

○ Kazuro Kizaki, Kim Kyusun, Yoshifumi Hashikawa, Takashi, Hirose, Yasujiro Murata 【京大】

P19 Development of "Heavy Aryl Anions"

Yoshiyuki Mizuhata, Shiori Fujimori, Shingo Tsuji, Ryuto Sasayama, Norihiro Tokitoh 【京大】

P20 DFT study on Iron-catalyzed Enantioselective Carbometalation of Azabicycloalkenes

○ Akhiles K. Sharma, Masaharu Nakamura 【京大】

P21 Organic Hole-Transporting Material with High-Lying HOMO Energy Level for Tin-Based Perovskite Solar Cells

○ Minh Anh Truong, Ruito Hashimoto, Tomoya Nakamura, Richard Murdey, Atsushi Wakamiya 【京大】

P22 Fabrication of Emissive Perovskite Materials by Ligand Exchange for Light-Emitting Diodes

○ Alwani Imanah Rafieh, Ai Shimazaki, Yuko Matsushige, Yasuko Iwasaki, Tomoya Nakamura, Richard Murdey, Atsushi Wakamiya 【京大】

P23 Investigation of Ru7+ and Os7+ quantum magnets with scheelite and scheelite-derivative structures

○ Sean Injac, Maxim Avdeev, Brendan J. Kennedy, Yuichi Shimakawa 【京大】

P24 Large latent heat by intersite charge transfer transition in A-site ordered perovskites

○ Yoshihisa Kosugi, Masato Goto, Takashi Saito, Yuichi Shimakawa 【京大】

P25 Polarization Switching via Electron Transfer in a Valence Tautomeric Cobalt Complex

○ Osamu Sato 【九大】

P26 Electronic Pyroelectricities in Heterometallic Dinucler Complexes

○ Shinji Kanegawa 【九大】

P27　Understanding the magnetic change in an Iron(II) complex without spin transition
〇Shengqun Su　【九大】

P28　Photoabsorption and Photoluminescence Properties of Donor-Acceptor π Conjugated Enamines and Their Additive Effects with B(C6F5)3
〇 Atsushi Tahara, Daichi Sakata, Ikumi Kitahara, Yoichiro Kuninobu, Hideo Nagashima　【九大】

P29　Structure-property Relationship of Rubber Materials Based on Complex Network Science
〇 Yoshifumi Amamoto, Ken Kojio, Atsushi Takahara, Yuichi Masubuchi, Takaaki Ohnishi　【九大】

P30　Synthesis of cage-shaped molecules based on 1,8,13-*syn*-substituted triptycenes
〇 Takayuki Iwata, Tatsuro Yoshinaga, Yusuke Maehata, Mitsuru Shindo　【九大】

P31　Artificial Neural Networks Applied as Molecular Wave Function Solvers
Yang Peng-Jian, Mahito Sugiyama, Koji Tsuda,〇 Takeshi Yanai　【名大】

P32　Development of A Reduced-Scaling Multireference Perturbation Theory
〇 Masaaki Saitow, Takeshi Yanai　【名大】

P33　Magnetic properties of electrochemically delithiated spinel-LiMn2O4
〇 Qi Chen, Zhongyue Zhang, Kunio Awaga　【名大】

P34　Convert covalent organic frameworks to the electrode materials for supercapacitive energy storage
〇 Dongwan Yan, Yang Wu and Kunio Awaga　【名大】

P35　Synthesis and Translational activity of Chemically modified mRNA
〇Daisuke Kawaguchi, Ayumi Kodama, Yoshihiro Shimizu, Naoko Abe, Fumitaka Hashiya, Fumiaki Tomoike, Yasuaki Kimura, Hiroshi Abe【名大】

P36　Disulfide - unit conjugation enables ultrafast cytosolic internalization of antisense DNA and siRNA
〇Saki Kawaguchi, Shu Zhaoma, Azumi Ota, Kousuke Nakamoto, Fumiaki Tomoike, Yasuaki Kimura, Hiroshi Abe　【名大】

P37　Boron-Stabilized Red Emissive Radicals
〇 Masato Ito, Shunsuke Shirai, Naoki Ando, Tomokatsu Kushida, Yongfa Xie, Hiroki Soutome, and Shigehiro Yamaguchi　【名大】

P38　Photoreaction of Dithienylborane Derivative Bearing Bis(trimethylsilyl)phenyl Group
〇 Hirofumi Kajita , Naoki Ando , Shigehiro Yamaguchi【名大】

P39　Self-Assembly of Amphiphilic Aromatic Hydrocarbons into Nanosheets via Multiple CH/π Interactions
〇 Hiroki Narita, Tsuyoshi Nishikawa, Soichiro Ogi, Yoshikatsu Sato, Shigehiro Yamaguchi　【名大】

P40　Methane Oxidation Reaction by μ-Nitrido-Bridged Iron Phthalocyanine Dimer Bearing Eight 12-crown-4 Groups

○ Junichi Kura, Yasuyuki Yamada, Kentaro Tanaka 【名大】

P41　Synthesis and physical property of Tb(III)-phthalocyanine double-decker complex having planar chirality

○ Hiroaki Nakajima, Chisa Kobayashi, Yasuyuki Yamada, Yoshiaki Syuku, Kunio Awaga, Kentaro Tanaka 【名大】

P42　Synthesis of □-Expanded Porphyrin Derived from Tetra(*N*-carbazolyl)porphyrin

○ Atsuya Matsubuchi, Shin-ichiro Kawano, Kentaro Tanaka 【名大】

P43　Pd/TiO2-Photocatalyzed Self-Condensation of Primary Amines To Afford Secondary Amines at Ambient Temperature

Lyu Ming Wang, Kensuke Kobayashi, Mitsuhiro Arisawa, Susumu Saito, ○ Hiroshi Naka【名大】

P44　Spatiotemporal control of amide radicals under photocatalysis

○ Shogo Mori, Takahiro Aoki, Kaliyamoorthy Selvam, Shunichi Fukuzumi, Jieun Jung, Susumu Saito* 【名大】

P45　Molecular-frame photoelectron angular distributions (MFPADs) of tunneling electrons from D_2 in circularly polarized intense laser fields

○ Hikaru Fujise, Minami Takahashi, Daimu Ikeya, Takeru Nakamura, Akitaka Matsuda, Mizuho Fushitani, Akiyoshi Hishikawa 【名大】

P46　Three-dimensional molecular frame momentum distribution of photoelectrons from O_2 in circularly polarized intense laser fields

○ Daimu Ikeya, Hikaru Fujise, Akitaka Matsuda, Mizuho Fushitani, Akiyoshi Hishikawa 【名大】

P47　Isotope effects in tunneling ionization of molecular hydrogen in intense circularly polarized laser fields

○ Minami Takahashi, Hikaru Fujise, Takeru Nakamura, Akiyoshi Hishikawa 【名大】

P48　Association reaction of C_6H_{14}/N_2 gas flow system in femtosecond laser filament : laser-field intensity dependence

○ Kentaro Tani, Chiaki Kubo, Kasumi Hashigaya, Akitaka Matsuda, Akiyoshi Hishikawa 【名大】

P49　Asymmetric Coulomb explosion of CH_4 in phase-locked two-color intense laser fields

○ Hiroka Hasegawa, Hikaru Fujise, Akitaka Matsuda, Akiyoshi Hishikawa 【名大】

P50　Preparation of Oxide-supported Heterobimetallic Catalysts from Transition Metal Complexes

○ Aiko Asai, Satoshi Muratsugu, Mizuki Tada 【名大】

P51　Preparation and catalytic oxidation performance of rutile type IrO2 nanoparticles

○ Takatoshi Sudoh, Satoru Ikemoto, Satoshi Muratsugu, Mizuki Tada 【名大】

P52 Synthesis of Cubic [Mo3FeS4] Clusters for Biomimetic Activation of N2
○ Kenichiro Munakata, Keisuke Uchida, Ryota Hara, Mami Kachi, Mizuki Tada, Tsutomu Takayama, Yoichi Sakai, Roger E. Cramer, Yasuhiro Ohki 【名大】

P53 Direct monitoring of gas coordination-adsorption on MOFs with an in situ XAFS system
○ Hirotoshi Sakamoto, Akihiro Hori, Hirosuke Matsui, Ryotaro Matsuda, Mizuki Tada 【名大】

P54 Ligand-promoted PtNi Nanoparticles in Hollow Porous Carbon Spheres as Highly Active and Stable Oxygen Reduction Reaction Catalysts
○ Gabor Samjeské, Xian-Kai Wan, Satoshi Muratsugu, Hirosuke Matsui, Mizuki Tada 【名大】

P55 Topological molecular nanocarbons: All-benzene catenane and trefoil knot
○ Motonobu Kuwayama, Yuh Hijikata, Masako Fushimi, Taishi Nishihara, Jenny Pirillo, Junya Shirasaki, Natsumi Kubota, Yasutomo Segawa, Kenichiro Itami 【名大】

P56 Synthesis of a zigzag type carbon nanobelt
○ Kwan Yin Cheung, Yasutomo Segawa, Kenichiro Itami 【名大】

P57 Synthesis of cycloiptycenes from carbon nanobelt
○ Hiroki Shudo, Motonobu Kuwayama, Yasutomo Segawa, Kenichiro Itami 【名大】

P58 Synthesis of negatively curved polyaromatics by octagon-forming annulative coupling
○ Satoshi Matsubara, Yoshito Koga, Kei Murakami, Kenichiro Itami 【名大】

P59 Switchable sp^2/sp^3 C − H arylation of *N*-alkylaniline via EDA complex
○ Bumpei Maeda, Genki Mori, Yota Sakakibara, Akiko Yagi, Kei Murakami, Kenichiro Itami 【名大】

P60 Decarboxylative methylamination of aryl halides toward the synthesis of benzylamine derivatives
○ Jaehyun Jung, Yota Sakakibara, Kei Murakami, Kenichiro Itami 【名大】

P61 Synthesis of Various Polycyclic Aromatic Hydrocarbons by Annulative π -Extension Reactions
○ Keigo Yamada, Wataru Matsuoka, Maciej Krzeszewski, Hideto Ito and Kenichiro Itami 【名大】

P62 An Efficient Synthesis of Highly Twisted Macrocycles: 4,5-Diphenylphenanthrene as a New ChiralThree-dimensional Building Block
○ Yuanming Li, Akiko Yagi, Kenichiro Itami 【名大】

P63 Catalytic C − H Arylation of Cubane
○ Ryo Okude, Genki Mori, Akiko Yagi, Kenichiro Itami 【名大】

P64 Development of a synthetic method for unsubstituted nanocarbon
○ Shusei Fujiki, Akiko Yagi, Kenichiro Itami 【名大】

P65　Direct C-H borylation of pristine hexabenzocoronene
〇 Mai Nagase, Kenta Kato, Akiko Yagi, Yasutomo Segawa, Kenichiro Itami 【 名大 】

P66　Stereoselective benzylic hydroxylation catalyzed by cytochrome P450BM3 with decoy molecules
〇 Kazuto Suzuki, Joshua Kyle Stanfield, Sota Yanagisawa, Hiroshi Sugimoto, Yoshihito Watanabe, Osami Shoji 【 名大 】

P67　Sequence-selective recognition of double-stranded DNA by peptide nucleic acid
〇 Masanari Shibata, Masaki Hibino, Yuichiro Aiba, Osami Shoji 【 名大 】

P68　Aqueous two-phase extraction of semiconducting single-wall carbon nanotubes with isomaltodextrin and thin-film transistor applications
〇 Haruka Omachi, Tomohiko Komuro, Kaisei Matsumoto, Minako Nakajima, Hikaru Watanabe, Jun Hirotani, Yutaka Ohno, and Hisanori Shinohara 【 名大 】

P69　Solution-based SWCNT film fabrication on plastic substrate using methoxycarbonylated polyallylamine
〇Kaisei Matsumoto, Jun Hirotani, Hisanori Shinohara, Yutaka Ohno, and Haruka Omachi【 名大 】

P70　Gelation of polysaccharides for semiconducting SWCNT separation
〇 Yuki Matsunaga and Haruka Omachi 【 名大 】

P71　Transfer Hydration of Dinitriles to Diamides
〇Asuka Naraoka, Hiroshi Naka 【 名大 】

P72　Photocatalytic N-Methylation of Amino Acids with Methanol
〇Ivven Huang, Yuna Morioka, Susumu Saito, Hiroshi Naka 【 名大 】

P73　Synthesis of α -Amino Amides by Transfer Hydration of Nitriles
〇 Tomoyo Tamura, Taimeng Liang, Ryoji Noyori, Hiroshi Naka 【 名大 】

P74　Direct alpha-C(sp3) - H arylation of amides by Ni complex/TiO2 cooperative catalysts
〇Masaki Nomura, Shogo Mori, Susumu Saito【 名大 】

P75　Electrochemical- and photo-reduction of CO2 using base metal complexes bearing PNNP-type tetradentate ligands
〇 Taku Wakabayashi, Kenji Kamada, Jieun Jung, Susumu Saito 【 名大 】

P76　Ir-catalyzed transformation of bio-renewable even-numbered carboxylic acids into odd-numbered carbon chain
〇 Kazuki Teramoto, Shota Yoshioka, Susumu Saito 【 名大 】

P77　Development of Fluoro-phosphoroamidate Prodrug for Nucleotide Analogs
〇 Zheng Ti, Yuki Yoshida, Hirotaka Murase, Yasuaki Kimura, Hiroshi Abe 【 名大 】

P78 Nanoporous Metal Complexes with Active Sites for Selective Removal of Anticancer Drag
○ Yuki Harada, Shinpei Kusaka, Akihiro Hori, Ryotaro Matsuda 【名大】

P79 Controlling the Ordered Structure of Metal-Organic Polyhedra Utilizing DNA
○ Toshinobu Nakajo, Kosuke Nakamoto, Shinpei Kusaka, Akihiro Hori, Hiroshi Abe, Ryotaro Matsuda【名大】

P80 Direct Observation of Adsorption Heats in Nanoporous Metal Complexes with Flexible Structure
○ Yuta Kodera, Shinpei Kusaka, Akihiro Hori, Ryotaro Matsuda 【名大】

P81 Oxygen Adsorption Properties of a Photo-responsive Nanopourous Metal Complex at Room Temperature
○Ayaka Masuda, Shinpei Kusaka, Akihiro Hori, Ryotaro Matsuda【名大】

P82 Selective Adsorption of Trace Amount of Sulfur Containing Molecules Using Nanoporous Metal Complexes with Open Metal Sites
○Akira Yonezu, Masashi Morita, Shinpei Kusaka, Akihiro Hori, Ryotaro Matsuda 【名大】


The 3rd IRCCS -
The 2nd Reaction Infography
Joint International Symposium
"Reaction Imaging
Meets Materials Science"
January 31 - February 1, 2020


The 3rd IRCCS -
The 2nd Reaction Infography
Joint International Symposium
"Reaction Imaging
Meets Materials Science"
January 31 - February 1, 2020

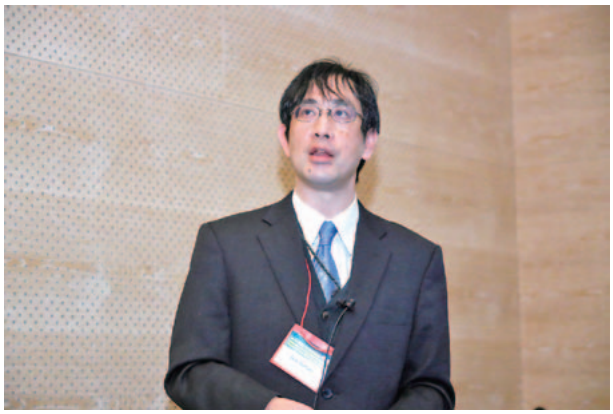


Closed
名古屋大学

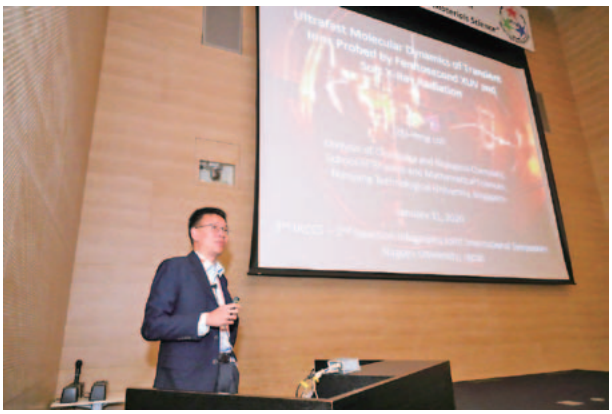

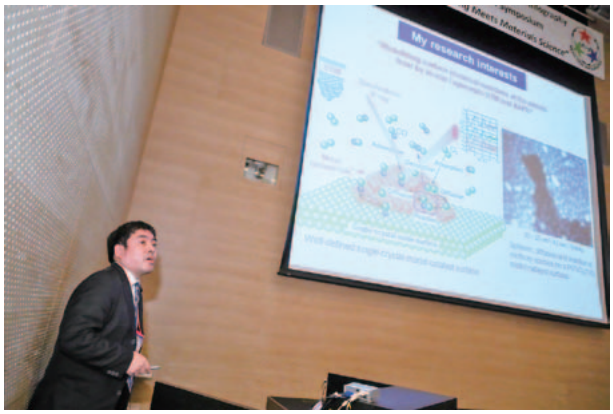
My research interests

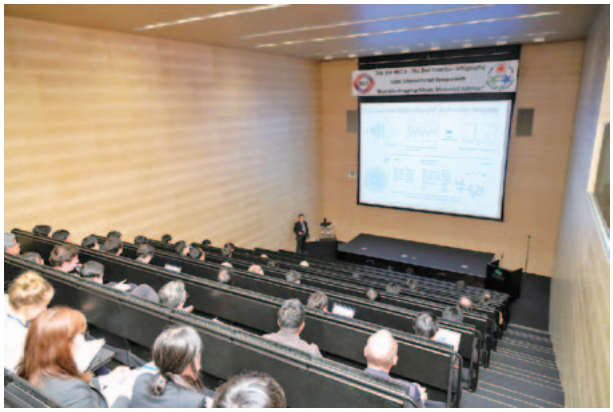

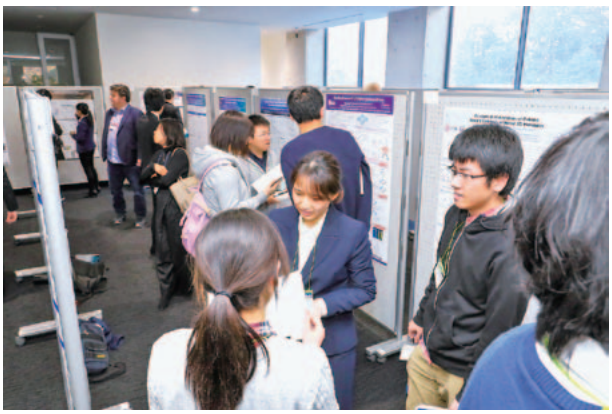

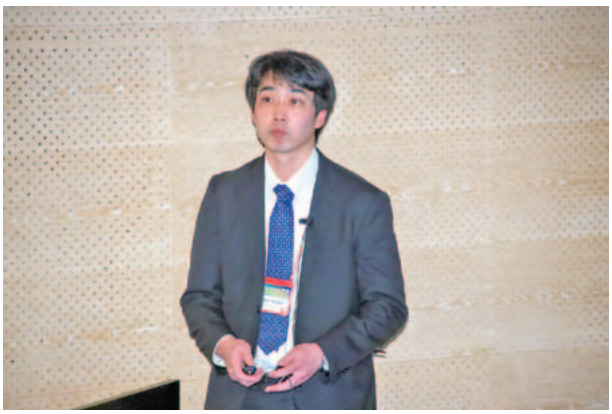


Closed

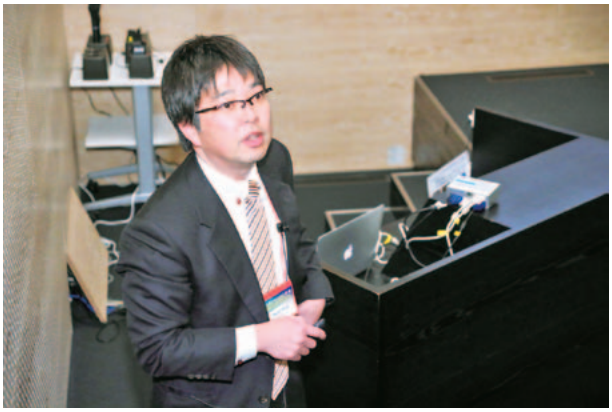

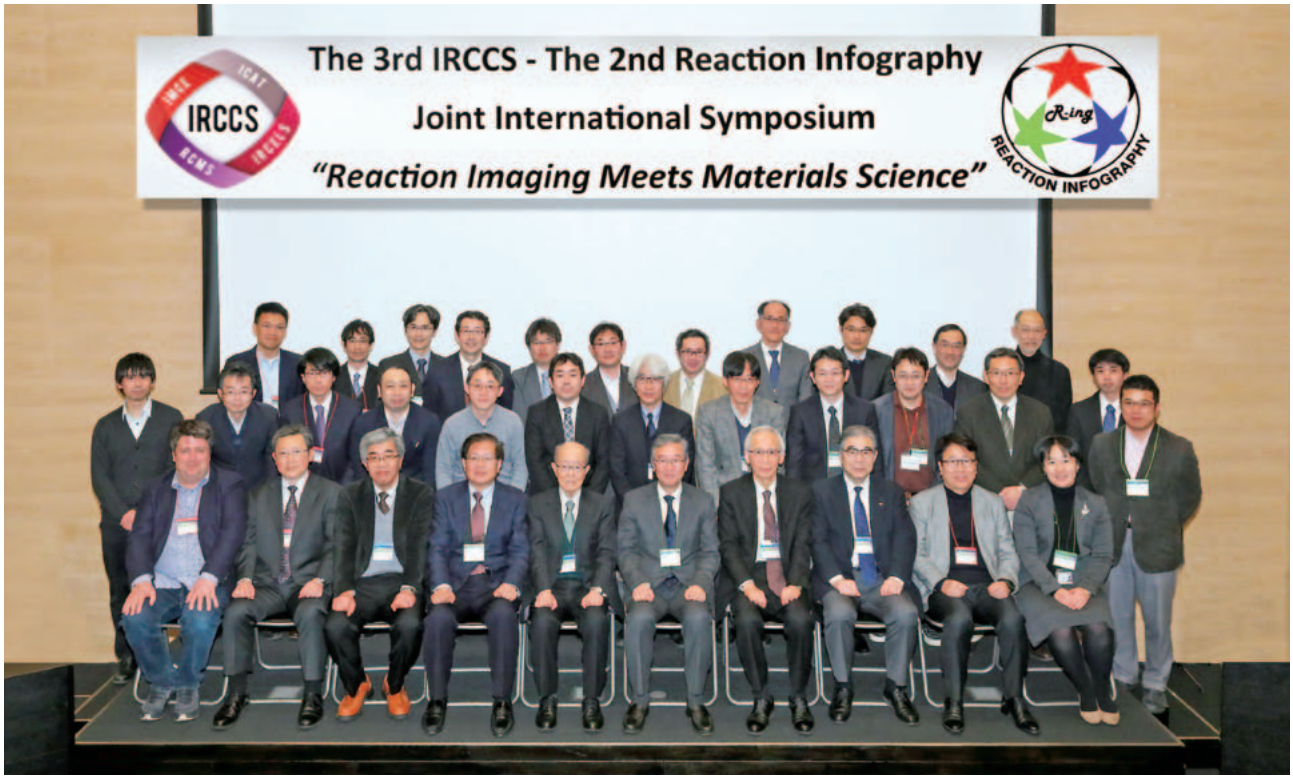
The 3rd IRCCS - The 2nd Reaction Infography
Joint International Symposium
"Reaction Imaging Meets Materials Science"
IRCCS
REACTION INFOGRAPHY

The first potential and polarization dependent BCLA+BI-XAFS studies on the PtAu model catalyst prepared by APD method

B. Hu [1], B. Bharate [1], J. D. Juan [2], K. Dong [1], H. Ariga-Miwa [1], S. Takakusagi [1], K. Asakura [1]

1. Institute for Catalysis, Hokkaido University, Hokkaido 001-0021, Japan
2. Department of Chemical Engineering, University of South Carolina, 541 Main St., Columbia, SC 29208, USA

Background

- The PtAu nanoclusters has demonstrated enhanced stability in acidic oxygen reduction reaction and has become a hot topic in electrocatalytic research.
- EXAFS can be used for structural investigation of Pt-Au/C under electrochemical conditions. However, due to the narrow gap (~350 eV) between Pt L3 edge and Au L3 edge, it is difficult to obtain EXAFS spectra on both edges.
- BI-XAFS ingeniously reduces the inelastic scattering of electrolyte.
- BCLA enables observation of both Pt L3 edge and Au L3 edge EXAFS.

BCLA+BI-XAFS Experiment

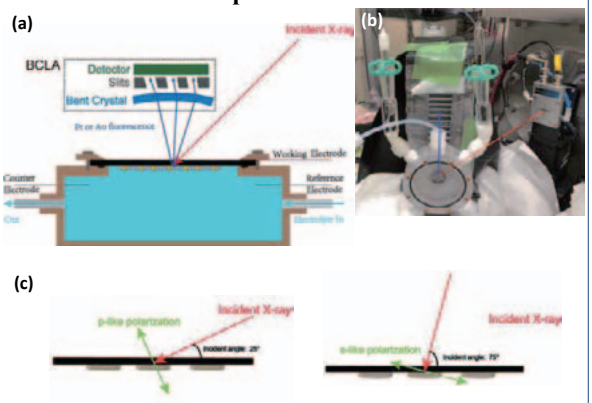

Fig.1 (a) Illustration of the experimental setup. (b) The real experimental setup. (c) Description of p-like and s-like polarization measurement (green arrows point polarization direction of X-ray).

XAFS Measurement

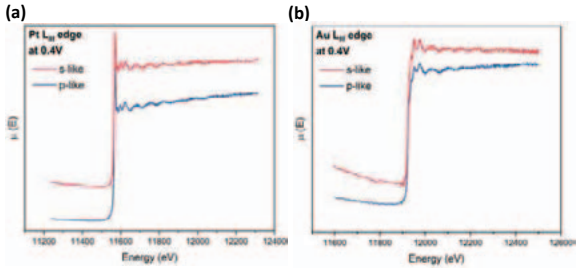

Fig.2 Polarization-dependent XAFS measurement of (a) Pt L3 edge and (b) Au L3 edge at 0.4 V vs. RHE.

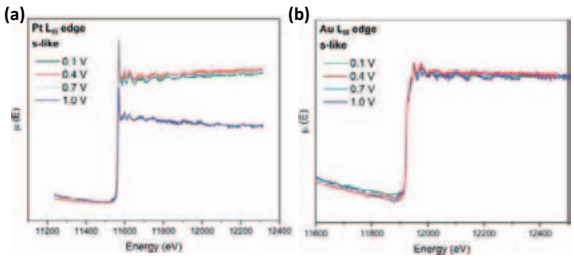

Fig.3 s-like XAFS measurement of (a) Pt L3 edge and (b) Au L3 edge at different electrochemical potentials vs. RHE.

- **We have successfully measured EXAFS at both Pt L3 and Au L3 edges.**
- **Results show dependence of EXAFS spectra on the polarization angle of X-ray and the electrochemical potential.**
- **Dissolution of Pt at 1.0V vs RHE is evidenced by the large drop of edge step. Meanwhile, there is no sign of Au dissolution.**

Surface Characterization

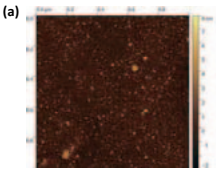

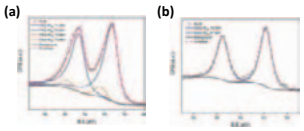

Figure.5 XPS spectra of the PtAu/HOPG sample. (a) Pt 4f spectra and (b) Au 4f spectra.

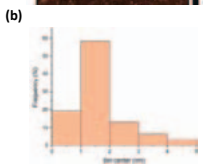

Figure.4 (b) AFM image and (b) particle-height histogram of the PtAu/HOPG model catalyst surface.

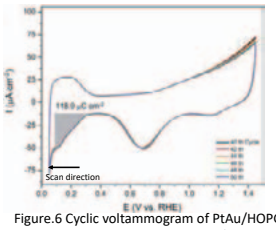

Figure.6 Cyclic voltammogram of PtAu/HOPG in 0.1 M $HClO_4$ with a scanning rate of 50 mV s^{-1}.

- **CV gives ~0.6ML of exposed Pt and ex-situ AFM shows cluster size of 1~2 nm, which suggest the Pt total amount is ~1 ML.**
- **XPS shows the Pt : Au is 2.5 : 1.**

Anisotropy in local structure

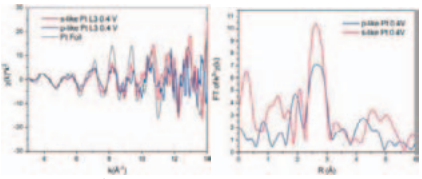

Pt L_{III}	N	Pt-M (Å)	dE (eV)	DW (Å)	R(%)
p-like	7.5 ±0.5	2.78 ±0.01	0.5 ±2.4	0.076	1.7
s-like	9.7 ±0.7	2.77 ±0.01	0.6 ±2.4	0.076	2.2

Fig.7 Analysis of Pt L3 edge EXAFS measured at s-like and p-like conditions at 0.4V vs. RHE.

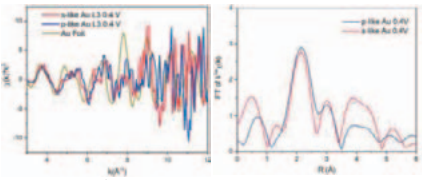

Au L_{III}	N	Au-M (Å)	dE (eV)	DW (Å)	R(%)
p-like	10.0 ±1.0	2.78 ±0.02	-1.4 ±2.1	0.085	6.6
s-like	9.1 ±0.9	2.78 ±0.02	-1.9 ±2.0	0.085	3.2

Fig.8 Analysis of Pt L3 edge EXAFS measured at s-like and p-like conditions at 0.4V vs. RHE.

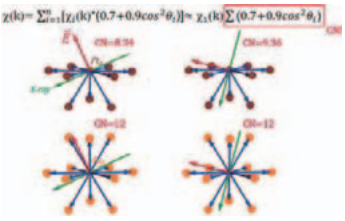

Fig.9 Coordination environment of Pt and Au based on polarization dependent EXAFS.

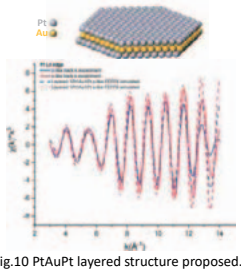

Fig.10 PtAuPt layered structure proposed.

Conclusions

- The BCLA + BI-XAFS setup enables both Pt L3 and Au L3 edges EXAFS measurement under electrochemical conditions.
- Based on the polarization dependence of Pt EXAFS oscillation and less polarization dependence of Au, a "PtAuPt" layered structure was proposed.

Acknowledgement

This work was finally supported by New Energy and Industrial Technology Development Organization (NEDO). We would also like to thank SPring-8 for the facility and staff support in XAFS measurement.

1. Takahashi S, Todoroki N, Myochi R, et al. Effective surface termination with Au on PtCo@ Pt core-shell nanoparticle: Microstructural investigations and oxygen reduction reaction properties[J]. Journal of Electroanalytical Chemistry, 2019, 842: 1-7.
2. Uehara, Hiromitsu, et al. "In situ back-side illumination fluorescence XAFS (BI-FXAFS) studies on platinum nanoparticles deposited on a HOPG surface as a model fuel cell: a new approach to the Pt-HOPG electrode/electrolyte interface." *Physical Chemistry Chemical Physics* 16.27 (2014): 13748-13754.

A theoretical study of the factors affecting the CO_2 and CO adsorption on Cobalt cluster

Min Gao, Hirokazu Kobayashi, Atsushi Fukuoka, Jun-ya Hasegawa

Institute for Catalysis, Hokkaido University

hasegawa@cat.hokudai.ac.jp; *gaomin@cat.hokudai.ac.jp*

Introduction

- **Catalyst for Partial oxidation of Methane**
  Noble metals with high activities and high cost
  Base metals require high temperature above 800 °C
- **Possible reaction mechanism**
  Direct Mechanism
  $CH_4 + 0.5O_2 \rightarrow CO + 2H_2$
  Indirect Mechanism
  $CH_4 + 2O_2 \rightarrow CO_2 + 2H_2O$
  $CH_4 + H_2O \rightarrow CO + 3H_2$
  $CH_4 + CO_2 \rightarrow 2CO + 3H_2$

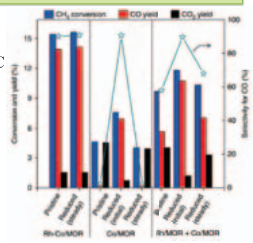

Figure. Effect of reduction of catalysts on the partial oxidation of methane.

- **Fukuoka & Kobayashi @ICAT[1]**

Cobalt catalyst modified with rhodium continuously gives 85~86% methane conversion and 90~91% CO selectivity with an H_2/CO ratio of 2.0 without serious coking at 650 °C.

- **Unsolved Problems**

➢ The main factor that influence selectivity of CO molecule is still not clear.

Computational Details

- **Computational model and Methods**
  Experimental Condition: mono-atomically dispersed rhodium (0.005 wt%)
  Computational Model: $Co_{12}Rh$, Co_{13} for comparison

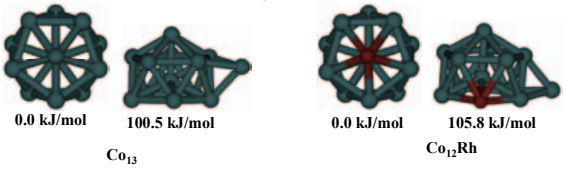

Totally 54/113 geometries are obtained for Co_{13}, $Co_{12}Rh$

- **Computational procedure**

Step 1. Search for all low-lying structures of metal clusters with SC-AFIR

Step 2. Search for geometries of CO/CO_2 adsorption on metal clusters at different environment conditions.

CO/CO_2 on Free Metal clusters

$E_{ads} = E_{Co13} + E_{COx} - E_{Tot}$

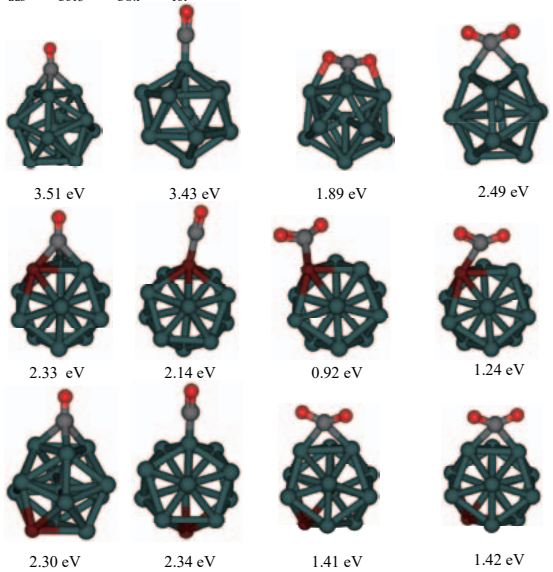

The doped Rh atom weakens interaction between Metal cluster and CO_2/CO

Effect of C/H ratio on CO/CO_2 adsorption

- **Geometries of Co_{13} Cluster with Dissociated CH_4**

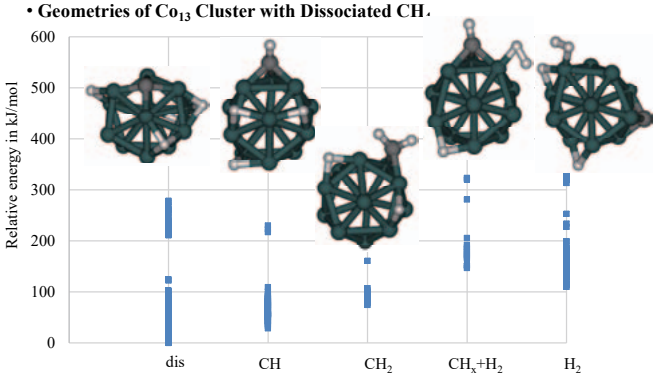

- **CO/CO_2 formation on the most stable Co_{13}-C-4H**

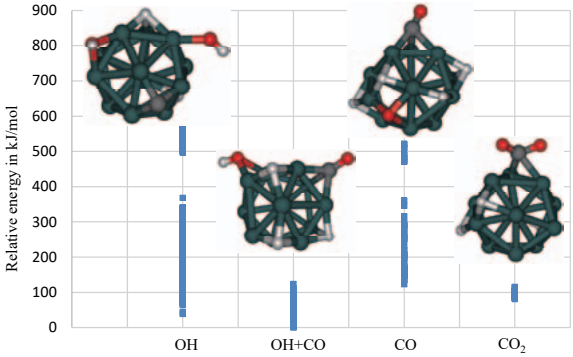

✓ The doped Rh atom weakens interaction between Metal cluster and CO_2/CO
✓ The CO_2 molecule can be formed when C:O is lager than 1:4
✓ The totally dissociated CH_4 is energetically favorable on Co_{13} clusters
✓ The CO molecule and OH species are more easily formed in the C/H environment.

Effect of C/O ratio on CO/CO_2 adsorption

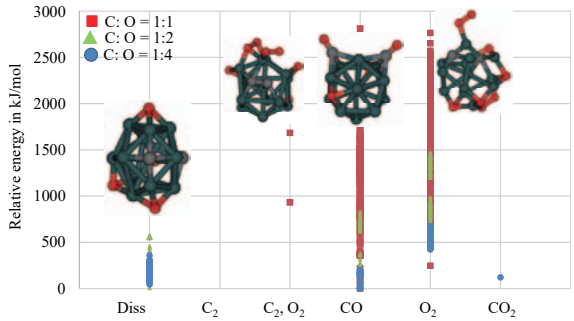

[1] Y. You, S. Nagamatsu, K. Asakura, A. Fukuoka, H. Kobayashi. Commun. Chem. 2018, 1, 41.

Theoretical Design for Efficient Intersystem Crossing based on Exploring Minimum Energy Intersystem Crossing Point (MEISCP)

Fuyu Yin[1], Min Gao[2], K-jiro Watanabe[2], Naoki Nakatani[3], Akira Nakayama[4], Jun-ya Hasegawa[2]
[1]Graduate School of Chemical Sciences and Engineering, Hokkaido University,
[2]Institute for Catalysis, Hokkaido University,
[3]Graduate School of Science and Engineering, Tokyo Metropolitan University,
[4]Graduate School of Engineering, The University of Tokyo

Introduction

Minimum Energy Intersystem Crossing Point (MEISCP): A point which has the lowest energy on the seam that formed by intersection of multiple potential energy surfaces. (see figure to the right)

Problems: Conventional methods using the energy gap of triplet and singlet states to evaluate the intersystem crossing (ISC) rate. The details of ISC was neglected.

This research: We proposed a straightforward approach improving the ISC by exploring MEISCP and extracting major reaction coordinates from the MEISCP.

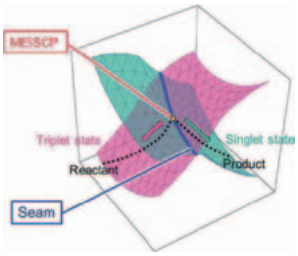

Schematic representation of minimum-energy intersystem-crossing point (MEISCP) in a spin-state changing reaction. (Frontiers of quantum chemistry. Springer Singapore; 2018.)

Computational Details

DFT calculations performed by Gaussian 09, E.01
Metallocene: M06L/def2-TZVP
Effective core potential for transition metals: ECP28MWB for Mo, ECP60MWB for W
Carotenoids: BP86/6-311g(d)
Algorithm optimizing MEISCP: coded based on a method optimizing conical intersections (Todd J. Martínez, J. Phys. Chem. B, 2008, 112, 405-413)

H_2 Binding Reaction on Metalltocene

Scheme of H_2 Binding Reaction on Metallocene (e.g. Molybdocene) [1]

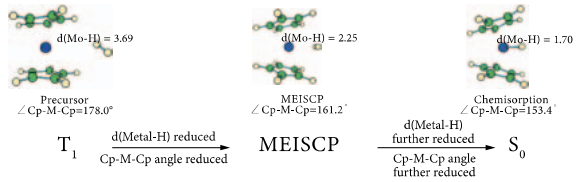

Important reaction coordinates:(1) d(Metal-H), (2) Cp-Metal-Cp angle

Energy decomposition analysis of H_2 binding reaction on molybdocene (left) and contribution of each reaction coordinate to ΔE^{ST}(right)

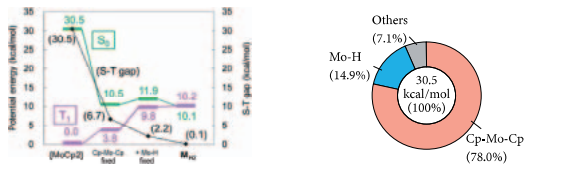

Cp-Metal-Cp has the major contribution reducing S-T gap

Proposed structure and energy profiles of **Molybdocene: original complex(a), ansa-complex(b)**

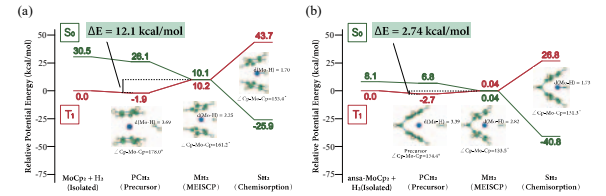

Proposed structure and energy profiles of **Tungstenocene: original complex(a), ansa-complex(b)**

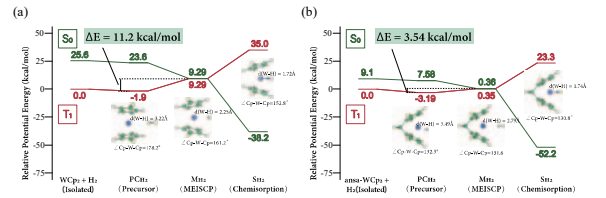

Proposed ansa-complexes have successfully reduced the energy barrier reaching MEISCP

Triplet Quenching of Carotenoids

Scheme of triplet quenching of carotenoids.(^{3}Car* → ^{1}Car + Heat) [2]

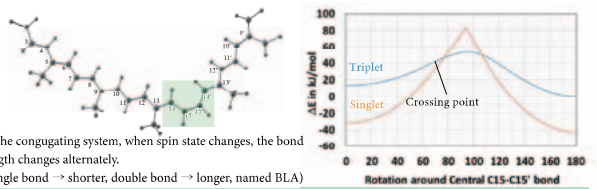

In the congugating system, when spin state changes, the bond length changes alternately.
(Single bond → shorter, double bond → longer, named BLA)

Important reaction coordinates:(1) Dihedral angle of C14-C15-C15'-C14', (2) BLA

Energy decomposition analysis (left). Contribution of each reaction coordinate to ΔE^{ST}(right)

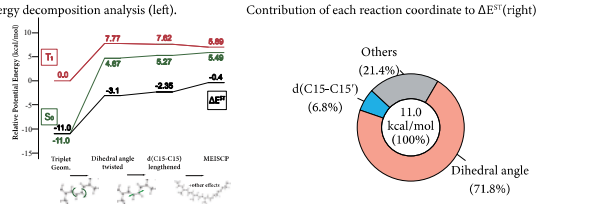

Dihedral angle of C14-C15-C15'-C14' has the major contribution reducing S-T gap

Modifying the dihedral angle by adding substituents

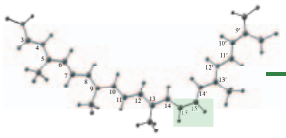

Hydrogen atoms adjacent to C15-C15' are replaced by: $-CH_3$,$-C_2H_5$, n-C_3H_7, $-NH_2$, $-OCH_3$, -F, etc.

Energy profile of carotenoids with replaced H atoms.

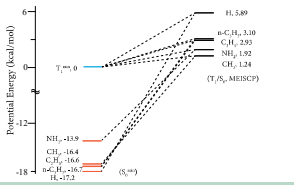

CH_3 substituted carotenoids gave the lowest energy barrier.

Conformation of CH_3 substituted carotenoid.

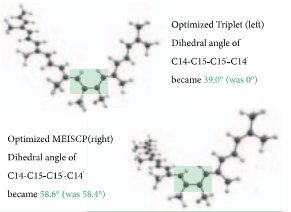

Substituents do not have significant effect on MEISCP.

Change in dihedral angle for different substituents.

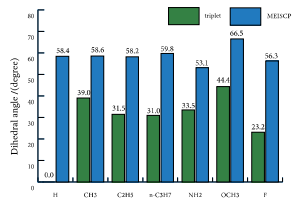

The dihedral in triplet state was twisted by substituents.

Conclusions

A general approach of molecular design was proposed for efficient intersystem crossing. The approach can be summarized as follows:

Exploring MEISCP → Specifying a major reaction coordinate → Design based on the reaction coordinate

References

[1] Watanabe KJ, Nakatani N, Nakayama A, Higashi M, Hasegawa JY., Inorg. Chem., 2016, 55 (16), 8082-8090.
[2] Arulmozhiraja S, Nakatani N, Nakayama A, Hasegawa JY., Phys. Chem. Chem. Phys., 2015, 17, 23468-23480.

Synthesis and Reactions of poly(naphthalene-1,4-diyl) as a Precursor of Tailor-made Graphenes

Zhiyi Song, Ka Son, Tamaki Nakano*

Institute for Catalysis (ICAT) and Graduate School of Chemical Sciences and Engineering, Hokkaido University, N 21, W 10, Kita-ku, Sapporo 001-0021, Japan

E-mail: tamaki.nakano@cat.hokudai.ac.jp

Graphene

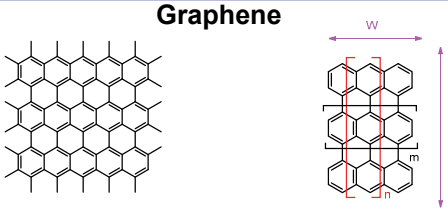

Graphene
Infinite in-plane structure,
zero-gap semiconductor
(uncontrollable)

Graphene segments
Confined in-plane structure,
Non-zero-gap semiconductor
(Controlled by Width (W) and Length (L))

Reported works:

Substrate-controlled growth limits the length while these methods lack versatility

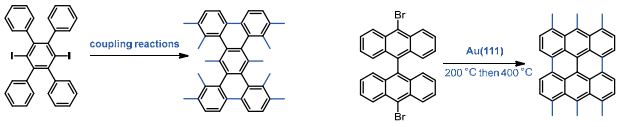

K. Mullen, *et al. J. Am. Chem. Soc.*, **2008**, *130*, 4216.

J. M. Cai, *et al. Nature*, **2010**, *466*, 470.

Our Strategies

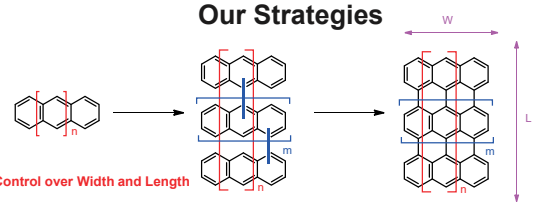

Control over Width and Length

This Work

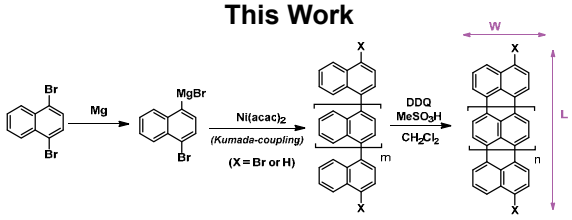

Polymerization of 1,4-Dibromonaphthalene

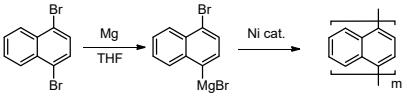

Run[a]	Temp. (°C)	Time (h)	[Ni]/[M]	Conv. [%]	MeOH-sol. Yield [%]	MeOH-insol.[c] Yield [%]	MeOH-insol.[c] M_n[b]
1	rt	1	0.01	88	54	43	970
2	rt	3	0.01	96	49	52	970
3	rt	6	0.01	96	34	65	930
4	rt	12	0.01	97	28	71	1020
5	rt	24	0.01	98	25	61	970
6	rt	24	0.02	96	33	58	950
7	rt	24	0.005	93	35	52	960
8	50	12	0.01	96	33	65	1010
9	reflux	3	0.01	95	21	77	1040

[a] $[Monomer]_0$ = 0.2 M in THF. [b]Determined by SEC (vs standard polystyrene). [c]THF soluable.

Soluble polymer with average molar mass of ca. 1000 was obtained.

Oxidative Structural Modification

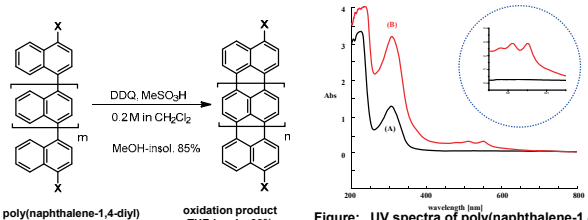

poly(naphthalene-1,4-diyl)
MeOH-insol.
THF-sol. M_n: 1000

oxidation product
THF-insol. >99%
THF-sol. <1%, M_n: 1600

Figure: UV spectra of poly(naphthalene-1,4-diyl)(THF-sol., 1cm, 0.0012 M, all) (A) and its oxidized product (THF-sol. part only) (B).

Raman Spectra

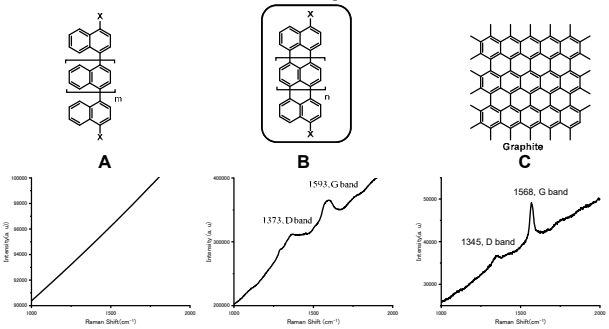

Figure: Lasa Raman spectra of poly(naphthalene-1,4-diyl) (A); its oxidized products (whole solid) (B) and Graphite (C) (λ_{ex} = 532 nm).

Insight into Oxidative Reaction

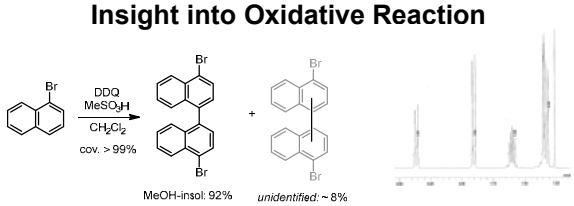

Insight into Oxidative Reaction

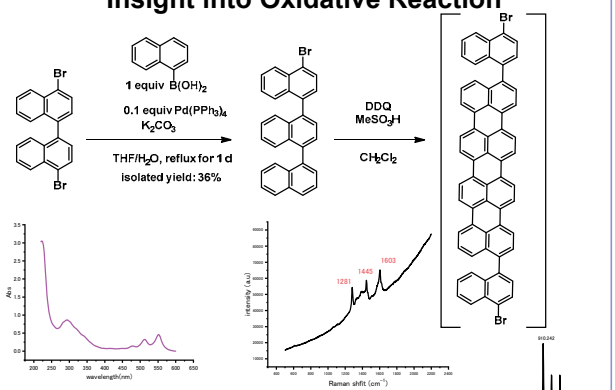

Figure: UV spectrum of the oxidized product (THF-sol., 1cm, 0.00018 M, all).

Figure: Lasa Raman spectrum of oxidized product (λ_{ex} = 532 nm).

Summary

1) Oxidation of poly(naphthalene-1,4-diyl) leads to an ordered GNR structure.
2) Intra-chain oxidation may not occur at chain terminal.
3) Inter-chain coupling may compete with intra-chain oxidation.

Synthesis and chirality of hyperbranched polyphenylenes

Yuting Wang,[1] Zhiyi Song,[1] and Tamaki Nakano[1,2]*

[1]*Institute for Catalysis (ICAT) and Graduate School of Chemical Sciences and Engineering, Hokkaido University, N 21, W 10, Kita-ku, Sapporo 001-0021, Japan;* [2]*Integrated Research Consortium on Chemical Sciences (IRCCS)*

E-mail: tamaki.nakano@cat.hokudai.ac.jp

Abstract: Main-chain conjugated polymers are an important class of materials that exhibit various photo electronic functions based on their long electronic conduction. Polyphenylene (poly(benzene-1,4-diyl)) is one of the simplest conjugated polymers consisting of benzene units directly connected to each other, and properties of polyphenylenes have been tuned mainly introducing side-chain alkyl groups. In this work, we introduce new polyphenylene derivatives having regular chain branching leading to hyperbranched, three-dimensional framework and studied their structures and basic properties as well as chirality induction using chiral external molecules and circularly polarized light (CPL).

Polymer Synthesis

Table 1. Synthesis of poly(benzene-1,3,5-triyl-*alt*-benzene-1,4-diyl) [**poly(BT-*alt*-BD)**] in dimethoxyethane at 80°C using $Pd(PPh_3)_4$ for 24 h[a]

Run	$[M_1]/[M_2]$ in Feed	Conv.[b] (%)	MeOH-insoluble product			
			THF-insol.	THF-sol.		
		M_2	Yield (%)	Yield (%)	M_n[c]	M_w/M_n[c]
1	1/1	90	0	47	430	1.50
2	1.5/1	>99	0	45	240	2.04
3	2/1	>99	51	21	580	1.88
4	3/1	>99	44	41	980	1.76
5	4/1	>99	92	15	860	1.47

[a]M_2 = 0.1 mmol, $[M_2]$ =0.05 M, $[Pd(PPh_3)_4]$ = 0.005 M (10 mol% with respect to M_2).
[b]Determined by ^{1}H NMR analysis of reaction mixture.
[c]Determined by SEC using polystyrene standard.

Table 2. Synthesis of poly(benzene-1,3,5-triyl-*alt*-biphenyl-4,4'-diyl) [**poly(BT-*alt*-BPD)**] in dimethoxyethane at 80°C using $Pd(PPh_3)_4$ for 24 h[a]

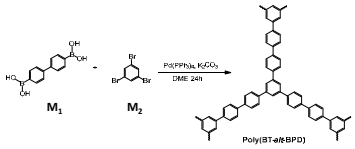

Run	$[M_1]/[M_2]$ in Feed	Conv.[b] (%)	MeOH-insoluble product			
			THF-insol.	THF-sol.		
		M_2	Yield (%)	Yield (%)	M_n[c]	M_w/M_n[c]
1	1/1	91	0	98	460	1.72
2	1.5/1	>99	4	97	520	1.86
3	2/1	>99	>99	9	710	1.65
4	3/1	>99	79	18	920	1.60
5	4/1	>99	>99	6	740	1.45

[a]M_2 = 0.1 mmol, $[M_2]$ =0.05 M, $[Pd(PPh_3)_4]$ = 0.005 M (10 mol% with respect to M_2).
[b]Determined by ^{1}H NMR analysis of reaction mixture.
[c]Determined by SEC using polystyrene standard.

Table 3. Synthesis of poly(benzene-1,3,5-triyl-*alt*-1,1':4',1''-terphenyl-4,4''-diyl) [**poly(BT-*alt*-TD)**] in dimethoxyethane at 80°C using $Pd(PPh_3)_4$ for 24 h[a]

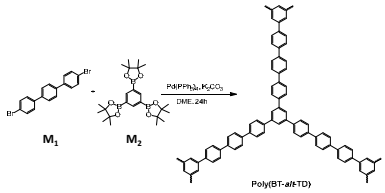

Run	$[M_1]/[M_2]$ in Feed	Conv.[b] (%)	MeOH-insoluble product			
			THF-insol.	THF-sol.		
		M_2	Yield (%)	Yield (%)	M_n[c]	M_w/M_n[c]
1	1/1	>99	35	>99	580	3.71
2	1.5/1	>99	12	>99	720	1.88
3	2/1	85	34	>99	660	2.32
4	3/1	>99	23	>99	660	2.22
5	4/1	>99	>99	>99	700	2.66

[a]M_2 = 0.1 mmol (runs 1,2,4,5) 1 mmol (run 3), $[M_2]$ =0.05 M, $[Pd(PPh_3)_4]$ = 0.005 M (10 mol% with respect to M_2).
[b]Determined by ^{1}H NMR analysis of reaction mixture.
[c]Determined by SEC using polystyrene standard.

Properties of THF-insoluble Polymers

Surface morphology

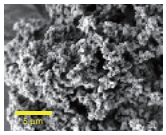

Fig. 1. SEM image of poly(BT-*alt*-BPD) (run 3 in Table 2). [3 kV, Pt coating]

Surface area and porosity

Table 4. BET analysis of **poly(BT-*alt*-BD)** and **poly(BT-*alt*-BPD)**

Polymer	$[M_1]/[M_2]$ in feed	Surface area (m^2/g)	Total pore volume (cc/g)
Poly(BT-*alt*-BD)	2/1	4.6	0.0109
	3/1	26.9	0.0423
	4/1	11.0	0.0378
Poly(BT-*alt*-BPD)	2/1	64.3	0.0532
	3/1	31.6	0.0547
	4/1	22.4	0.0526

Absorbance and fluorescence spectra

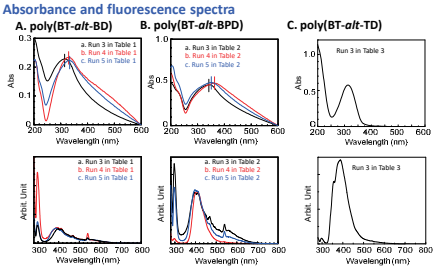

Fig. 2. UV (top) and fluorescence spectra of THF-insoluble poly(BT-*alt*-BD)s (A), poly(BT-*alt*-BPD)s (B), and poly(BT-*alt*-TD)s (C) made under different conditions: [suspension in paraffin, r.t; λ_{ex} for fluorescence 270 nm].

Properties of THF-soluble polymers

NMR spectra

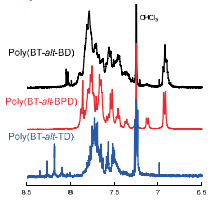

Fig. 3. ^{1}H NMR spectra of THF-soluble poly(BT-*alt*-BD) (run 4 in Table 1) (a), poly(BT-*alt*-BPD) (run 3 in Table 2) (b), and poly(BT-*alt*-TD) (run 3 in Table 3) [400 MHz, $CDCl_3$, r.t.].

Absorbance and fluorescence spectra *in THF solution*

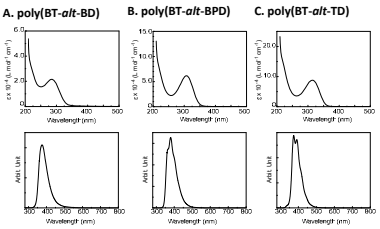

Fig. 4. UV (top) and fluorescence (bottom) spectra *in THF solution* of THF-soluble poly(BT-*alt*-BD) (run 4 in Table 1) (A), poly(BT-*alt*-BPD) (run 3 in Table 2) (B), and poly(BT-*alt*-TD) (C) (run 3 in Table 3) [r.t.; λ_{ex} for fluorescence 270 nm].

Absorbance and fluorescence spectra *in film*

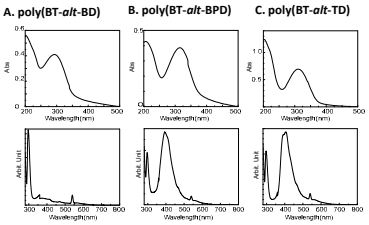

Fig. 5. UV (top) and fluorescence (bottom) spectra *in film* of THF-soluble poly(BT-*alt*-BD) (run 4 in Table 1) (A), poly(BT-*alt*-BPD) (run 3 in Table 2) (B), and poly(BT-*alt*-TD) (C) (run 3 in Table 3 [film samples coated on a quartz plate, r.t., λ_{ex} for fluorescence 270 nm].

Chirality Induction

Chirality induction to THF-insoluble polymers using α-pinene

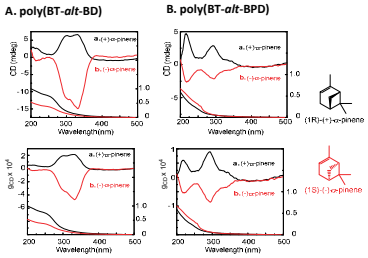

Fig. 6. CD-UV (top) and g_{CD}-UV spectra of THF-insoluble poly(BT-*alt*-BD) (run 4 in Table 1) (A) and poly(BT-*alt*-BPD) (run 3 in Table 2) (B) suspended in α-pinene enantiomers [(3 mg in 2 mL (pinene)]. The samples were heated at 100 °C for 20 h .

Chirality induction to THF-soluble polymers using CPL

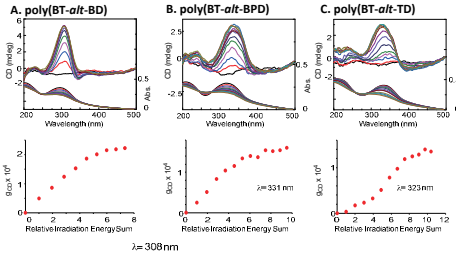

Fig. 7. CD-UV (top) spectra (top) observed on L-CPL irradiation and g_{CD}-vs.-irradiation energy plots (bottom) for cast film samples of THF-soluble poly(BT-*alt*-BD) (run 4 in Table 1) (A), poly(BT-*alt*-BPD) (run 3 in Table 2) (B), and poly(BT-*alt*-TD) (C) (run 3 in Table 3)

Conclusions: The Suzuki-Miyaura coupling polymeriztaions of relevant monomers led to THF-insoluble and –soluble polymers which are expected to possess hyperbranced structures. Surface morphology, surface areas and pore volume of the insoluble materials as well as photo physical properties of the soluble and insoluble materials were disclosed. In addition, chirality was successfully introduced to insoluble polymers using α-pinene as an additive and to soluble polymers in film form using circularly polarized light (CPL).

Unexpected Structural Defects Found in Fluorene-based Conjugated Copolymer through Suzuki-Miyaura Coupling

Yuehui Yuan,[1] Zhiyi Song,[1] and Tamaki Nakano[1,2]*

[1]Institute for Catalysis (ICAT) and Graduate School of Chemical Sciences and Engineering, Hokkaido University, N 21, W 10, Kita-ku, Sapporo 001-0021, Japan; [2]Integrated Research Consortium on Chemical Sciences (IRCCS);

E-mail: tamaki.nakano@cat.hokudai.ac.jp

Abstract: In order to expanded the scope of polymer ligand for catalysis,[1] a polymer ligand consisting of alternating 9,9-dioctylfluorene-2,7-diyl and 1,10-phenanthroline-3,8-diyl units (**poly(DOF-*alt*-Phen)**)[2] as well as a polymer consisting of alternating 9,9-dioctylfluorene-2,7-diyl and benzene-1,4-diyl (**poly(DOF-*alt*-Bz)**)[3] were synthesized through the Suzuki-Miyaura coupling method. The reaction was conducted in a toluene-ethanol mixture in the presence of $Pd(PPh_3)_4$ and K_2CO_3 at a temperature in the range of 60-120 °C; the conditions used in this work are consistent with standard methods of the coupling.[4] We found that **poly(DOF-*alt*-Phen)**s obtained at 80 °C or a higher temperature contained structural defects.

Polymer Synthesis

Table 1. Synthesis of **poly(DOF-*alt*-Bz)** using $Pd(PPh_3)_4$[a]

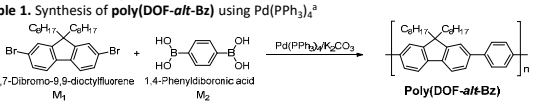

Entry	$[M_0]$[b] (M)	Catalyst Loading (%)	Temp. (°C)	Time (h)	Solvent	Conv.[c] (%)	$CHCl_3$-insol.[d] Yield (%)	$CHCl_3$-sol.[d] Yield (%)	M_n	M_w/M_n
1	0.067	3	130	6	Xylene	>99	1	4	1160	1.05
2	0.067	3	130	12	Xylene	>99	8	63	1210	1.05
3	0.067	3	130	24	Xylene	>99	29	39	1240	1.09
4	0.067	10	80	24	DME[e]	>99	8	7	4860	3.66
5	0.167	10	80	24	DME[e]	>99	9	68	3670	3.30
6	0.167	10	80	12	DME[e]	>99	6	>89	2480	1.07
7[f]		0.75	70	24	THF		79		23000	2.90

[a]M_1 0.5484 g (1 mmol) (entries 1,2 and 3), solvent 15 mL; 0.0957 g (0.2 mmol) (entry 4), 0.2743 g (0.5 mmol) (entries 5, 6), solvent 3 mL; M_2 0.1658 g (1 mmol) (entries 1, 2 and 3), solvent 15 mL; 0.0332 g (0.2 mmol) (entry 4), 0.0829 g (0.5 mmol) (entries 5, 6), solvent 3 mL. [b]$[M_0]$ denotes conentration of reactants. [c]Determined by NMR analysis of reaction mixture. [d]In entries 4, 5 and 6, the solvent was THF instead of $CHCl_3$. In entry 7, the solvent was methanol. [e]DME stands for dimethoxyethane. [f]Literature 3.

Table 2. Synthesis of **poly(DOF-*alt*-Phen)** using $Pd(PPh_3)_4$[a]

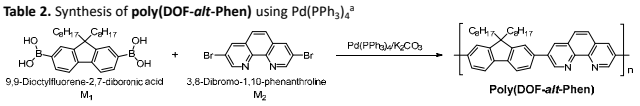

Entry	$[M_0]$[b] (M)	Catalyst Loading (%)	Temp. (°C)	Time (h)	Solvent	Conv. (%)[c]	THF-insol.[d] Yield (%)	THF-sol. Yield (%)	M_n	M_w/M_n
1	0.067	10	80	24	DME[e]	>99	13	60	1760	1.59
2	0.067	10	80	24	Toluene/Ethanol[f]	>99	71	28	1210	2.39
3	0.067	10	120	24	Toluene/Ethanol[f]	>99	25	99	1050	2.48
4	0.067	10	30	24	Toluene/Ethanol[f]	58	0	10	2070	1.60
5	0.067	10	60	24	Toluene/Ethanol[f]	>99	25	67	3000	1.85
6[g]	0.05	4	60	72	THF		84		6700	1.90

[a]M_1 0.0957 g (0.2 mmol), M_2 0.0676 g (0.2 mmol), solvent 3 mL. [b]$[M_0]$ denotes conentration of reactants. [c]Determined by NMR analysis of reaction mixture. [d]In entry 6, the solvent was methanol. [e]DME stands for dimethoxyethane. [f]Volunme ratio: Toluene/Ethanol = 2/1. [g]Literature 4.

Polymer Structure

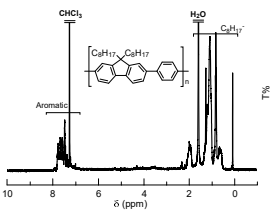

Fig. 1. 400 MHz ^{1}H NMR spectrum of **poly(DOF-*alt*-Bz)** (entry 1 in Table 1). [$CDCl_3$, rt]

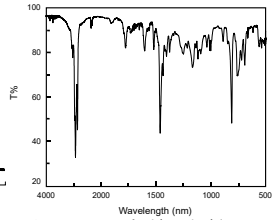

Fig. 2. IR spectrum of **poly(DOF-*alt*-Bz)** (entry 5 in Table 1). [KBr, rt]

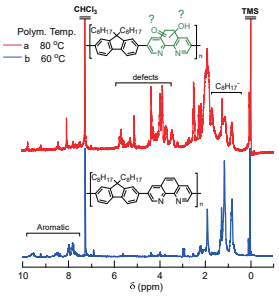

Fig. 3. 400 MHz ^{1}H NMR spectrum of **poly(DOF-*alt*-Phen)** (entry 1 and entry 5 in Table 2). [$CDCl_3$, rt]

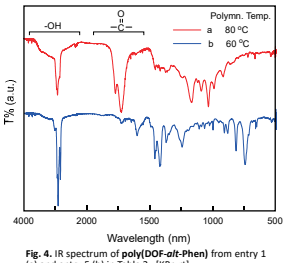

Fig. 4. IR spectrum of **poly(DOF-*alt*-Phen)** from entry 1 (a) and entry 5 (b) in Table 2. [KBr, rt]

Polymer Properties

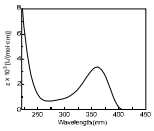

Fig. 5. UV spectrum of **poly(DOF-*alt*-Bz)** (entry 5 in Table 1). [THF, rt, 10-mm cell].

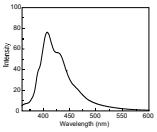

Fig. 6. Fluorescence spectrum of **poly(DOF-*alt*-Bz)** (entry 5 in Table 1). [THF, rt, 10-mm cell, λ_{ex} = 350 nm].

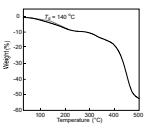

Fig. 9. TGA of **poly(DOF-*alt*-Bz)** (entry 5 in Table 1). [rate : 10 °C/min].

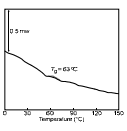

Fig. 10. DSC profile of **poly(DOF-*alt*-Bz)** (entry 5 in Table 1). [2nd heating scan at a rate of 10 °C/min. Intensity of the profile has been normalized to a sample amount of 10.0 mg.]

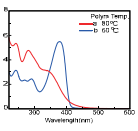

Fig. 7. UV spectra of **poly(DOF-*alt*-Phen)** from entry 1 (a) and entry 5 (b) in Table 2. [THF, rt, 10-mm cell].

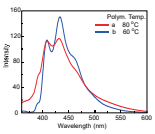

Fig. 8. Fluorescence spectra of **poly(DOF-*alt*-Phen)** from entry 1 (a) and entry 5 (b) in Table 2. [THF, rt, 10-mm cell, λ_{ex} = 350 nm].

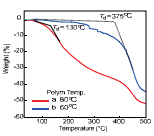

Fig. 11. TGA of **poly(DOF-*alt*-Bz)** (entry 5 in Table 2). [rate : 10 °C/min].

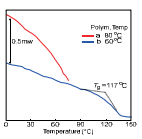

Fig. 12. DSC profiles of **poly(DOF-*alt*-Phen)** from entry 1 (a) and entry 5 (b) in Table 2. [2nd heating scan at a rate of 10 °C/min. Intensity of all profiles has been normalized to a sample amount of 10.0 mg.]

Control Reactions

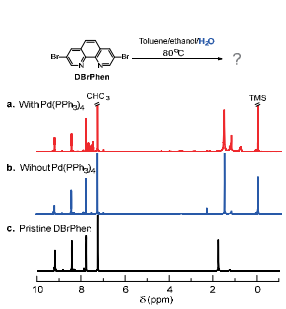

NMR spectra of reaction mixtures of poly(DOF-*alt*-Phen) with H_2O with $Pd(PPh_3)_4$ (a) and without $Pd(PPh_3)_4$ (b) and that of pristine poly(DOF-*alt*-Phen) (c). [400MHz, r.t, $CDCl_3$]

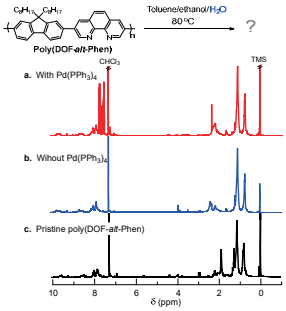

NMR spectra of reaction mixtures of DBrPhen with H_2O with $Pd(PPh_3)_4$ (a) and without $Pd(PPh_3)_4$ (b) and that of pristine DBrPhen (c). [400MHz, r.t, $CDCl_3$]

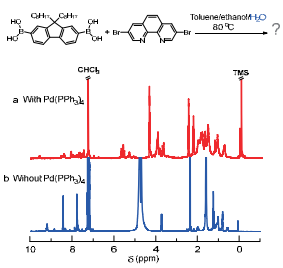

NMR spectra of Poly(DOF-*alt*-Phen) of entry 2 in Table 1(a), products after same reaction without $Pd(PPh_3)_4$ (b). [400MHz, r.t, $CDCl_3$]

Conclusions:

Poly(DOF-*alt*-Phen)s prepared at 80°C or a higher temperature appeared to have defective chemical structures while the structure of **poly(DOF-*alt*-Bz)** was good under all conditions we examined. The defects may be based on H_2O addition to aromatic systems.

1) A. Kimura, H. Hayama, J.-y. Hasegawa, H. Nageh, Y. Wang, N. Naga, M. Nishida and T. Nakano, *Polym. Chem.*, **2017**, *8*, 7406-7415.
2) T. Yasuda and T. Yamamoto, *Macromolecules*, **2003**, *36*, 7513-7519.
3) Bondarev, D. , Zedník, J. , Vohlídal, J. , Podhájecká, K. and Sedláček, J., *J. Polym. Sci. A Polym. Chem.*, **2009**, *47*, 4532-4546.
4) (a) N. Miyaura and A. Suzuki, *Chem. Rev.*, **1995**, *95*, 2457–2483; (b) A. Suzuki, *Angew. Chem. Int. Ed.*, **2011**, *50*, 6722–6737; (c) N. Miyaura, K. Yamada and A. Suzuki, *Tetrahedron Lett.*, **1979**, *20*, 3437–3440.

A theoretical and spectroscopic study of In-CHA zeolite for activation of light alkanes

Shunsaku Yasumura, Chong Liu, Takashi Toyao, Zen Maeno, Ken-ichi Shimizu
Institute for Catalysis, Hokkaido university, N-21, W-10, Sapporo 001-0021, Japan

Introduction

Isolated surface hydrides

Christophe Copéret *et al.*, Chem. Rev. 2016, 116, 8463−8505

- Ubiquitous as intermediates in catalytic reactions
- Difficulty in structure analysis of solid surfaces

➢ Ga-hydride in zeolite

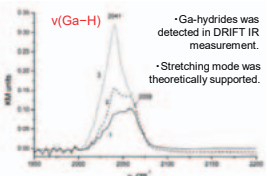

- Ga-hydrides was detected in DRIFT IR measurement.
- Stretching mode was theoretically supported.

R. A. van Santen *et al.*, J. Phys. Chem. A, 2000, 104, 2468-2475
E. J. M. Hensen *et al.*, J. Catal., 2004, 227, 263–269

➢ Surface hydride on indium oxides

- Unique hydrogenation catalysis

In_2O_3 supported on ZrO_2 for selective hydrogenation of CO_2 to MeOH
J. Pérez-Ramírez *et al.*, ACIE, 2016, 55, 6261-6265

Semihydrogenation of acetylene on In_2O_3
J. Pérez-Ramírez *et al.*, ACIE, 2017, 56, 10755-10760

- Characterization of In-hydrides

H_2 activation by frustrated Lewis pairs on In_2O_3
G. A. Ozin *et al.*, ACIE, 2019, 58, 9501-9505

Characterization and catalysis of surface In-hydrides have attracted much attention.

Our recent work: CH_4 activation by In-oxo cluster in zeolites

Zen Maeno, Shunsaku Yasumura and Ken-ichi Shimizu *et al.*, Phys. Chem. Chem. Phys., 2019, 21, 13415-13427
Highlighted in Front Cover

In K-edge XAFS analysis implied the formation of In-hydrides rather than bare In cation via reductive solid-state ion exchange.

This work

✔Comprehensive characterization of In-hydrides in CHA zeolites based on spectroscopic and theoretical studies

✔Catalytic application of CHA-supported In-hydrides for C_2H_6 dehydrogenation

Synthesis & Characterization

Synthesis

CHA zeolite + $In(NO_3)_3 \cdot nH_2O$

↓ 1. Impregnation 2. Calcination (773 K)

Yellow powder

In_2O_3/CHA

↓ H_2, 773 K — Reductive solid-state ion-exchange

White powder

In-CHA

In situ FT-IR

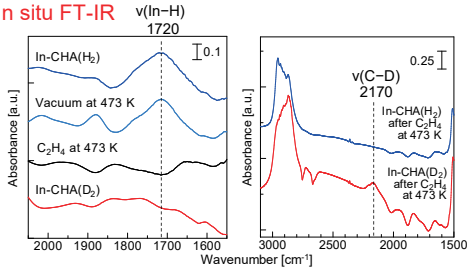

- Stretching mode of In−H bond was observed.
- C−D bond was formed via reaction of In−D with C_2H_4.

In situ XANES

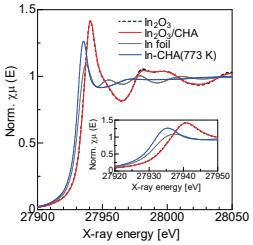

- Absorption edge shifted toward lower energy than In foil after H_2 treatment.

FT-EXAFS

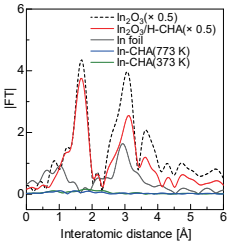

- Scattering peak was hardly observed after H_2 treatment.

NH_3 adsorption (FT-IR)

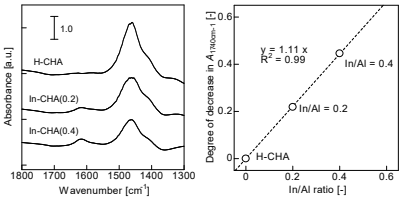

- One H^+ was exchanged with one In-hydride species.

Vibrational analysis

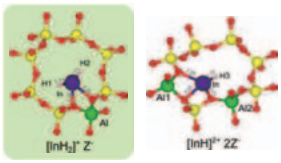

Frequency	$[InH_2]^+$	$[InH]^{2+}$
Single 1Al site	1735.6	-
Paired 2Al site	1721.2	1793.0

TS calculation for feasibility of $[InH_2]^+$

- H_2 elimination from $[InH_2]^+$
- $[InH_2]^+$ formation form $[InH]^{2+}$

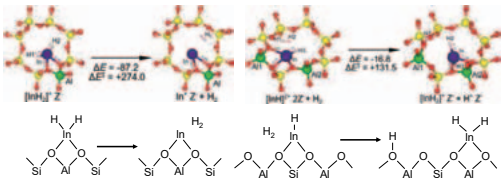

$[InH_2]^+ Z^-$ is the most plausible In-hydride species.

C_2H_6 dehydrogenation

High durability of In-CHA

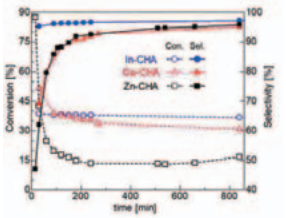

Temperature: 700°C, Catalyst: 0.1 g, Flow: 10% C_2H_6/He (Total flow: 10 mL/min)

In-CHA maintained high selectivity.

Kinetic study

- $p(H_2)$ dependency

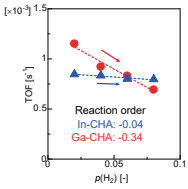

In-CHA showed zero-order kinetics with respect to $p(H_2)$.

- M/Al dependency

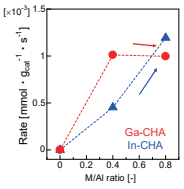

Reaction rate linearly increased with In/Al ratio.

- Apparent activation energy: E_a = 235 kJ/mol

Reaction mechanism

cf. Proposed mechanism on $[GaH]^{2+}$ in Ga-zeolites
A. T. Bell et al, J. Am. Chem. Soc. 2019, 141, 1614-1627

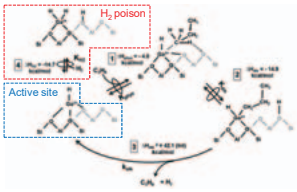

C_2H_6 dehydrogenation by In-CHA occurs
✔ on $[InH_2]^+$ rather than $[InH]^{2+}$
✔ via concerted mechanism

1) H_2 does not inhibit the reaction.
2) Reaction rate increased beyond In/Al = 0.5.
3) $[InH_2]^+$ is stable in the presence of H_2.
4) Calculated E_a for concerted mechanism is in agreement with the experimental value.

TS calculation for C_2H_6 dehydrogenation on $[InH_2]^+$

- Concerted mechanism

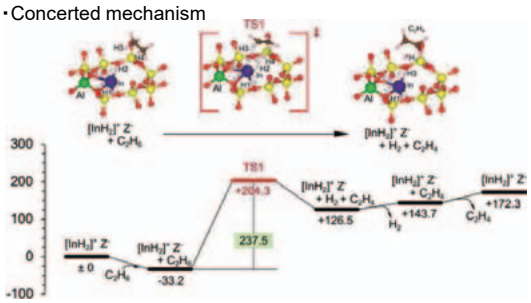

- Stepwise alkyl mechanism

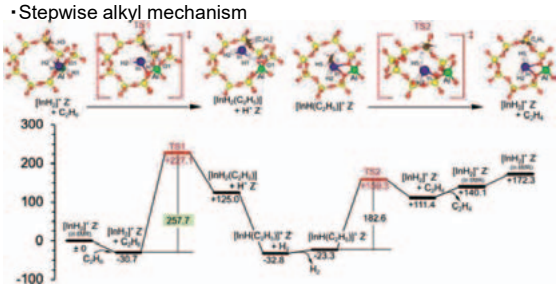

Application of Machine Learning to Discover New Heterogeneous Catalyst
A Case Study on Oxidative Coupling of Methane

Motoshi Takao,[a] Takashi Toyao,[a,b] Zen Maeno,[a] Satoru Takakusagi,[a] Ichigaku Takigawa,[c] Kenichi Shimizu[b]

[a]Institute for Catalysis, Hokkaido university, N-21, W-10, Sapporo 001-0021, Japan
[b] Elements Strategy Initiative for Catalysts and Batteries, Kyoto University, 615-8520, Kyoto, Japan
[c] Institute for Chemical Reaction Design and Discovery (WPI-ICReDD), Hokkaido University,N-21, W-10, Sapporo 001-0021, Japan

Introduction

Our previous studies

◆ ML prediction of the d-band center

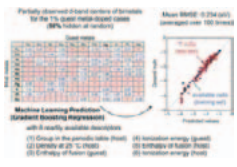

I. Takigawa, K. Shimizu, K. Tsuda, S. Takakusagi, RSC Advances, 2016, 6, 52587 Highlighted in Chemistry World

◆ ML prediction of adsorption energies

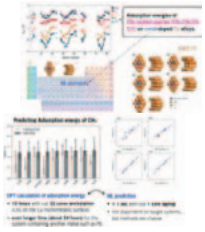

T. Toyao, K. Suzuki, S. Kikuchi, S. Takakusagi, K. Shimizu, I. Takigawa, The Journal of Physical Chemistry C, 2018, 122, 8315-8326

◆ Oxidation Coupling of Methane(OCM)

$$CH_4 + O_2 \Rightarrow C_2H_4, C_2H_6, CO_2, H_2O$$

This catalytic process can concert methane to ethylene and ethane "directly".

◆ Dataset of OCM reaction

This dataset was collected from published data.
It reflected the trend and history of the study of OCM reaction.
Therefore, there is a large bias of the number of the study of elements.

This study

◆ ML prediction of experimental data on oxidative coupling of methane (OCM)

In this study, we propose a new ML model based on published data for catalyst design and discovery and it was applied to oxidative coupling of methane. Our new ML method considers elemental features as input representations instead of inputting catalyst compositions directly. This model would be useful for small datasets and datasets having limited catalyst composition overlap, and possibly find catalyst compositions not yet tested.

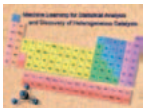

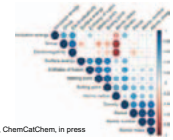

K. Suzuki, T. Toyao, Z. Maeno, S. Takakusagi, K. Shimizu, I. Takigawa, ChemCatChem, in press

Machine-learning analysis

◆ **The proposed machine learning approach**

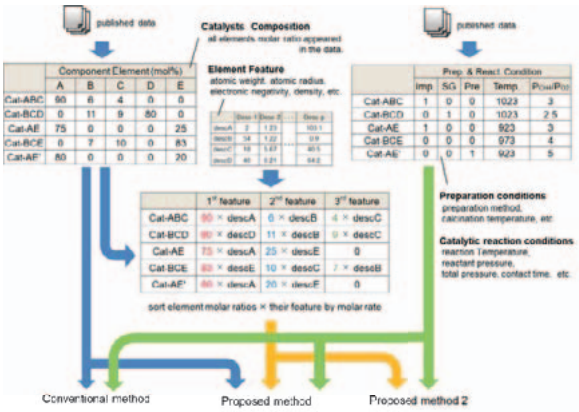

◆ **Feature Importance**

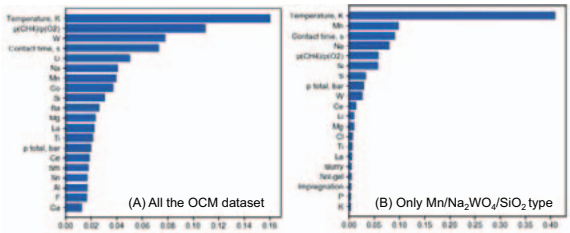

Top 20 contributing descriptors for predicting C_2 yield from OCM based on the best RFR models. (A) OCM dataset and (B) the dataset of Mn/ Na_2WO_4 / SiO_2 catalyst

◆ **Partial Dependence Plot for $Mn/Na_2WO_4/SiO_2$ type catalysts**

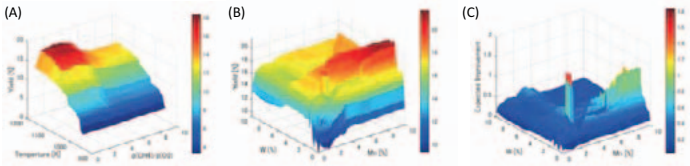

Partial dependence plot on $Mn/Na_2WO_4/SiO_2$ catalyst against (A) temperature and P_{CH4} / P_{O2} (B) Na_2WO_4 ratio and Mn ratio and (C) Expected Improvement against Na_2WO_4 ratio and Mn ratio at T = 1173 K and P_{CH3}/P_{O2} = 4

◆ **Catalysts discovery**

Top 20 promising candidate catalysts for OCM, worth testing next, as suggested by the entire OCM dataset using the proposed method. Similar catalysts are clustered, and representative catalysts with the greatest EI in each group are shown.

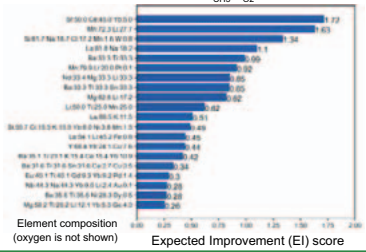

Element composition (oxygen is not shown)

Expected Improvement (EI) score

◆ **Machine learning methods**

◆ LASSO regression (L1-penalized)(Lasso): Linear model
◆ Supporting Vector regression (SVR) : Kernel model
◆ Kernel Ridge regression (KRR): Kernel model
◆ Random forest regression (RFR): Tree-ensemble model
◆ Extra trees regression (ETR): Tree-ensemble model
◆ XGBoost regression (XGB): Tree-ensemble model

$$RMSE = \sqrt{\sum \frac{(y_{pred} - y_{ref})^2}{N}}$$

ML model	Lasso	SVR	KRR	RFR	ETR	XGB
Conventional Method						
Training Error [%]	5.77	3.96	5.22	1.59	0.87	2.22
Test Error [%]	5.84	5.67	5.39	3.84	3.84	3.78
Test R2	0.219	0.252	0.332	0.662	0.661	0.672
Proposed Method						
Training Error [%]	5.66	1.16	3.57	1.57	0.87	**1.67**
Test Error [%]	5.74	5.18	5.88	3.80	3.70	**3.68**
Test R2	0.243	0.382	0.206	0.668	0.686	**0.690**
Proposed Method 2						
Training Error [%]	5.88	3.74	3.84	1.59	0.89)	**1.26**
Test Error [%]	5.94	5.21	5.97	3.84	3.74	**3.69**
Test R2	0.191	0.376	0.186	0.661	0.679	**0.689**

Comparison of prediction accuracy (RMSE, 10-fold cross-validation) for C_2 yield (%). Three representation patterns (composition only, composition + condition, and the proposed) were tested with six ML methods.

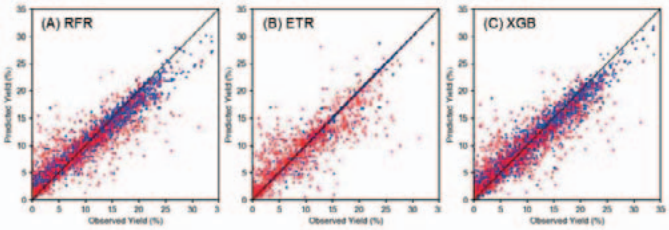

Comparison of 90%/10% training-test error plots for three representation patterns for catalyst performance (C_2 yield) for OCM. (A) Random Forest Regression (B) Extra Tree Regression (C) XGBoost Regression. Training data (blue), test data (red).

Pros and Cons of ML

There often exists a hidden trend behind many cases and ML can uncover it, and can also transfer it to as-yet-unidentified cases.

Pros of ML

• can characterize a target value of a system by those of other systems.
• first-principle free, and can be applied to complicated targets which would be usually too difficult to precisely model.
• usually very quick, and good for large-scale screening or exploration.

Cons of ML

• highly depends on the quality and amount of the data we use for training, i.e. "garbage in, garbage out" "can't predict anything not in the data"
• The descriptors need to cover the wide spectrum of the target properties as much as possible, and this is not trivial at all in many cases.
• "first-principle free" also means we can have misleading results at some risk.

References

• Takigawa, K. Shimizu, K. Tsuda, S. Takakusagi, Machine-learning prediction of the d-band center for metals and bimetals, RSC Advances, 2016, 6, 52587

• T. Toyao, K. Suzuki, S. Kikuchi, S. Takakusagi, K. Shimizu, I. Takigawa, Toward Effective Utilization of Methane: Machine Learning Prediction of Adsorption Energies on Metal Alloys, The Journal of Physical Chemistry C, 2018, 122, 8315

• K. Suzuki, T. Toyao, S. Takakusagi, K. Shimizu, I. Takigawa, Statistical Analysis and Discovery of Heterogeneous Catalysts Based on Machine Learning from Diverse Published Data, 2019, in press

Role of Mesoporosity for Low Temperature Ethylene Oxidation over Hydrophobic Pt/Silica

Shazia Sharmin Satter, Kiyotaka Nakajima, Atsushi Fukuoka
Institute for Catalysis, Hokkaido University

Introduction

- Ethylene is a natural ripening hormone released by fruits and vegetables in trace amounts at low temperature.
- Our finding revealed efficient conversion of ethylene to carbon dioxide at 0°C over Pt/MCM-41 catalyst [1].

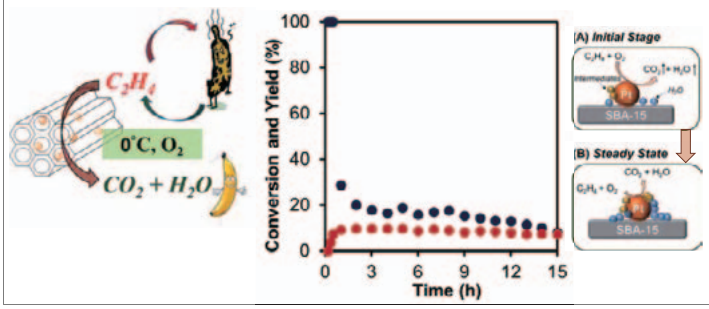

OBJECTIVE

Clarify the effect of hydrophobic mesoporous silica in effective removal of H_2O vapor, resulting in increased activity during ethylene oxidation

[1] A. Fukuoka *et al.*, *Angew. Chem. Int. Ed.* **52**, 6265-6268, (2013).
[2] Satter, S. S., Fukuoka, A. *ACS Sustainable Chem. Eng.* **2018,** *6*, 11480.
[3] Satter, S. S., Fukuoka, A. *Chem. Lett.* **2018,** *47*, 1000.

Catalyst Preparation and Activity

SBA-15 or Aerosil (calc. temp.) + H_2O
+
$Pt(NH_3)_2(NO_2)_2$

Impregnation
H_2 reduction

Pt/SBA-15
Pt/SBA-15(800)
Pt/A380
Pt/A380(800)

1.8 wt% Pt/support material

Normally, SBA-15 is calcined at 560 °C.

	Calcination Temp. (°C)	Conv. (%)	Yield (%)
Pt/A380	-	30	11
Pt/A380(800)	800	35	17
Pt/SBA-15	560	30	16
Pt/SBA-15(800)	800	45	28

Flow Reactor System

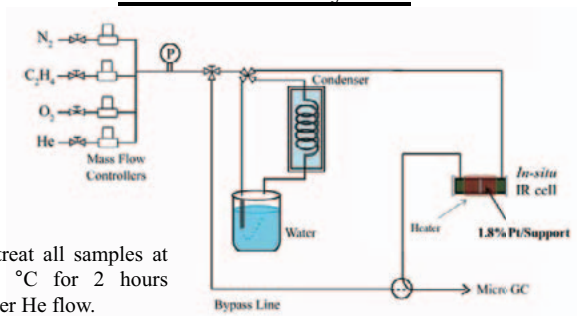

Pretreat all samples at 150 °C for 2 hours under He flow.

In-Situ FTIR for Identification of Pt Sites

Dehydrated Sample

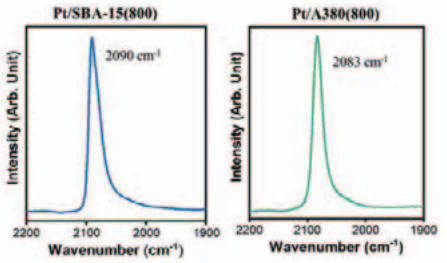

CO: 100 ppm, He: balance, Temperature = 28 °C

Hydrated Sample

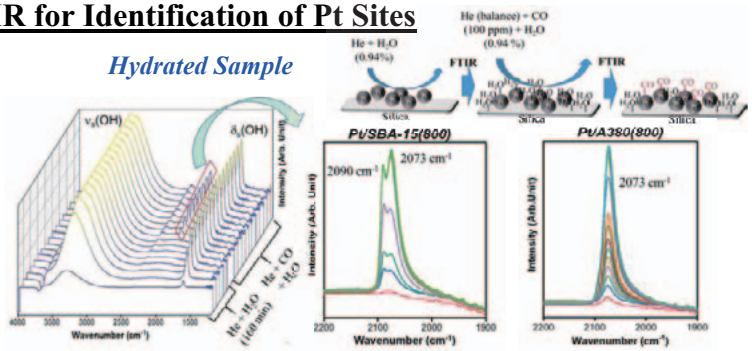

CO: 100 ppm; He: Balance; H_2O content: 0.94%, *Temperature: 28 °C*

Operando Study During C_2H_4 Oxidation

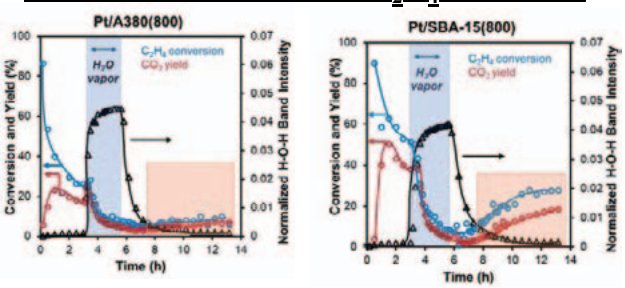

1.8 wt% Pt/SBA-15(800) and Pt/A380(800); *SV: 15000 mL h^{-1} g^{-1}*; C_2H_4: 50ppm; O_2 20%; N_2: 5%, He: Balance; *Temperature: 28 °C, Water content: 0.95%*

Pt/SBA-15(800) shows faster recovery of the activity in presence of water.

^{29}Si NMR Spectroscopy

	S_{BET} / m^2 g^{-1}	Q content (%)			Catalytic activity	
		Q_2	Q_3	Q_4	Conv (%)	Yield (%)
Pt/SBA-15	867	3.2	22.2	74.7	30	16
Pt/SBA-15 (800)	572	0.0	15.1	84.9	45	28
Pt/A380	392	7.7	28.5	63.8	30	11
Pt/A380(800)	313	0.0	26.5	73.5	35	17

Conclusion

The bare Pt site of Pt/SBA-15(800) is active for ethylene oxidation which shows successful recovery of the catalytic activity even in presence of water vapor.

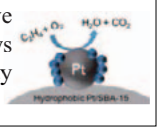

Kinetics of β-1,4 glycosidic bond hydrolysis in cello-oligosaccharides over carbon catalysts

Pengru Chen,[1,2] Abhijit Shrotri,[1] Atsushi Fukuoka[1]
[1]Institute for catalysis, [2]Graduate School of Chemical Sciences and Engineering, Hokkaido University
email: chenpr@cat.hokudai.ac.jp

Introduction

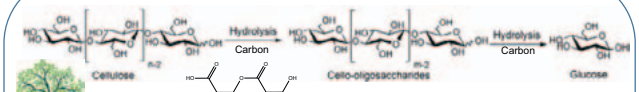

P. Chen et al., ChemSusChem 2019, 12, 2576.

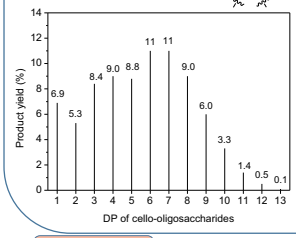

Cello-oligosaccharides are valuable chemicals in healthcare and agriculture industry. They are produced by partial hydrolysis of cellulose. The distribution of their DP after hydrolysis suggests a decrease in rate of β-1,4 glycosidic bond hydrolysis as reaction progresses.

Objective in this work:
Investigate the change in rate of hydrolysis for cello-oligosaccharides over various catalysts

Methods

Hydrolysis

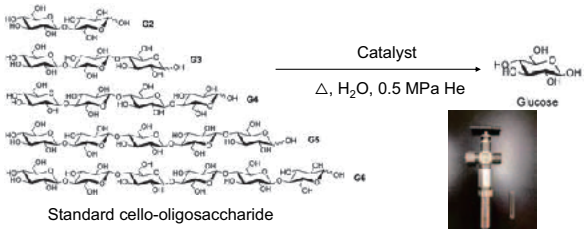

Standard cello-oligosaccharide

Catalysts: Carbon catalyst (AC-Air), H-Beta, Amberlyst 70, H_2SO_4

Adsorption

Cello-oligosaccharides (1 μmol) + 0.5 mg Catalyst → Stirring 30min, RT, 0.5 mL H_2O → HPLC analysis

Results

Determining hydrolysis rate

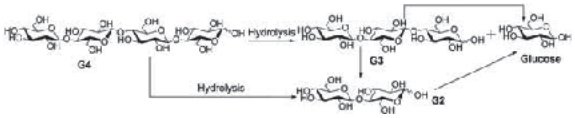

Rate equation:

$$\frac{d[Oligosaccharide]}{dt} = k_x[Oligosaccharide]$$

$$[Oligosaccharide] = [Oligosaccharide]_0\, e^{-k_x t}$$

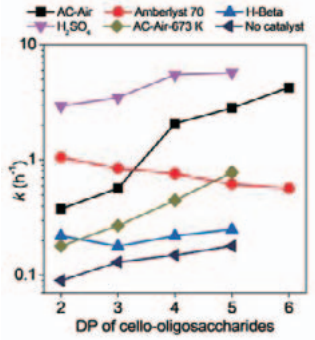

- Carbon catalyst showed an increase in rate of hydrolysis with the increase of DP of cello-oligosaccharides.
- This increasing trend was unique to carbon catalyst, and other solid catalysts showed no increasing trend.

The adsorption of cello-oligosaccharides over carbon

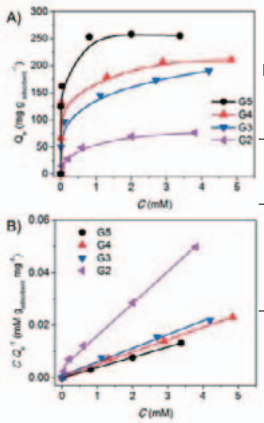

Langmuir equation: $\frac{C}{Q_e} = \frac{1}{Q_{max}} C + \frac{1}{K_{ads} Q_{max}}$

Substrate	k (h^{-1})	Langmuir constants	
	AC-Air	Q_{max} (mg g^{-1})	K_{ads} (M^{-1})
G2	0.38	84	2429
G3	0.57	192	6500
G4	2.15	213	15667
G5	2.66	256	97500

Increase

- Stronger affinity for adsorption of larger oligosaccharides on carbon.
- Stronger adsorption contributes to the increase in rate of hydrolysis rate.

The activation energy for cello-oligosaccharide hydrolysis

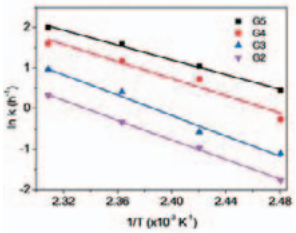

Arrhenius equation: $\ln k = -\frac{E_a}{R}\frac{1}{T} + \ln A$

Substrate	E_a (kJ mol^{-1})	A (h^{-1})
G2	100	1.74×10^{12}
G3	98	1.71×10^{12}
G4	87	2.16×10^{11}
G5	77	1.10×10^{10}

- Activation energy decreased with increase in chain length of cello-oligosaccharides.
- This reduction is caused by distortion of cello-oligosaccharides within the micropore surface of carbon after adsorption.

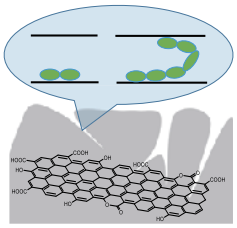

Conclusions

- Larger cello-oligosaccharides underwent hydrolysis at a much faster rate in the presence of a carbon catalyst.
- Adsorption of cello-oligosaccharides over carbon catalysts are responsible for the unique change in rate of hydrolysis.
- A decrease in activation energy was observed with an increase in size of cello-oligosaccharide.
- We propose that adsorption of cello-oligosaccharide over carbon causes structural distortion, which lowers the activation energy.

Single Atom Rh Promoted In_2O_3 for CO_2 Hydrogenation to Methanol

Shaikh Nazmul Hasan Mohammad Dostagir,[1,2] Abhijit Shrotri,[1] Atsushi Fukuoka[1]

[1]Institute for Catalysis, Hokkaido University, Sapporo 001-0021, Japan

[2]Graduate School of Chemical Sciences and Engineering, Hokkaido University, Sapporo, 060-8628, Japan

Background

$$CO_2 + 3\,H_2 \longrightarrow CH_3OH + H_2O$$

- Industrial catalyst, Cu-ZnO/Al_2O_3 requires high pressure and CO rich feedstock and experiences rapid deactivation.
- In_2O_3 solves the issues of selectivity and stability.
- In_2O_3 can convert pure CO_2 to methanol.
- In_2O_3 shows low space time yield (STY) due to low conversion.

Working Hypothesis and Objective

- Idea: Doping of single atom transition metals into In_2O_3 is expected to improve catalytic activity of In_2O_3 with low metal utilization.
- Objective: utilization of transition metal-indium mixed oxide to achieve high methanol productivity.

Catalyst preparation

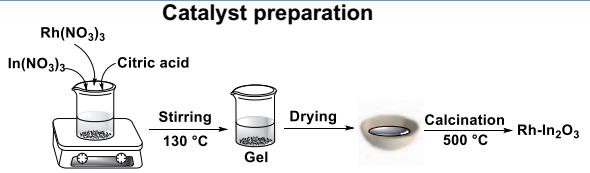

Pretreatment of catalysts: Activation under 0.5 MPa Ar at 300 °C for 1 h.
Reaction condition: M-In_2O_3 , temp. = 270-315 °C, total pressure = 5 MPa, H_2/CO_2 = 4, Space velocity = 30000-90000 mL h^{-1} g_{cat}^{-1}, Total flow rate = 100 mL min^{-1}.

Reaction set-up

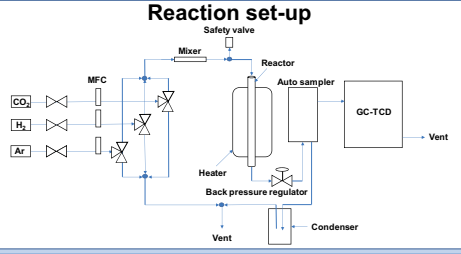

Results

❑ **Metal screening:**

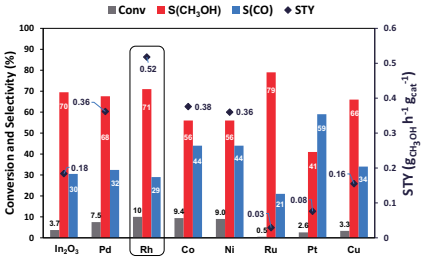

- Rh promoted In_2O_3 shows the highest STY.
- Condition: 5 mol% M-In_2O_3 (200 mg), 270 °C, 5 MPa, SV = 30000 mL h^{-1} g^{-1}.

❑ **Optimal metal loading:**

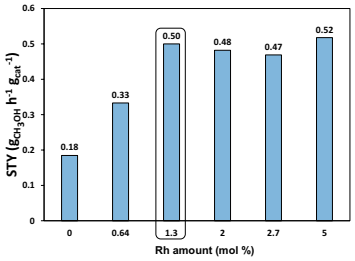

- Condition: 270 °C, 5 MPa, SV = 30000 mL h^{-1} g^{-1}.

❑ **Catalyst stability:**

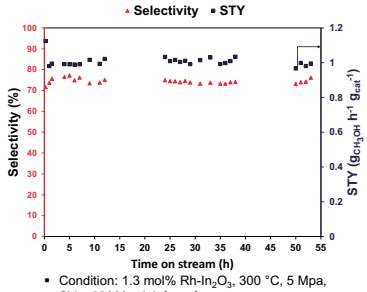

- Condition: 1.3 mol% Rh-In_2O_3, 300 °C, 5 Mpa, SV = 60000 mL h^{-1} g_{cat}^{-1}.

- **1.3 mol% Rh-In_2O_3 shows one of the highest STYs compared to reported catalysts.**
- **This catalyst maintains high stability while retaining its catalytic activity.**

Characterization

❑ **XRD:**

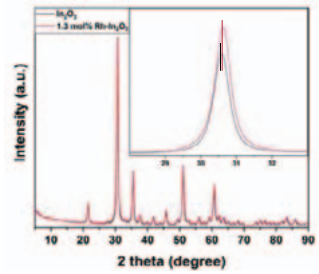

- No Peaks of Rh were appeared.
- Shifting of peak position suggests mixed oxide formation.

❑ **H_2-TPR:**

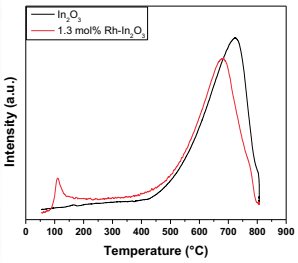

- H_2- TPR suggests that under reaction condition Rh is present as Rh^0 species.

❑ **Rh 3d XPS:**

❑ **Fresh catalyst:**

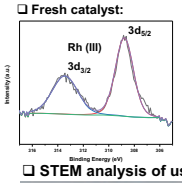

❑ **used catalyst:**

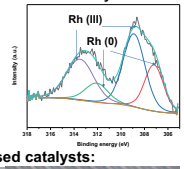

- In used catalyst, Rh is reduced to 0 oxidation state.
- Rh (III) present in the used catalysts are due to re-oxidation of Rh (0) or subsurface Rh (III) species.

❑ **STEM analysis of used catalysts:**

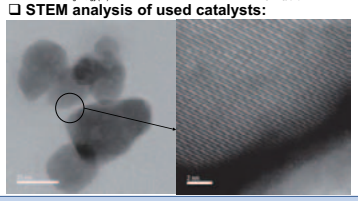

- No Rh nanoparticles or subnanometer clusters were detected.
- Rh atoms are evenly distributed in the In_2O_3 matrix.

Active site

❑ **Comparison between different preparation methods and supports:**

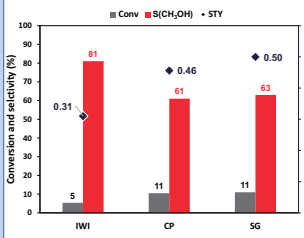

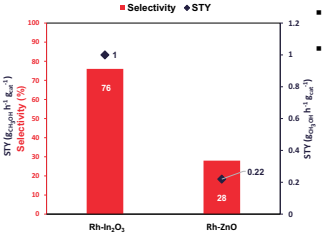

- Rh on inactive ZnO produces CO as major product suggesting -O-Rh-O-In-O- as the main active species in Rh-In_2O_3 for the enhanced methanol synthesis.

Role of Rh

- Rh increases oxygen vacancy in In_2O_3 matrix thus increases number of CO_2 adsorbed.
- Rh helps in the dissociation of H_2 thus increases the rate of the reaction.

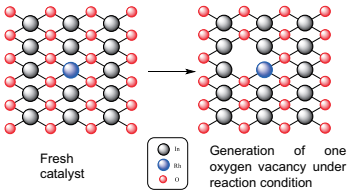

Conclusion

- Rh which is mainly known for RWGS and CO_2 methanation has been shown to actively participate in methanol formation reaction from CO_2.
- Single atom Rh promoted In_2O_3 made using sol-gel method shows one of the highest STYs.
- Rh plays a vital role in enhancing catalytic activity by dissociating more H_2 and incorporating more oxygen vacancies in the In_2O_3 matrix.

Production of hexitols from a real biomass molasses using a sponge Ni catalyst

Cheng Yang, Hirokazu Kobayashi, Atsushi Fukuoka

HOKKAIDO UNIVERSITY

Institute for Catalysis ICAT

Introduction

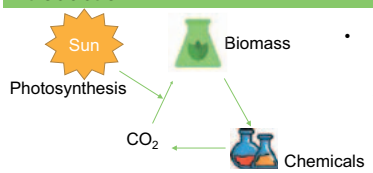

- Biomass is an abundant natural resource for energy supply and chemical production. In this study, we use molasses as a precursor to sugar alcohols.

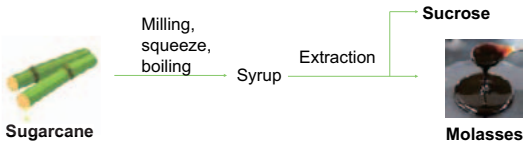

- The annual production of molasses is about 50 million tons. It is a food biomass derivative produced in the manufacturing of sucrose.

Objective of this work

- To produce sugar alcohols using cane molasses.

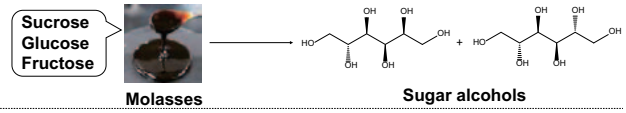

- The reaction mechanism of hydrolytic hydrogenation is shown as follows:

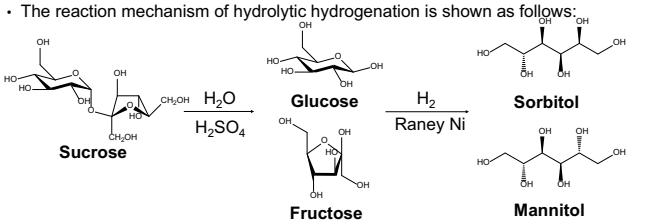

Experimental

❖ Material: Cane molasses

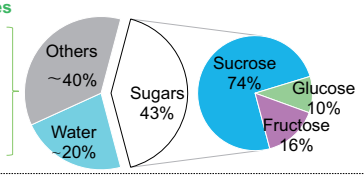

❖ Purification

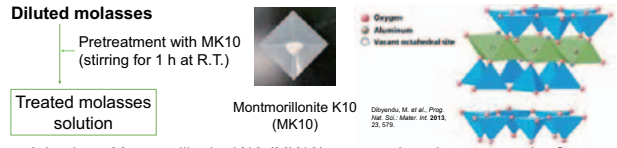

- Adsorbent Montmorillonite K10 (MK10) was employed to remove the S-compounds.

❖ Reaction

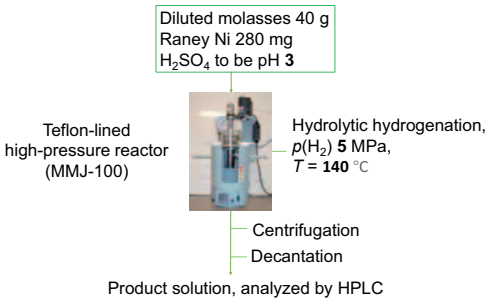

Results and discussion

❖ Results

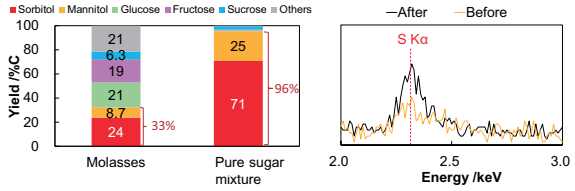

- Compared to the reaction with pure sugars, that with molasses gives a lower yield of sugar alcohols.
- The suppression of sugar alcohol formation indicates the presence of inhibitors, which may be N- or S-compounds such as proteins.
- Adsorption of S-compounds on Raney Ni surface is detected after the reaction using molasses.

❖ Effect of N- and S-compounds on the reaction

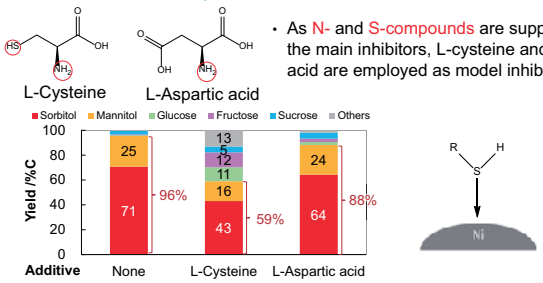

- As N- and S-compounds are supposed to be the main inhibitors, L-cysteine and L-aspartic acid are employed as model inhibitors.
- S-compounds are confirmed to be the main inhibitor, and the mechanism of inhibition is supposed to be the chemisorption on Ni surface.

❖ Effect of S-compounds removal

- As S-compounds is removed, the sugar alcohol yield given by MK10-treated molasses is promoted from 33% to 53% at 4 h.

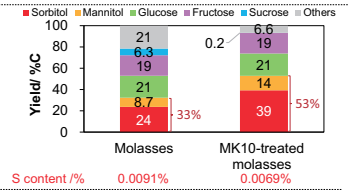

❖ Effect of pH on sugar alcohol production

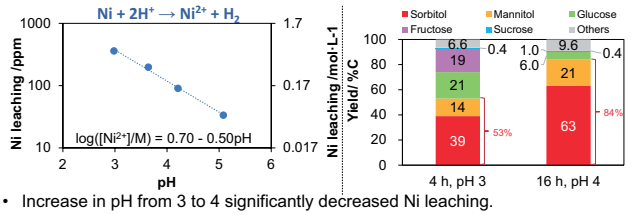

- Increase in pH from 3 to 4 significantly decreased Ni leaching.
- The reaction at pH 4 gave 84% yield of sugar alcohols is achieved at 16 h.

❖ Kinetic analysis of molasses hydrolytic hydrogenation

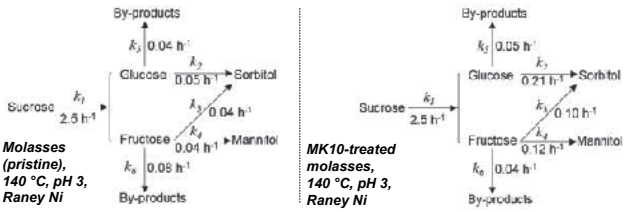

- The rate-determining step, hydrogenation of monomeric sugars, is significantly promoted after pretreatment.

Summary

- A biomass waste, molasses, was used for the feedstock to produce sugar alcohols by hydrolytic hydrogenation using Raney Ni catalyst.
- The reaction using non-treated molasses shows low yield of sugar alcohols, due to the presence of inhibitors which are mainly S-compounds.
- Adsorbent MK-10 selectively removes the poisonous compounds for the heterogeneous Ni catalyst. Sugar alcohols are obtained in 84% yield at 140 °C, pH 4, 16 h after the MK10-pretreatment.

Travelling of Carbon Atoms in Organic Molecules

Masayoshi Bando[1], Kiyohiko Nakajima[2], Zhiyi Song[1], and Tamotsu Takahashi[1]

[1]*Institute for Catalysis and Graduate School of Life Science, Hokkaido University, Kita-ku, Sapporo 001-0021*
[2]*Department of Chemistry, Aichi University of Education, Igaya, Kariya, Aichi 448-8542*

Previous Research

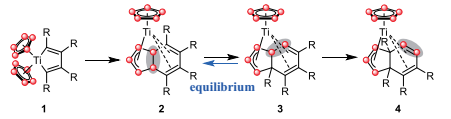

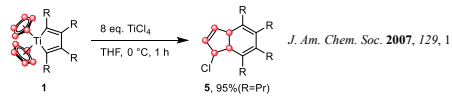

J. Am. Chem. Soc. **2007**, *129*, 11678.

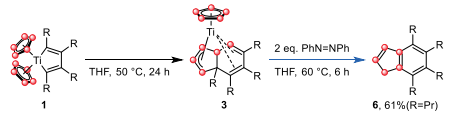

J. Am. Chem. Soc. **2008**, *130*, 15236.

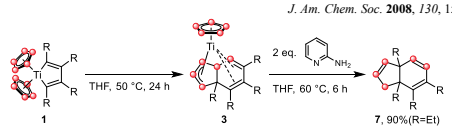

Organometallics. **2016**, 35, 1092.

This Study

We proposed two hypotheses for the travelling of carbon atoms in organic molecules.

1. When compounds with different carbon positions are in equilibrium, carbons move to the position of the most thermodynamically stable compound among them.
2. When one of the compounds is removed from the equilibrium by an irreversible path, carbons move to the position of the removed compound.

To verify the hypothesis 1, we examined whether we could make the carbons move to the farthest position by designing complex **8** as the most stable compound among **2**, **3**, **4** and **8**.

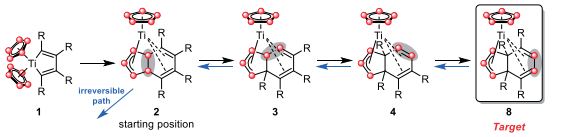

To verify the hypothesis 2, we examined whether we could make the carbons come back to the starting position from **8** by removing complex **2** irreversibly from the equilibrium between **2**, **3**, **4** and **8**.

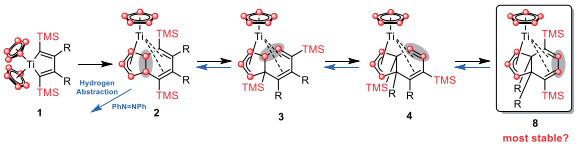

Results and Discussion

Preparation for Starting Material 1

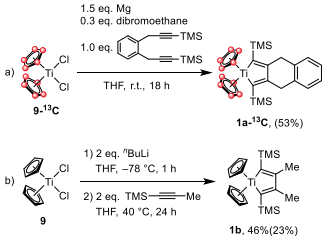

NMR yields.
Isolated yields were given in parenthesis.

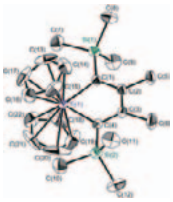

X-ray structure of **1b**

Travelling of Carbons to the Farthest Position in Complex 8

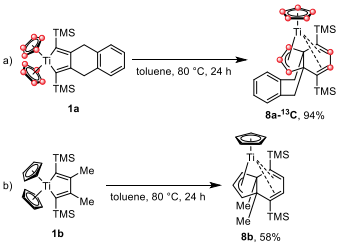

NMR yields.

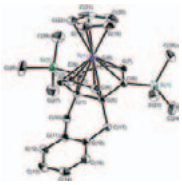

X-ray structure of **8a**

Coming Back to the Starting Position of Carbons

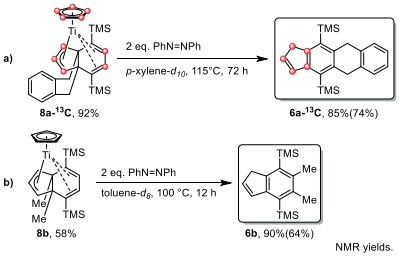

NMR yields.
Isolated yields were given in parenthesis.

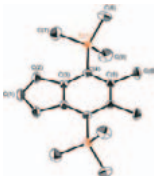

X-ray structure of **6b**

Different Viewpoints on the Reactions

Travelling of the Two Carbons

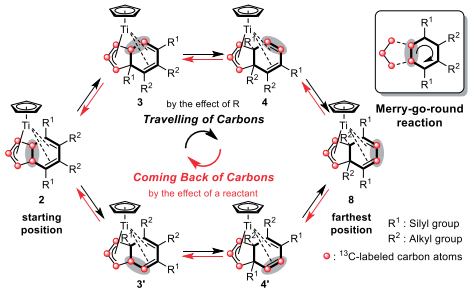

When the molecular structures are drawn by fixing the three carbons of the five-membered ring, **the two carbons move with the rotation of the six-membered ring like a merry-go-round**.

Travelling of the Three Carbons

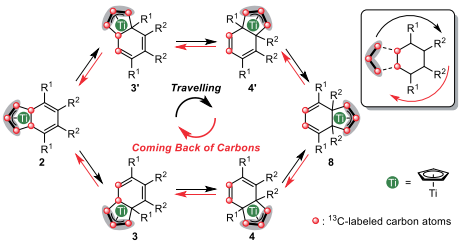

When the molecular structures are drawn by fixing the six-membered ring, **the three carbons move around the six-membered ring**.

Summary

We proposed the hypotheses that carbon atoms travelled in organic molecules through equilibrium between the molecules. To verify the hypotheses experimentally, we examined whether we could make the two carbons move to the farthest position and come back to the starting position by use of the hypotheses. As a result, we found that the two carbons moved to the farthest position with the rotation of the six-membered ring by the effect of TMS substituents and came back to the starting position by the effect of azobenzene. All of the products were isolated and fully characterized. These results strongly supported the proposed hypotheses. There is another viewpoint on the reaction. When the six-membered ring is fixed and the movement of the three carbons of the five-membered ring is focused, those three carbons moved around the six-membered ring. This dual aspects are important for the concept of *"Traveling of Carbon Atoms in Organic Molecules: Merry-Go-Round Reaction"*.

Cation-Distribution-Tuned Perpendicular Magnetic Anisotropy in $NiCo_2O_4$ Epitaxial Films

Yufan Shen[1], Daisuke Kan[1], Zhenhong Tan[1], Yusuke Wakabayashi[2] and Yuichi Shimakawa[1]
1 Kyoto Univ. ICR
2 Tohoku Univ. Dep of Physics

Introduction

- $NiCo_2O_4$ (NCO), which has the inverse spinel structure, displays various properties.

Above-room temperature Ferrimagnetism with perpendicular anisotropy[1]

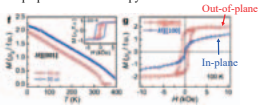

[1] X. Chen, et al. *Adv Mater* **2018**, 1805260.

Tunable Conduction [2]

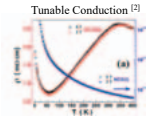

[2] Y. Bitla, et al. *Sci. Rep.* **2015**, 5.15201

Our Study

1.We tuned cation distribution in NCO.

2.Cation distribution in NCO films was determined by synchrotron X-ray diffraction technique.

3.We revealed the impacts of cation distribution on ferrimagnetism and perpendicular anisotropy.

$Co(NiCo)O_4$

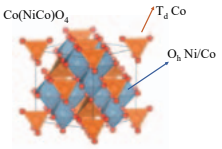

Film Deposition and Characterization

Pulse laser deposition:

- Substrate: $MgAl_2O_4$ (001) (8.083 Å)
- Target : $NiO+Co_2O_3$ (Ni : Co = 1:2)
- Growth conditions: Laser Energy density: 1.2 J/cm^2
  Substrate Temp. : 350 °C
  Oxygen pressure P_{O2}: 0.03 Torr, 0.05 Torr, 0.1 Torr, 0.15 Torr
- Film Thickness: ~30 nm

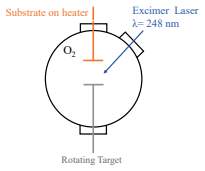

Characterization:

- Laboratory source and synchrotron x-ray diffraction for structure analysis of grown films.
- Superconducting quantum interference device (SQUID) magnetometry for magnetic properties.
- Van der Pauw pattern for electrical conductivity, four-terminal configuration Hall bar for transverse (Hall) conductivity.

Results and Discussion

Structure Analysis

Epitaxy

(BL-4C Photon Factory)

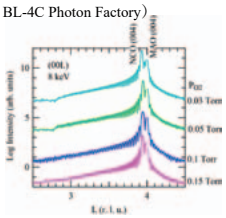

(00L) Profiles

Lab-source x-ray

RSM around (408) MAO reflection

- All films were grown epitaxially on the substrate. Out-of-plane lattice constant is about 8.19 Å for all samples (8.128 Å for bulk).
- All NCO films are in fully compressive strained state along as in-plane direction.

Cation Distribution — $(Co_{1-x}Ni_x)_{Td}(Co_{2-y}Ni_y)_{Oh}O_4$

(022) reflection originating only from T_d cations

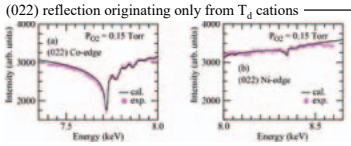

P_{O2} = 0.15 Torr Film

(222) reflection originating only from O_h cations

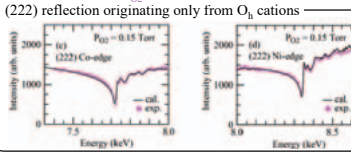

- Reproducing the incident x-ray energy dependence of the NCO (022) and (222) reflection intensity allows for determining the Ni and Co distribution. (BL-4C Photon Factory)
- The cation composition of the film grown under P_{O2} = 0.15 Torr is determined to be $(Co_{0.87}Ni_{0.13})(Co_{0.98}Ni_{1.02})O_4$

P_{O2} dep. of Ni comp. in NCO films

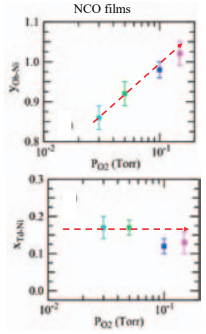

- Higher P_{O2} introduces more Ni to the O_h site.
- The cation distribution can be controlled by simply adjusting the P_{O2} during the growth.

Magnetization

M-H

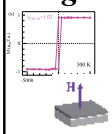

M-T

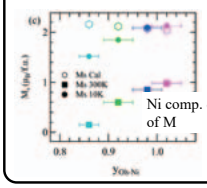

- All NCO films display above-room-temperature ferrimagnetism with perpendicular magnetic anisotropy.
- Cation Distribution impacts exchange interaction between cations in T_d site and O_h site.
- Both the transition temperature and magnetization strongly depend on the Ni comp in O_h site (y_{Oh-Ni}).

Resistivity

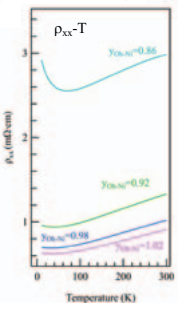

- Higher y_{Oh-Ni} (higher P_{O2}) leads to lower electrical resistivity

Perpendicular Anisotropy

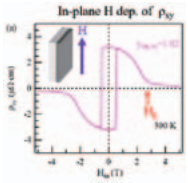

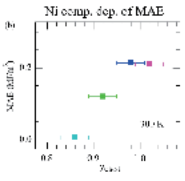

- NCO films with y_{Oh-Ni} close to stoichiometric value display the enhanced perpendicular anisotropy, highlighting the importance cation distribution brings to the perpendicular anisotropy.

H_k: Anisotropy Field
MAE: Magnetic anisotropy energy
$MAE = M_s \cdot H_k/2$ Eq.1

Conclusion

$NiCo_2O_4$ thin film has been grown epitaxially on $MgAl_2O_4$ with thickness around 30 nm. We quantitatively evaluated cation distribution in NCO epitaxial films and elucidated how it impacts magnetization as well as perpendicular anisotropy:

- The Ni concentration in O_h-site (y_{Oh-Ni}) can be tuned by simply adjusting the oxygen partial pressure P_{O2} during the growth of films. Higher P_{O2} will introduce more Ni to O_h site.
- Films whose cation distribution close to the stoichiometric value show the transition temperature higher than 400K and the enhanced perpendicular magnetic anisotropy.

Synthesis of π-Conjugated Polymers Containing Benzodithiophene and Benzotriazole Units via Highly Selective Direct Arylation Polymerization (DArP): Effects of Homocoupling Defects on Photovoltaic Performance

Masayuki Wakioka, Naohiro Torii, and Fumiyuki Ozawa

International Research Center for Elements Science, Institute for Chemical Research, Kyoto University, Uji, Kyoto 611-0011

1. Introduction: π-Conjugated Polymers

Synthetic Routes

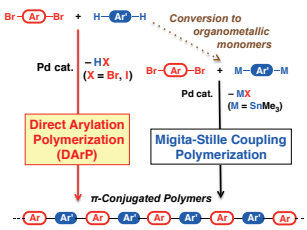

✔ *DArP realizes shortcut routes with reduced waste generation.*

Review on DArP: Leclerc *et al.*, *Chem. Rev.* **2016**, *116*, 14225.

Effects of Homocoupling Defects

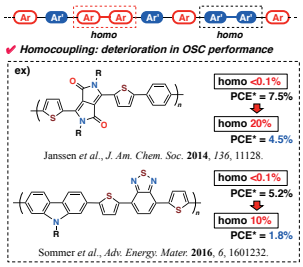

✔ *Homocoupling: deterioration in OSC performance*

*Power conversion efficiency in bulk-heterojunction organic solar cells (BHJ OSCs)

2. Previous Work

Synthesis of π-Conjugated Polymers Containing BDT and BTz Units

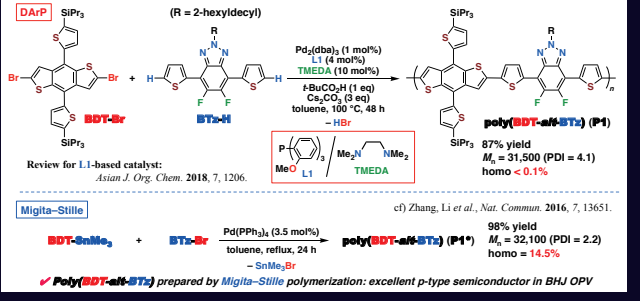

cf) Zhang, Li *et al.*, *Nat. Commun.* **2016**, *7*, 13651.

✔ *Poly(BDT-alt-BTz) prepared by Migita–Stille polymerization: excellent p-type semiconductor in BHJ OPV*

3. This Work and Summary

Effects of Homocoupling Defects on Photovoltaic Performance

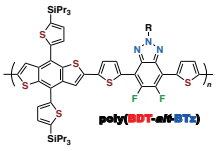

✔ *Preparation of poly(BDT-alt-BTz) with known amounts of BDT-BDT and BTz-BTz homocoupling defects via DArP*

✔ *BDT-BDT defects significantly deteriorate the OSC performance, whereas BTz-BTz defects little affect the performance.*

✔ *Poly(BDT-alt-BTz) prepared by Migita–Stille cross-coupling polymerization contains a large amount of BTz-BTz defects. However, the polymer shows the OSC performance comparable to Poly(BDT-alt-BTz) with well controlled structure (P1), because the deterioration due to BTz-BTz defects is small.*

4. Synthesis of Poly(BDT-alt-BTz) with Homocoupling Defects

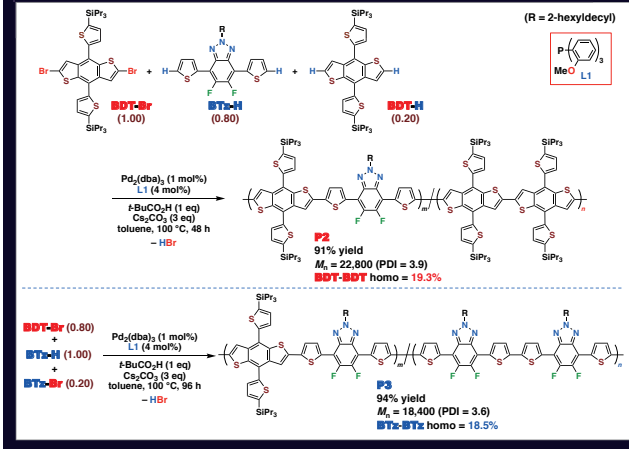

5. Structures of Poly(BDT-alt-BTz)s

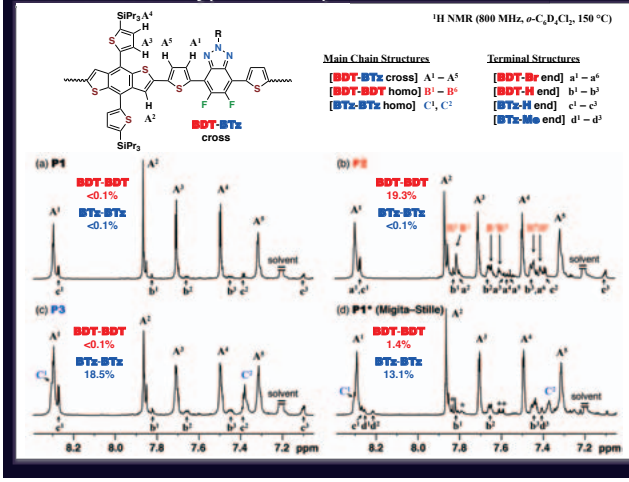

6. Optical Properties of Poly(BDT-alt-BTz)s

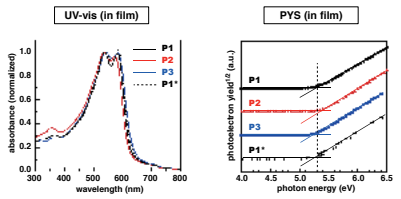

polymer	M_n [PDI]	BDT-BDT homo (%)	BTz-BTz homo (%)	λ_{max} (nm)[a]	E_g^{opt} (eV)[b]	E^{HOMO} (eV)[c]
P1	31,500 [4.1]	<0.1	<0.1	538, 582	1.99	−5.30
P2	22,800 [3.9]	19.3	<0.1	536, 574	2.01	−5.38 deeper HOMO
P3	18,400 [3.6]	<0.1	18.5	542, 583	1.97	−5.26
P1*	32,100 [2.2]	1.4	13.1	541, 584	1.98	−5.26

[a]UV-vis (thin films). [b]$E_g^{opt} = 1240/\lambda_{onset}$. [c]Photoemission yield spectra (PYS).

✔ *The UV-vis spectra of four kinds of polymer were almost the same.*

7. Photovoltaic Performance (BHJ OSCs)

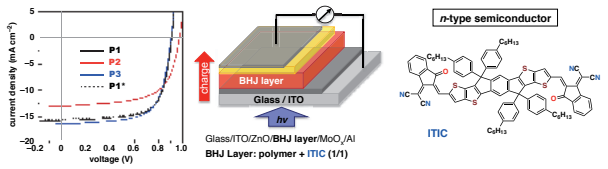

polymer	M_n [PDI]	BDT-BDT homo (%)	BTz-BTz homo (%)	J_{SC} (mA cm^{-2})[a]	V_{OC} (V)[a]	FF[a]	PCE (%)[a]
P1	31,500 [4.1]	<0.1	<0.1	15.6(1) [15.7]	0.909(1) [0.913]	0.66(2) [0.693]	9.5(1) [9.9]
P2	22,800 [3.9]	19.3	<0.1	12.5(2) [12.9]	0.973(2) [0.976]	0.62(2) [0.637]	7.5(3) [8.0]
P3	18,400 [3.6]	<0.1	18.5	16.1(2) [16.3]	0.903(2) [0.905]	0.66(1) [0.678]	9.7(2) [10.0]
P1*	32,100 [2.2]	1.4	13.1	15.2(2) [15.5]	0.909(1) [0.910]	0.683(5) [0.693]	9.4(1) [9.8]

[a]The values are average values obtained over 6 devices. The values in brackets are for the cell with the highest PCE.

✔ *P1, P3, P1*: almost identical optical properties and comparable d_π (see below)*
→ *comparable photovoltaic parameters (J_{SC}, V_{OC}, FF, PCE)*

✔ *P2: deeper E^{HOMO} and larger d_π (see below)*
→ *higher V_{OC} but lower J_{SC} and FF*

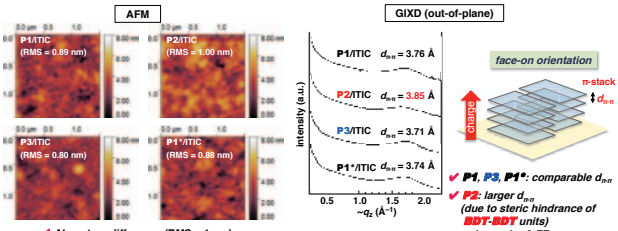

✔ *Almost no difference (RMS ~ 1 nm)*

✔ *P1, P3, P1*: comparable $d_{\pi\text{-}\pi}$*

✔ *P2: larger $d_{\pi\text{-}\pi}$ (due to steric hindrance of BDT-BDT units)*
→ *lower J_{SC} & FF*

Acknowledgement

The GIXD experiments were performed on beamline BL19B2 of SPring-8 with the approval of the Japan Synchrotron Radiation Research Institute (JASRI) (Proposal 2018A1584). We are grateful to Prof. I. Osaka and Dr. M. Saito (Hiroshima Univ.) for BHJ OPV measurement and Prof. A. Wakamiya (ICR, Kyoto Univ.) for analytical GPC, UV-vis, PYS assistance.

Artificial curvature inducing peptide triggering cellular endocytic uptake

○Toshihiro Masuda, Shiroh Futaki
Institute for Chemical Research, Kyoto University, Kyoto 611-0011, Japan

INTRODUCTION

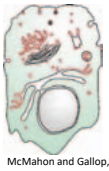

McMahon and Gallop, *Nature*, 2005

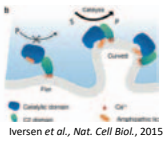

Iversen *et al.*, *Nat. Cell Biol.*, 2015

Membrane curvature is no longer seen merely as a passive feature of membranes, but plays an important in regulating protein activities.

Iversen *et al.*, *Nat. Cell Biol.*, 2015

Developing a new tool for regulating membrane curvature is an important challenge.

- **Some amphipathic helices inserted into the bilayer induced membrane curvature**
- **Endocytosis-related proteins are regulated by membrane curvature.**

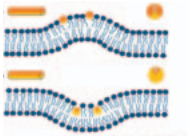

Bassereau *et al*, *J. Phys. D: Appl. Phys.*, 2018

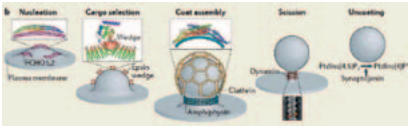

McMahon and Boucrot, *Nat. Rev. Mol. Cell Biol.*, 2017

Purpose

To develop a new peptide tool for regulating endocytosis by inducing membrane curvature.

STRATEGY

As a new peptide tool candidate, we focused on R6W3, an artificially designed amphipathic peptide.

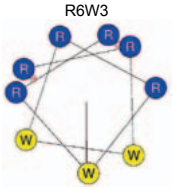

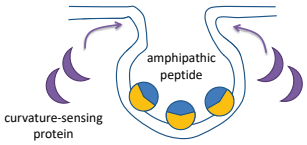

Endocytosis

hypothesis

R6W3 can control endocytic events by inducing membrane curvature.

Amphiphysin; membrane curvature sensing proteins

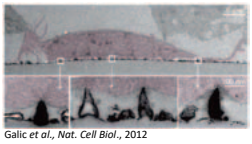

Galic *et al.*, *Nat. Cell Biol.*, 2012

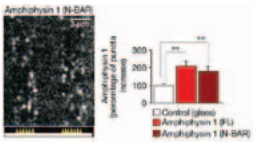

It was reported that Amphiphysin recruited to nanocone-induced plasma membrane curvature.

Investigate membrane remodeling abilities by observing effects on Amphiphysin distribution.

RESULTS

▪R6W3 effects on Amphiphysin distribution

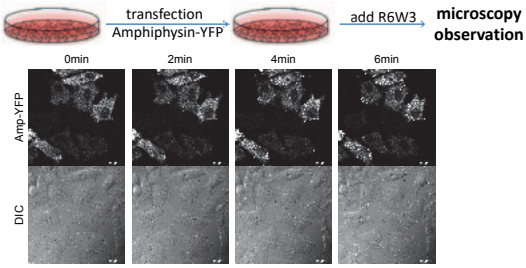

R6W3 treatment increased the number of Amp-YFP puncta signals.

▪R6W3 abilities of affecting endocytosis events

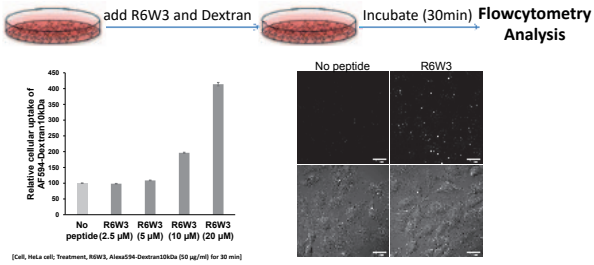

[Cell, HeLa cell; Treatment, R6W3, Alexa594-Dextran10kDa (50 μg/ml) for 30 min]

R6W3 increased the amount of dextran cellular uptake.

▪R6W3 derivatives abilities of affecting endocytosis events.

Name	Sequence
WT	RRWWRRWRR
Inverse	RRWRRWWRR
R6DW3	RRwwRRwRR

[Cell, HeLa cell; Treatment, R6W3 and derivatives (20 μM), Alexa594-Dextran10kDa (50 μg/ml) for 30 min]

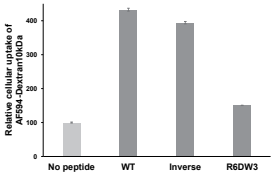

Inverse-R6W3 increased dextran cellular uptake as WT-R6W3. R6DW3 hardly changed dextran cellular uptake.

▪R6W3 derivatives effects on Amphiphysin distribution

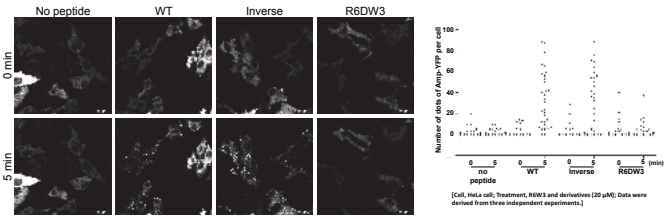

[Cell, HeLa cell; Treatment, R6W3 and derivatives (20 μM); Data were derived from three independent experiments.]

Inverse-R6W3 increased the number of Amp-YFP puncta signals as WT-R6W3. R6DW3 hardly affected Amp-YFP distribution.

Importance of amphipathic structure was implied.

▪Invovement of clathrin-mediated endocytosis (CME)

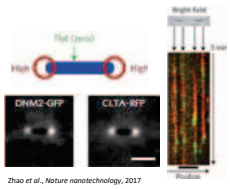

Zhao *et al.*, *Nature nanotechnology*, 2017

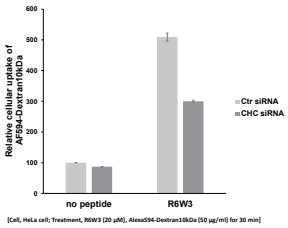

[Cell, HeLa cell; Treatment, R6W3 (20 μM), Alexa594-Dextran10kDa (50 μg/ml) for 30 min]

CHC knockdown decreased R6W3-mediated dextran cellular uptake.

CONCLUSION

- **R6W3 stimulated endocytic events.**
- **R6W3 increased the number of Amphiphysin-YFP puncta signals.**
- **Amphipathic structure in R6W3 sequence was important for endocytosis induction and membrane remodeling ability.**
- **CME is involved in R6W3-mediated endocytosis events.**

Programmable RNA methylation and demethylation using PUF RNA binding proteins

Miki Imanishi, Kouki Shinoda, Akiyo Suda, Shiroh Futaki
Institute for Chemical Research, Kyoto University, Kyoto 611-0011, Japan

m6A is an important RNA modification

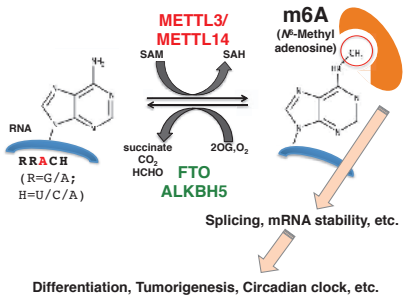

Concept of the targeted (de)methylation

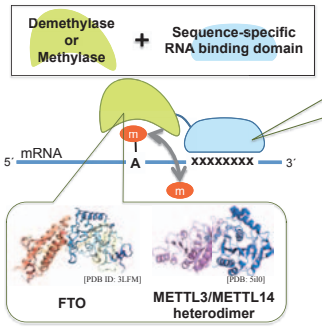

Pumilio/fem-3 mRNA binding factor (PUF)

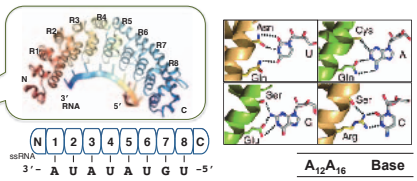

- Contains 8 repeat and the N- and C-terminal regions
- Each repeat recognizes a single nucleotide
- Targets desired 8-nt sequence

$A_{12}A_{16}$	Base
(S/C)Q	A
NQ	U
SE	G
SR	C

PUF has great potential as an RNA binding domain for RNA regulation tools.

FTO-PUFs showed sequence-specific RNA demethylation activities

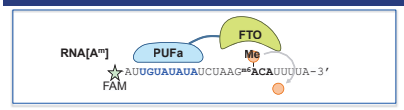

PUF binding site (-)

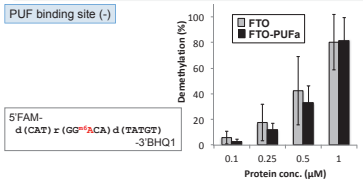

Fusion of the PUF domain did not interfere the FTO demethylase activity.

PUF binding site (+)

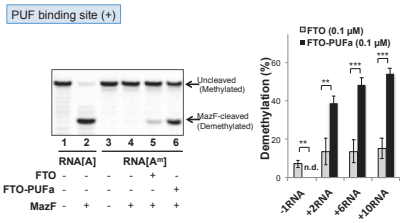

-1RNA	5′FAM-AUUGUAUAUm6ACAUUUUA-3′
+2RNA	5′FAM-AUUGUAUAUAAGm6ACAUUUUA-3′
+6RNA (RNA[Am])	5′FAM-AUUGUAUAUAUCUAAGm6ACAUUUUA-3′
+10RNA	5′FAM-AUUGUAUAUAUCGGCUUUAGm6ACAUUUUA-3′

FTO-PUFa showed significant demethylation activity for RNA with PUFa binding site.

Targeted RNA demethylation in the presence of HeLa total RNA

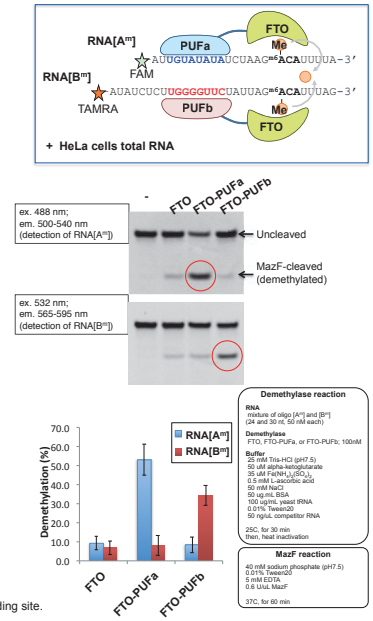

Evaluation method of m6A RNA methylation and demethylation

(Imanishi, et al., *Chem. Commun.* **53**, 12930 (2017))

MazF endoribonuclease

- Part of the toxin-antitoxin system of bacteria / archaea
- **ACA sequence-specific RNA endonuclease**
- **m6A sensitive !!!**

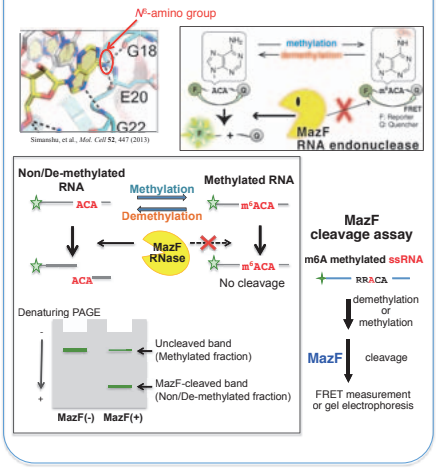

MTase-PUFs showed sequence-specific RNA methylation activities

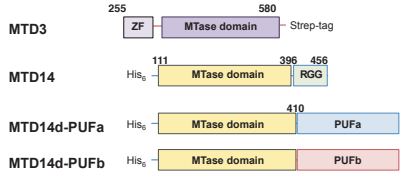

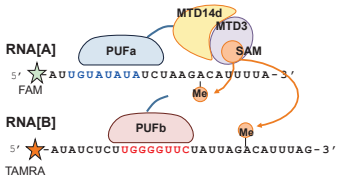

Effects of non-specific RNA on targeted RNA methylation

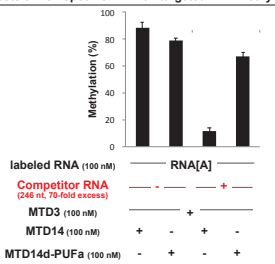

Addition of non-specific RNAs strongly lowered the methylation level of RNA[A] by MTD3/MTD14,but not by MTD3/MTD14-PUFa.

Targeted RNA methylation in the presence of HeLa total RNA

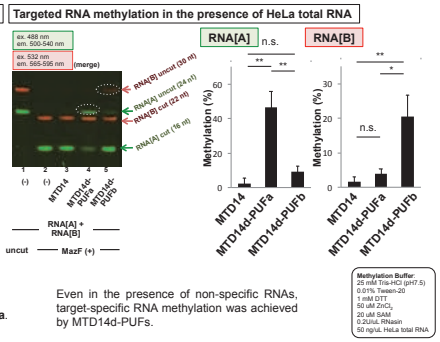

Even in the presence of non-specific RNAs, target-specific RNA methylation was achieved by MTD14d-PUFs.

Summary

FTOPUFs demethylated m6A close to the binding site of the PUF RNA binding domain.

MTD3/MTD14d-PUFs methylated the N^6-adenosine in a 5′-RRACH-3′ consensus sequence close to the binding site of PUFs.

Sequence-specific (de)methylation was demonstrated in vitro even in the presence of an excess amount of non-specific RNA fragments derived from mammalian cells.

Chem. Commun. (in press)

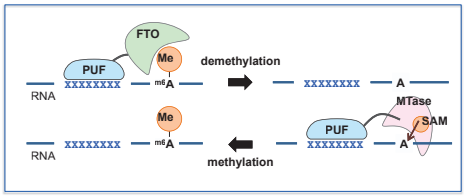

Development of a Method for Large Scale Synthesis of $H_2O@C_{60}$ Using a Triazine Derivative

○Kazuro Kizaki, Kyusun Kim, Yoshifumi Hashikawa, Takashi Hirose, and Yasujiro Murata

Institute for Chemical Research, Kyoto University

Introduction

Fullerene C_{60}

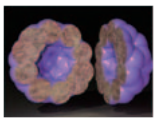

4 Å × 4 Å

Endohedral C_{60}

$H_2@C_{60}$ — Komatsu, K. et al. *Science* **2005**, *307*, 238-240.

$He@C_{60}$ — $He@C_{60}$ / C_{60} = 3 / 7; Murata, Y. Komatsu, K. et al. *Chem. Commun.* **2010**, *46*, 4532-4534.

$H_2O@C_{60}$ — Murata, Y. et al. *Science* **2011**, *333*, 613-616.

$CH_4@C_{60}$ — Whitby, R. J. et al. *Angew. Chem. Int. Ed.* **2019**, *58*, 5038-5043.

Molecular Surgery Methods

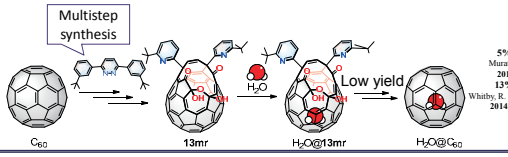

5% overall yield Murata, Y. et al. *Science* **2011**, *333*, 613-616.
13% overall yield Whitby, R. J. et al. *Chem. Commun.* **2014**, *50* 13037-13040.

This Work

- Synthesis of $H_2O@C_{60}$ using triazine derivative?
- Effects of C=N introduction?

Reactivity, Solubility, Opening size

Commercially available

- Fast addition reaction

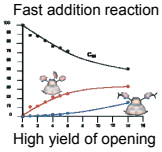

- High yield of opening closing reaction

Summary

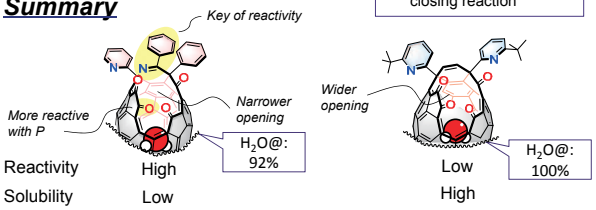

Results and Discussion

Diels-Alder reaction and opening expanding reaction

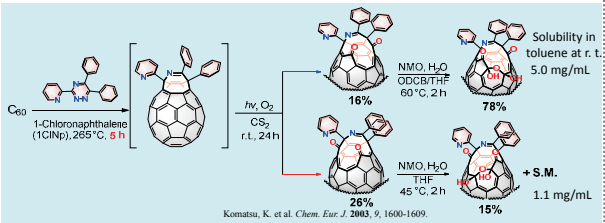

Komatsu, K. et al. *Chem. Eur. J.* **2003**, *9*, 1600-1609.

Previous method

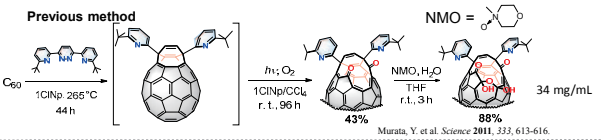

Murata, Y. et al. *Science* **2011**, *333*, 613-616.

Formation of 16mr and encalsulation of H_2O

^{1}H NMR, APCI-MS

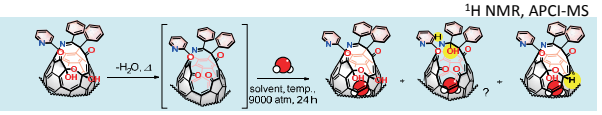

Entry	Scale	Solvent	Temp.	Yield (encaps. %)		
1	50 mg, 4.6 mM	1ClNp	140 °C	56% (36%)	44% (43%)	-
2	50 mg, 4.6 mM	1ClNp	160 °C	53 % (75%)	47% (53%)	-
3	50 mg, 15 mM	1ClNp	160 °C	35% (39%)	20% (56%)	45% (100%)
4	50 mg, 15 mM	1ClNp +Toluene	160 °C	30% (71%)	33% (72%)	37% (83%)
Pyridazine[a]	340 mg, 30 mM	toluene	120 °C	quant. (100%)	-	-

Yield and encapsulation ratio were estimated by ^{1}H NMR.
[a] Murata, Y. et al. *Science* **2011**, *333*, 613-616.

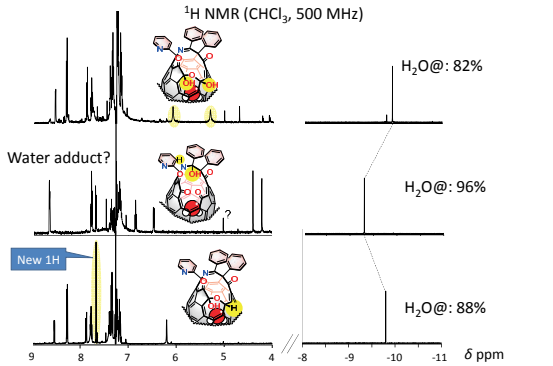

Dehydration reaction in ODCB (Preliminary data)

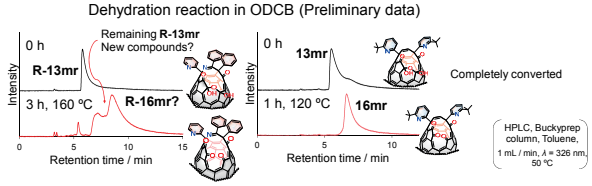

HPLC, Buckyprep column, Toluene, 1 mL / min, λ = 326 nm, 50 °C

DFT calculation (B3LYP-D3/6-31G(d))

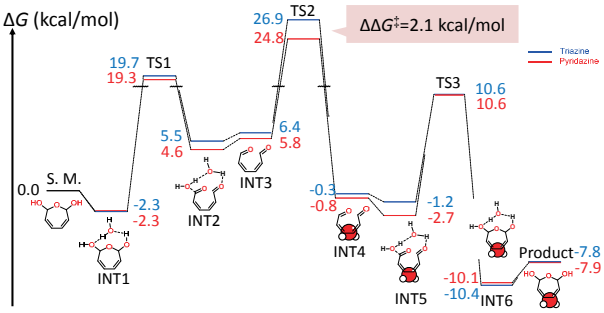

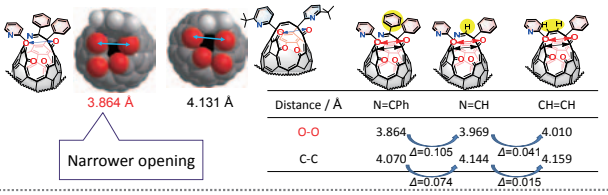

Distance / Å	N=CPh	N=CH	CH=CH
O-O	3.864	3.969	4.010
	Δ=0.105		Δ=0.041
C-C	4.070	4.144	4.159
	Δ=0.074		Δ=0.015

Ring closing reaction

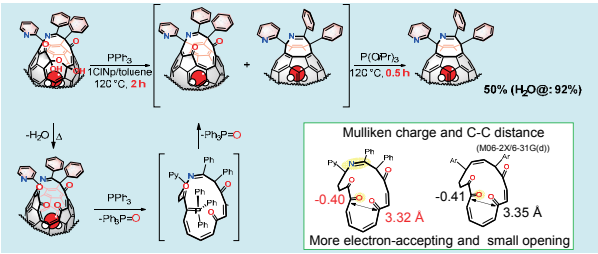

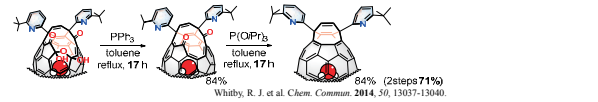

Whitby, R. J. et al. *Chem. Commun.* **2014**, *50*, 13037-13040.

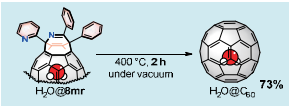

Retro Diels-Alder reaction proceeded without any dilution by Al_2O_3 and solvents.

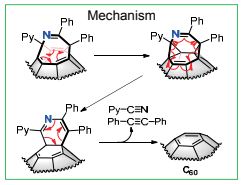

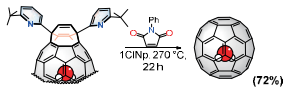

Whitby, R. J. et al. *Chem. Commun.* **2014**, *50*, 13037-13040.

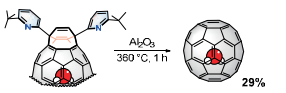

Murata, Y. et al. *Science* **2011**, *333*, 613-616.

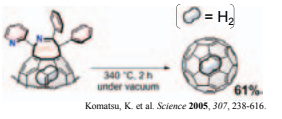

Komatsu, K. et al. *Science* **2005**, *307*, 238-616.

Development of "Heavy Aryl Anions"

Yoshiyuki Mizuhata,* Shiori Fujimori, Shingo Tsuji, Ryuto Sasayama, Norihiro Tokitoh*
Institute for Chemical Research, Kyoto University, Gokasho, Uji, Kyoto 611-0011, Japan
mizu@boc.kuicr.kyoto-u.ac.jp

Introduction

Germabenzenes

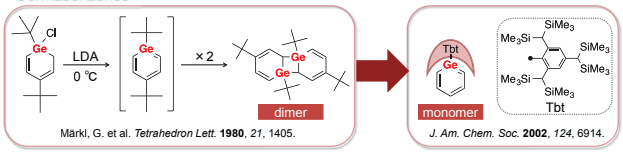

Märkl, G. et al. *Tetrahedron Lett.* **1980**, *21*, 1405. *J. Am. Chem. Soc.* **2002**, *124*, 6914.

A kinetic stabilization by a bulky aryl group, Tbt, has been recognized to be efficient to stabilize germabenzene.

Heavy Aryl Anions

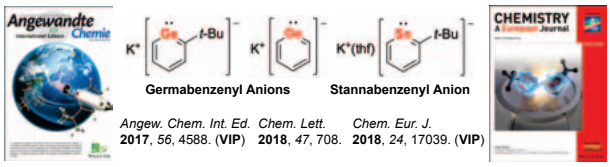

Germabenzenyl Anions — Stannabenzenyl Anion

Angew. Chem. Int. Ed. **2017**, *56*, 4588. (**VIP**) *Chem. Lett.* **2018**, *47*, 708. *Chem. Eur. J.* **2018**, *24*, 17039. (**VIP**)

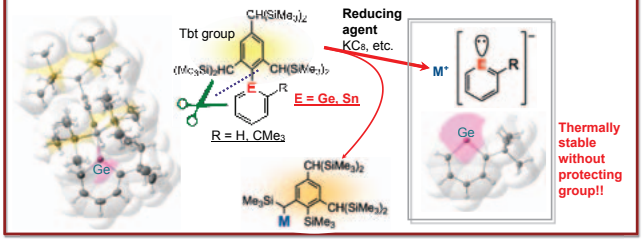

Structures of Heavy Phenyl Anions

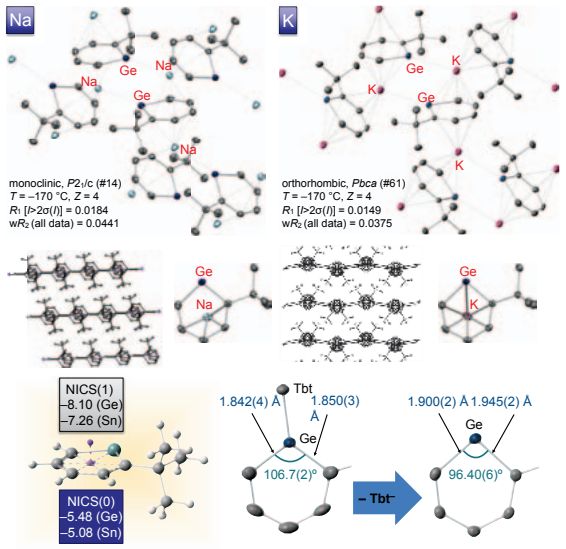

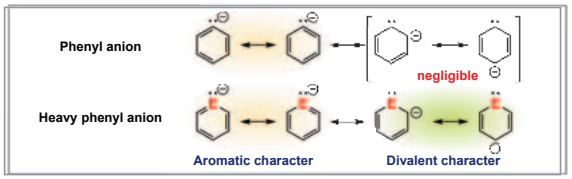

Acknowledgements
This work was supported by Grants-in-Aid for Scientific Research (S) (No. 19H05635), Scientific Research on Innovative Areas (No. 24109013), Scientific Research (B) (Nos. 18H01963, 16H04110, 25288021), and Scientific Research (C) (No. 26410044) from the Ministry of Education, Culture, Sports, Science and Technology, of Japan. S. F. thanks Research Fellowships of the Japan Society for the Promotion of Science for Young Scientists.

Complexation

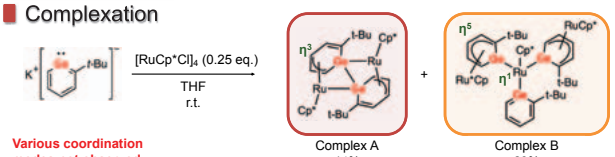

Various coordination modes not observed in the parent phenyl anion system

Thermal ellipsoid plots (50% probability)

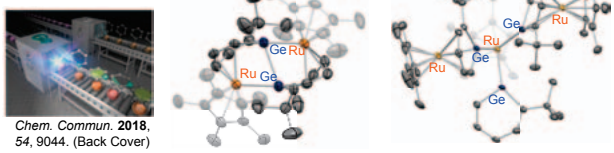

Chem. Commun. **2018**, *54*, 9044. (Back Cover)

The First "Metal-substituted" Germabenzene

Crystal Data (–170 °C) triclinic, *P*-1, GOF = 1.117 R_1 [I>2σ(I)] = 0.0442 wR_2 (all data) = 0.1289

Crystal Data (–170 °C) triclinic, *P*-1, GOF = 1.196 R_1 [I>2σ(I)] = 0.0312 wR_2 (all data) = 0.0821

9-Germaanthracenyl Anion

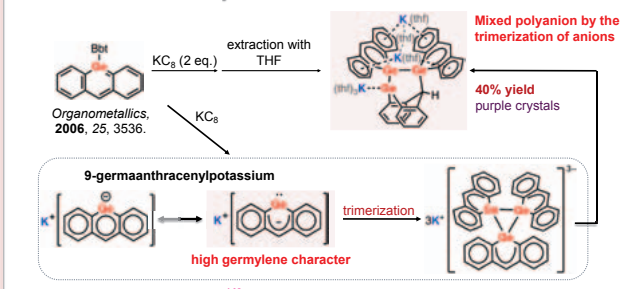

Organometallics, **2006**, *25*, 3536.

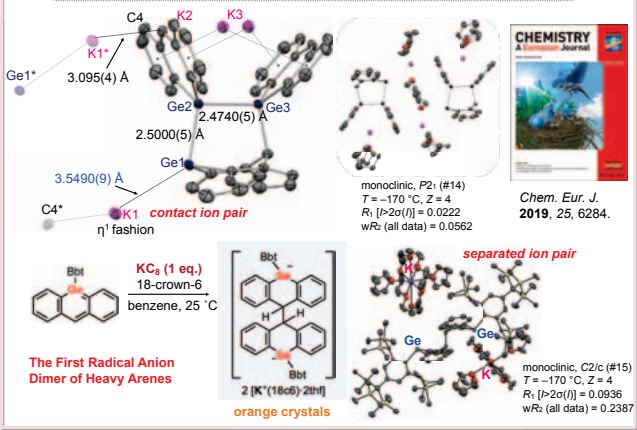

2-Germanaphthalenyl Anion

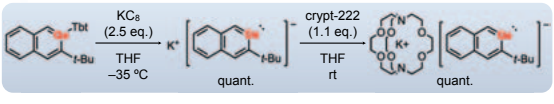

triclinic, *P*-1 (#2), *T* = –170 °C, *Z* = 4, R_1 [I>2σ(I)] = 0.0540, wR_2 (all data) = 0.1320

monoclinic, $P2_1/c$ (#14), *T* = –170 °C, *Z* = 4, R_1 [I>2σ(I)] = 0.0234, wR_2 (all data) = 0.0611

Unpublished

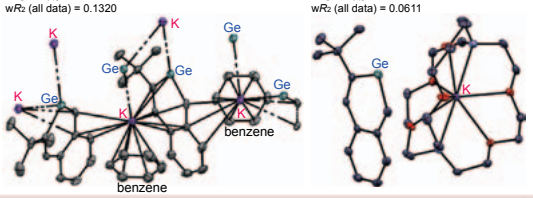

DFT study on Iron-catalyzed Enantioselective Carbometalation of Azabicycloalkenes

Akhilesh K. Sharma[1,2], Miho Isegawa[2,3], W. M. C. Sameera[2,4], Masaharu Nakamura[1]

[1] Institute for Chemical Research, Kyoto University, Kyoto, Japan
[2] Fukui Institute for Fundamental Chemistry, Kyoto University, Kyoto, Japan.
[3] International Institute for Carbon Neutral Energy Research, Kyushu University, Fukuoka, Japan
[4] Institute of low temperature science, Hokkaido University

Introduction

- Asymmetric addition of carbon and heteroatom-nucleophiles to oxa- and azabicyclic alkenes is an useful strategy for enantioselective synthesis of chiral building blocks of many natural products.
- Recently, we reported the iron-catalyzed diastereoselective carbometalation of oxa- and azabicyclic alkenes.[1]
- Currently our group is working on iron-catalyzed enantioselective carbometalation reactions of azabicycloalkenes with arylzinc reagents.

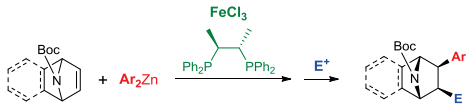

Objective and Computational Methods

- Computational methods (DFT methods) have nowadays become integral part of reaction mechanism study.[2]
- Delineate the mechanistic details of the iron-catalyzed enantioselective carbometalation reactions using computational (DFT) methods.
- Identify the origin of enantioselectivity in the reaction by DFT method.
- Gaussian 16 program used for all calculations.

Optimization: $PCM_{Toluene}$/B3LYP-D2/SDD(Fe),6-31G*(other atoms)

Free energies (electronic energies) are in kcal/mole at 25˚C temperature with total electronic energy with zpe correction in parenthesis.

AFIR method as implemented in GRRM program with Gaussian 09 was used for initial TS search for carbometalation step.[3]

Proposed Mechanism

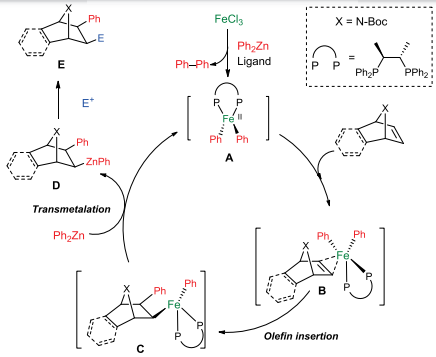

- *Spin-crossover* occurs before and after carbometalation TS.
- For carbometalation **TS** and alkene coordinated Fe^{II} complex (**B**) in triplet spin state is lowest energy.

Free Energy Profile

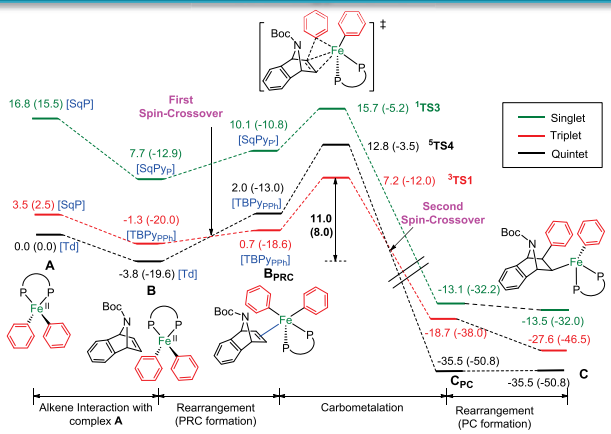

Note: Stationary point of lowest energy are given and their geometry is different in each spin state.

Origin of Enantioselectivity

- > 45 distinct TSs were obtained and 20 TSs have Gibbs free energy < 3 kcal/mol.
- Due to flexible coordination environment of iron, and sterically bulky chiraphos ligand TSs with distorted square pyramidal (**TS1** & **TS3**) and trigonal bipyramidal (**TS2** & **TS4**) geometry were obtained. The TS with SqPy geometry is lowest energy.

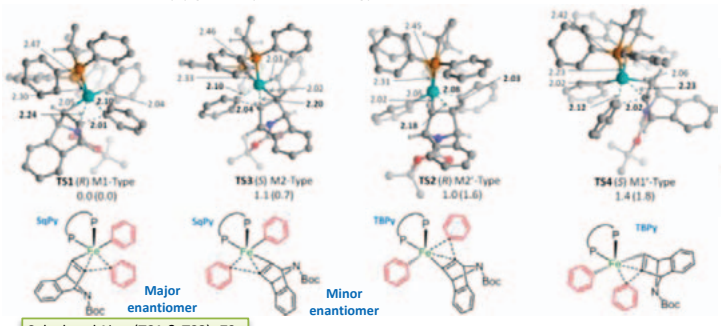

Calculated %ee (**TS1** & **TS3**): 73
Experimental %ee: 77

Energy Decomposition analysis

TS	ΔE_d [E_d(X), E_d(Y)]	ΔE_i	$\Delta\Delta E$
TS1	0.0 (0.0, 0.0)	0.0	0.0
TS2	-1.1 (0.8, -2.0)	3.5	2.4
TS3	-0.1 (-1.2, 1.1)	1.2	1.1
TS4	-4.3 (-0.8, -3.5)	6.7	2.4

Interaction energy (E_i) is controlling the enantioselectivity.

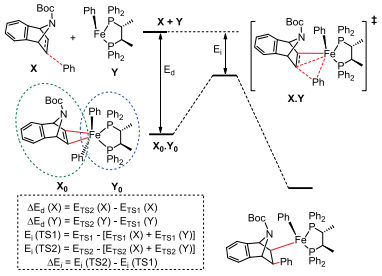

ΔE_d (X) = E_{TS2} (X) - E_{TS1} (X)
ΔE_d (Y) = E_{TS2} (Y) - E_{TS1} (Y)
E_i (TS1) = E_{TS1} - [E_{TS1} (X) + E_{TS1} (Y)]
E_i (TS2) = E_{TS2} - [E_{TS2} (X) + E_{TS2} (Y)]
ΔE_i = E_i (TS2) - E_i (TS1)

Spin-Crossover in Iron(II) complex (^{5}A and ^{3}A)

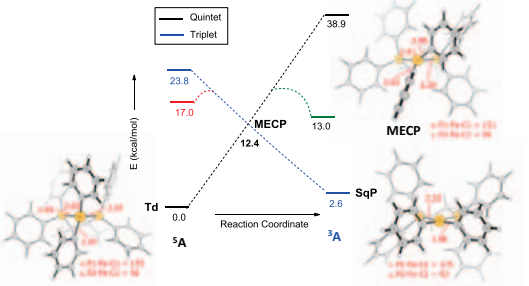

- Spin-crossover before alkene interaction with iron is less likely.

References

(1) S. Ito, T. Itoh, M. Nakamura, *Angew. Chem. Int. Ed.* **2011**, *50*, 454–457.
(2) A. K. Sharma, W. M. C. Sameera, M. Jin, L. Adak, C. Okuzono, T. Iwamoto, M. Kato, M. Nakamura, K. Morokuma, *J. Am. Chem. Soc.* **2017**, *139*, 16117–16124; c) T. Iwamoto, C. Okuzono, L. Adak, M. Jin, M. Nakamura, *Chem. Commun.* **2019**, *55*, 1128–1131.
(3) [4] W. M. C. Sameera, A. K. Sharma, S. Maeda, K. Morokuma, *Chem. Rec.* ***2016***, *16*, 2349-2363.

Acknowledgement

- **Super-computing resources:** Institute of Molecular Science, Japan
- **Reaction Development:** Experimental group members involved in development of the reaction.
- Prof. Satoshi Maeda for giving access to the developmental version of GRRM program.

Organic Hole-Transporting Materials with High-Lying HOMO Energy Levels for Tin-Based Perovskite Solar Cells

Institute for Chemical Research, Kyoto University

Minh Anh Truong, Ruito Hashimoto, Tomoya Nakamura, Richard Murdey, Atsushi Wakamiya

Introduction

ABX_3-Type Perovskite

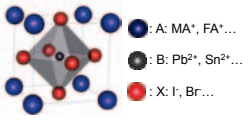

$MA^+ = CH_3NH_3^+$ $FA^+ = (NH_2)_2CH^+$

Perovskite Solar Cell and Mechanism

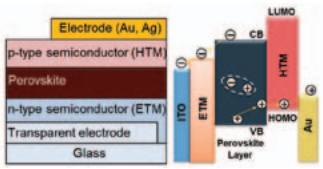

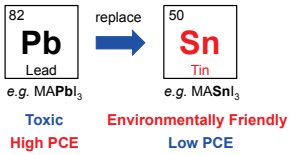

Progress in Power Conversion Efficiencies

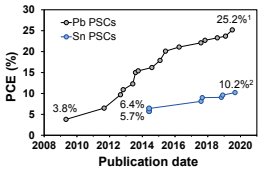

1. https://www.nrel.gov/pv/assets/pdfs/best-research-cell-efficiencies.20191106.pdf
2. S. Hayase, *et al. J. Phys. Chem. Lett.* **2019**, *10*, 5277.

Problem: HOMO Levels of HTMs Lie Below Valence Bands (VBs) of Perovskite

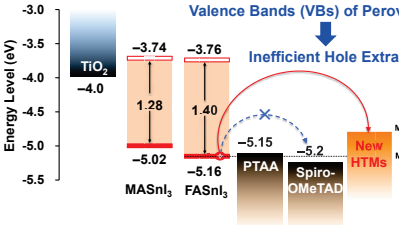

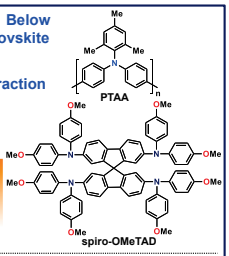

This Work: HTMs with High-Lying HOMO Levels → Efficient Hole Extraction

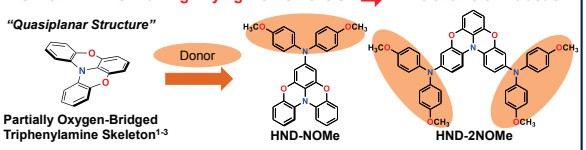

1. A. Wakamiya, H. Kaji, Y. Murata, *et al. Angew. Chem. Int. Ed.* **2014**, *53*, 5800.
2. A. Wakamiya, L. T. Scott, Y. Murata, *et al. J. Am. Chem. Soc.* **2015**, *137*, 15656.
3. M. A. Truong, T. Nakamura, R. Murdey, A. Wakamiya, *et al. Chem. Eur. J.* **2019**, *25*, 6741.

Results and Discussion

Synthesis and Thermal Properties

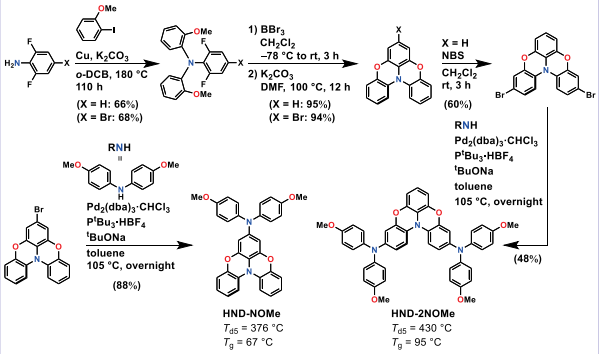

Amorphous solids with high thermal stability (T_{d5} > 370 °C)

Photophysical and Electrochemical Properties

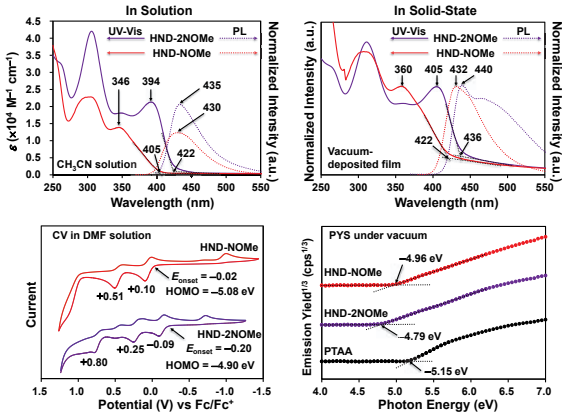

DFT Calculations and Energy Diagram

(DFT: B3LYP/6-31G(d), TD-DFT: CAM- B3LYP/6-31G(d))

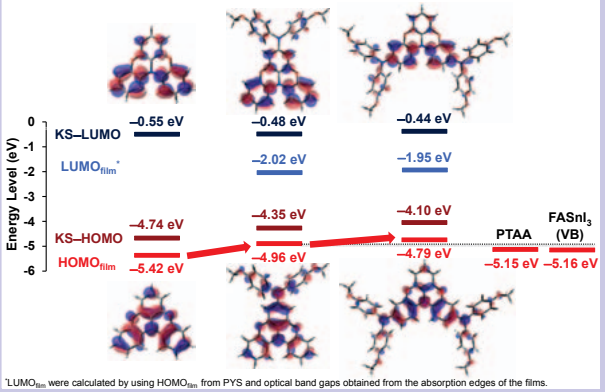

*LUMO$_{film}$ were calculated by using HOMO$_{film}$ from PYS and optical band gaps obtained from the absorption edges of the films.

Tin-Based Perovskite Solar Cells Fabrication and Evaluation

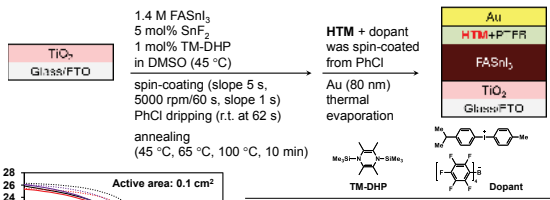

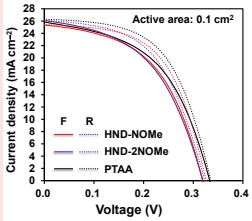

HTM[a]	Scan[b]	J_{sc} (mA cm^{-2})	V_{oc} (V)	FF	PCE (%)
HND-NOMe	F	25.34	0.32	0.51	4.12
	R	25.47	0.33	0.56	4.68
HND-2NOMe	F	26.08	0.32	0.49	4.04
	R	26.11	0.32	0.53	4.46
PTAA	F	25.86	0.33	0.50	4.31
	R	26.30	0.34	0.56	4.93

a) HTM was spin-coated from the solution with additive in PhCl (**HND-NOMe** 0.06 M, **HND-2NOMe** 0.06 M, or **PTAA** 20 mg/ml with 7.0 mM dopant). b) F: Forward scan, R: Reverse scan

Summary

- Two thermally stable hole conducting materials were synthesized by connecting the partially oxygen-bridged triarylamine structure to one or two 4,4′-dimethoxydiphenylamine through Buchwald-Hartwig C-N cross coupling reaction.
- The synthesized materials possess high-lying HOMO energy levels of above −5.0 eV. These high-lying HOMO energy levels are suitable for efficient hole extraction in tin-based perovskite solar cells.
- The best power conversion efficiency of the regular structural $FASnI_3$-based Perovskite solar cells using **HND-NOMe**, **HND-2NONe** as HTM is 4.68%, and 4.46%, respectively; which is comparable to that of devices using **PTAA** as HTM (4.93%).

Acknowledgement

Financial supported from **IRCCS**, **NEDO**, **COI**, **JSPS**, and **ALCA.**

Preparation of Highly Emissive Perovskite Materials for Light-Emitting Diodes

Alwani Imanah Rafieh, Ai Shimazaki, Yuko Matsushige, Yasuko Iwasaki, Tomoya Nakamura, Richard Murdey, Atsushi Wakamiya

Institute for Chemical Research, Kyoto University, Uji 611-0011, Japan

Introduction

External Quantum Efficiency (EQE):
Blue = 6% < Green = 20%, Red = 21%

Optoelectronic property of perovskite nanoparticles is size dependent. In another words, emission wavelength of the perovskite nanoparticles can be tuned with respect to the size aside from chemical composition. Varying the size can be done by changing the ligand.

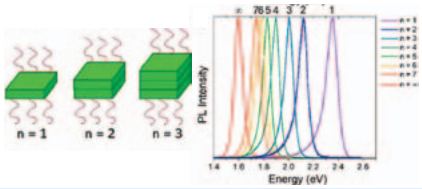

Synthesis of $CsPbBr_3$ Nanoparticles with Ligands

Hot Injection

Ref: L. Protesescu et al. *Nano Lett.* **2015**, *15*, 3602..

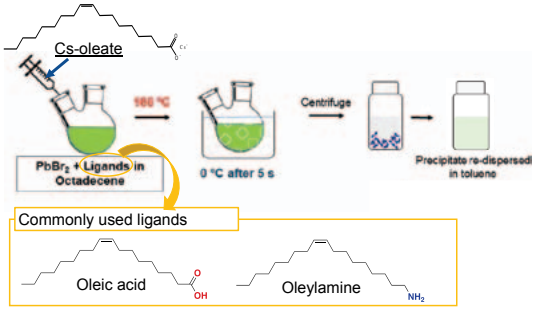

Ligand Exchange

Ref: T. Chiba et al. *ACS Appl. Mater. Interfaces* **2017**, *9*, 18054.

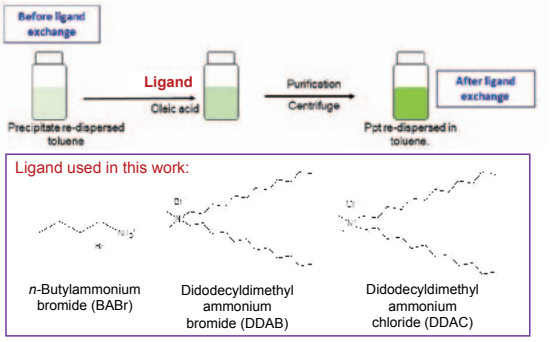

Results

BABr Ligand Exchange

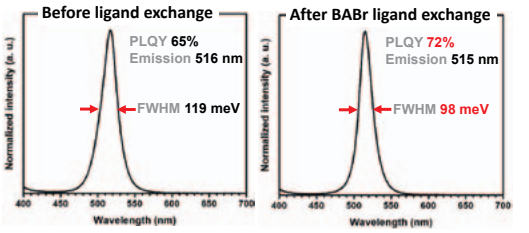

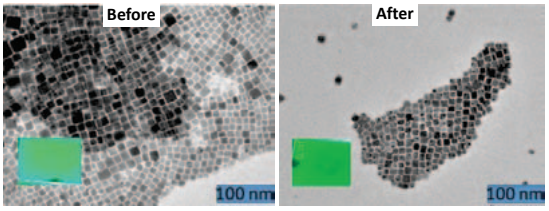

Long chain ligands were successfully replaced with short ligand

DDAB and DDAC Ligand Exchange

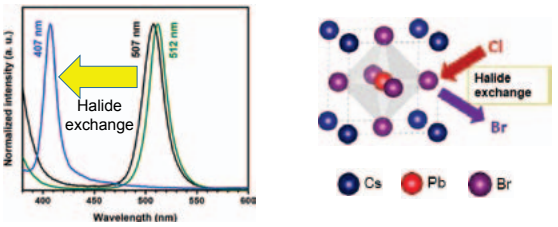

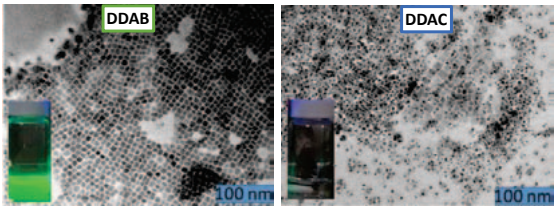

Tuning the emission wavelength through halide exchange is successful

Summary

- $CsPbBr_3$ nanoparticles with long alkyl chain ligands were synthesized using the hot injection method.
- Long chain ligands were successfully substituted with short ligand to reduce the distance between nanoparticles and improve charge injection in LED devices.
- Emission wavelength can be tuned by halide exchange.

京都大学
KYOTO UNIVERSITY

Investigation of Ru^{7+} and Os^{7+} Quantum Magnets with Scheelite and Scheelite-derivative Structures

Sean Injac[1,3], Maxim Avdeev[2], Brendan J. Kennedy[3], Yuichi Shimakawa[1]
1. Institute for Chemical Research, Kyoto University, Japan
2. Australian Centre for Neutron Scattering, ANSTO, Australia
3. School of Chemistry, University of Sydney, Australia

Introduction

Within this work we investigate a number of oxides of the form ABO_4 where A = K, Rb, Cs; and B = Ru, Os. The stabilisation of the Ru^{7+} and Os^{7+} cations allows for investigation and comparison between $4d^1$ and $5d^1$ $S = 1/2$ quantum magnets, while the increasing ionic radius of the A cation investigates the effect of structural change and increasing intermetallic distances has on physical properties. These materials were synthesised by the reduction of the associated tetroxide. Structural chacterisation was undertaken using a combination of X-ray synchrotron (SXRD) and single crystal diffraction (SCXRD) experiments, and neutron powder diffraction (NPD) measurements undertaken at the ECHIDNA beamline at ANSTO, Australia and the WISH instrument at ISIS, UK. Variable temperature X-ray diffraction measurements were undertaken at the powder diffraction beamline of the Australian Synchrotron. The magnetic properties of these oxides were investigated using temperature dependent, and field dependent magnetisation measurements, heat capacity measurements and low temperature neutron powder diffraction measurements which allowed for the determination of the magnetic structures of $KOsO_4$ and $RbRuO_4$.

Room Temperature Structures

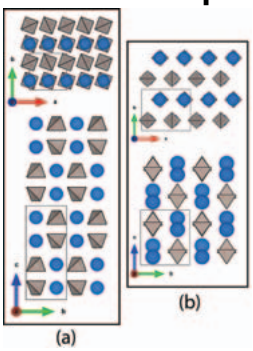

Figure 1: Representations of the $I4_1/a$ scheelite structure (a) and ***Pnma*** $CsRuO_4$ structure (b).

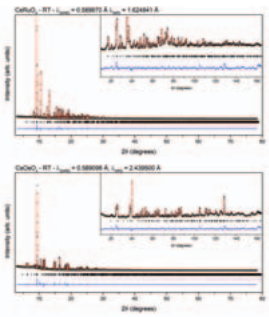

Figure 2: Combined SXRD/NPD refinement profiles for $CsRuO_4$ (top) and $CsOsO_4$ (bottom) at room temperature.

Room temperature structures were determined for all compounds via Rietveld refinement undertaken against combined SXRD and NPD datasets. At room temperature, $KRuO_4$, $KOsO_4$ and $RbOsO_4$ crystallise in the scheelite structure in space group $I4_1/a$. A representation of this structure is shown in Figure 1(a). $RbRuO_4$ and $CsOsO_4$ crystallise in a distorted pesudo-scheelite structure in space group *Pnma*, as a result of the larger *A*:*B* ionic radii ratio for these compounds. A relationship between these two structures is shown in Figure 3, which differ in the axis of rotation of the BO_4 tetrahedra. $CsRuO_4$ was determined to crystallise as a baryte type structure in space group *Pnma*. This structure is similar to that recently reported for $PbSbO_4$, and was confirmed through SCXRD measurements.[x] A representation of this structure is shown in Figure 1(b) and the associated refinement profiles are given in Figure 2. The distinct structural change is evident in diffraction data when compared to the pesudo-scheelite $CsOsO_4$, which also crystallises in apce group *Pnma*, with the associated refinement profiles shown in Figure 2. From these compounds the ionic radius of the Os^{7+} cation in a tetrahedral coordination environment was determined to be 3.79 Å, it is noted that no ionic radius for these conditions is given in the Shannon tables.

Variable Temperature Structures

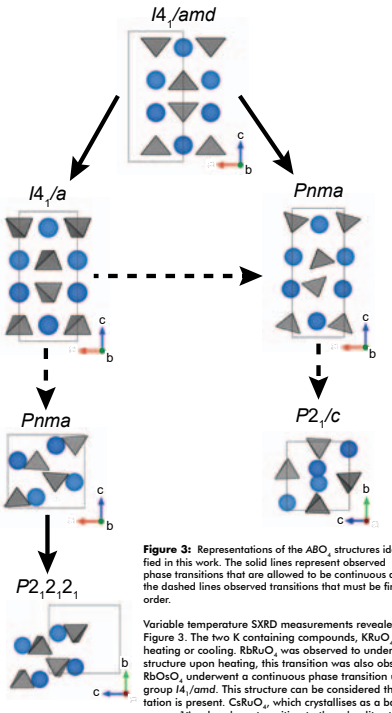

Figure 3: Representations of the ABO_4 structures identified in this work. The solid lines represent observed phase transitions that are allowed to be continuous and the dashed lines observed transitions that must be first order.

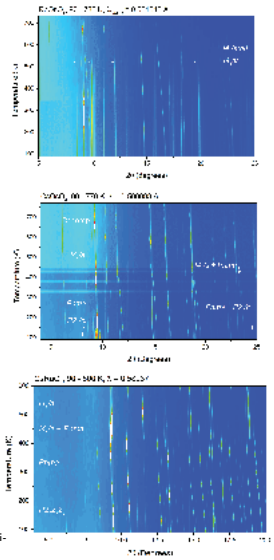

Figure 4: Variable temperature SXRD data collected for $RbOsO_4$ (top), $CsOsO_4$ (middle), and $CsRuO_4$ (bottom).

Variable temperature SXRD measurements revealed interesting phase behaviour, which is summaried in Figure 3. The two K containing compounds, $KRuO_4$ and $KOsO_4$ did not undergo any phase transitions upon heating or cooling. $RbRuO_4$ was observed to undergo a 1st order phase transition to the $I4_1/a$ scheelite structure upon heating, this transition was also observed for $CsOsO_4$, data for which is shown in Figure 4. $RbOsO_4$ underwent a continuous phase transition upon heating to a related scheelite structure in space group $I4_1/amd$. This structure can be considered the "undistorted" scheelite structure, as no tetrahedral rotation is present. $CsRuO_4$, which crystallises as a baryte-like structure in *Pnma* at room temperature undergoes a 1st order phase transition to the scheelite structure in $I4_1/a$ upon heating, the baryte and scheelite phase coexist over a large temperature regime, as shown in Figure 4. Upon cooling $CsRuO_4$ underwent a continuous phase transition to a post-baryte structure in $P2_12_12_1$. $P2_12_12_1$ is a direct subgroup of *Pnma*, and this transition occurs through a softening of the the Γ_{1-} mode. This transition was also observed in variable temperature SCXRD measurements. $CsOsO_4$ showed unique phase behaviour, upon heating a 1st order phase transition to the $I4_1/a$ scheelite structure is observed, consistent with the other *Pnma* compounds. Upon cooling at approximately 140 K a 1st order phase transition to a distorted structure in the monoclinic space group $P2_1/c$ is observed, with a = 8.22278(11), b = 7.921734(7), c = 8.23025(11), and β = 119.0845(6). This structure is similar to the monazite structure, however no relationship between this structure and the scheelite structure could be determined using the ISOTROPY software suite.

Magnetic Properties

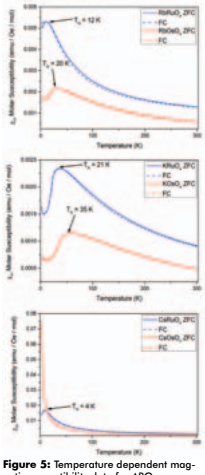

Figure 5: Temperature dependent magnetic susceptibility data for ABO_4 compounds where A = K (top), Rb (middle) and Cs (bottom). ZFC and FC measurements are indicated.

Temperature dependent magnetisation, isothermal magnetisation and heat capacity measurements were undertaken on all samples. Temperature dependent DCMS data are shown in Figure 5. All data were consistent with long range antiferromagnetism (AFM) for all compounds except for $CsOsO_4$ which remained paramagnetic to 2 K. DCMS and heat capacity data reveals a trend for Os compounds to show higher ordering temperature compared to their Ru counterparts, and magnetic susceptibilities were observed to decrease with increasing intermetallic distance, as the size of the A cation is increased. These observations suggest that magnetic ordering in these compounds is mediated through direct exchange mechanisms which must result in antiferromagnetic exchange. The higher ordering temperatures for Os compounds are rationalised by consideration of the larger spatial diffusion of the 5*d* orbitals compared to the Ru 4*d* orbitals. As orbital overlap is increased the strength of magnetic exchange interactions also increases, resulting in higher magnetic ordering temperatures. In all cases superexchange, which would involve the AO_4 polyhedra and entail a long *B*-O-*A*-O-*B* pathway, is expected to be very weak, rather direct exchange should be dominant. As suggested by Marjerrison et al.[x] nearest neighbour interactions are expected to be the strongest and this suggestion is apparently verified by noting the increase in *B*-*B* separation correlates with the decrease in the Néel temperature in both the Ru and Os scheelites. $CsOsO_4$ is an outlier in this series reflecting the different configuration of the OsO_4 tetrahedra. Effective magnetic moments determined from fits to inverse susceptibility were consistent with a $S = 1/2$ magnetic ground state. A reduction of this moment was observed for the Os compounds compared to their Ru analogues, this is consistent with the enhanced spin orbit coupling effect of the 5*d* orbitals. This is due to a 2nd order spin orbital coupling effect, as a 1st order effect does not impact the occupied e_g orbitals.

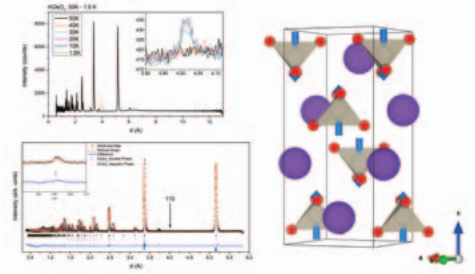

Figure 6: NPD data collected at the WISH diffractometer for $KOsO_4$. Temperature dependent data is shown above-left, with data collected above and below the magnetic transition. The magnetic refinement profile carried out against data collected at 3 K is shown below. A representation of the magnetic structure of KOsO4 is shown to the right.

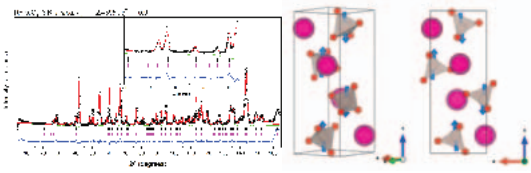

Figure 7: A refinement profile for $RbRuO_4$ carried out against NPD data collected at ECHIDNA at 3 K. A magnetic contribution is indicated by magneta tickmarks. A representation of the magnetic structure is shown to the right.

Magnetic structures were determined for $KOsO_4$ and $RbRuO_4$. The magnetic unit cell for $KOsO_4$ was determined by Rietveld refinement carried out against NPD data collected at the WISH instrument at ISIS. A single, weak reflection was observed to gain intensity below the magnetic ordering transition and was indexed as *hkl* = (110) with a *k* = 0,0,0 magnetic propagation vector in space group $I4_1/a$. Group theory analysis, performed with the ISODISTORT software suite, indicated four possible irreducible representations namely Γ_1, Γ_2, Γ_3 and Γ_4. Of these only Γ_2 allows for intensity in the (110) but not the (002) reflection showing that magnetic structure to be antiferromagnetic with the moments parallel to the *c*−axis. This is consistent with AFM ordering of spins along the 001 direction, as represented in Figure 6. A miniscule ordered magnetic moment of 0.46(18) μ_B was determined. This structure is equivalent to that previously determined for $KRuO_4$, which was reported to have a slightly larger magnetic moment of 0.57(7) μ_B.[x] A magnetic structure for $RbRuO_4$ is tentatively proposed. Rietveld refinements carried out against NPD data collected at 3 K for this compound using the ECHIDNA diffractometer at ANSTO show a slight increase of intensity of several reflections compared to data collected above the magnetic ordering transition temperature. Therefore a magnetic propagation vector of *k* = 0,0,0 was determined. Eight possible irreps were identified. Of these, Γ_{2+}, Γ_{3+}, and Γ_{4+} show ferromagnetic order, and are therefore inconsistent with the magnetisation data. The remaining representations show AFM ordering. For irreps Γ_{1-}, Γ_{2-}, and Γ_{3-} the moments are required to lie parallel to the *b*-axis. Irreps Γ_{1-} and Γ_{4+} show AFM ordering along the *c*-axis, with canting of moments within the 100 plane. All AFM irreps resulted in similar quality of Rietveld fits to the NPD data, indicating that better data quality is required in order to unequivocally determine the magnetic structure of $RbRuO_4$. Nevertheless, a magnetic cell is tentatively proposed using Γ_{1-} as this magnetic structure is effectively equal to that determined for $KRuO_4$ and $KOsO_4$, with a small AFM canting of magnetic moments within the 100 plane. A refinement profile using this model is shown in Figure 7. The magnetic moments were refined to be 0.77(24) μ_B along the *c* direction and 0.21(9) μ_B along the *a* direction. A representation of this magnetic structure is also shown in Figure 7.

Large latent heat by intersite charge transfer transitions in *A*-site ordered perovskites

Yoshihisa Kosugi[1], Masato Goto[1], Takashi Saito[1,2], Yuichi Shimakawa[1]
[1] *Institute for Chemical Research, Kyoto University, Uji, Kyoto 611-0011, Japan*
[2] *High Energy Accelerator Research Organization (KEK), Tokai, Ibaraki 319-1106, Japan*

Introduction

A-site ordered perovskite-structure $AA'_3B_4O_{12}$

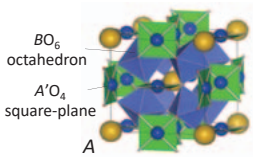

A-site order $A : A' = 1 : 3$

Because the structure has $A'O_4$ square-plane, Cu^{2+} or Mn^{3+} can occupy A' site.

A'-B interaction causes various physical property.

inter-site Charge Transfer (CT) transition in $ACu_3Fe_4O_{12}$

(A = Bi^{3+}, La^{3+}~Tb^{3+})

Low-T		High-T
$ACu^{3+}{}_3Fe^{3+}{}_4O_{12}$	⟷	$ACu^{2+}{}_3Fe^{3.75+}{}_4O_{12}$
insulator	⟷	metal
antiferromagnetic	⟷	paramagnetic

Large volume change (1~2%) but no symmetry change

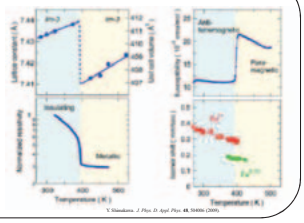

A-site substitution

$ACu_3Fe_4O_{12}$

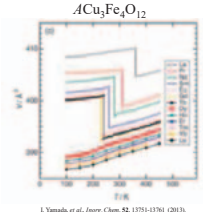

A=La~Tb
Inter-site charge transfer(CT) transition
$3Cu^{2+} + 4Fe^{3.75+} \rightarrow 3Cu^{3+} + 4Fe^{3+}$

A=Dy~Lu
charge disproportionation(CD) transition
$8Fe^{3.75+} \rightarrow 3Fe^{5+} + 5Fe^{3}$

We focus on inter-site CT transition because this tunability of transition temperature by *A*-site substitution is useful for application.

This research

We studied heat physical properties at the CT transition in $NdCu_3Fe_4O_{12}$ and found that the transition is accompanied by large latent heat near room temperature.

Experimental
- synchrotron XRD (SXRD)
- Electric resistivity measurement
- Differential scanning calorimetry (DSC)
- Magnetic measurement
- Neutron diffraction

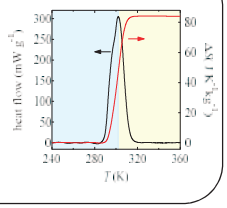

Results and Discussion

synthesis and structure

High pressure synthesis:
9 GPa, 1100 ℃

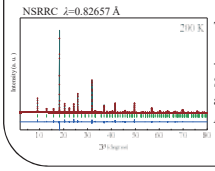

There are no impurity peaks.

<Rietveld analysis>
Space group: $Im\bar{3}$
a=7.39693 Å
R_{wp}=4.245%

physical properties

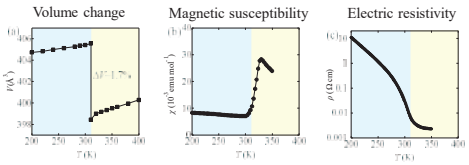

All physical properties change in the inter-site CT transition temperature.

DSC

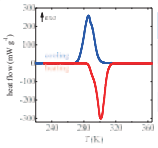

	cooling process	heating process
peak top position	302.1 K	316.1 K
entropy change ΔS	84.2 J K^{-1} kg^{-1}	80.6 J K^{-1} kg^{-1}
latent heat $\lvert Q \rvert$	25.5 kJ kg^{-1}	25.1 kJ kg^{-1}

So large entropy change!

DSC curve shows hysteresis loop, indicating inter-site CT transition is of a first-order transition.

Neutron diffraction

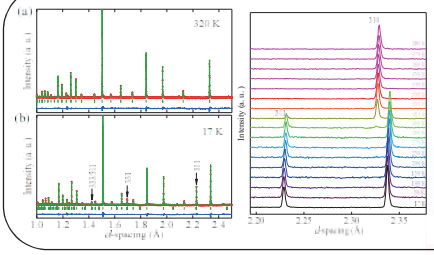

In ND pattern, 311, 331 and 333/511 peaks are observed in LT phase.

G-type antiferromagnetic ordering

From temperature evolution of ND pattern, magnetic Bragg peaks 311 abruptly disappear together with LT phase.

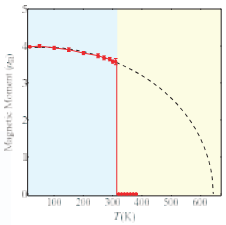

S=5/2 Brillouin function fitting

Neel temperature T_N=643 K

Near 300 K
charge transfer energy > antiferromagnetic interaction

S=5/2
$\Delta S_M = R\ln(2S+1) = 79$ J K^{-1} kg^{-1}
$\Rightarrow$ Q = 24 kJ kg^{-1} (300 K)

An unusual first-order magnetic transition induced by the intersite CT causes a colossal entropy change.

Conclusions

- $NdCu_3Fe_4O_{12}$ was obtained as a single phase by high pressure synthesis and showed inter-site charge transfer transition near room temperature.

- The inter-site CT transition is accompanied by a colossal latent heat (25.5 kJ kg^{-1}) near room temperature. This entropy change is attributed to the unusual first-order magnetic transition induced by CT transition.

- The large entropy change is possibly used for a magnetocaloric effect, which provides environment-friendly and highly-efficient refrigeration systems compared to the widely used conventional vapor-compression cooling systems.

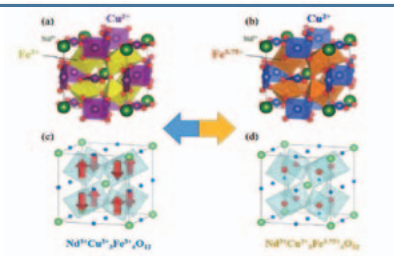

Polarization Switching via Electron Transfer in a Valence Tautomeric Cobalt Complex

Shu-Qi Wu, S. Kanegawa, and O. Sato
Institute for Materials Chemistry and Engineering, Kyushu University, 744 Motooka, Nishi-ku, Fukuoka 819-0395, Japan

Soft Molecular assemblies

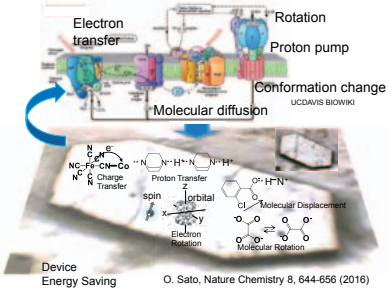

O. Sato, Nature Chemistry 8, 644-656 (2016)

Electron Transfer

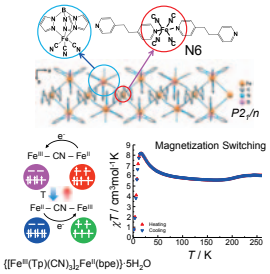

{[Fe^{III}(Tp)(CN)$_3$]$_2$Fe^{II}(bpe)}·5H$_2$O

Angew. Chem. Int. Ed., **55**, 6047-6050 (2016)

Proton Transfer

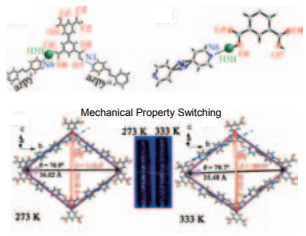

[(H$_4$BPTC)(azpy)$_2$]$_n$

Angew. Chem. Int. Ed., 55, 14628-14632 (2016)

Molecular Transfer

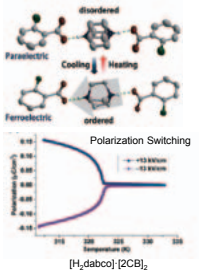

[H$_2$dabco]·[2CB]$_2$

J. Am. Chem. Soc. 138, 12005-12008 (2016)

Results

Polarization Switching

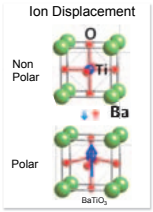

D. Fu et al. Intech DOI: 10.5772/61017
Ferroelectric Materials – Synthesis and Characterization

Valence Tautomerism in Cobalt Complexes

Valence tautomeric transitions involve a stimulated intramolecular electron transfer between a redox-active metal center and redox-active ligand.

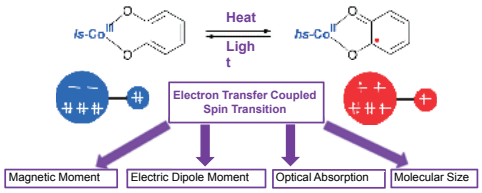

Strategy and Potential Advantages

Crystallize valence tautomeric molecules in the polar space group.

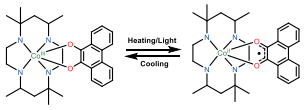

Energy-economic: Repeatable without polarization field.

Light-controllable: Switching with suitable light excitation.

Magnetometry: Two-step Valence Tautomerism

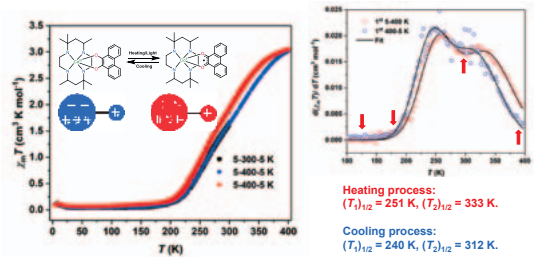

Crystal Packing: Steric Effect and Non-cancelable Polarization

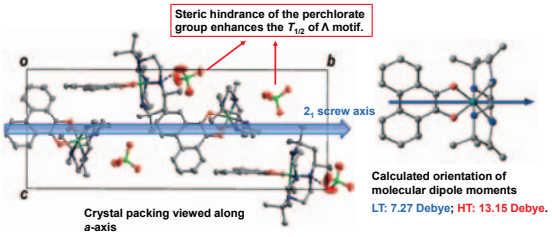

Pyroelectricity: Two-step Polarization Switching

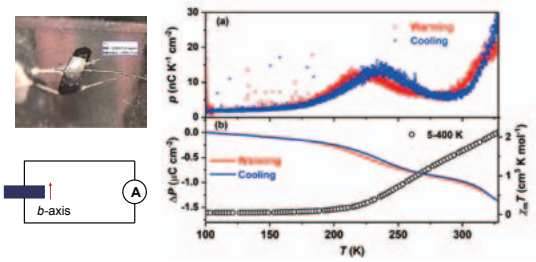

Light-induced Polarization Switching: Magnetometry

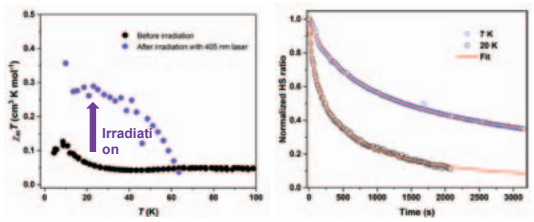

Light-induced Polarization Switching: Spectroscopy

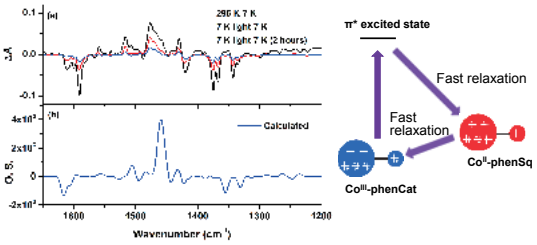

Light-induced Polarization Switching: Dynamics

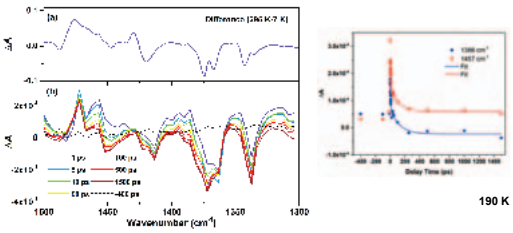

Electronic Pyroelectricities in Heterometallic Dinucler Complexes

(IMCE, Kyushu Univ.)Shinji Kanegawa and Osamu Sato
E-mail: kanegawa@cm.kyushu-u.ac.jp

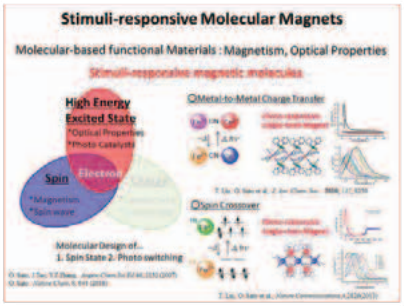

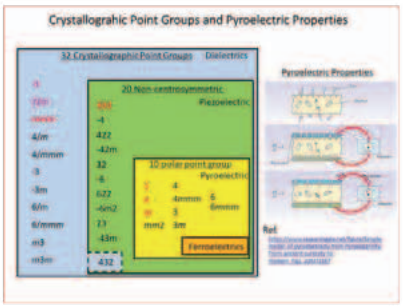

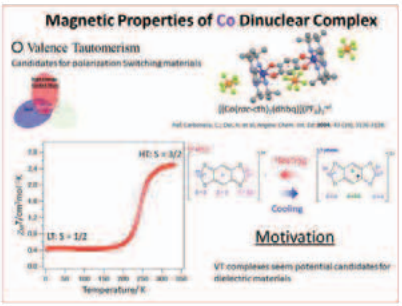

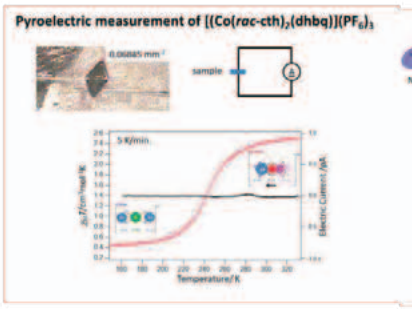

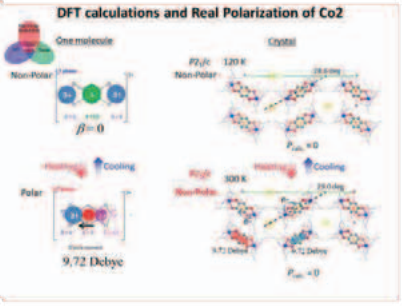

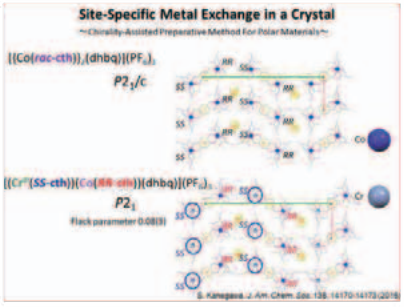

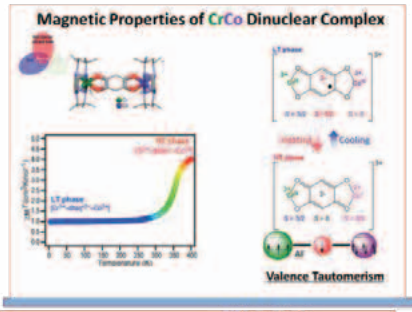

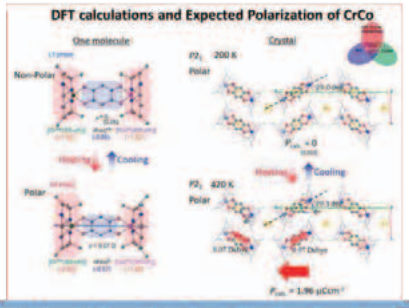

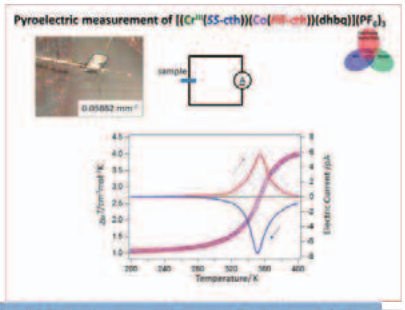

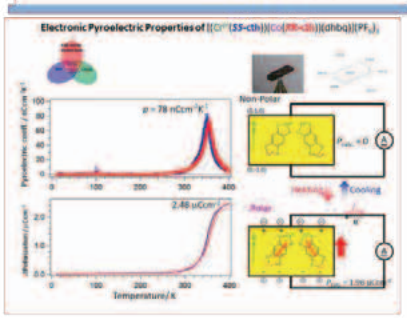

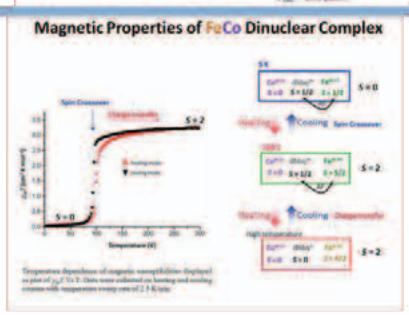

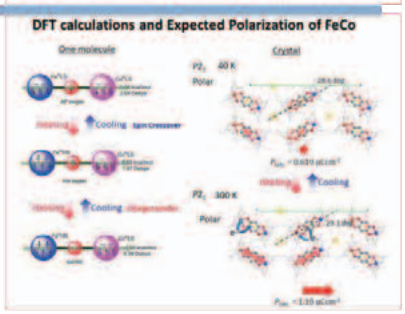

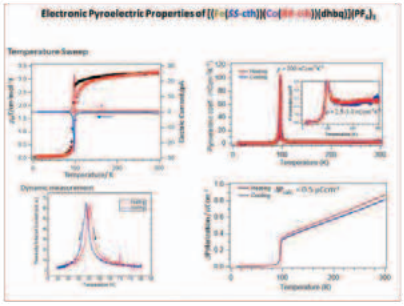

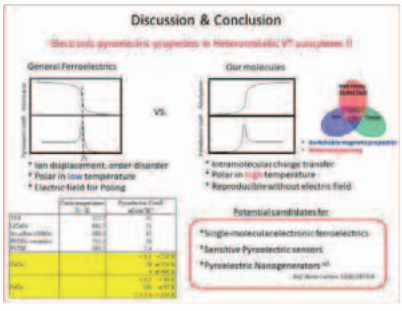

Magnetic switching without spin transition in an Iron(II) complex

Sheng-Qun Su, Shu-Qi Wu, Shinji Kanegawa, Osamu Sato
Institute for Materials Chemistry and Engineering, Kyushu University, and IRCCS

Control of Magnetic Property

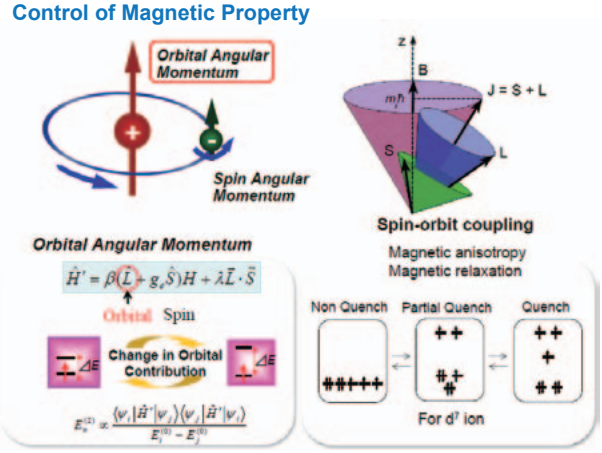

Control of Spin Angular Momentum

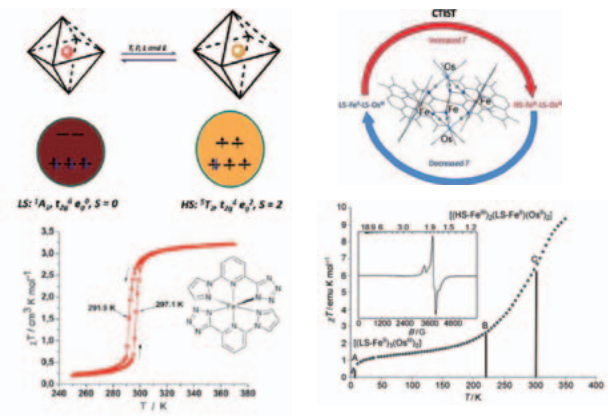

Coord. Chem. Rev. 346 (2017) 176–205 Angew. Chem. Int. Ed. 2010, 49, 1410 –1413

Multistep transition In Fe(II) complex

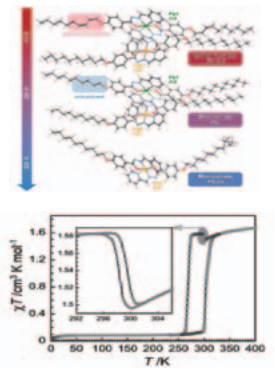

J. Am. Chem. Soc. 2018, 140, 98−101

Control of Orbital Angular Momentum

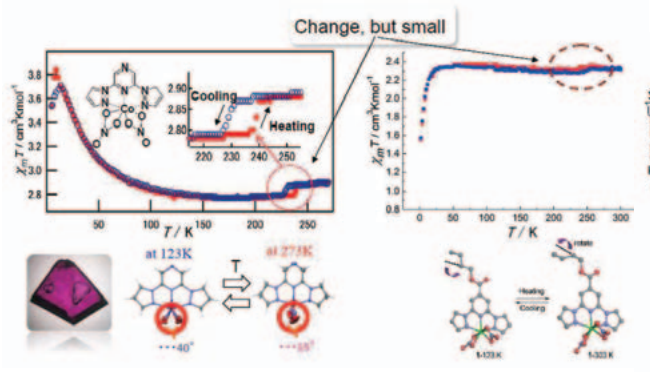

J. Am. Chem. Soc. 131, 4560–4561 (2009)

Previous work about Co(II) complex

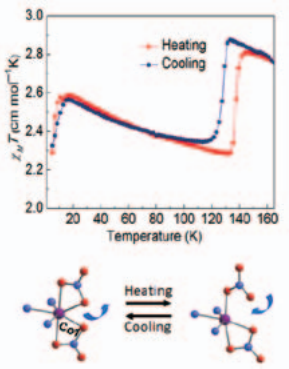

Nature Commun. 6, 8810 (2015)

Current work about Fe(II) complex

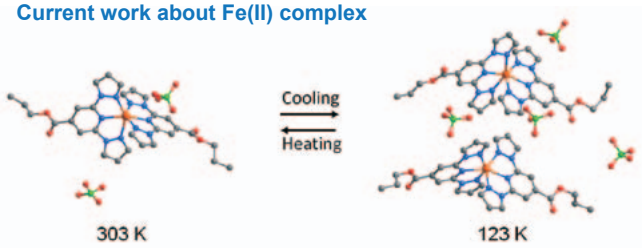

Molecular structures at the low and high temperature phase

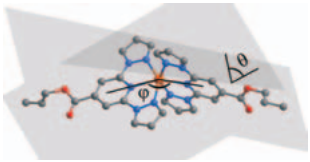

The two components in the angular Jahn–Teller distortion

	303 K	123 K	
φ (deg.)	155.52	151.93	151.83
θ (deg.)	88.11	78.98	80.15

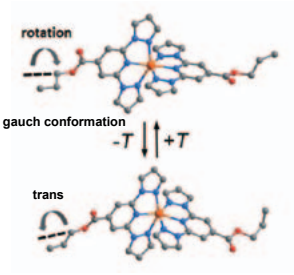

The propyl group rotated

	123 K	303 K
ΔE1 (ev)	0.122	0.049
ΔE2 (ev)	0.204	0.106

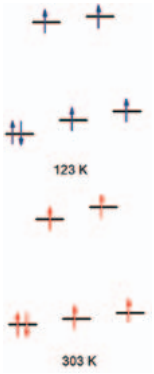

calculated d-orbital splitting

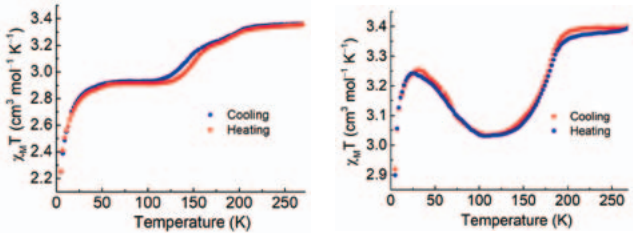

The magnetic susceptibility depends on the temperature for the microcrystals (left) and oriented sample (right)

Conclusion

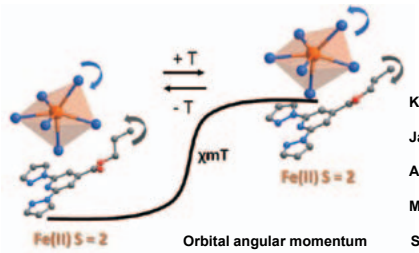

Key words

Jahn- Teller distortion

Alkyl rotation

Magnetic transition

Orbital angular momentum **Spin transition**

◆ Magnetic transition was induced by the variation of coordination geometry, which was attained by the rotation of the propyl group.

Photoabsorption and Photoluminescence Properties of Donor-Acceptor π-Conjugated Enamines and Their Additive Effects with $B(C_6B_5)_3$

Atsushi Tahara, Daichi Sakata, Ikumi Kitahara, Yoichiro Kuninobu, Hideo Nagashima

Institute for Materials Chemistry and Engineering ,Kyushu University, 6-1, Kasugakoen, Kasuga-shi, Fukuoka, 816-8580

Introduction

●Donor-Acceptor (D-A) compounds

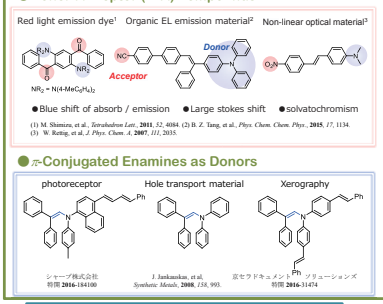

●Previous Work : Ir-catalyzed Syntheses of aldenamines

(1) Hydrosilane reduction of *N,N*-dialkylcarboxamides catalyzed by Vaska's complex

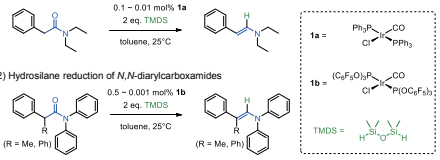

(2) Hydrosilane reduction of *N,N*-diarylcarboxamides

(1) Moteyama, Y.; Aoki, M.; Takaoka, N.; Aoto, R.; Nagashima, H. *Chem. Commun.* **2009**, 1574.
(2) Tahara, A.; Miyamoto, Y.; Aoto, R.; Shigeta, K.; Ure, Y.; Sunada, Y.; Moteyama, Y.; Nagashima, H. *Organometallics*, **2015**, *34*, 4895.

●This Work

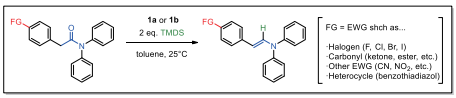

●Chemoselective Hydrosilane Reduction of Amides

(1) Charette's work (Hantzsch Ester)

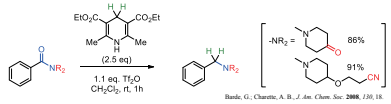

Barde, G.; Charette, A. B., *J. Am. Chem. Soc.* **2008**, *130*, 18.

(2) Adolfsson's work ($Mo(CO)_6$ & TMDS)

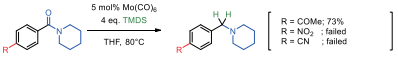

F. Tinnis, A. Volkov, T. Slagbrand, H. Adolfsson, *Angew. Chem. Int. Ed.* **2016**, *55*, 4562.

(2) Mashima's & Okuda's work (BPh_3 & $PhMeSiH_2$)

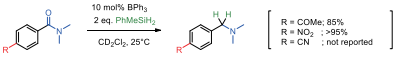

Mukherjee, D.; Shirase, S.; Mashima, K.; Okuda, J., *Angew. Chem. Int. Ed.* **2016**, *55*, 13326.

Results (1)

●Hydrosilane Reduction of Amides **2** catalyzed by **1X** or **1Y**

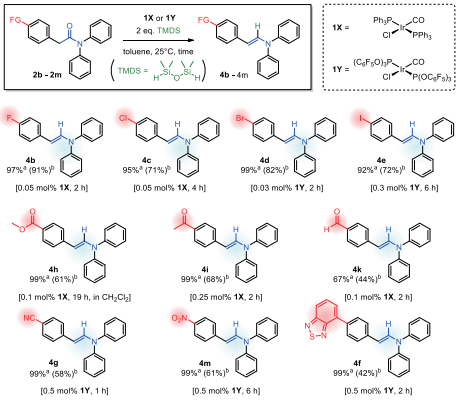

Chemoselective hydrosilane reduction of amides into enamines

●Photoabsorption and photoluminescence properties of 4m (FG = NO_2) Unique solvatofluorochromism was observed

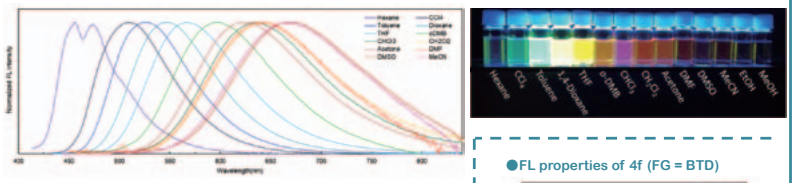

Entry	Solvent	$E_T(30)$	l_{abs} [nm (eV)]a	e_{max} [cm^{-1}·M^{-1}]	l_E [nm (eV)]b	Stokes shift [cm^{-1}]	Φ_Ec
1	Hexane	31.0	404 (3.069)	26,000	458 (2.707) 474 (2.616)	2918 3655	0.02
2	CCl_4	32.4	416 (2.981)	23,000	508 (2.441)	4353	0.27
3	Toluene	33.9	424 (2.925)	21,700	525 (2.361)	4537	0.54
4	1,4-Dioxane	36.0	425 (2.918)	26,300	546 (2.271)	5214	0.69
5	THF	37.4	431 (2.877)	30,200	568 (2.183)	5596	0.65
6	o-Dimethoxybenzene	38.4	441 (2.812)	11,400	595 (2.084)	5869	0.38
7	$CHCl_3$	39.1	438 (2.831)	24,200	637 (1.947)	7132	0.09
8	CH_2Cl_2	40.7	439 (2.825)	22,200	640 (1.937)	7154	0.05
9	Acetone	42.2	433 (2.864)	15,500	623 (1.990)	7043	0.08
10	DMF	43.2	446 (2.780)	22,400	655 (1.893)	7154	0.03
11	DMSO	45.1	452 (2.743)	21,000	669 (1.854)	7176	0.02
12	MeCN	45.6	434 (2.857)	34,800	671 (1.848)	8138	<0.01
13	EtOH	51.9	429 (2.890)	18,000	634 (1.956)	7537	<0.01
14	MeOH	55.4	430 (2.883)	14,300	643 (1.928)	7703	<0.01
15d	H_2O	62.8	–	–	–	–	–

aMaximum absorption wavelengths of **4m** in various solvent at 1.0×10^{-5} M were described [nm and eV in the parentheses]. bMaximum fluorescence wavelengths of **4m** in various solvent at 1.0×10^{-5} M were described [nm and eV in the parentheses]. cAbsolute fluorescence quantum yield was described. dThe data was not available due to lack of solubility of **4m** in H_2O.

●FL properties of 4f (FG = BTD)

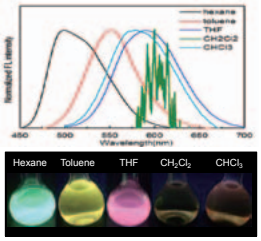

Results (2)

●Additive effect of Lewis acid

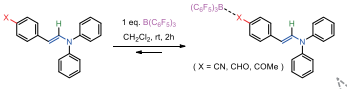

✓Blue shift of absorption wavelength

✓Blue shift of emission wavelength

✓Increase of quantum yield for FL.

(cf.) previous reports

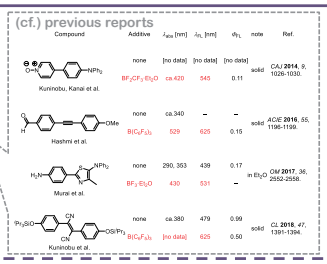

●Treatment of 4k (formyl) with $B(C_6F_5)_3$

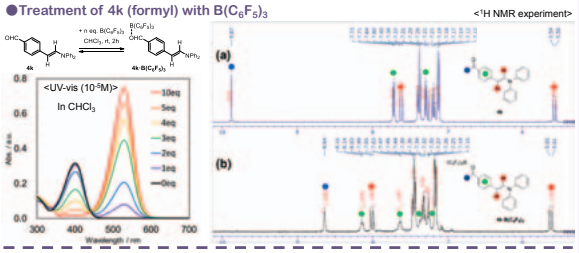

●FG = CN

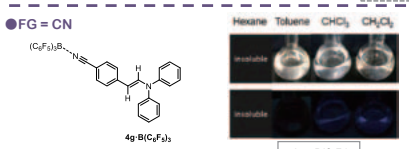

4g·$B(C_6F_5)_3$

<UV and FL for **4g** (1.0×10^{-5} M)>

Solvent	λ_{abs} [nm]a	λ_{FL} [nm]b	Φ_Ec
Hexane	–	–	–
Toluene	370	370	<0.01
$CHCl_3$	374	370	<0.01
CH_2Cl_2	374	370	<0.01

<UV and FL for **4g** + $B(C_6F_5)_3$ (1.0×10^{-5} M)>

Solvent	λ_{abs} [nm]a	λ_{FL} [nm]b	Φ_Ec
Hexane	422	478	0.01
Toluene	429	502	0.04
$CHCl_3$	427	512	0.08
CH_2Cl_2	426	522	0.11

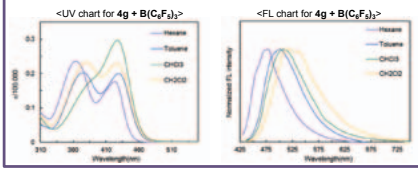

●FG = COMe

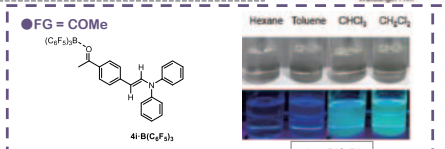

4i·$B(C_6F_5)_3$

<UV and FL for **4i** (1.0×10^{-5} M)>

Solvent	λ_{abs} [nm]a	λ_{FL} [nm]b	Φ_Ec
Hexane	370	415, 427	<0.01
Toluene	380	440, 465	<0.01
$CHCl_3$	380	479	0.03
CH_2Cl_2	389	485	0.04

<UV and FL for **4i** + $B(C_6F_5)_3$ (2.0×10^{-5} M)>

Solvent	λ_{abs} [nm]a	λ_{FL} [nm]b	Φ_Ec
Hexane	504	544	0.40
Toluene	514	587	*0.97*
$CHCl_3$	515	601	0.41
CH_2Cl_2	516	623	0.05

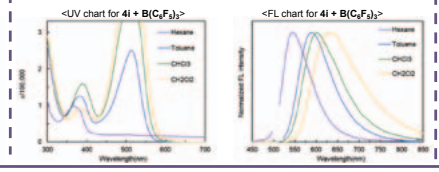

●FG = CHO

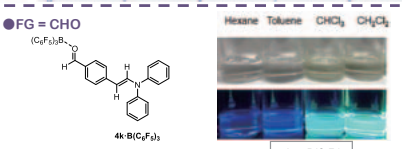

4k·$B(C_6F_5)_3$

<UV and FL for **4k** (1.0×10^{-5} M)>

Solvent	λ_{abs} [nm]a	λ_{FL} [nm]b	Φ_Ec
Hexane	379	428	<0.01
Toluene	392	450	<0.01
$CHCl_3$	390	496	0.04
CH_2Cl_2	399	506	0.05

<UV and FL for **4k** + $B(C_6F_5)_3$ (5.0×10^{-5} M)>

Solvent	λ_{abs} [nm]a	λ_{FL} [nm]b	Φ_Ec
Hexane	515	569	*0.70*
Toluene	529	618	0.22
$CHCl_3$	528	642	0.04
CH_2Cl_2	531	683	<0.01

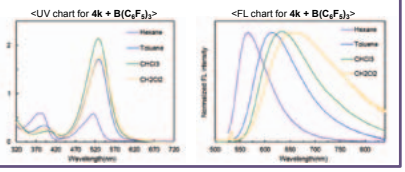

Structure-property Relationship of Rubber Materials Based on Complex Network Science

Y. Amamoto[1,2,3], K. Kojio[1], A. Takahara[1], Y. Masubuchi[2], T. Ohnishi[3]

[1]Institute for Materials Chemistry and Engineering, Kyushu University

[2]Graduate School of Engineering, Nagoya University

[3]Graduate School of Information Science and Technology, The University of Tokyo

1. Background: *Elastic property of Rubber Materials*

1.1 Rubber Material

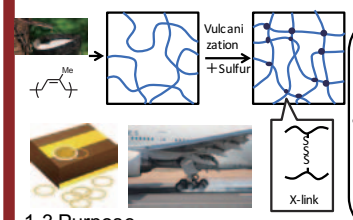

1.2 Rubber Elastic Model

Phantom network model

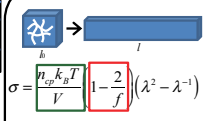

$$\sigma = \frac{n_{cp} k_B T}{V}\left(1-\frac{2}{f}\right)\left(\lambda^2-\lambda^{-1}\right)$$

λ: Elongation ratio (l/l_0)
σ: stress
l: length toward elongation
G: Shear modulus
f: Number of branching
n_{cp}: Number of monomer between x-link points
V: Volume of rubber

Stress increases with
1) number of branches
2) number of x-link density

1.3 Purpose

- To obtain significant parameter for heterogeneous elastomer based on complex network
- To explain effect of centrality for stress under uniaxial elongations

2. Method: *Distance btw x-link points and centrality*

2.1 Distance between x-link points ($D(\lambda)$)

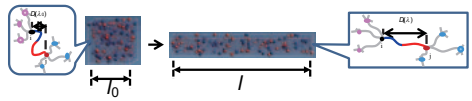

✔ $D(\lambda)$ determines stress under uniaxial elongation

2.2 Closeness centrality

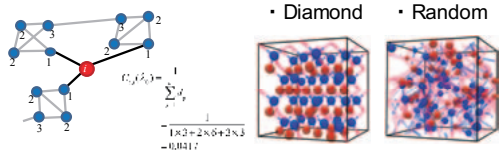

3. Randomly Cross-linked Rubber

3.1 Chain exchange and stress-strain curve

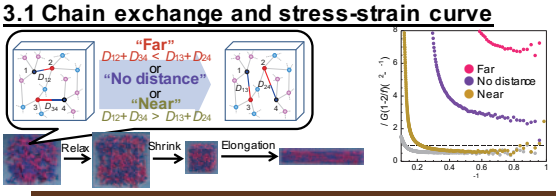

Exchange of chains were performed with distance condition, in which "Far" condition afforded high modulus

3.2 Correlation between initial distance ($D(\lambda_0)$) & $D(\lambda)$

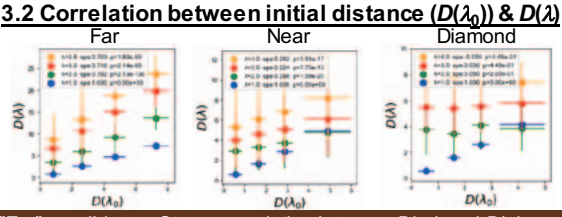

- "Far" condition ➡ Strong correlation between $D(\lambda_0)$ and $D(\lambda)$
- Homogeneous network ➡ $D(\lambda)$ did not depend on initial distance

3.3 Correlation between centrality $C_c(\lambda)$ and $D(\lambda)$

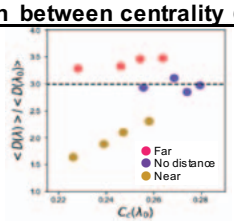

In "Near" condition, correlation between $C_c(\lambda)$ and $D(\lambda)$ was observed, indicating the connectivity is significant for mechanical property.

4. Star Cross-linked Rubber

4.1 Preparation of rubber and stress-strain curve

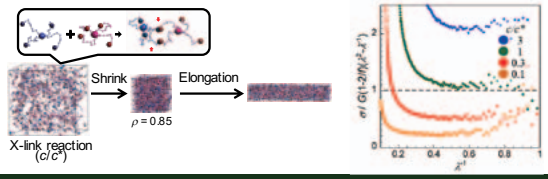

Stress under uniaxial elongation increased with increasing x-link conc.

4.2 Correlation between initial distance ($D(\lambda_0)$) & $D(\lambda)$

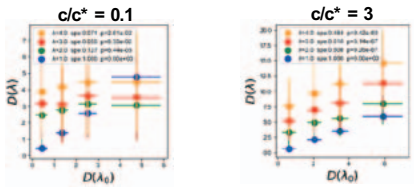

In the case of high conc., strong correlation between $D(\lambda_0)$ and $D(\lambda)$ was observed to afford high modulus

4.3 Correlation between centrality $C_c(\lambda)$ and $D(\lambda)$

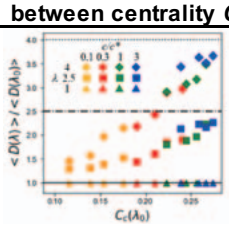

In the case of high conc., centrality increased to result in long distance between x-link points and high modulus

5. Conclusion: *Initial distance between x-link points and centrality are significant parameters for heterogeneous elastomers*

- Initial distance between x-link points indicated strong correlation for the distance under uniaxial elongations to afford high modulus and extended chains in early stage.
- In the case of low initial distance, the effect of centrality increased, in which x-link points with high centrality indicated much contribution for the stresses.

Acknowledgement
JSPS Grant-in-Aid for Scientific Research on Innovative Areas "Discrete Geometric Analysis for Materials Design": (17H06460, 17H06468)

Synthesis of cage-shaped molecules based on 1,8,13-*syn*-substituted triptycenes

Takayuki Iwata[1], Tatsuro Yoshinaga[2], Yusuke Maehata[2], Mitsuru Shindo[1]

[1]*Institute for Materials Chemistry and Engineering, Kyushu University* [2]*Interdisciplinary Graduate School of Engineering Sciences, Kyushu University*

Introduction

Triptycene

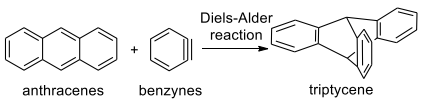

D_{3h} symmetry
Rigid three-dimentional molecule
Firstly synthesized by Bartlett
Usually synthesized by DA reaction

P. D. Bartlett, *et al.*, *J. Am. Chem. Soc.* **1942**, *64*, 2649.
G. Wittig, *et al.*, *Angew. Chem.* **1956**, 68, 40.

Structural feature of *syn*-substituted triptycenes

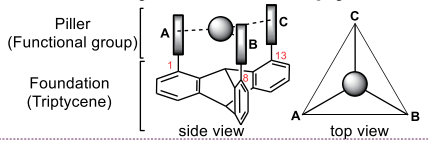

Ynolate-aryne triple cycloaddition reaction

Umezu, S.; Gomes, G. B.; Yoshinaga, T.; Sakae, M.; Matsumoto, K.; Iwata, T. Alabugin, I.; Shindo, M. *Angew. Chem. Int. Ed.*, **2017**, *56*, 1298.

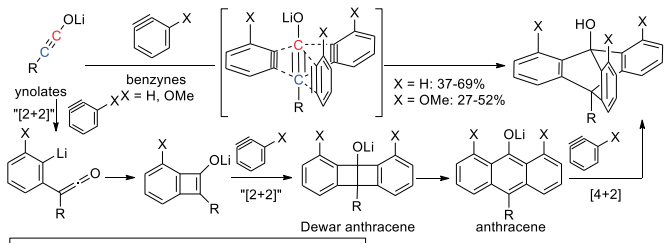

This work

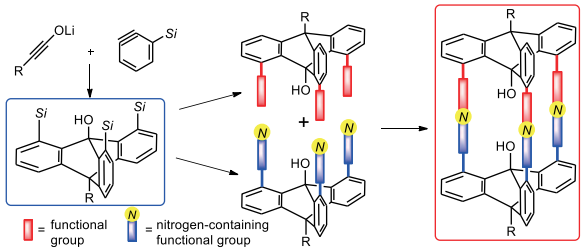

Results and Discussions

Yoshinaga, T.; Fujiwara, T.; Iwata, T.; Shindo, M. *Chem. Eur. J.* **2019**, *25*, 13855

(1) Synthesis of silyltriptycenes ⇒ distorted benzene/pentacoordinated silicon

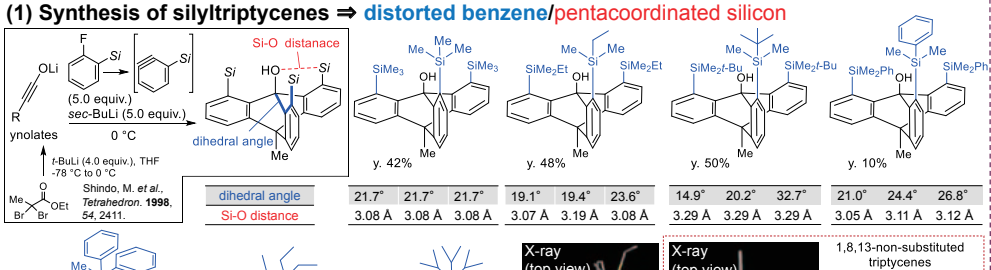

dihedral angle	21.7°	21.7°	21.7°	19.1°	19.4°	23.6°	14.9°	20.2°	32.7°	21.0°	24.4°	26.8°
Si-O distance	3.08 Å	3.08 Å	3.08 Å	3.07 Å	3.19 Å	3.08 Å	3.29 Å	3.29 Å	3.29 Å	3.05 Å	3.11 Å	3.12 Å

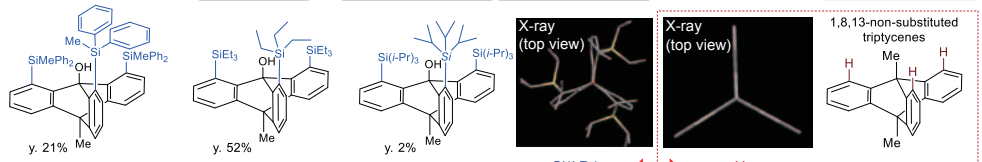

12.2°	15.9°	18.2°	18.4°	30.7°	31.9°	29.7°	34.7°	35.4°
3.19 Å	3.14 Å	3.13 Å	3.29 Å	3.19 Å	3.08 Å	3.21 Å	3.27 Å	3.21 Å

*Sum of Van der Waals radius 1.52 Å (O) + 2.10 Å (Si)= 3.62 Å

$Si(i\text{-}Pr)_3$ highly distorted ⇔ H less distorted

0.35 °	0.35°	0.35°

Nieger, M.; Konig, A.; Vogtle, F. *CSD Communication*. **2004**.

(2) Synthesis of anthrones

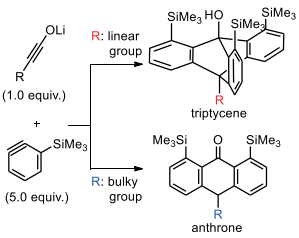

R	triptycene	anthrone
Et	39%	-[a]
n-Bu	20%	-[a]
hexyl	26%	-[a]
i-Pr	-[a]	39%
t-Bu	-[a]	20%
Ph	-[a]	9%

[a] not obtained.

(3) Synthesis of cage-shaped molecules

T.; Iwata, Yoshinaga, T.; Shindo, M. *Manuscript in preparation*

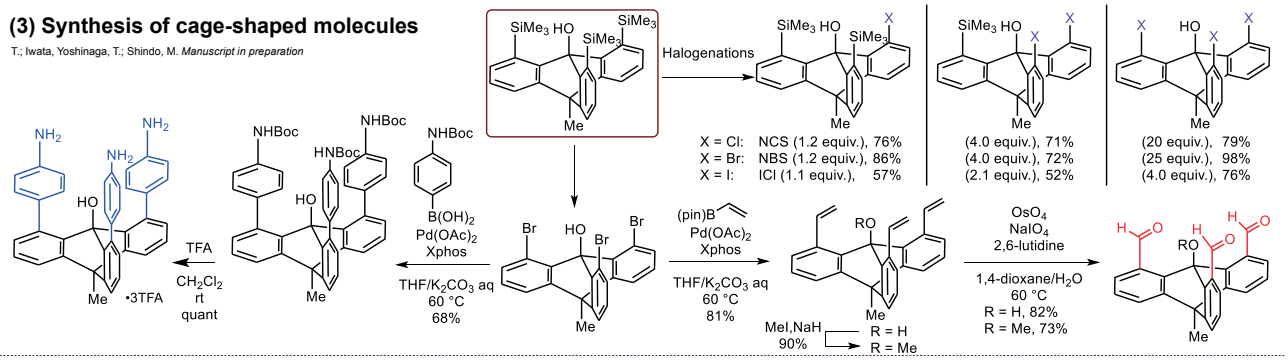

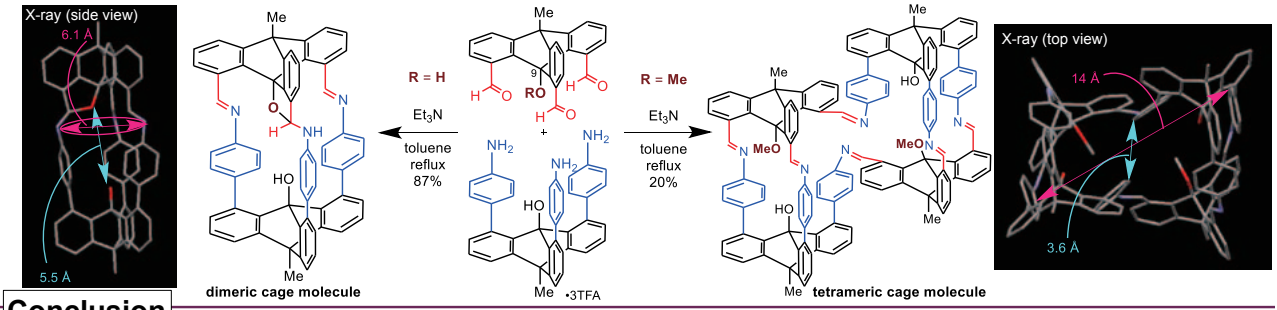

Conclusion

- 1,8,13-*syn*-substituted tris(trialkylsilyl) triptycenes synthesized via triple cycloaddition of ynolates to benzynes.
- Cage-shaped molecules were synthesized based on transformation of the silyl triptycene.

Artificial Neural Networks Applied as Molecular Wave Function Solvers

Nagoya University
Institute of Transformative Bio-Molecules (ITbM)
Takeshi Yanai

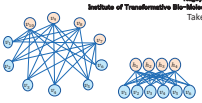

Y. Peng-Jian, M. Sugiyama, K. Tsuda, T. Yanai, *submitted*.

Acknowledgements

My group (Nagoya WPI-ITbM)

- Mr. Lester Yang (B4 in my group)
  Just graduated
  → *datoscience@berkeley*

G30 student from Taiwan

Data scientists

- Prof. Mahito Sugiyama (National Institute of Informatics)
- Prof. Koji Tsuda (Univ of Tokyo)

杉山恵人先生
(国立情報学研)
さきがけ+
社会デザイン

Basic ansatz of neural network quantum states

- Quantum entangled form of many-electron wavefunction

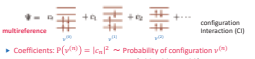

- Coefficients: $P(v^{(n)}) = |c_n|^2$ ~ Probability of configuration $v^{(n)}$
- Occupancies of configuration $v^{(n)} = \{v_1^{(n)}, v_2^{(n)}, \ldots, v_N^{(n)}\}$
- Use of probabilistic model of machine learning

Carleo and Troyer (Science 2017)
RBM based theory
→ Neural-Network Quantum State (NQS)

$P(v^{(n)})$ → $P(v|\theta)$
distribution parameterized

Neural network ansatz with ML technology

- Boltzmann machines
  - ML model of a distribution over the set of their inputs.
    - Generative model
  - Representability theorem
    - Existence of network that can approximate sufficiently smooth and regular high dimension functions
  - **Question and interests**
    - **Feasibility of BM models** used as an encoder of **multireference** (CAS-CI) **wave function** for ab initio QC
    - Efficacy of information compression of CI coefficients C_v parameterized with occupancies v that act as descriptors.

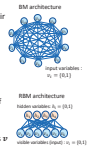

Hidden-node free BM versus RBM

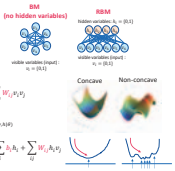

Strategies to address the observed issues

RBM	BM
Non-convex	Convex
Generally hard to optimize	Should be less hard
Flexibility increased due to presence of hidden variables	Fixed flexibility
Extension to deep learning architecture	Extension to higher order BM

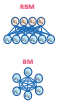

BM's energy func

$$\Phi(v|\theta) = \sum_i a_i v_i + \sum_{ij} W_{ij} v_i v_j \quad \text{2-body}$$

Higher order BM's energy func

$$\Phi(v|\theta) = \sum_i a_i v_i + \sum_{ij} W_{ij} v_i v_j + \sum_{ijk} X_{ijk} v_i v_j v_k \quad \text{3-body}$$

RBM/BM wavefunction

- Complex RBM/BM wf with real-valued parameterization
  - Real-parameterized RBM/BM that can consider phases

$$C_v = e^{\frac{i}{2}\log\psi(v|\tau)} \sqrt{\frac{1}{Z(\theta)}\psi(v|\theta)}$$

phase amplitude

- $\psi(v|\theta), \psi(v|\tau)$: RBM/BM distributions
- θ, τ : RBM/BM params, which are **real-valued**.

Formulation of RBM/BM state for QC calcs

- QC wavefunction expansion

$$|\Psi\rangle = \sum_v c_v |v\rangle$$
$$v = \left(v_1^\uparrow, v_2^\uparrow, \ldots, v_N^\uparrow, v_1^\downarrow, v_2^\downarrow, \ldots, v_N^\downarrow\right)$$

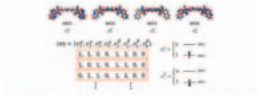

Figure 1: Configurations of molecules given in CAS(4e,4o) for the singlet state, and the corresponding underlying orbitals. This should give a total of $\binom{8}{4}^2 = 36$ configurations.

RBM/BM wavefunction

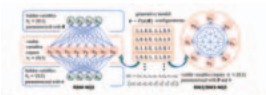

Figure 2: An example of the implemented sandwich RBM and BM2 BM3 architectures. A CAS(4e,4o) calculation with 4 molecular orbitals will give 8 input nodes to contain both α and β spins, while arbitrary number of hidden nodes can be specified. In this case, 4 hidden nodes for both θ and τ. Configurations are fed into visible nodes as inputs.

RBM/BM wavefunction

- RBM/BM training for **quantum state**
  - Minimize state energy $E(\theta,\tau)$

our big data

$$E(\theta,\tau) = \langle\Psi(\theta,\tau)|\, H\, |\Psi(\theta,\tau)\rangle = \sum_v P(v|\theta)\, E^{\text{loc}}(v|\theta,\tau)$$

$$\frac{\partial}{\partial\theta} E(\theta,\tau) = 0, \quad \frac{\partial}{\partial\tau} E(\theta,\tau) = 0$$

What is done in machine-learning RBM/BM ....

Given dataset $\{v^{(1)}, v^{(2)}, \ldots, v^{(N)}\}$ ~ big data

- Maximize $\log L(\theta)$ w.r.t. θ (or minimize its negative)
  - $\log L(\theta) = \sum_{i=1,\ldots,N} \log P(v^{(i)}|\theta)$: log likelihood function

Quantum chemistry Hamiltonian

- Hamiltonian with generators

$$\hat{H} = \sum_{ij}^{n} (i|h|j) E_{ij} + \frac{1}{2}\sum_{ijkl}^{n} (ij|kl)(E_{ij}E_{kl} - \delta_{jk}E_{il})$$

Non-zero coupling $\langle v|\, H\, |v'\rangle$ arises from only **single- and double-excited** configurations $|v'\rangle$ relative to $|v\rangle$.

local energy

$$E^{\text{loc}}(v|\theta,\tau) = \frac{\langle v|\, H\, |\Psi(\theta,\tau)\rangle}{C_v} = \frac{\sum_{v' \in S \cup D} \langle v|\, H\, |v'\rangle C_{v'}}{C_v}$$

O(polynomial)

single and double excitations

Metropolis-Hasting (MH) algorithm

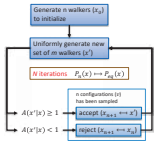

Sequence of distribution approach a limiting equilibrium:

$$P_n(x) \mapsto P_{\text{eq}}(x)$$

when satisfying the detailed balanced condition:

Accepting proposed states (x') with probability $A(x'|x)$

$T(x|x')$, uniform probability used → $T(x|x') = T(x'|x)$

$$A(x'|x) = Min\left(1, \frac{P_{\text{eq}}(x')T(x|x')}{P_{\text{eq}}(x)T(x'|x)}\right) = Min\left(1, \frac{P_{\text{eq}}(x')}{P_{\text{eq}}(x)}\right),$$

This does not require the partition function $Z(\theta)$.

MH implementation for training RBM state

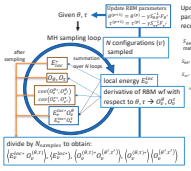

Updating RBM/BM2/BM3 parameter θ, τ with stochastic reconfiguration

$S_{\theta\theta'}$ and $S_{\tau\tau'}$ are Hermitian covariance matrices

$$S_{\theta\theta'} = Re\left[\sum_v |v\rangle^* \langle v|\, (O_\theta^* - \langle O^*\rangle)(O_\theta^{\prime*} - \langle O'^*\rangle)|P(v)\rangle\right]$$
$$S_{\tau\tau'} = Re\left[\sum_v |v\rangle^* \langle v|\, (O_\tau - \langle O_\tau\rangle)(O_\tau' - \langle O_\tau'\rangle)|P(v)\rangle\right]$$
$$\Rightarrow Re\left[\langle O_\theta^{(n+1)} O_\theta^{(n'+1)}\rangle - \langle O_\theta^{(n+1)}\rangle\langle O_\theta^{(n'+1)}\rangle\right]$$

F_θ and F_τ are the forces

$$F_\theta = -2Re\left[\sum_v E_\theta^{\text{loc}} |v\rangle^* \langle v|\, (O_\theta^* - \langle O^*\rangle)|P(v)\rangle\right]$$
$$F_\tau = -2Re\left[\sum_v E_\tau^{\text{loc}} |v\rangle^* \langle v|\, (O_\tau - \langle O\rangle)|P(v)\rangle\right]$$
$$\Rightarrow Re\left[\langle E_\theta^{\text{loc}} O_\theta^{(n+1)}\rangle - \langle E_\theta^{\text{loc}}\rangle\langle O_\theta^{(n+1)}\rangle\right]$$

Indocyanine Green: CAS(4e,4o)

CAS(4e,4o)

- Canonical orbitals (CMO)
- Localized orbitals (LMO)

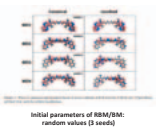

Initial parameters of RBM/BM: random values (3 seeds)

Distribution of weights of configurations (CAS-CI)

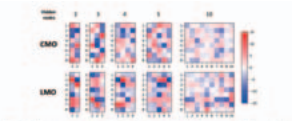

Figure 4: Interaction matrices w_{ij} of θ, the parameters of RBM's parameters of the amplitude $\psi(v;\theta)$ (top, (2)), determined using 2, 3, 4, 5, and 10 hidden nodes for ICG with CAS(4e,4o) in CMO and LMO basis.

Potential energy curve of N_2: CAS(6e,6o)

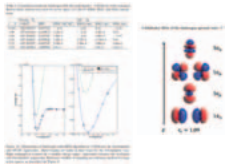

Development of A Reduced-Scaling Multireference Perturbation Theory

Masaaki Saitow and Takeshi Yanai

masa.saitow@chem.nagoya-u.ac.jp

NAGOYA UNIVERSITY

DEPARTMENT OF CHEMISTRY NAGOYA UNIVERSITY

Introduction

Accurate *ab initio* computation of the electronic wave function in a linear-scaling scheme opens an unprecedented possibility for modelling chemical reactions for large, real-life molecules:

- Low costs methods such as semi-empirical theory or DFT often give qualitatively wrong results. [1]
- Use of pair-natural orbitals (PNOs) as a compact set of virtual MOs can be used to drastically reduce the computational costs for solving accurate many-electron wave functions.
- Reduced-scaling multireference perturbation theory in the local PNO framework (PNO-CASPT2) for large, strongly-correlated systems.
- A simple, yet higher-order extension to PNO-CASPT2 method as a hybrid of highly accurate Multireference Coupled-Electron Pair Approximation (MR-CEPA) and CASPT2 models formulated in the PNO basis (PNO-CEPT2). [2]

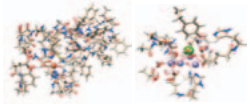

Figure 1: Quinone-Iron cluster (593 atoms) and oxygen evolving complex (243 atoms) active site models which are the large, real-life open-shell systems and are possible to treat with the accurate PNO-based Coupled-Cluster method. [3,4]

Theory

Compaction of Wave Function by Pair-Natural Orbitals:

In PNO-CASPT2/CEPT2 theory, the pair-natural orbitals (PNOs) are first constructed for each of the 2-exteral subspaces by diagonalizing the pair-density:

$$(D^{ij})_{ab} = \langle \Psi_{ij} | E_b^a | \Psi_{ij} \rangle \quad (\text{for } \{\Psi_{ij}^{ab}\} \text{ subspace})$$

$$(D^{\mu\nu})_{ab} = \langle \Psi_{\rho\mu} | E_b^a | \Psi_{\rho\nu} \rangle \quad (\text{for } \{\Psi_{\rho\mu}^{ab}\} \text{ subspaces})$$

$$(D^{\rho})_{ab} = \langle \Psi_{\rho} | E_b^a | \Psi_{\rho} \rangle \quad (\text{for } \{\Psi_{\rho}^{ab}\} \text{ subspaces})$$

The PNOs are obtained for each electron pair as eigenfunctions of the pair-density. Those PNOs with occupation number smaller than a user defined threshold are discarded. The total number of PNOs is asymptotically linear scaling with respect to the size of the molecule.

The Reduced-scaling CASPT2/CEPT2 Formalism:

In CASPT2 formalism, the wave function is defined as

$$|\Psi_{\mathrm{CASPT2}}\rangle = \sum_{ijab} t_{ab}^{ij} |\Psi_{ij}^{ab}\rangle + \sum_{\rho ab} t_{ab}^{\rho} |\Psi_{\rho}^{ab}\rangle + \sum_{i\rho ab} t_{ab}^{i\rho} |\Psi_{i\rho}^{ab}\rangle$$

$$+ 5 \text{ more excitations}$$

where the configurations with ρ indices are the spin-adapted, non-redundant internally-contracted basis (nr-ICB) which are generated by removing the linear-dependency of the redundant ICB:

$$|\Psi_{\rho}^{ab}\rangle = \frac{1}{2} \sum_{pq}^{\text{active}} C_{pq}^{\rho} |\Psi_{pq}^{ab}\rangle = \frac{1}{2} \sum_{pq}^{\text{active}} C_{pq}^{\rho} E_{pq}^{ab} |\Psi_0\rangle$$

The orthonormalization matrix is obtained by solving the following equations:

$$\sum_{rs}^{\text{active}} \left(\langle \Psi_{ab}^{pq} | H_0 | \Psi_{rs}^{ab} \rangle - E_{\rho} \langle \Psi_{ab}^{pq} | \Psi_{rs}^{ab} \rangle \right) C_{rs}^{\rho} = 0$$

The first-order wave function is determined by solving the residual equations in nr-ICB basis:

$$R_{ab}^{\rho} = \langle \Psi_{ab}^{\rho} | H | \Psi_0 \rangle + \sum_{cd}^{\text{virt.}} \sum_{\tau}^{\text{nr-ICBs}} \langle \Psi_{ab}^{\rho} | H_0 | \Psi_{\tau}^{cd} \rangle t_{cd}^{\tau} + \cdots \to 0$$

The multireference PNOs are defined for each of nr-ICBs and the residua are transformed into the following form:

$$R_{a_\rho b_\rho}^{\rho} = \langle \Psi_{a_\rho b_\rho}^{\rho} | H | \Psi_0 \rangle + \sum_{\tau}^{\text{nr-ICBs}} \sum_{c_\tau d_\tau} \langle \Psi_{a_\rho b_\rho}^{\rho} | H_0 | \Psi_{\tau}^{c_\tau d_\tau} \rangle t_{c_\tau d_\tau}^{\tau} + \cdots \to 0$$

The PNO-CASPT2 residua are obtained by taking a derivative of the following energy functional with respect to the amplitude:

$$\mathscr{F}_{\mathrm{CASPT2}} = 2\mathrm{Re}[\langle \Psi_{\mathrm{CASPT2}} | H | \Psi_0 \rangle] + \langle \Psi_{\mathrm{CASPT2}} | F - \langle F \rangle | \Psi_{\mathrm{CASPT2}} \rangle$$

In the PNO-MR-CEPA model, the residua are obtained by minimizing the following functional:

$$\mathscr{F}_{\text{MR-CEPA}} = \langle \Psi_{\text{MR-CEPA}} | H - E_0 | \Psi_{\text{MR-CEPA}} \rangle$$

In the hybrid PNO-CEPT2 model, the MR-CEPA functional is used for the 2-external subspaces which are more important for capturing the dynamic correlation while the CASPT2 functional is used for the rests.

Results

Non-Parallelity Errors by CEPT2 model for N_2 dissociation:

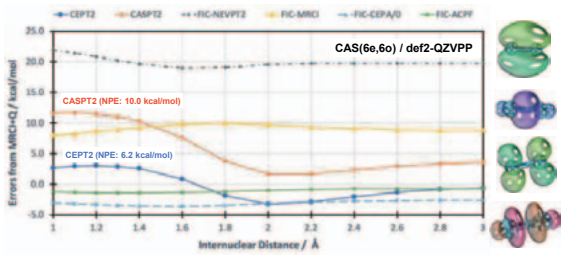

Figure 2: Non-parallelity errors by canonical CASPT2 and CEPT2 models for N_2 dissociations with CAS(6e,6o) treatment using all the *2p* orbitals of nitrogen atoms. The def2-QZVPP and def2-QZVPP/JK auxiliary basis sets were used.

Singlet-Triplet Gaps for Free-base Porphyrin:

Table 1: The singlet-triplet gap for free-base porphyrin calculated by PNO-CASPT2 and PNO-CEPT2 models with various PNO truncation thresholds using CAS(8e,8o) all of which are composed of $2p_z$ orbitals of carbon atoms. The def2-SVP and def2-SVP/JK auxiliary basis sets were used. The threshold for pair-energy-based screening was set to 1.0 x 10-5 Eh.

TCutPNO	Ecorr (S0) / Eh	%Accuracy	Ecorr (T0) / Eh	%Accuracy	S-T Gap / eV
PNO-CASPT2					
Full	-3.2332337	100.00	-3.2192668	100.00	1.67
1.00E-09	-3.2294806	99.88	-3.2149734	99.87	1.69
1.00E-08	-3.2283818	99.85	-3.2139397	99.83	1.69
5.00E-08	-3.2270253	99.81	-3.2125440	99.79	1.69
PNO-CEPT2					
1.00E-09	-3.4208555		-3.4112125	-	1.55
1.00E-08	-3.4195743		-3.4100063	-	1.55
5.00E-08	-3.4180262		-3.4084610	-	1.55
Exp.					1.58

Benchmark Case: Diketopyrrolopyrrole Supramolecules

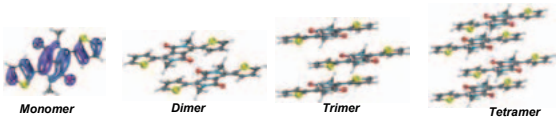

Table 2: Computational timings for DPP supramolecules using def2-ASVP and def2-SVP/JK auxiliary basis functions.

	Monomer	Dimer	Trimer	Tetramer
RI Integral Generations (sec.)	44	425	1,438	4,699
PNO Generations (sec.)	157	3793	26,698	Running
PNO-CASPT2 Iterations (sec.)	314	4612	31,556	Running
Total Timings (sec.)	557	9,308	64,119	Running
Size of Active Space	4e in 4o	8e in 8o	12e in 12o	16e in 14o
# of AO Functions	538	1,076	1,614	2,152
# of Auxiliary Basis Functions	1,662	3,324	4,986	6,648

Summary

An efficient and accurate PNO-CASPT2 program has been developed for calculating the electronic wave functions of large, real-life systems. The PNO-CASPT2 has been extended to higher-order by using MR-CEPA Ansatz.

References

[1] F. Neese *et al.*, J. Am. Chem. Soc., **DOI:** 10.1021/jacs.8b13313.

[2] M. Saitow and T. Yanai, *under review*.

[3] M. Saitow *et al.*, J. Chem. Phys. **146**, 164105 (2017).

[4] M. Saitow and F. Neese, J. Chem. Phys. **149**, 034104 (2018).

[5] M. Saitow, Y. Kurashige, T. Yanai, J. Chem. Phys. **139**, 044118 (2013).

Magnetic properties of electrochemically delithiated spinal-$LiMn_2O_4$

Qi CHEN, Zhongyue ZHANG and Kunio AWAGA

名古屋大学 NAGOYA UNIVERSITY

Department of Chemistry, Graduate School of Science, Nagoya University

Introduction

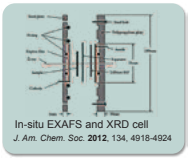

In-situ EXAFS and XRD cell
J. Am. Chem. Soc. **2012**, 134, 4918-4924

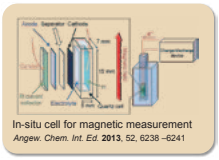

In-situ cell for magnetic measurement
Angew. Chem. Int. Ed. **2013**, 52, 6238 –6241

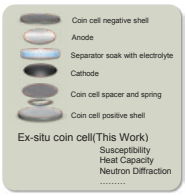

Ex-situ coin cell(This Work)
Susceptibility
Heat Capacity
Neutron Diffraction
.....

Using In-situ or Ex-situ Magnetic measurement to reveal the mechanism of electrochemical process

- **Structure and magnetic phase transition**
- **electronic structures and element distributions**
- **oxide state and Local coordination environments**

Geometrical Frustration

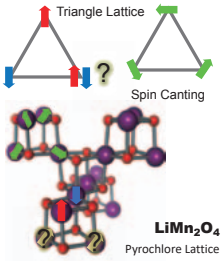

Jahn-Teller Distortion

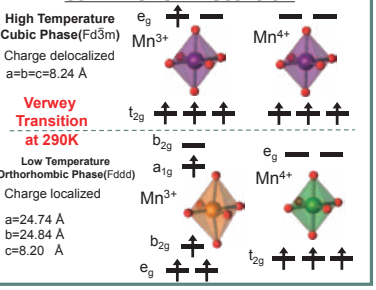

Method and structure

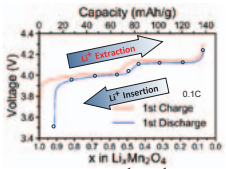

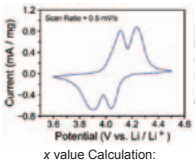

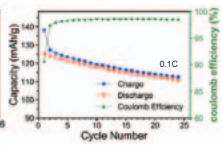

$$LiMn_2O_4 \leftrightarrow Li_{0.5}Mn_2O_4 + \frac{1}{2}Li^+ + \frac{1}{2}e^- \quad 4.0\ V\ vs.\ Li/Li^+$$

$$Li_{0.5}Mn_2O_4 \leftrightarrow 2\lambda - MnO_2 + \frac{1}{2}Li^+ + \frac{1}{2}e^- \quad 4.1\ V\ vs.\ Li/Li^+$$

x value Calculation:

$$x = 1 - \frac{\text{Charge Capacity}}{\text{Theoretical Capacity}} \qquad x = 1 - \frac{\text{Charge Capacity}}{\text{Theoretical Capacity}} + \frac{\text{Disharge Capacity}}{\text{Theoretical Capacity}}$$

Theoretical Capacity of $LiMn_2O_4$–MnO_2 redox coupler is 148.226 mAh/g

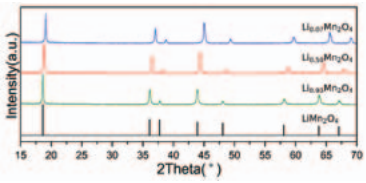

$LiMn_2O_4$ was synthesized by solid state method, sintered at 700℃.

Electrochemical reversible tuning range: 0.93~0.07

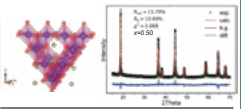

x	Temp.	a/Å	Mn-Mn/Å
0.07	300K	8.04(4)	2.84(4)
0.50	300K	8.16(1)	2.88(5)
0.93	300K	8.24(5)	2.91(5)

The space group symmetry was maintained throughout the electrochemical process

Result

Antiferromagnetism

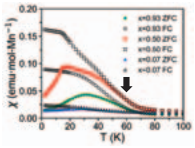

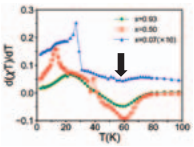

Using Large Magnetic field to quench the spin canted state.

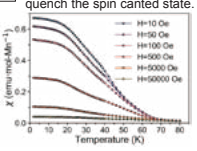

DC magnetic susceptibility at 500Oe and derivatives of χT

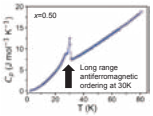

Heat capacity of $Li_{0.07}Mn_2O_4$

Fitting with Curie-Weiss Law:

$$C_{mol} = \frac{N\mu_B^2}{3k_B}\left[4.90^2\frac{x}{2} + 3.87^2\frac{2-x}{2}\right] \times 0.04749[mol/cm^3]$$

$$\chi = \frac{C}{T-\theta} \qquad C = \frac{N\mu_{eff}^2}{3k_B}$$

X	T_c [K]	T_f [K]	T_N [K]	θ [K]	C_{mol} [emu K / mol]	C_{mol}^{cal} [emu K / mol]
0.07	-	-	60	-93.4	1.80	1.912
0.50	16	40	61	-111	1.81	2.155
0.93	-	38	61	-255	2.24	2.398

Spin Glass

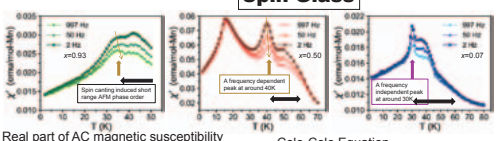

Real part of AC magnetic susceptibility

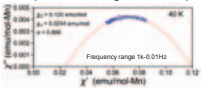

Cole-Cole Plot of $Li_{0.5}Mn_2O_4$

Cole-Cole Equation

$$\tilde{\chi}(\omega) = \chi' - i\chi'' = \chi_s + \frac{\chi_0 - \chi_s}{1 + (i\omega\tau_c)^{1-\alpha}}$$

The median relaxation time $\tau_c \approx 0.90s$

α value close to 1 means a variety of size of domain are coexist with broad relaxation time

Ferrimagnetism

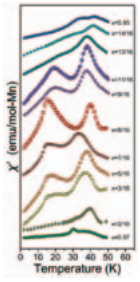

Li content dependence of the real part of χ_{AC} (f=2 Hz).

A frequency independent intermediate state appearing and disappearing at 16K when x tuned from 0.07 to 0.93

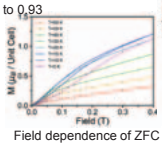

Field dependence of ZFC χ_{DC} for x=0.50

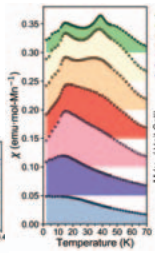

Not completely saturated by large magnetic field is usually attributed spin anisotropy.

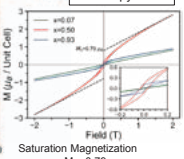

Saturation Magnetization
M_S=0.79 μ_B
weak coercive force
weak magnetic interaction

Discussion

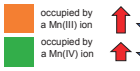

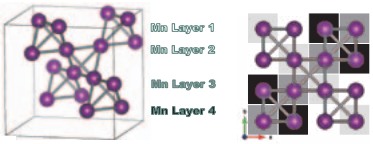

Spin configurations of $Li_xMn_2O_4$

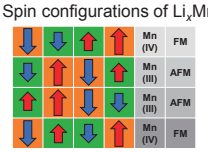

x=1.00 $\mu_{net} = 0$

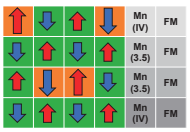

x=0.50 $\mu_{net} = 0$

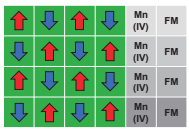

x=0.00 $\mu_{net} = 0$

Charge Ordering

Strong Anisotropy!

Lang range AFM ordering

The magnetic structures will be further verify by Neutron Diffraction.

6 possible spin configurations for x=0.50

	x=1.00	1	2	3	4	5	6	x=0.00
Layer 2								
Layer 3								
μ_{net} (μ_B)	0.00	15.48	9.80	7.74	4.12	0.00	2.06	0.00

Unbalanced spin moment of Mn(IV) and Mn(III) would generate a large and strong ferrimagnetic ordering with a saturated magnetization.

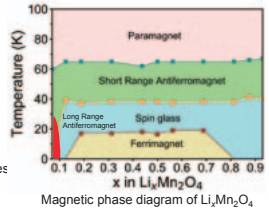

Magnetic phase diagram of $Li_xMn_2O_4$

Conclusion

- We performed the reversible and continuous electrochemical tuning the oxide state of Mn ion in $Li_xMn_2O_4$ ($0.07 \le x \le 0.93$) by electrochemical process.
- A magnetic intermediate state, ferrimagnetic ordering, was observed at x=0.50 below 16k, which was examined by Ex-situ AC/DC susceptibility, field dependent magnetization, hysteresis loops measurement.
- Since the breaking of the symmetry, a considerable strong magnetic anisotropy was exist in $Mn^{III}Mn^{IV}_3$ tetrahedron, as a consequence, the ferrimagnetic ground state emerged.

Convert Covalent Organic Frameworks to the Electrode Materials of Supercapacitors

○ Dongwan Yan, Yang Wu and Kunio Awaga

Department of Chemistry, Nagoya University, Nagoya, Japan

Introduction

Covalent Organic Frameworks (COFs)

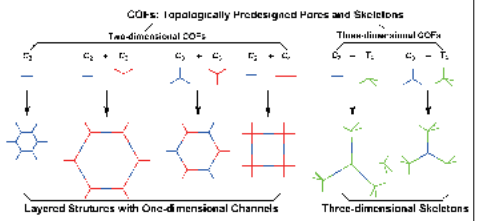

Chem. Soc. Rev., 2012, 41, 6010–6022

- Large Surface Area: Thousands m^2g^{-1}
- Designed Pore Size: Micropore (< 2 nm) / Mesopore (> 2 nm)
- Lightweight Elements: C, H, B, O, N, P, S
- Strong Covalent Bonds

A class of porous crystalline polymers periodic structures

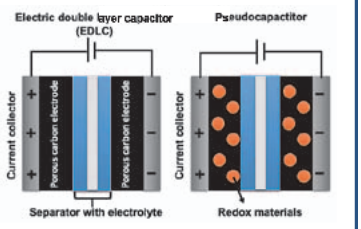

Electrode Materials : Stability, Porosity and Conductivity.

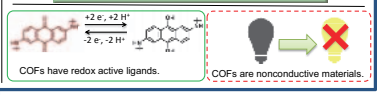

Purpose

AQ-COF
- Introduce conductive activator
- Pyrolysis to carbon materials

·PEDOT introduce into AQ-COF

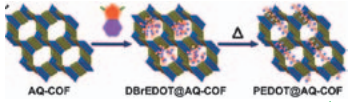

Solid-state polymerization (SSP)

·Pyrolysis with Salt-assisted methods

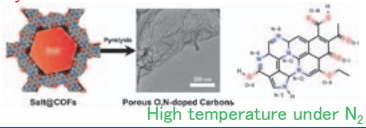

High temperature under N_2

Methods and Characteristic of AQ-COF

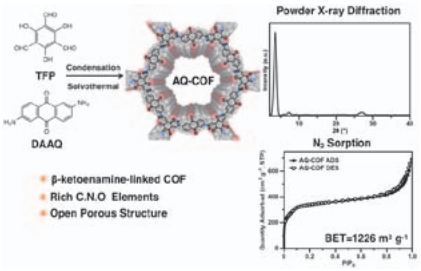

- β-ketoenamine-linked COF
- Rich C,N,O Elements
- Open Porous Structure

This COF has redox active sites in the frameworks and owns strong stability.

Methods and Characteristics of PEDOT@AQ-COF

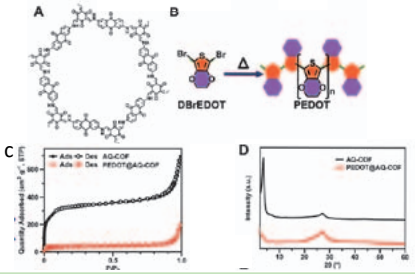

(A). Chemical structure. (B). SSP process. (C). N_2 sorption isotherms. (D). PXRD patterns.

Electrochemistry Performance of PEDOT@AQ-COF

Two-probe *I-V* measurement

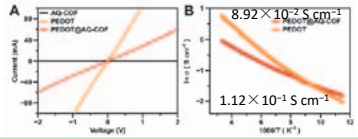

(A). Room-temperature *I-V* plots and (B). temperature-dependent conductivity profiles

The conductivity of AQ-COF, PEDOT and AQ@PEDOT is 1×10^{-10} 1.9 and 1.1 S cm^{-1}.

Three-electrode system in 1M H_2SO_4

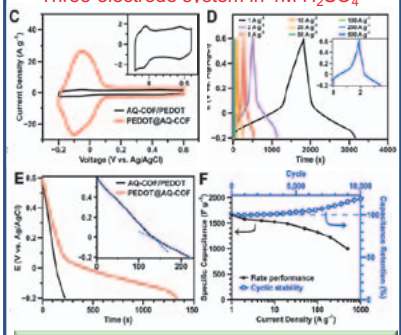

(C). CV curves at 5 mV s^{-1}. (D). GCD profiles of PEDOT@AQ-COF at different current densities. (E). Discharge Profiles. (F). Specific capacitance and cyclic stability at 50 A g^{-1}.

Characteristics : Salt-assisted pyrolysis of AQ-COF

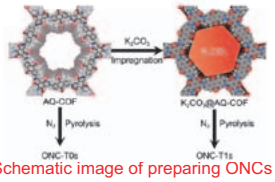

Schematic image of preparing ONCs .

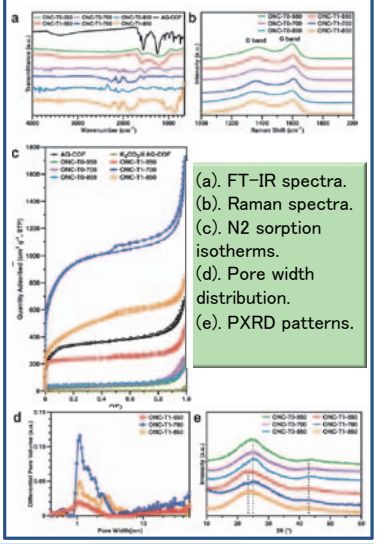

(a). FT-IR spectra.
(b). Raman spectra.
(c). N2 sorption isotherms.
(d). Pore width distribution.
(e). PXRD patterns.

Electrochemistry Performance of Porous O, N-doped Carbons

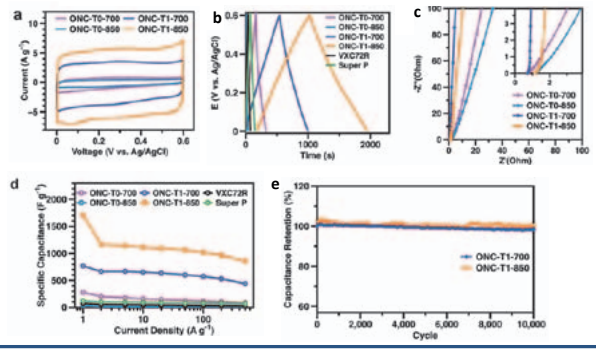

Three-electrode system in 1M H_2SO_4

(a). CV curves at a scan rate of 5 mV s^{-1}.
(b). GCD curves at current density of 1 A g^{-1}.
(c). The Nyquist plots.
(d). Specific capacitance.
(e). Cycling stabilities over 10000 cycles at 10A g^{-1}.

Conclusion

- PEDOT@AQ-COF nanocomposite with an excellent electrical conductivity of 1.1 S cm^{-1} and a remarkably improved performance in faradaic energy storage (1663 F g^{-1} at 1 A g^{-1}).
- ONC-T1s show a hierarchical porous structure with an ultra-high specific surface area (up to 3451 m^2 g^{-1}). The ONC-T1-850-based supercapacitor exhibits a high specific capacitance of 1711 F g^{-1} at 1 A g^{-1}.

化学修飾mRNAの合成と翻訳活性

Synthesis and Translational efficiency of chemically modified mRNA

○川口 大輔[1], 児玉 亜有実[1],清水 義宏[2],阿部 奈保子[1], 橋谷 文貴[1], 友池 史明[1,3], 木村 康明[1], 阿部 洋[1]
○Daisuke Kawaguchi[1], Ayumi Kodama[1], Yoshihiro Shimizu[2], Naoko Abe[1], Fumitaka Hashiya[1], Fumiaki Tomoike[1,3], Yasuaki Kimura[1], Hiroshi Abe[1,4]
[1] 名古屋大学大学院理学研究科, [2] 理化学研究所生命機能化学研究センター, [3] 学習院大学理学部, [4] JST CREST
[1] Graduate School of Science, Nagoya University, [2] Biodynamics Research Center, RIKEN , [3] School of Science, Gakushuin University , [4] JST CREST

1. Introduction

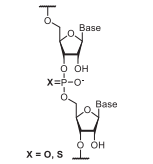

Structure of phosphate bond and phosphorothioate bond

Phosphorothioate modification (PS)
Increase biological stability
Used in antisense nucleic acids, siRNAs

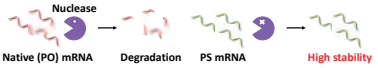

PS modification of mRNA was reported for few cases from nearly 30 years ago. *Nucleic. Acids. Res.*, **1991**, *19*, 547-552.

2. Abstract

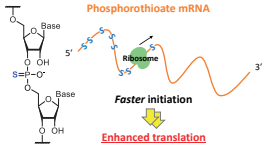

- Phosphorothioate mRNA (PS-mRNA) was synthesized by *in vitro* transcription and the translation reaction was evaluated using an *E. coli* cell-free protein translation system.
- The amount of produced protein from PS-mRNA was increased and the rate of translation initiation was positively affected by the PS-modifications.

3. Sequence design and synthesis of PS-mRNA

Transcription

DNA template for FLAG-EGF mRNA (310-bp)

T7 RNA polymerase → FLAG-EGF mRNA (284-nt)

NTP or NTPαS

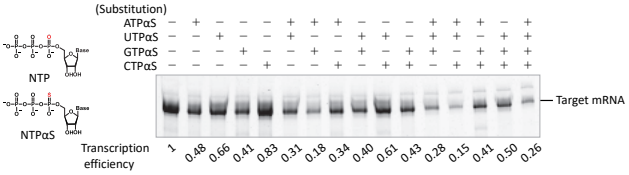

All transcripts were analyzed by denaturing polyacrylamide gel electrophoresis (PAGE). The gels were stained with SYBR Green II and the relative amount of RNA transcripts was calculated.

4. Protein synthesis in *E.coli* cell-free translation system

Translation

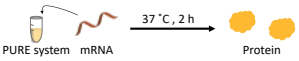

PS modified mRNA showed high translation efficiency.

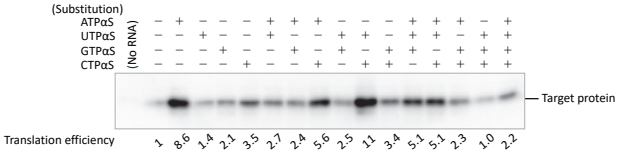

Western blot analysis of translation of FLAG-EGF mRNAs in the PURE system. After being transcribed, purified RNA (0.2 μM) was incubated in the system at 37 ˚C for 2 h. The modification pattern of RNAs at the time of transcription is expressed by showing substituted NTPαS(s) with a + sign. The translation product was detected using anti-FLAG M2 antibody.

5. Kinetic analysis of the translation reaction

Single-turnover analysis of translation reaction

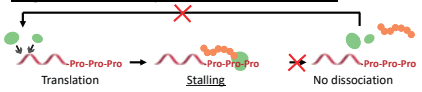

Embo Rep., **2016**, *17*, 1776-1784.

3 proline (Pro) repeats at the end of a protein sequence causes the ribosome to pause prematurely in the presence of elongation factor P.

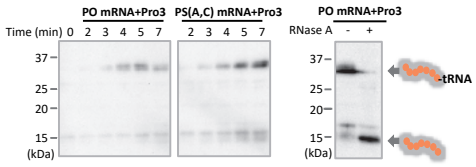

Time-course of the translation reaction on phosphorothioate mRNA (PS(A,C) mRNA+Pro3) or non-modified mRNA (PO-mRNA+Pro3) analyzed by western blot.

Western analysis of translation product after RNase A treatment.

Time-course of translation reaction

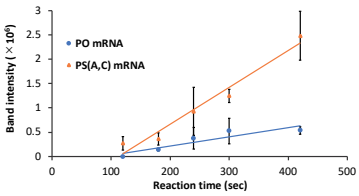

Reaction time-translation plot. Signal intensity of the bands which appeared between 25-kDa and 37-kDa markers were plotted.

PS modification may promote the formation of the ribosomal initiation complex.
The initial rate of translation with PS-mRNA was approximately four times faster than that of PO-mRNA.

6. Stability of mRNA in PURE system

qRT-PCR analysis

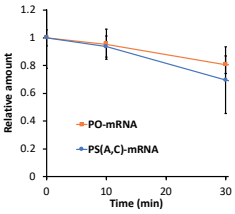

Stability of phosphorothioate mRNA in the PURE translation mixture. The quantitative reverse transcription polymerase chain reaction (qRT-PCR) measurement of PO-mRNA and PS(A,C)-mRNA after translation at 0, 10, 30 min. The error bars mean ±SD, n = 3.

No significant difference in stability was observed between the two mRNAs.

7. Effect of site-specific PS-modification on translation

Synthesis scheme of each mRNAs

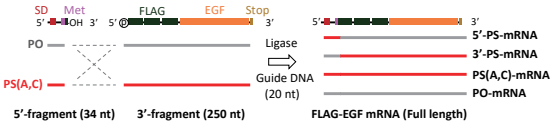

Sequence of 5'-PS-mRNA

(Ligated at this position)

5' GGG*AU*C*CG*A*AGG*AG*AU*AU*AU*C*CG*AUGG*A*CU*A*C*A*A-GGACGACGACGA
CAAGAUCAUCGACUAUAAGACGACGACGAUAAAGGUGGCGACUAUAAGGACGACGACGACAAAG
CCAUUAAUAGUGACUCUGAGUGUCCCCUGUCCCACGACGGGUACUGCCUCCACGACGGUGUGUGGC
AUGUAUAUUGAAGCAUUGGACAAGUACGCCUGCAACUGUGUGUGUGGCUACAUCGGGGAGCGCUG
UCAGUACCGAGACCUGAAGUGGUGGGAACUGCGCCUGCAGUAG 3'

*: Phosphorothioate bond

Translation efficiency of each mRNAs

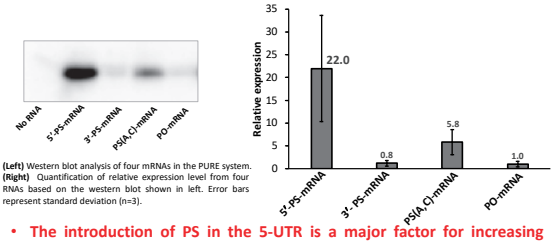

(Left) Western blot analysis of four mRNAs in the PURE system. **(Right)** Quantification of relative expression level from four RNAs based on the western blot shown in left. Error bars represent standard deviation (n=3).

- **The introduction of PS in the 5-UTR is a major factor for increasing translation efficiency.**
- **PS-introduction to the 3'-end side after the start codon had negative effects on translation.**

8. Coupled transcription/translation reaction using NTPαSs

Transcription and translation in PURE system

ATPαS gave no translation products.

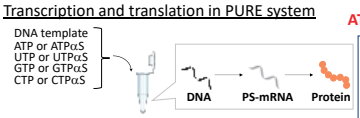

ATP is hydrolyzed to AMP by aminoacyl-tRNA synthetases in the PURE system and ATPαS may have inhibited this enzymatic reaction and then inhibited the whole translation reaction.

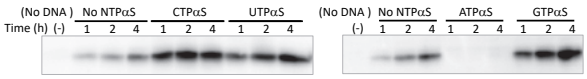

Western blot analysis of the translation product using template DNA coding FLAG-EGF mRNA with one NTPαS substituted. Substituted NTPαS was indicated in the figure.

Strategy to enhance translation using NTPαS

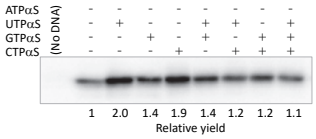

All substitution patterns gave higher amounts of translation product than the case using natural NTPs.

Western blot analysis of the reactions with one or more NTPαS substitution except ATPαS using a template DNA coding FLAG-EGF mRNA.

9. Summary and prospect

- The incorporation of PS into mRNA enhanced the protein synthesis in the *E. coli* cell-free translation system by up to 22-fold.
- The introduction of PS accelerated the initiation stage of the translation reaction.
- Simultaneous transcription and translation with NTPαS gave more translation products than with native NTP.
- These results provide a useful mRNA design guideline for improving the translation efficiency by chemical modification on mRNA.

Disulfide - unit conjugation enables ultrafast cytosolic internalization of antisense DNA and siRNA

○Saki Kawaguchi[1], Zhaoma Shu[1], Kousuke Nakamoto [1], Naoko Abe[1] , Yasuaki Kimura[1], Hiroshi Abe[1,2]

[1] Graduate School of Science, Nagoya University , [2] RIKEN Center for Emergent Matter Science

Introduction

Poor permeability is the main barrier for oligonucleotides therapeutics.

Oligonucleotides is promising for therapy

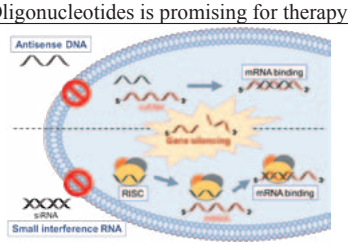

- Antisense DNA inhibits mRNA translation.
- siRNA leads to the cleavage of target mRNA.

Current delivery method

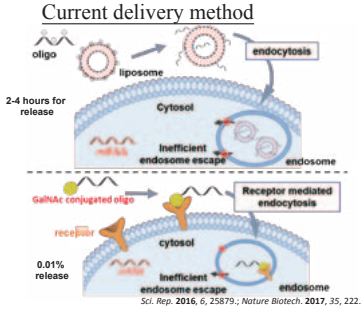

Sci. Rep. **2016**, *6*, 25879.; *Nature Biotech.* **2017**, *35*, 222.

Membrane Permeable Oligonucleotides (MPON)

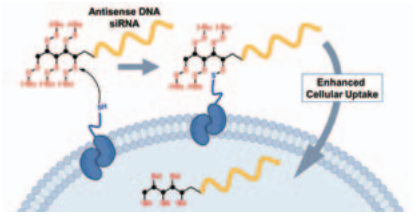

Z. Shu, H.Abe, et al., , *Angew Chem Int Ed Engl, 58, 6611-6615 (2019)*

Results

Design and Synthesis of MPON.

■ **Phosphoramidite Synthesis**

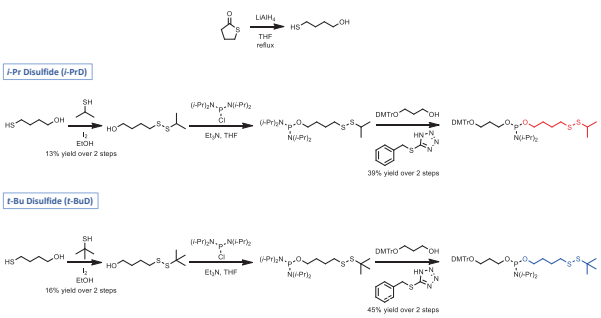

■ **Oligonucleotides Synthesis**

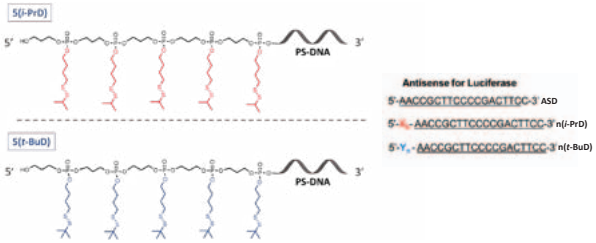

Permeability enhancement

(A)

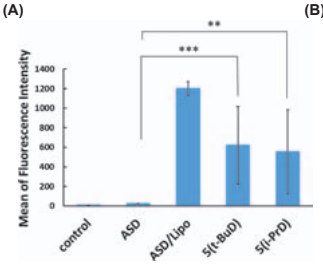

(B)

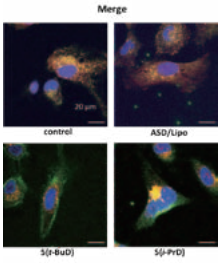

(A) DNA concentration: 1 μM; Incubation time: 3h The experiment was performed for three times independently. Data are represented as mean±SEM, n = 3, *P < 0.05, **P < 0.01, ***P < 0.001 versus ASD
(B) DNA Concentration: 1 μM; Incubation time: 10 min. Endosome/Lysosome were stained with Lysotracker Red following manufacturer's protocol. The images was obtained by a confocal microscope at 10 min. (Green: 488 nm, Red:594 nm)

➡ **Rapid cytosolic distribution in Only 10 minutes!**
Never been achieved!

Mechanism investigation

■ **Disulfide inhibition experiment**

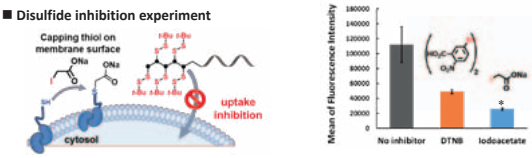

Inhibitory assays for cellular uptake using DTNB and iodoacetate. The cellular uptake of 1 μM 5LD in HeLa cells after 30-min pre-incubation of 1.2mM inhibitors (DTNB or sodium iodoacetate) or no inhibitor. The experiment was performed for three times independently. Data are represented as mean ± SEM, *P < 0.05, **P < 0.01, ***P < 0.001 versus no inhibitors.

■ **Endocytosis inhibition experiment**

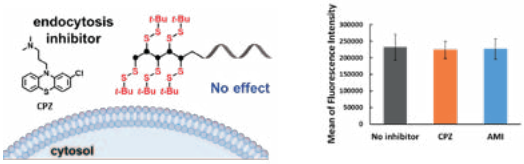

➡ **The cellular uptake of MPON is via thiol-disulfide exchange reaction.**

Gene silencing effect of MPON

■ **Dual Luciferase Assay**

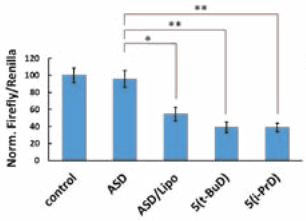

➡ **MPON effect depends on hydrophobicity, not terminal structure**

DNA concentration: 100 nM, The experiment was performed for three times independently. Data are represented as mean±SEM, n = 3, *P < 0.05, **P < 0.01, ***P < 0.001 versus ASD

Summary

- **Disulfide - unit conjugation enables ultrafast cytosolic internalization of antisense DNA and siRNA**
- **This unit forms a disulfide bond with the cell membrane surface**
- **MPON effect depends on hydrophobicity, not terminal structure**
- **Development of simplified MPON with disulfide - unit and hydrophobicity is required**

Emissive Radicals Stabilized by a Boron Atom at a Distant Position

○Masato Ito[1], Shunsuke Shirai[1], Yongfa Xie[1], Hiroki Soutome[1], Naoki Ando[1], Shigehiro Yamaguchi[1,2]
([1]Grad. Sch. Sci., Nagoya Univ.; [2]Institute of Transformative bio-Molecules, Nagoya Univ.)

1. Introduction

Neutral Radical Compounds

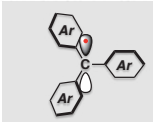

- ☑ reversible redox character
- ☑ long λ_{abs} and λ_{em}
- ☑ narrow energy gap
- ☐ stability
- ☐ efficient emission

Ambipolar carrier transport materials

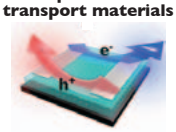

OLED materials

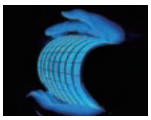

Luminescence Properties of Stable Radicals

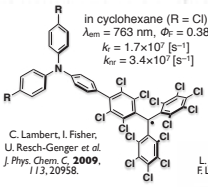

in cyclohexane (R = Cl)
λ_{em} = 763 nm, Φ_F = 0.38
k_r = 1.7×10^7 [s^{-1}]
k_{nr} = 3.4×10^7 [s^{-1}]

C. Lambert, I. Fisher, U. Resch-Genger *et al.* *J. Phys. Chem. C*, **2009**, *113*, 20958.

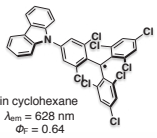

in cyclohexane
λ_{em} = 628 nm
Φ_F = 0.64

L. Julia *et al.* *Tetrahedron. Lett.*, **2006**, *47*, 2305.
F. Li *et al.* *Angew. Chem. Int. Ed.*, **2015**, *54*, 7091.

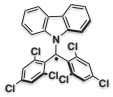

in CH_2Cl_2
λ_{em} = 585 nm, Φ_F = 0.022
k_r = 0.50×10^7 [s^{-1}] k_{nr} = 25×10^7 [s^{-1}]

F. Li *et al.* *Angew. Chem. Int. Ed.*, **2018**, *57*, 2869.

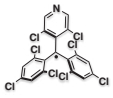

in cyclohexane
λ_{em} = 697 nm, Φ_F = 0.020
k_r = 0.34×10^7 [s^{-1}] k_{nr} = 1.5×10^7 [s^{-1}]

T. Kusamoto, H. Nishihara *et al.* *Angew. Chem. Int. Ed.*, **2014**, *53*, 11845.

Conventional Methods for Stabilization

Steric protection

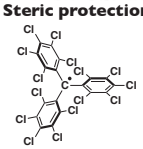

M. Ballester *et al.* *J. Am. Chem. Soc.*, **1971**, *93*, 2215.

Planarization

F. A. Neugebauer, D. Hellwinkel *et al.* *Tetrahedron Lett.*, **1978**, *49*, 4871.

Spin delocalization

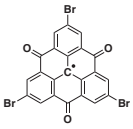

Y. Morita, K. Takui *et al.* *Nat. Mater.*, **2011**, *10*, 947.

This Work

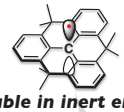

stable in inert environment

F. A. Neugebauer, D. Hellwinkel *et al.* *Tetrahedron Lett.*, **1978**, *49*, 4871.

B

Introduction of boron atom into

- **Elucidation of the correlation between structures and physical properties (stability, photophysical property…)**
- **Development of stable and luminescent radicals**

New Strategy for Stabilization of Radicals

stable, ambipolar, emissive

T. Okamoto, J. Takeya, S. Yamaguchi *et al.* *J. Am. Chem. Soc.*, **2017**, *139*, 14336.

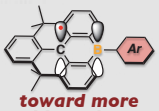

toward more stable and more emissive

2. Synthesis of Sterically Protected Derivative

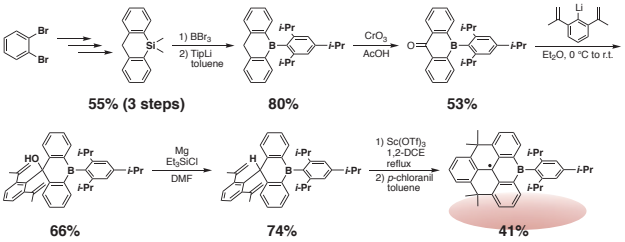

3. Effect of Spin Delocalization

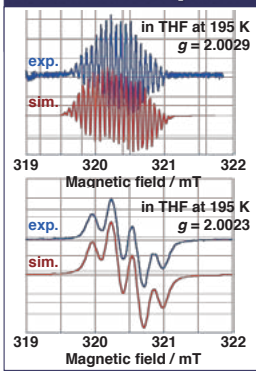

Spin density UB3LYP/6-31+G(d) level

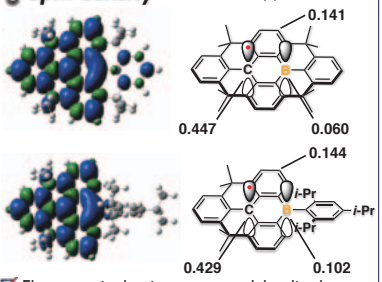

☑ Electron spin density was more delocalized onto a boron moiety in sterically protected derivative relative to planarized derivative.

4. Improvement of Stability

Degradation of toluene solution under ambient condition monitored by UV-vis spectra

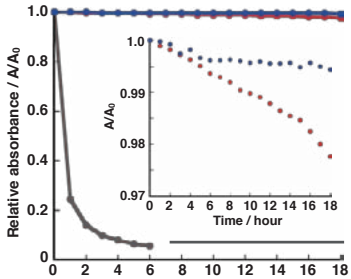

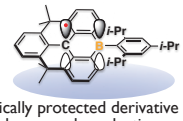

☑ Sterically protected derivative did not show any degraduation.

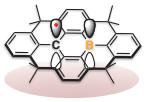

Planarized trityl radical

☑ The introduction of boron atom drastically improved the stability.

5. Impacts of Structural Effects

Photophysical properties in toluene

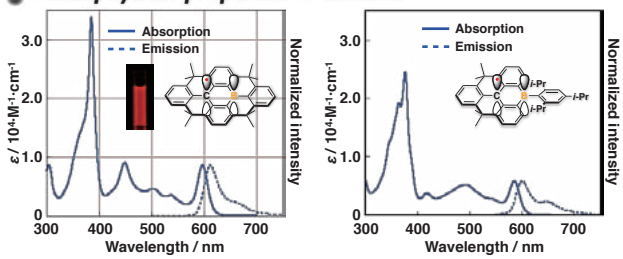

Compounds	λ_{abs} [nm]	ε [10^3·M^{-1}·cm^{-1}]	λ_{em} [nm]	Φ_F	τ [ns]	k_r [10^7·s^{-1}]	k_{nr} [10^7·s^{-1}]
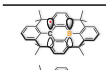	596	8.61	612	0.78	34.6	2.1	0.72
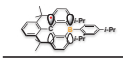	586	5.86	600	0.08	14.7	0.54	6.3

☑ Although both compounds exhibited red emission, the values of Φ_F and k_{nr} changed drastically by deplanarization.

Theoretical calculations UB3LYP/6-31+G(d) level

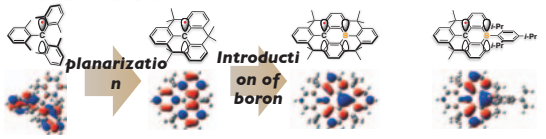

☑ Effective interaction between p (boron) and π* (π skeleton).

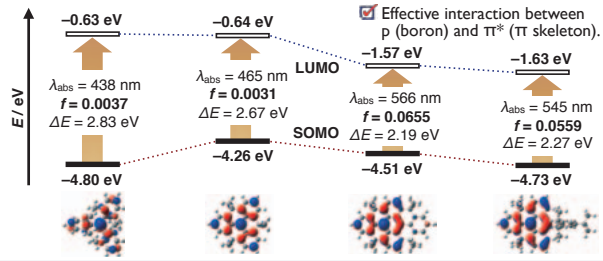

6. Summary

- ☑ Spin delocalization and steric protection around boron atom are both essential for improvement of stability.
- ☑ The vacant p orbital on the boron atom not only functions to delocalize the spin density, but also functions as an electron acceptor to generate ICT character.
- ☑ The rigid structure by planarization and ICT character are important for achieving highly efficient luminescence.

Photoreaction of Dithienylborane Derivative Bearing Bis(trimethylsilyl)phenyl Group

○Hirofumi Kajita[1], Naoki Ando[1], Shigehiro Yamaguchi[1,2]

[1]Graduate School of Science, Nagoya University, [2]Institute of Transformative Bio-Molecules (WPI-ITbM), Nagoya University

1. Introduction

Photoreaction of Organoboron Compounds

Di-π-borate Rearrangement

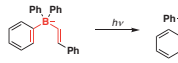

G. B. Schuster *et al.* *J. Am. Chem. Soc.* **1988**, *110*, 6252.

Ligand Coupling

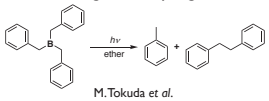

M. Tokuda *et al.* *Chem. Lett.* **1976**, 209.

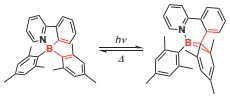

S. Wang *et al.* *J. Am. Chem. Soc.* **2008**, *130*, 12898.

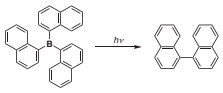

B. G. Ramsey *et al.* *J. Am. Chem. Soc.* **1967**, *99*, 3182.

Bora-Nazarov Cyclization

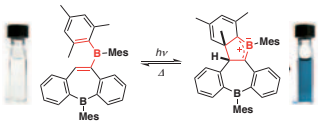

S. Yamaguchi *et al.* *Angew. Chem. Int. Ed.* **2013**, *52*, 3760.

☑ Drastic color changes ☑ Reversibility

Cf.) Nazarov cyclization

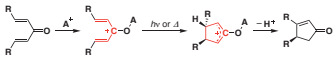

Photoreaction of $BMes_2$-arenes

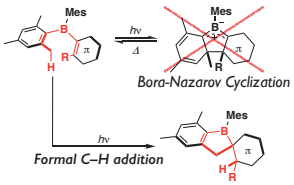

N. Ando, K. Yoshizawa, H. Ikeda, S. Yamaguchi *et al.* *Angew. Chem. Int. Ed.* **2017**, *56*, 12210.

Problem

Benzylic C–H bonds give rise to another photoreaction mode.

2. Photoreaction

Molecular Design

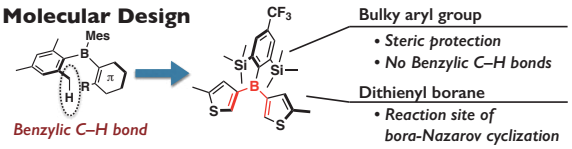

Benzylic C–H bond

Bulky aryl group
- *Steric protection*
- *No Benzylic C–H bonds*

Dithienyl borane
- *Reaction site of bora-Nazarov cyclization*

Photoreaction of Dithienylborane

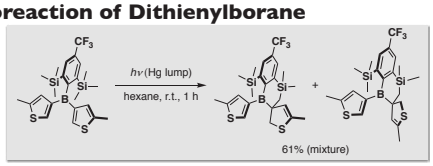

• UV-vis Absorption Spectra

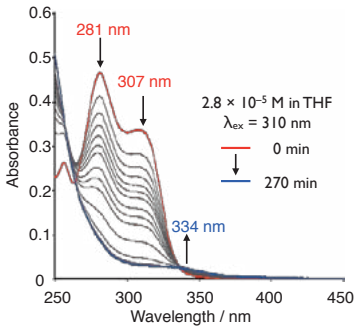

• TD-DFT Calculation

[B3LYP/6-31(d) in gas phase]

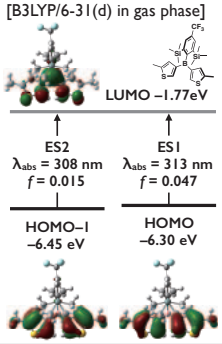

3. Determination of Photoproduct

Crystal Structure of Photoproduct as a Py Complex

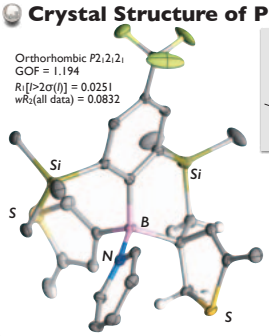

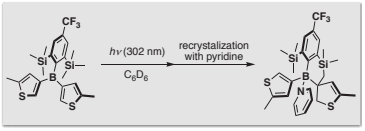

☑ *H atom rearrangement from trimethylsilyl group to thiophen moiety*

☑ *C–C bond formation to generate spiro cycle structure*

Not the bora-Nazarov cyclization but a new type of photoreaction proceeded upon photo irradiation.

4. Plausible Mechanism

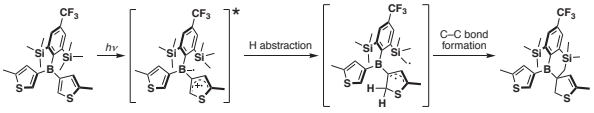

5. BN-allene formation

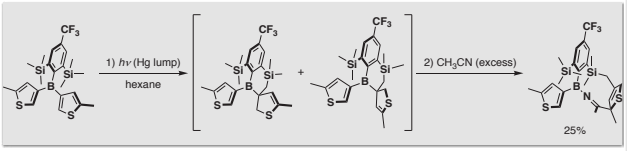

Reaction of Photoproducts with Acetonitrile

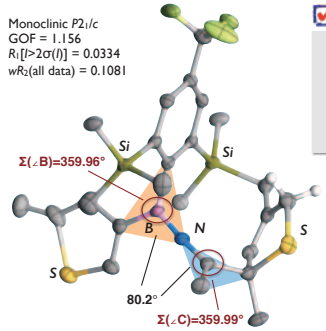

☑ *BN-allene*

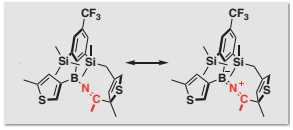

BN-allene moiety

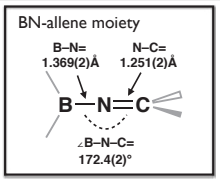

Cf.) Examples of BN-allene

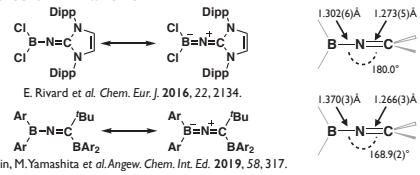

E. Rivard *et al.* *Chem. Eur. J.* **2016**, *22*, 2134.

Z. Lin, M. Yamashita *et al.* *Angew. Chem. Int. Ed.* **2019**, *58*, 317.

6. Reaction with Acetone

Reaction of Photoproducts with Acetone

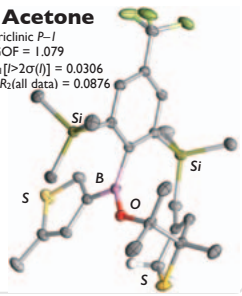

☑ *10-membered ring formation*

Ring-expansion reaction similar to BN-allene formation proceeded even with reaction with acetone.

7. Conclusion

☑ A new type of photoreaction proceeds upon UV irradiation.

☑ This reaction suggests that H atom rearrangement proceeds even at the methyl group on the trimethylsilyl group.

☑ Photoproduct reacts with CH_3CN to form a BN-allene derivative.

Self-Assembly of Amphiphilic Aromatic Hydrocarbons into Nanosheets via Multiple CH/π Interactions

Hiroki Narita,[1] Tsuyoshi Nishikawa,[1] Soichiro Ogi,[1] Yoshikatsu Sato,[2] and Shigehiro Yamaguchi[1,2]
[1]Department of Chemistry, Graduate School of Science, [2]Institute of Transformative Bio-Molecules (WPI-ITbM), Nagoya University

1. Introduction

Covalent nanosheets

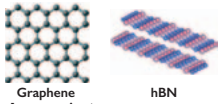

Graphene hBN

- Large anisotropy
- High surface-to-volume ratio
- Unique surface charge

Non-covalent nanosheets

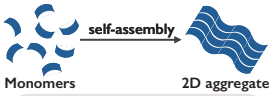

Problem
Structural requirements have not been established.

CH/π interaction, a type of hydrogen bond

- Dispersion force
- Cooperative and multiple features
- High symmetry of PAH

Effective interaction in aqueous media
Enthalpic and entropic advantage

Two-dimensional assemblies of amphiphilic π-systems in aqueous media

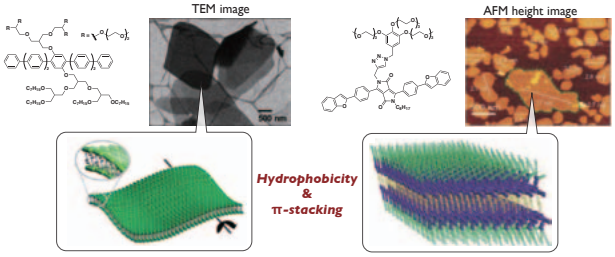

E. Lee, J.-K. Kim, M. Lee, *Angew. Chem. Int. Ed.* **2009**, *48*, 3657. S. Ghosh, D. S. Philips, A. Saeki, A. Ajayaghosh, *Adv. Mater.* **2017**, *29*, 1605408.

2. This work

CH/π interaction-driven self-assembly into nanosheets in aqueous media

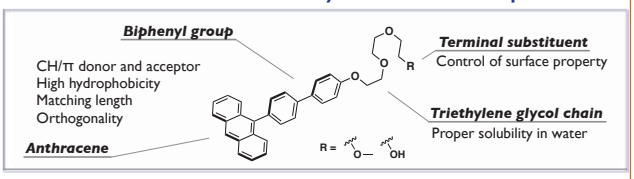

Schematic representation

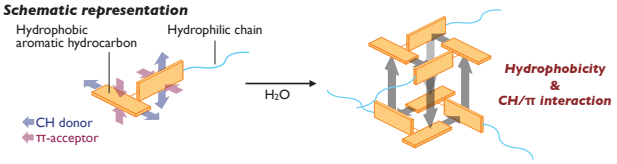

3. Self-assembly in aqueous media

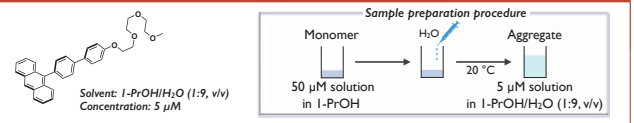

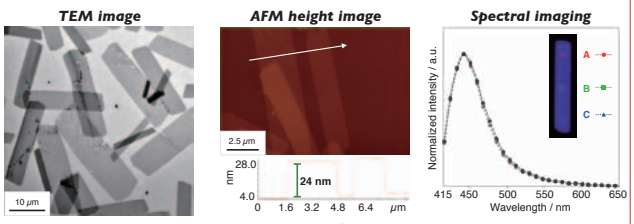

The sheet-like aggregates were formed in aqueous media.

4. X-ray crystallographic analysis

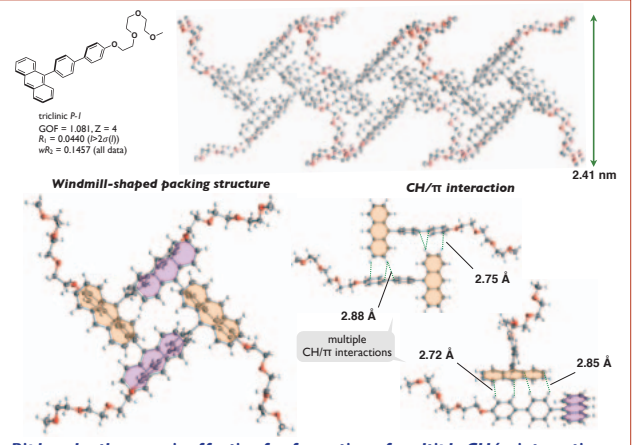

Biphenylanthracene is effective for formation of multiple CH/π interactions.

5. Molecular orientation of aggregates

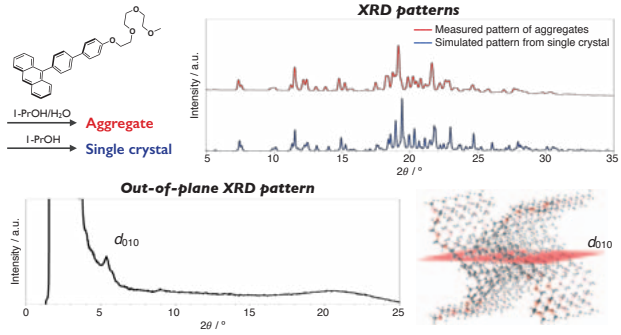

Sheet-like aggregates and single crystal have a similar molecular packing.

6. Effect of terminal substituent on aggregates

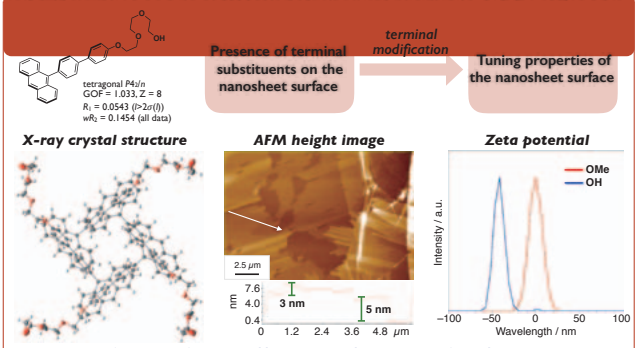

Terminal substituents affect the surface properties of nanosheets.

7. Possible mechanism of nanosheet formation

1st step: one-dimensional growth

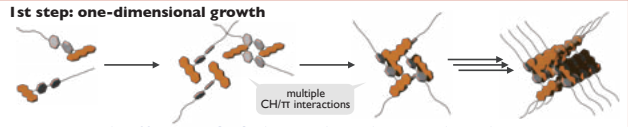

Hydrophobic effect and CH/π interaction drive one-dimensional assembly.

2nd step: two-dimensional growth

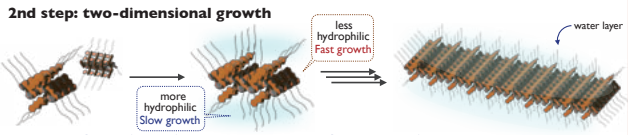

One-dimensional aggregates self-assemble into nanosheets.

8. Summary

- ☑ *Two-dimensional self-assembly driven by CH/π interaction in aqueous media*
- ☑ *Windmill-shpaed packing structure composed of biphenylanthracene units*
- ☑ *Versatility of biphenylanthracene-based amphiphiles*
- ☑ *Control over the surface property of nanosheets by terminal modification*

Synthesis and Catalytic Methane Oxidation Property of μ-Nitride-Bridged Iron Phthalocyanine Dimer Bearing Eight 12-crown-4 Groups

○Junichi Kura[1], Yasuyuki Yamada[1,2,3], Kentaro Tanaka[1]
[1]Graduate School of science, Nagoya University, [2]RCMS, Nagoya University, [3]PRESTO/JST
kentaro@chem.nagoya-u.ac.jp

1. Introduction

CH_4
- Major constituent of natural gas
- Abundant in the sea near Japan as methane hydrate
- Difficulty of direct C-H activation

C–H dissociation energy	
CH_4	104.9 kcal / mol
CH_3–CH_3	101.4 kcal / mol
$(CH_3)_2$–CH_2	98.6 kcal / mol
Ph–CH_3	89.7 kcal / mol

Novel catalysts are desired for direct and efficient conversion of CH_4.

μ-Nitrido-Bridged Iron Phthalocyanine Dimer Catalyst for Oxidation of Methane

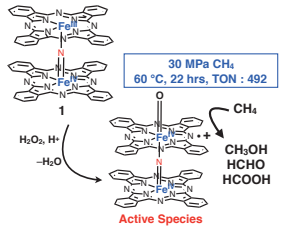

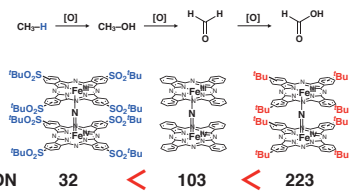

Electron-donating substituents would enhance the activity of catalytic methane oxidation.

2. This Work

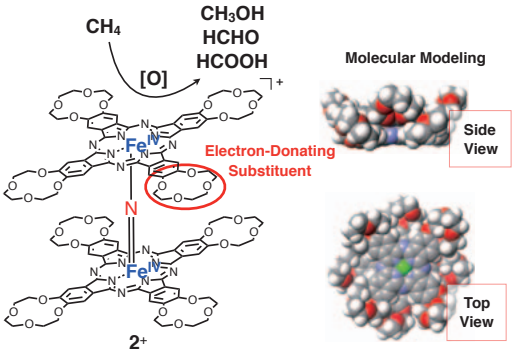

3. Synthesis of 2+

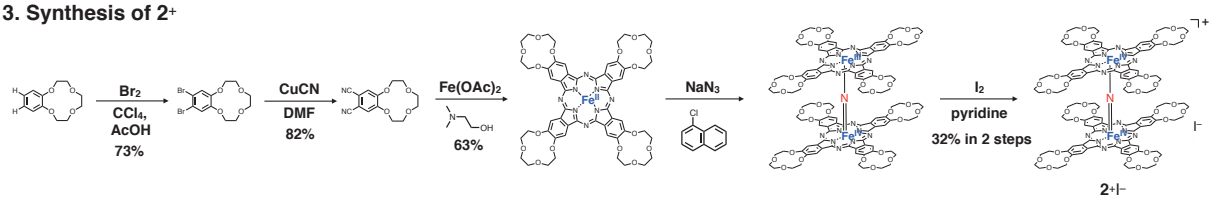

4. Spectra of 2+·I–

MALDI-TOF-MS

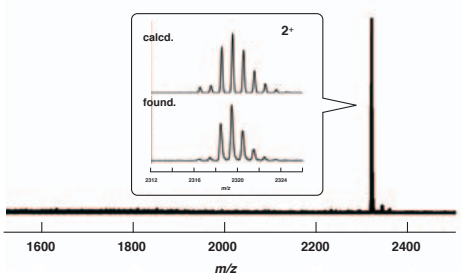

^{1}H-NMR in Pyridine-d_5

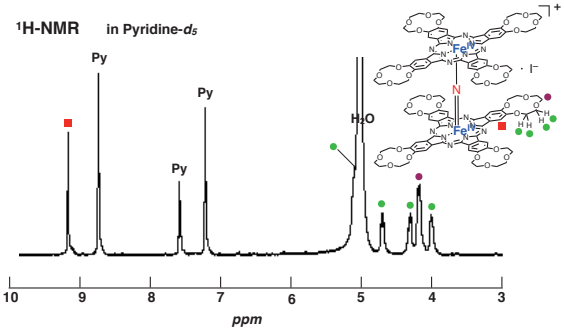

5. Electrochemical property of 2+·I–

Cyclic voltammogram

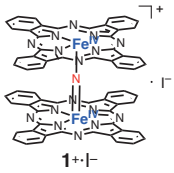

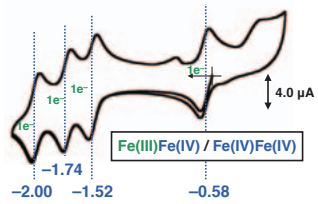

1+·I– 400 μM in Pyridine containing 0.1 M $TBAPF_6$. scan rate : 100 mV/s, 20°C

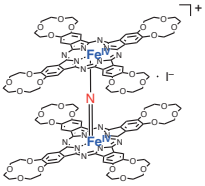

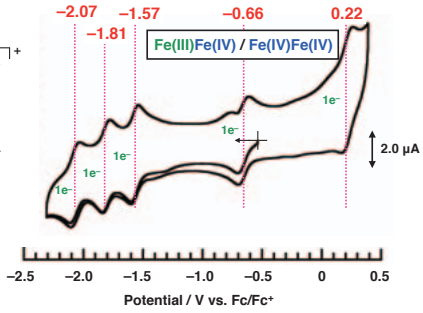

2+·I– 200 μM in Pyridine containing 0.1 M $TBAPF_6$. scan rate : 100 mV/s, 20°C

Each redox waves of 2+·I– showed significant negative shifts by the effect of the electron-donating character of the 12-crown-4s.

6. Conclusion and Perspective

We synthesized a novel complex **2**+·I– having four 12-crown-4 units on each of the phthalocyanines. A cyclic voltammogram of **2**+·I– showed four reversible one-electron redox waves in the range between –2.0 V to 1.0 V (vs. Fc/Fc+) which significantly shifted to more negative potentials compared to the corresponding redox waves of **1**+·I–. This result clearly demonstrates the effect of the electron-donating character of the 12-crown-4s. Methane oxidation activity of **2**+·I– is under investigation.

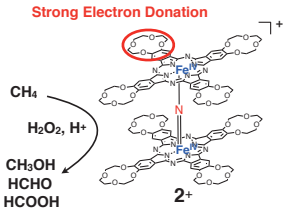

Synthesis and physical property of Tb(III)-phthalocyanine double-decker complex having planar chirality

○Hiroaki Nakajima[1], Chisa Kobayashi[1], Yasuyuki Yamada[1,2,3], Yoshiaki Shuku[1], Kunio Awaga[1] and Kentaro Tanaka[1] *

[1]Graduate School of science, Nagoya University, [2]RCMS, Nagoya University, [3]PRESTO/JST

kentaro@chem.nagoya-u.ac.jp

1. Introduction

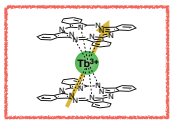

- Tb(III)-phthalocyanine double-decker complex is known as a single-molecule-magnet.
- Physical property can be tuned by changing the environment around terbium ion.

Our previous work

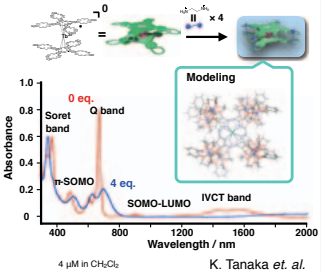

K. Tanaka *et. al.*

2. Concept

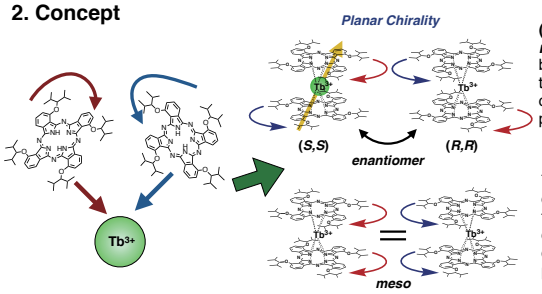

(*S,S*), (*R,R*), and ***meso*** isomers can be generated due to the coordinating orientation of the two phthalocyanines.

The structural difference around terbium ion should cause the difference of their physical property.

3. Synthesis and Separation

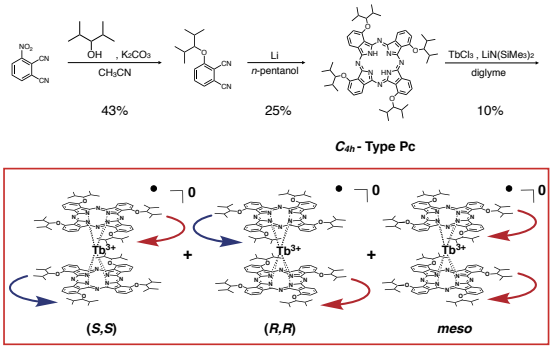

Isomers were separated by using a chiral column (CHIRAL ART Amylose-SA, Hexane : MTBE = 95 : 5).

^{1}H-NMR (400 MHz, $CHCl_3$, TMS)

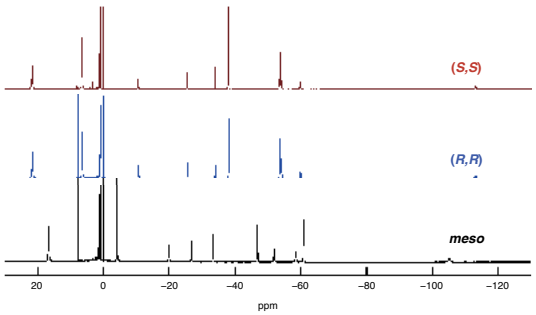

4. Identification of Chiral Complex

X-ray Crystal Structure

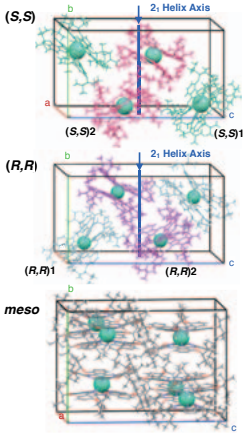

	(S,S)1	(S,S)2
Twisted angle	41.3	38.9
Pc-Pc distance	2.803	2.800

	(R,R)1	(R,R)2
Twisted angle	41.4	39.0
Pc-Pc distance	2.799	2.795

	meso
Twisted angle	40.9
Pc-Pc distance	2.778

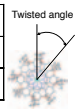

- Twisted angle and Pc-Pc distance of ***meso*** were slightly different compared to those of enantiomers.

CD spectrum

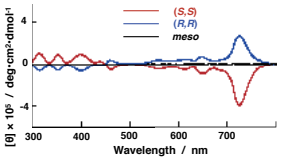

- (*R,R*) and (*S,S*) showed opposite Cotton effect, whereas ***meso*** isomer showed no Cotton effect.

5. Magnetic Property

Alternating current (ac) magnetic susceptibility (powder, dc field : 0 Oe)

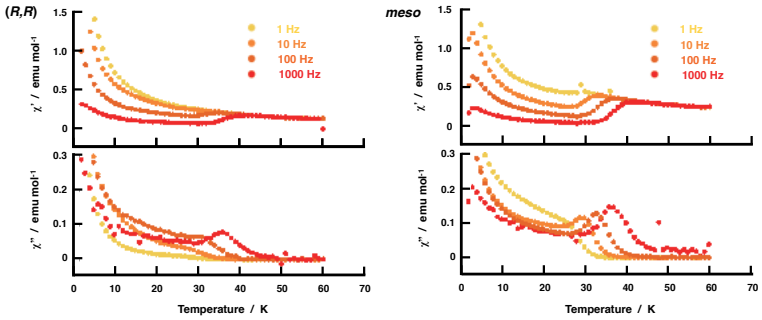

- χ'' shows a local maximum at 26.2, 28.3, 30.5, and 36.4 K at 1, 10, 100, and 1000 Hz, respectively.
- χ'' shows a local maximum at 26.4, 29.9, 33.3, and 36.9 K at 1, 10, 100, and 1000 Hz, respectively.
- These results indicate that the complexes have slow magnetic relaxation.

Arrhenius Plot

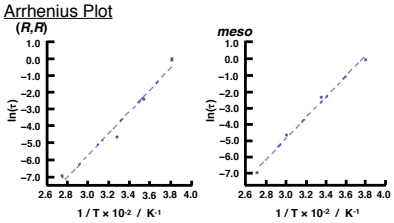

- In the high temperature region, the χ'' peaks of the data for fitting was carried out on the basis of a thermally activated mechanism, $\tau = \tau_0 \exp(U_{eff} / k_B T)$.

	(R,R)	meso
U_{eff}/k_B (K)	644	603
τ_0 ($\times 10^{-11}$ s)	1.39	1.12
T_B (K)	21.8	21.9

τ : relaxation time, τ_0 : frequency factor U_{eff} / k : effective energy barrier, T_B : blocking temperature

- Magnetic property of (*R,R*) isomer was similar to that of ***meso*** isomer in spite of the difference of structure.

6. UV-vis-NIR spectrum

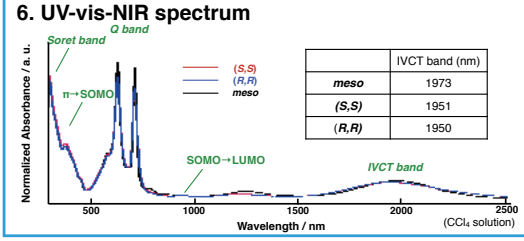

	IVCT band (nm)
meso	1973
(S,S)	1951
(R,R)	1950

- UV absorption spectra of the enantiomers were similar.
- IVCT band of ***meso*** was slightly different from that of enantiomers.
- Structural difference of ***meso*** and enantiomer might have caused the difference in IVCT energy.

7. Summary

- We synthesized new chiral Tb(III)-phthalocyanine double-decker complexes based on planar chirality.
- (*R,R*) and ***meso*** complex showed single molecule magnet character in spite of their lower symmetry compared to non-substituted double-decker complex.
- The structural difference between ***meso*** and enantiomer did not result in the difference in their magnetic susceptibility, but it was caused the difference in IVCT energy.

Synthesis of π-Expanded Porphyrin Derived from Tetra(*N*-carbazolyl)porphyrin

○*Atsuya Matsubuchi, Shin-ichiro Kawano, and Kentaro Tanaka**

Department of Chemistry, Graduate School of Science, Nagoya University

kentaro@chem.nagoya-u.ac.jp

1. Introduction

Fused Porphyrins

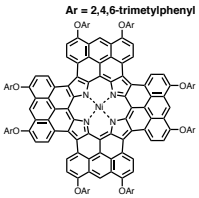

λ_{max} = 1417 nm

$E_{ox}^1 - E_{red}^1$ = 0.61 eV

H. L. Anderson, et al., *J. Am. Chem. Soc.*, **2011**, *133*, 30

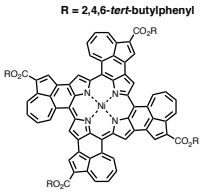

λ_{max} = 1136 nm

$E_{ox}^1 - E_{red}^1$ = 1.01 eV

A. Osuka, et al., *Angew. Chem. Int. Ed.*, **2006**, *45*, 3944

π-Expanded porphyrins exhibit absorptions in near IR region and small electrochemical HOMO-LUMO gaps.

This Work

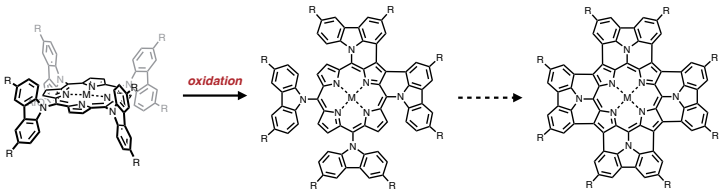

Synthesis of novel π-expanded porphyrin by oxidative coupling of tetra(*N*-carbazolyl)porphyrin.

2. Synthesis of 1(Ni)

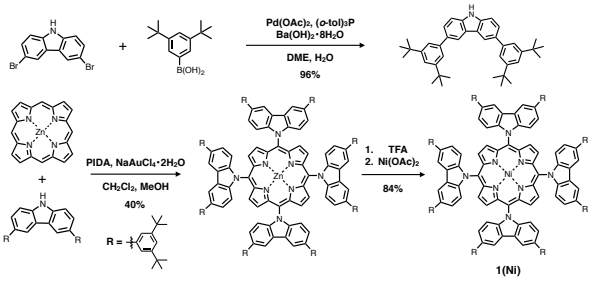

Cyclic Voltammetry

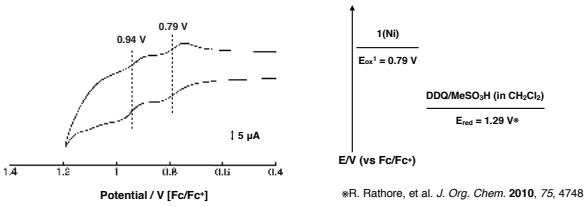

[1(Ni)] = 400 μM in CH_2Cl_2 containing 100 mM Bu_4NPF_6 scan rate: 100 mV/s

*R. Rathore, et al. *J. Org. Chem.* **2010**, *75*, 4748

DDQ/MeSO3H is suitable for oxidative coupling of 1(Ni).

3. Synthesis of 2(Ni)

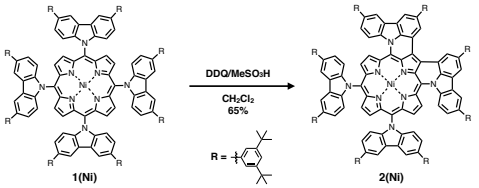

MALDI-TOF MS

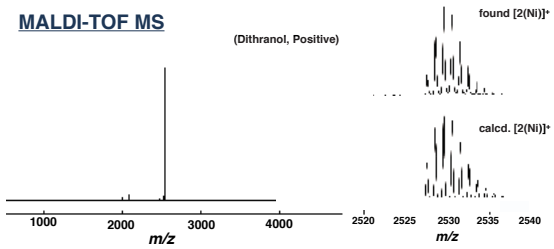

^{1}H NMR

The structure of 2(Ni) can be explained by the NMR symmetry. The aromatic signals are intensified 2.5 times.

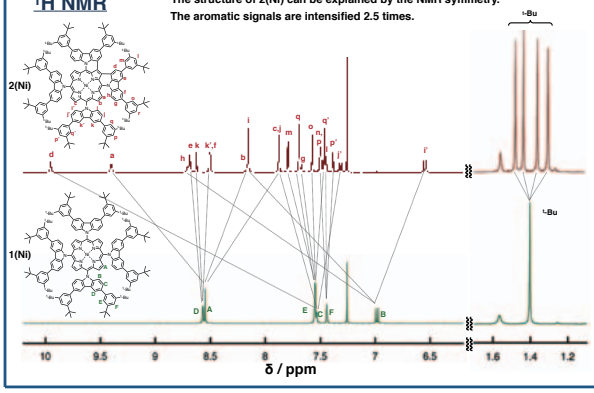

UV-vis

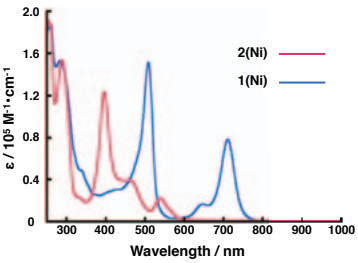

[1(Ni)] = [2(Ni)] = 5.0 μM in $CHCl_3$ at 293 K

Table. Redox potential of 1(Ni) and 2(Ni)

compound	E_1^{ox} (V)	E_1^{red} (V)	$E_1^{ox} - E_1^{red}$ (eV)
1(Ni)	0.79	−1.34	2.13
2(Ni)	0.11	−1.19	1.30

- Both of Soret band and Q band of 2(Ni) have shifted to long wavelength region.
- 2(Ni) has small HOMO-LUMO gap in comparison with porphyrin 1(Ni).

CV

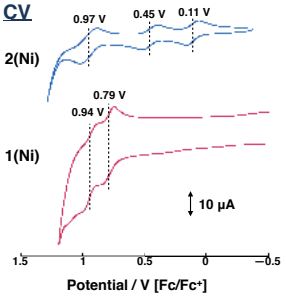

[1(Ni)] =[2(Ni) = 400 μM in CH_2Cl_2, containing 100 mM Bu_4NPF_6

DPV

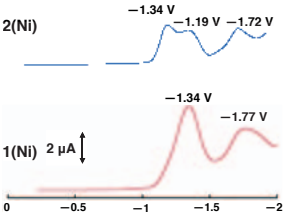

[1(Ni)] = [2(Ni)] = 400 μM in CH_2Cl_2, containing 100 mM Bu_4NPF_6

5. Summary and Perspectives

- π-Expanded porphyrin 2(Ni) was synthesized from the tetra(*N*-carbazolyl)porphyrin 1(Ni).
- 2(Ni) has the red-shifted absorption bands and small HOMO-LUMO gaps.
- Further oxidation will be investigated.

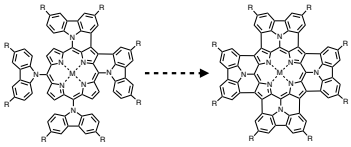

R = 3,5-di-*tert*-butylphenyl, M = Ni

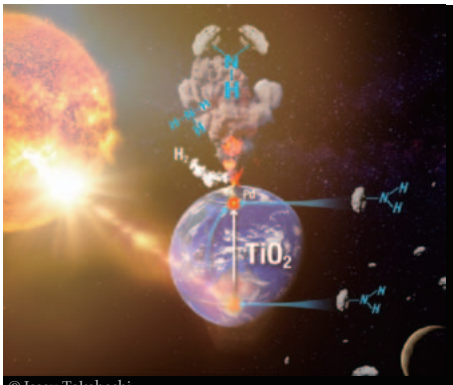

© Issey Takahashi

Pd/TiO_2-Photocatalyzed Self-Condensation of Primary Amines to Afford Secondary Amines at Ambient Temperature

Wang, L.-M.; Kobayashi, K.; Arisawa, M.; Saito, S.; Naka, H.

Grad. Sci., Nagoya Univ.; Grad. Pharm., Osaka Univ.; RCMS, Nagoya Univ.

Symmetric secondary amines were synthesized by the self-condensation of primary amines over a Pd / TiO_2 photocatalyst. The reactions afforded a series of secondary amines in moderate to excellent isolated yields at ambient temperature in cyclopentyl methyl ether. Applicability for one-pot pharmaceutical synthesis was demonstrated by a photocatalytic reaction sequence of self-condensation of an amine followed by N-alkylation of the resulting secondary amine with an alcohol.

Org. Lett. **2019**, *21*, 341-344.

1. Background: Intermolecular Self-Condensation

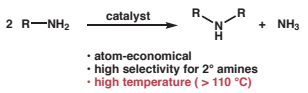

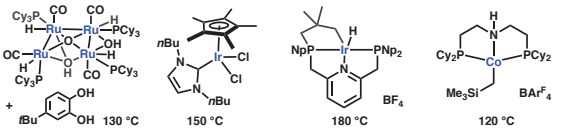

Yi, C. S. *et al.* *J. Org. Chem.* **2018**, *83*, 4932.
Peris, E. *et al.* *CEJ* **2008**, *14*, 11474.
Yamashita, M.; Nozaki, K. *et al.* *Inorg. Chim. Acta.* **2011**, *369*, 15.
Zhang, G. *et al.* *ACS Catal.* **2016**, *6*, 6546.

Pt-Sn/γ-Al_2O_3	Cu/γ-Al_2O_3	Pd_3Pb/Al_2O_3	Pd@porous graphene oxide
145 °C	140 °C	O_2, 110 °C	$H_2 + O_2$, 90 °C
Yu, Z. *et al.* *CEJ* **2011**, *17*, 13308.	Mizuno, N. *et al.* *Catal. S&T* **2013**, *3*, 2397.	Furukawa, S.; Komatsu, T. *et al.* *Chem. Commun.* **2014**, *50*, 3277.	Loh, C. T. *et al.* *J. Am. Chem. Soc.* **2015**, *137*, 685.

2. This Work: Photocatalytic Self-Condensation

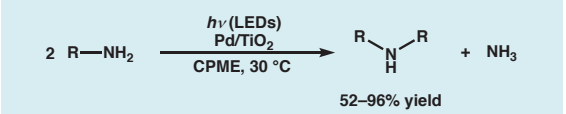

- Pd/TiO_2 photocatalyst selectively promotes the self-condensation of primary amines.
- Various secondary amines were synthesized under mild reaction conditions.
- Cross-condensation and one-pot dialkylation were demonstrated.

Pioneering works

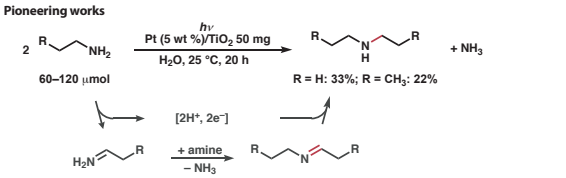

Nishimoto, S.-i.; Ohtani, B.; Yoshikawa, T.; Kagiya, T. *J. Am. Chem. Soc.* **1983**, *105*, 7180.
Intramolecular versions: Ohtani, B.; Tsuru, S.; Nishimoto, S.-i.; Kagiya, T. *J. Org. Chem.* **1990**, *55*, 5551.

3. Result and Discussion

3.1 Initial Discovery

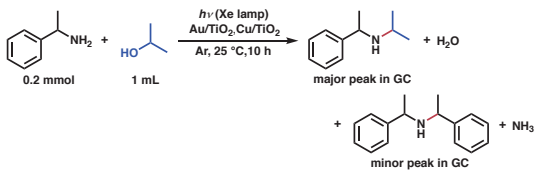

3.2 Optimized Conditions and Controls

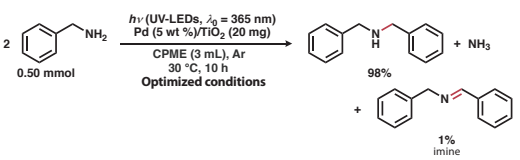

Changes from the optimized conditions

Without Pd: < 1% (<1% imine)	in the dark: < 1% (<1% imine)
Pt (5 wt %) in place of Pd: <1 % (78% imine)	THF in place of CPME: 75 % (<1% imine)
Cu (5 wt %) in place of Pd: <1 % (20% imine)	acetonitrile in place of CPME: 88 % (9% imine)
Ag (4 wt %) in place of Pd: <1 % (<1% imine)	ethyl acetate in place of CPME: 88% (4% imine)
Au (4 wt %) in place of Pd: <1 % (22% imine)	toluene in place of CPME: 90% (3% imine)

3.3 Substrate Scope

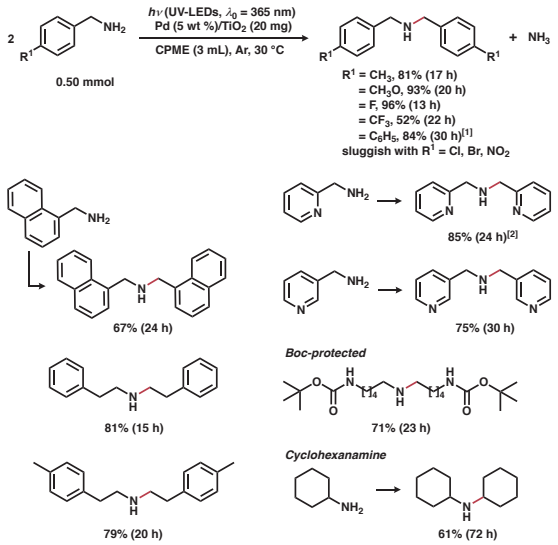

Core structures in functional molecules

[1] Fang, Y.-Q.; Jacobsen, E. N. *J. Am. Chem. Soc.* **2008**, *130*, 5660.
[2] Schiller, A. *et al.*, *J. Am. Chem. Soc.* **2017**, *139*, 4991.

3.4 One-pot Photocatalytic Pharma Synthesis

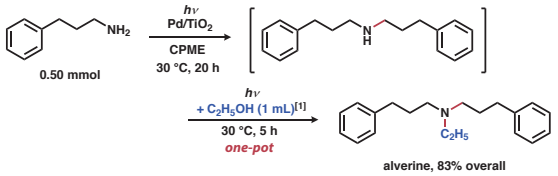

[1] 17 mmol. see: Wang, L.-M.; Jenkinson, K.; Wheatley, A. E. H.; Kuwata, K.; Saito, S.; Naka, H. *ACS Sustainable Chem. Eng.* **2018**, *6*,15419.

3.5 Mechanistic Hypothesis

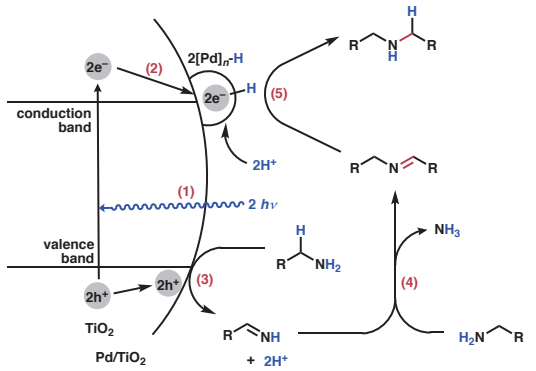

Cf. Nishimoto, S.-i.; Ohtani, B.; Yoshikawa, T.; Kagiya, T. *J. Am. Chem. Soc.* **1983**, *105*, 7180.
Ohtani, B.; Tsuru, S.; Nishimoto, S.-i.; Kagiya, T. *J. Org. Chem.* **1990**, *55*, 5551.

Acknowledgement: The authors sincerely thank Prof. Ryoji Noyori for his continuous support.

Spatio-temporal Control of Formation and Reaction of Formamide Radicals under Nickel-complexes/TiO_2 Cooperative Photocatalysis

Shogo Mori,[1] Takahiro Aoki,[1] Kaliyamoorthy Selvam[2], Jieun Jung[1], Susumu Saito*[,1,2]
[1]Graduate School of Science, [2]Research Center for Materials Science , Nagoya University

Abstract

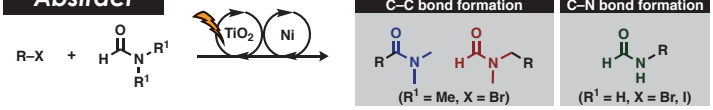

We report herein C–C and C–N bond formation reactions between organic halides and formamides under nickel-complexes/TiO_2 cooperative photocatalysis. The key to selective reactions would be spatio-temporal control of formation and reaction of formamide radicals, where kinetically favorable radicals would be formed around TiO_2 surface and then they would be transformed into thermodynamically stable radicals in solution.

1. C–C Bond Formation with DMF

1-1. Spatio-temporal transition of DMF radicals

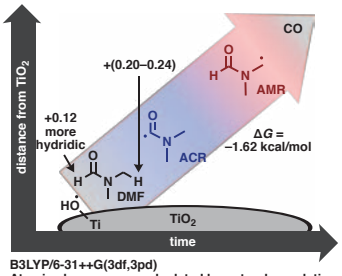

B3LYP/6-31++G(3df,3pd)
Atomic charges were calculated by natural population analysis.

C–H abstraction of DMF by O-centered radicals: DiLabio, G. A.; Bietti, M. *et al. J. Org. Chem.* **2013**, *78*, 5909.
Utilization of CO derived from DMF under Pd(II)/TiO_2 photocatalysis: Li, Z. *et al. J. Photochem. Photobio. A: Chem.* **2017**, *337*, 19.

1-2. Ligand Design

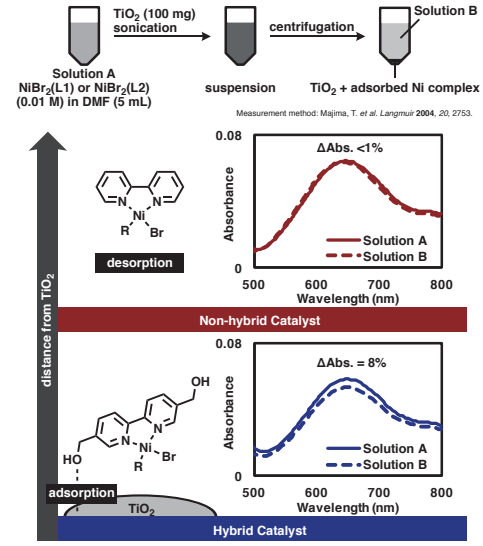

Measurement method: Majima, T. *et al. Langmuir* **2004**, *20*, 2753.

1-3. Scope

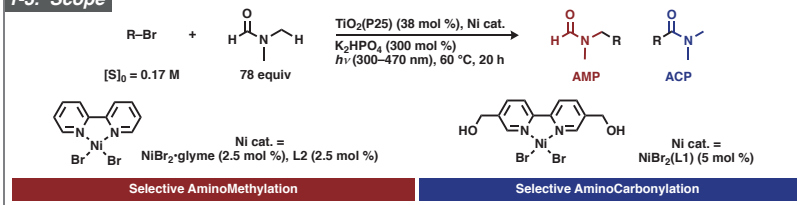

Selective AminoMethylation

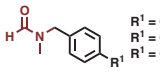

R^1 = CN, AMP+ACP = 77% (AMP:ACP= 2.7:1)
R^1 = CO_2Et, 90% (3.8:1)
R^1 = OMe, 68% (8.1:1)

Selective AminoCarbonylation

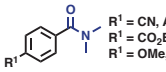

R^1 = CN, AMP+ACP = 79% (AMP:ACP = 1:8.1)
R^1 = CO_2Et, 81% (1:9.0)
R^1 = OMe, 61% (1:6.1)

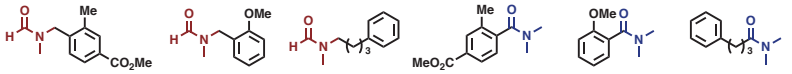

77% (7.3:1) (30 h) | 75% (3.5:1) | 46% (4.9:1) | 64% (1:3.3) (30 h) | 57% (1:15.7) | 33% (1:1.3)

1-4. Ligand Effect on Radical Trapping (Competition with TEMPO)

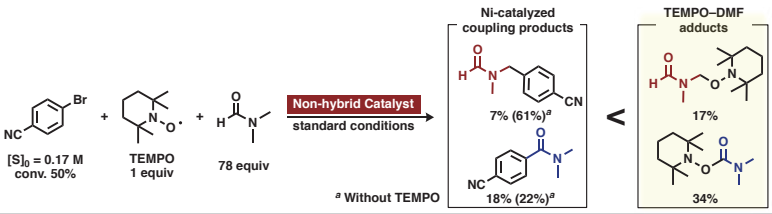

Non-hybrid catalysis in solution was sufficiently prevented by TEMPO.

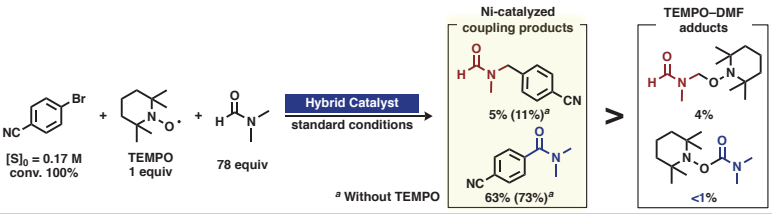

Hybrid catalysis around TiO_2 surface was hardly prevented by TEMPO.

2. C–N Bond Formation with Formamide

2-1. Background

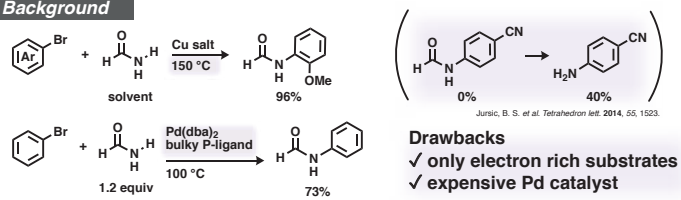

Jursic, B. S. *et al. Tetrahedron lett.* **2014**, *55*, 1523.

Zhang, Z. *et al. J. Org. Chem.* **2012**, *77*, 5279.

Drawbacks
✓ only electron rich substrates
✓ expensive Pd catalyst

2-3. Radical Trapping Experiment

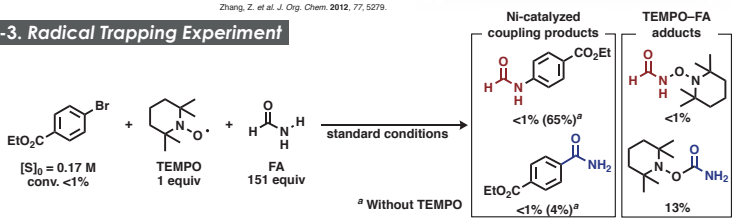

Thermodynamically less stable N-centered radical of formamide would be involved. (ΔG = +19.63 kcal/mol to C-centered radical)

2-2. Scope

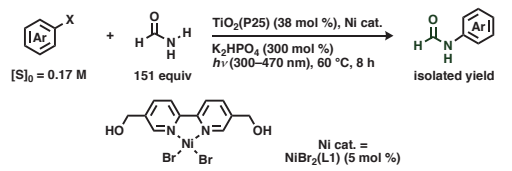

Selective C–N Bond Formation

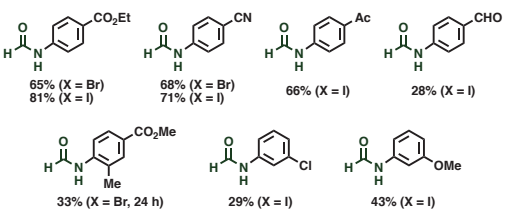

65% (X = Br) 81% (X = I) | 68% (X = Br) 71% (X = I) | 66% (X = I) | 28% (X = I)
33% (X = Br, 24 h) | 29% (X = I) | 43% (X = I)

Complementary synthetic method with cheap reagents

Molecular-frame momentum imaging of tunneling electrons from molecular deuterium in circularly polarized intense laser fields

H. Fujise[1], M. Takahashi[1], D. Ikeya[1], T. Nakamura[1], A. Matsuda[1], M. Fushitani[1], A. Hishikawa[1, 2]

1 Graduate School of Science, Nagoya University, 2 Research Center for Materials Science, Nagoya University

Introduction

Laser Tunneling Ionization Process

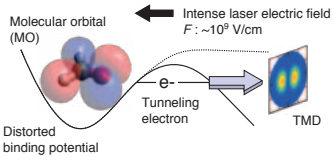

Observables

1. Tunneling ionization rate
2. Transverse Momentum Dsitribution

➡ **Sensitive to molecular orbitals**

THIS STUDY

Investigation of the effects of molecules on TMDs

▶ Electron-ion coincidence imaging

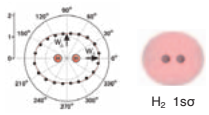

A. Staudte *et al.*, Phys. Rev. Lett. **102** 033004 (2009)

Tunneling ionization rate

▶ Visualization of excited states of NO

T. Endo *et al.* Phys. Rev. Lett. **116** 163002 (2016)

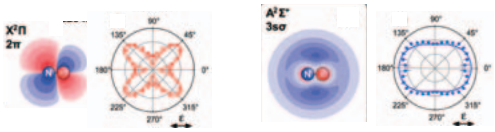

N^+ fragment ion distribution with respect to laser polarization portrays MO shapes

Transverse Momentum Distribution

▶ Three-dimensional molecular orbital imaging[1]

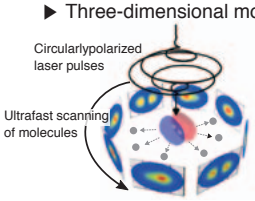

TMD Momenta perpendicular to laser polarization

⬇

Photoelectron momenta distribution depends on electron wavefunction[1, 2]

1 V. N. Pham *et al.*, Phys. Rev. A **89** 033426 (2014)
2 L. Arissian *et al.*, Phys. Rev. Lett. **105** 133002 (2010)

Experimental Results

Molecular Frame Photoelectron Angular Distribution

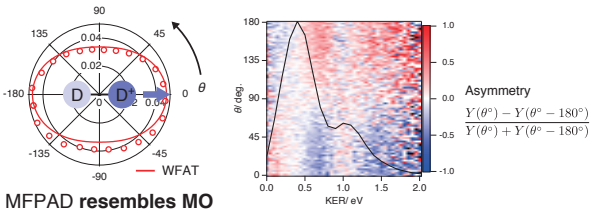

MFPAD **resembles MO**

Asymmetric yields observed perpendicular to molecular axis

Observed clear **KER dependence in MFPADs**

➡ Correlation between ionization process and dissociation observed from MFPADs

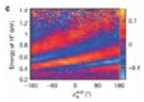

J. Wu *et al.* Nat. Commun. 4 2177 (2013)

Transverse Momentum Distribution

Three-dimensional momentum distribution: torus

➡ TMD appears in cross section

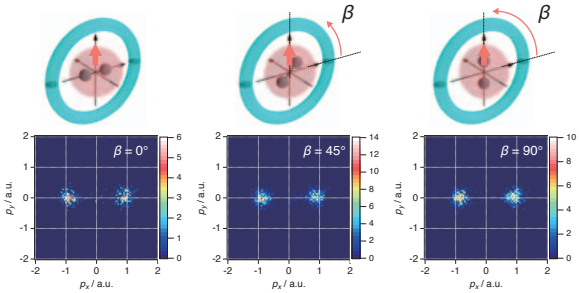

Evaluation of TMD and comparison with WFAT

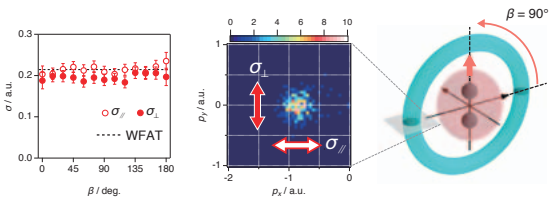

TMD width in agreement with WFAT prediction

➡ TMD could be utilized for three-dimensional MO imaging

➡ KER dependence is required to explore the similar effects seen in MFPADs

Weak Field Asymptotic Theory (WFAT)

O. I. Tolstikhin *et al.*, Phys. Rev. A. **84** 053423 (2011)

TMD $P(\boldsymbol{k}_\perp) = \Gamma \frac{4\pi\kappa}{F} \exp\left[-\frac{\kappa k_\perp}{F}\right]$

Ionization potential I_p , $\kappa = \sqrt{2I_p}$

Tunneling ionization rate $\Gamma(\beta, F) \approx W_{00}(F)|G_{00}(\beta)|^2$

⬇

TMD width $\sigma = \sqrt{F/\kappa}$ @ $F = 0.049$ a.u. $\sigma = 0.214$ a.u.

Experimental

Electron-ion coincidence momentum imaging

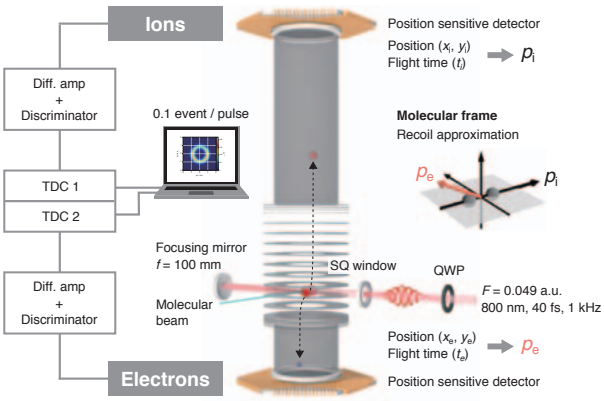

Three-dimensional molecular frame momentum distribution of photoelectrons from O_2 in circularly polarized intense laser fields

IKEYA, Daimu[1]; FUJISE, Hikaru[1]; NAKAMURA, Takeru[1]; MATSUDA, Akitaka[1]; FUSHITANI, Mizuho[1]; HISHIKAWA, Akiyoshi[1,2]
([1]Dept.Chem.,Nagoya Univ.; [2]RCMS,Nagoya Univ.)

Laser tunneling imaging

Tunneling Ionization

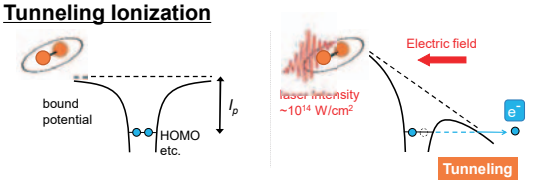

Molecular Orbital Imaging

1. Tunneling ionization rate

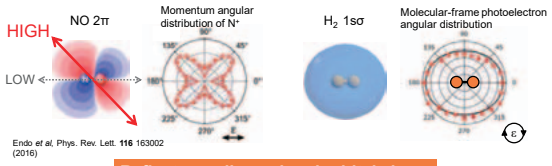

Endo *et al*, Phys. Rev. Lett. **116** 163002 (2016)

Reflect one-dimensional orbital shape

2. Transverse momentum distribution (TMD)

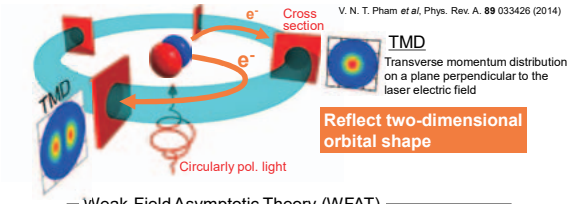

V. N. T. Pham *et al*, Phys. Rev. A. **89** 033426 (2014)

TMD
Transverse momentum distribution on a plane perpendicular to the laser electric field

Reflect two-dimensional orbital shape

Weak-Field Asymptotic Theory (WFAT)

- TMD

$$P(\boldsymbol{p}_\perp) = \Gamma \frac{4\pi\kappa}{F} \exp\left(-\frac{\kappa \boldsymbol{p}_\perp^2}{F}\right)$$

Depends on orbital shape

$\kappa = \sqrt{2I_p}$
I_p : ionization energy
F : laser electric field

This work

1. Tunneling ionization rate
2. Transverse momentum distribution (TMD)

➡ in attempt to image **three-dimensional molecular orbital structure**

Electron-ion coincidence measurement

Three-dimensional momentum imaging

$O_2 \rightarrow O_2^+ + e^- \rightarrow O^+ + O + e^-$: Dissociative ionization process of O_2

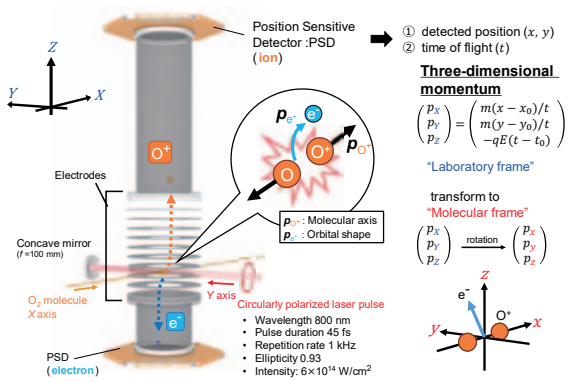

① detected position (x, y)
② time of flight (t)

Three-dimensional momentum

$$\begin{pmatrix} p_x \\ p_y \\ p_z \end{pmatrix} = \begin{pmatrix} m(x-x_0)/t \\ m(y-y_0)/t \\ -qE(t-t_0) \end{pmatrix}$$

"Laboratory frame"

transform to "Molecular frame"

$$\begin{pmatrix} p_x \\ p_y \\ p_z \end{pmatrix} \xrightarrow{\text{rotation}} \begin{pmatrix} p_x \\ p_y \\ p_z \end{pmatrix}$$

Results

Laboratory-frame 3D fragment ion momentum distribution

$O_2 \rightarrow O_2^+ + e^- \rightarrow O^+ + O + e^-$

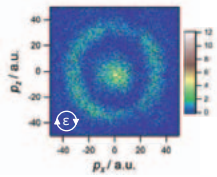

Multiple peaks
→ different dissociative pathways

Peak assignment: H. Liu *et al*., Phys. Rev. A **88**, 061401(R) (2013).

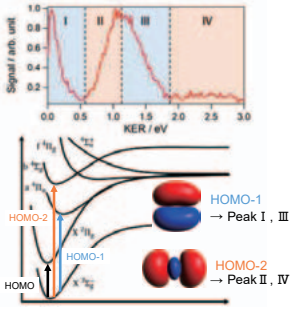

Molecular-frame 3D photoelectron momentum distribution

$O_2 \rightarrow O_2^+ + e^- \rightarrow O^+ + O + e^-$

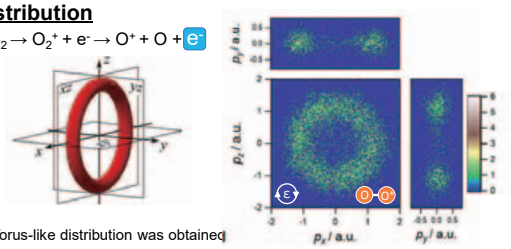

Torus-like distribution was obtained

1. Tunneling ionization rate

Peak Ⅱ (0.6-1.2 eV) Peak Ⅲ (1.2-1.9 eV)

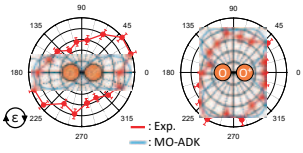

Angular distributions reflected orbital shapes

Simulation of Classical electron trajectory in a circularly pol. field

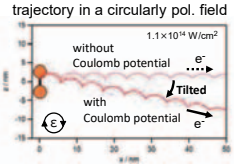

2. Transverse momentum distribution (TMD)

TMDs in Peak Ⅲ

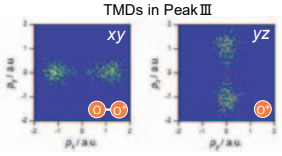

xy: Qualitative agreement with prediction
yz: Nodal structure was not visible

➢ Angular momentum

S. Eckart *et al*., *Nat. Phys.* **14**, 701 (2018).

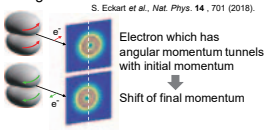

TMDs predicted from MOs

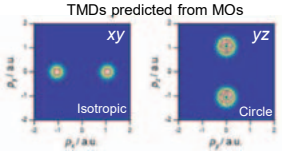

➢ Laser-focus volume

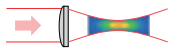

Variation in laser intensity in focal point
↓
broadens longitudinal momentum distribution.

T. Morishita *et al*., *Phys. Rev. A* **75**, 023407 (2007).

Summary

Image three-dimensional orbital of O_2 in intense laser field

1.Tunneling ionization rate
- Reflected orbital shape

2.Transverse momentum distribution
- Obtained transverse momentum distribution from cross section of torus

Outlooks
Visualization of O_2 HOMO

- Promotion of dissociation by second pulse
- Fix molecular axis by alignment

円偏光強レーザー場による水素分子のトンネルイオン化における同位体効果

Isotope effects in tunneling ionization of molecular hydrogen in intense circularly polarized laser fields

○高橋みなみ[1]，藤瀬光香[1]，仲村武瑠[1]，菱川明栄[1,2]
○M. Takahashi[1], H. Fujise[1], T. Nakamura[1], A. Hishikawa[1,2]
1. 名大院理，2. 名大RCMS
1. Grad. Sch. Science, Nagoya U 2. RCMS, Nagoya U

1 BACKGROUND

Tunneling ionization

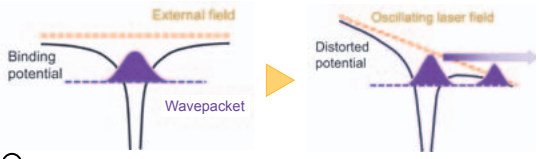

Molecular frame photoelectron angular distribution (MFPAD)

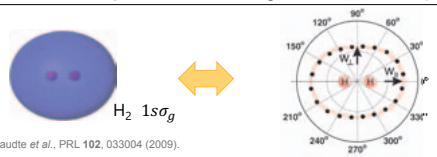

A. Staudte *et al.*, PRL **102**, 033004 (2009).

MFPAD provides molecular structure and ionization rate information.

Theoretical calculation H_2 / D_2

Nuclear mass effect on the tunneling ionization

Rate $H_2 > D_2$ experimental confirmation! X. Wang *et al.*, PRL **117**, 083003 (2016).

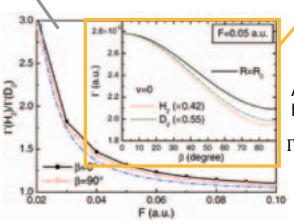

Angular distribution

yet to be known experimentally

Angle between R and F — Internuclear distance — Laser field

$$\Gamma_v(\beta) = \int |G_{00}(R,\beta)|^2 W_{00}(F;R)\chi_{v0}^2(R)\,dR$$

Structure factor — Field factor

O. I Tolstikhin *et al.*, Phys. Rev. A **87**, 041401(R) (2013).

Purpose **Clarify effects of nuclear motion on the angular distribution of ionization rates that reflect molecular orbitals (electron distribution)**

2 METHOD

Electron-ion coincidence method

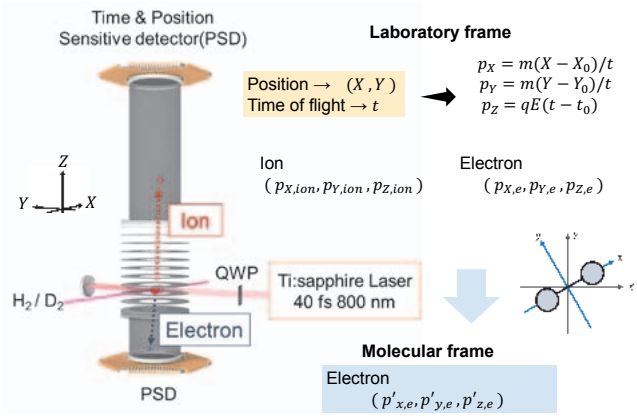

3 RESULTS

H_2 and D_2 in circularly polarized laser fields

$F \sim 0.06$ [a.u.]

Kinetic energy spectrum

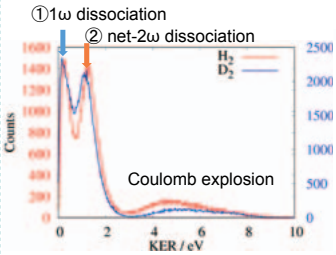

The pathways leading to dissociation

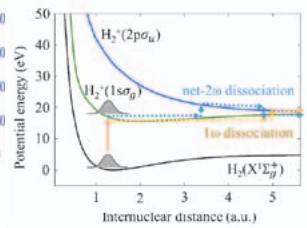

Molecular frame photoelectron momentum distribution (KER<3.0 eV)

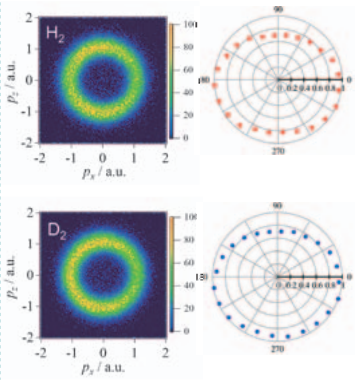

MFPAD (Symmetrized)

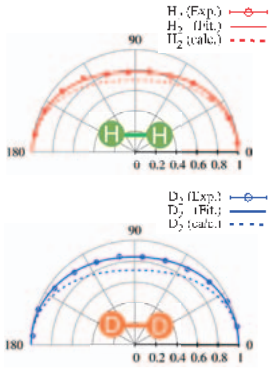

D_2 shows a higher ionization rate in the perpendicular direction

But there is a difference from the calculated value

Orientation dependencies of each KER peak

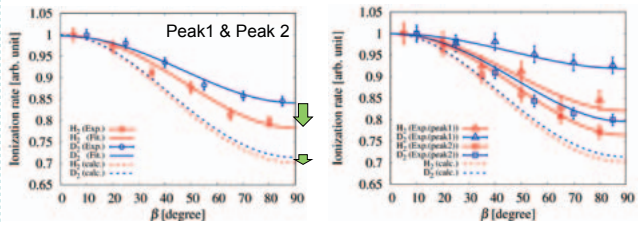

Different orientation dependencies for $\beta = 90°$ and $270°$ and each peak
➡ Influence of correlation between ionization and dissociation processes

J. Wu *et al.*, Nature communications **4**, 2177 (2013).

4 SUMMARY

Measured MFPAD of H_2 / D_2

D_2 has a higher yield in the direction perpendicular to the molecular axis
➡ Agreement with the trend expected from the WFAT

Asymmetry in the angular distribution
➡ Need to reduce the correlation between ionization and dissociation process for accurate reading of MO.

Observation of association reaction of C_6H_{14}/N_2 gas flow system induced by femtosecond laser filament

Kentaro Tani[1], Chiaki Kubo[1], Kasumi Hashigaya[1], Akitaka Matsuda[1], Akiyoshi Hishikawa[1,2]
[1]Department of Chemistry, Nagoya University, [2]Research Center of Materials Science, Nagoya University

Introduction

Unimolecular reactions in intense laser fields

Intense laser field ($\sim 10^{15}$ W/cm^2) ~ Intermolecular Coulombic potential

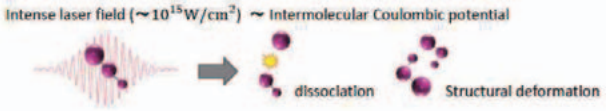

▶ Selective Bond Dissociation

Laser pulse shaping + Closed loop control

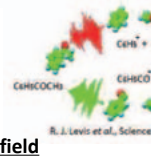

Multimolecular reactions in intense laser field

- $[AuCl_4]^-$ ⟶ Gold nanoparticle
  Behzad Tangeysh, *et al.*, J. Phys. Chem. C **117**, 18719 (2013).
- C_6H_{14} ⟶ C_nH_2 (H-capped polyyne)
  Y. Taguchi *et al.*, Carbon **115**, 169 (2017).

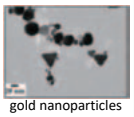
gold nanoparticles

- C_2H_4 ⟶ amorphous carbon
  A. Matsuda *et al.*, Chem. Lett. **46, 1426 (2017).**

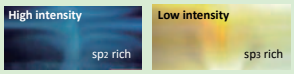

- Hydrogenated **amorphous carbon films** and **nanoparticles** were produced
- Products **depends on laser-field intensity**

C_2H_4 ⟶ $C_2H_3^{*(+)}$, $CH^{*(+)}$, $C_2^{*(+)}$, etc ⟶ ⟶ ⟶ ⟶ Nano particle

Batch reaction ➡ Multiple laser irradiations ➡ Complex reaction process

This work

Observation of association reaction of gaseous C_6H_{14} in intense laser fields

- Laser-field intensity dependence of multimolecular reaction
- Gas flow system ➡ Simplification of reaction

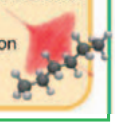

Experiment

Gas flow system

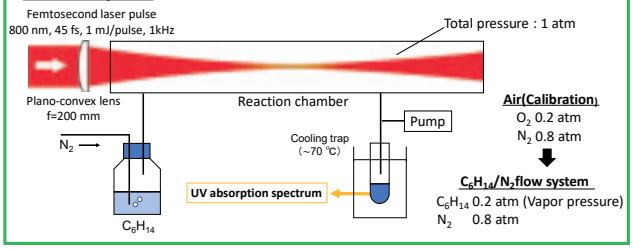

Summary

Laser-field intensity dependence of association reaction of gaseous C_6H_{14}

- ☐ Simplification of reaction by gas flow system
- ☐ Calibration of the laser-field intensity using filament plasma diameter

Nonlinear coefficient (n) about laser-field intensity

➡ Hydrogen capped polyyne ~ Fragmentation of C_6H_{14}

C_6H_{14} ⟶ C_2H_4, C_3H_6 etc ⟶ C_nH_2
C_6H_{14}

Laser field intensity in laser filament

Laser field intensity

$$I = \frac{2E}{\pi d^2 \cdot \tau}$$

E : Input laser energy, τ : Pulse duration,
d : Beam diameter at $1/e^2$

In ultra high vacuum : $d = 4f\lambda/\pi D$

f : Focal length, λ : Laser wavelength, D : Input beam diameter

Laser filamentation

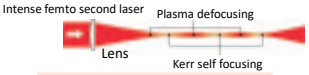

Beam diameter can't be determined in laser filament

Spatial distribution of plasma density

$$Ne(r) = \sigma(I_0 e^{-r^2/d^2})^n \quad \sqrt{n}\text{ times}$$

$$= \sigma {I_0}^n e^{-r^2/(d/\sqrt{n})^2}$$

σ : Cross section of ionization , n : Nonlinear order
d : Beam diameter at $1/e^2$

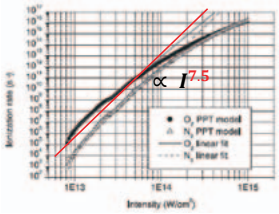

A Tlebpour, *et al.*, Opt Commun. **163**, 29 (1999)

➡ $d_{laser} = \sqrt{7.5}\, d_{plasma}$

S, Xu, *et al.*, Opt Express, **20**, 299(2012)

Plasma diameter mesurement

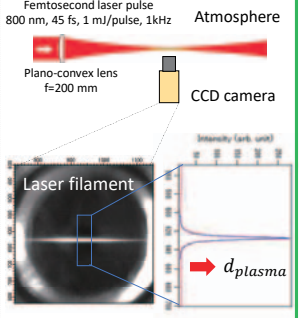

Calibration curve

$$I = 4.9 \times 10^{13}\{1 - \exp(-16E)\}$$

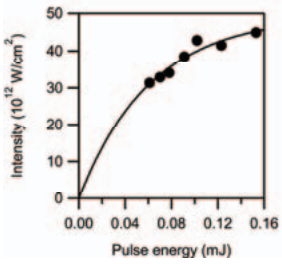

Results and Discussion

Laser-field intensity dependence

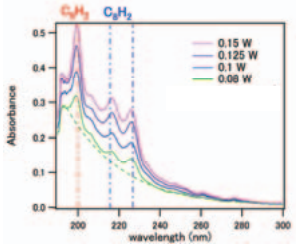

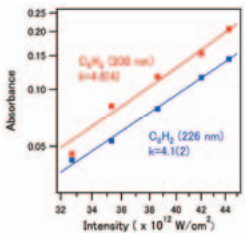

Single molecule dissociation reaction

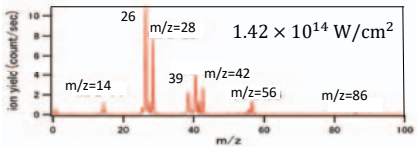

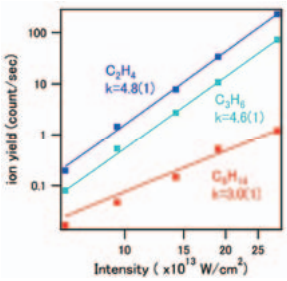

$C_6H_{14} \xrightarrow{5h\nu} C_aH_b, C_cH_d$, etc (fragment)

$[C_aH_b, C_cH_d, \text{etc}] \propto I^5$

Polyyne production process

Collision between fragments

$C_aH_b + C_cH_d +$ etc ⟶ C_nH_2 (polyyne)

$[C_nH_2] \propto I^{5m}$ ➡ disagreement with the result

Collision between fragment and parent

$C_aH_b + C_6H_{14}$ ⟶ C_nH_2 (polyyne)

Pseudo first-order reaction : $[C_6H_{14}]$ = constant

$[C_nH_2] \propto I^5$ ➡ agreement

Asymmetric Coulomb explosion of CH_4 in phase-locked two-color intense laser fields

H. Hasegawa[1], H. Fujise[1], A. Matsuda[1], A. Hishikawa[1,2]
([1]Dept. Chem., Nagoya Univ., [2]RCMS, Nagoya Univ.)

Introduction

Coherent reaction control in intense laser fields

Optimally tailored pulse

Spatial phase modulator + machine learning

R. J. Levis *et al*, Science 295, 709 (2001)
A. Assion *et al*., Science 282, 5390 (1998)

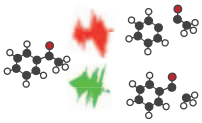

Two-color laser fields

$$E_{\omega}\cos(\omega t) + E_{2\omega}\cos(2\omega t + \Phi) = E_{\omega+2\omega}$$

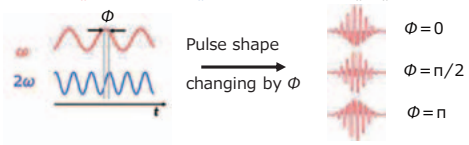

Asymmetry of laser fields altered by phase Φ

Selective breaking of equivalent bonds:

C_2H_2 : Q. Song *et al*., J. Phys. B 48, 094007 (2015)
CO_2 : T. Endo *et al*., Phys. Chem. Chem. Phys. 19, 3550 (2017)

Deformation of the potential energy surfaces
Y. Sato *et al*., J. Am. Chem. Soc. 125, 8019 (2003)
demonstrated with linear molecules

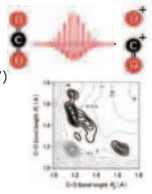

This Work

Tetrahedral molecule: CH_4

Four equivalent C-H bonds

Coulomb explosion processes

(1) $CH_4^{2+} \rightarrow CH_3^+ + H^+$

(2) $CH_4^{2+} \rightarrow CH_2^+ + H_2^+$

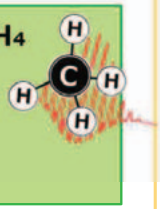

Experiment

Coincidence 3D momentum imaging

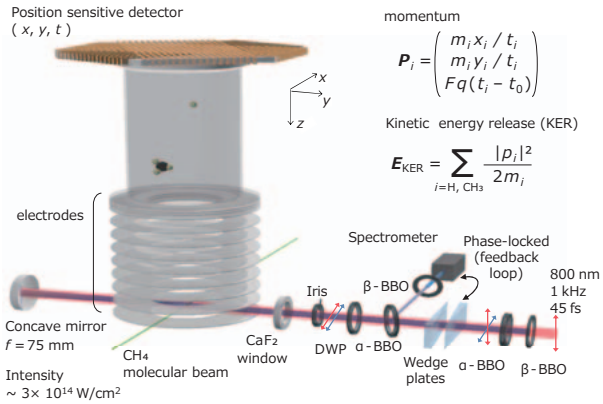

momentum

$$P_i = \begin{pmatrix} m_i x_i / t_i \\ m_i y_i / t_i \\ Fq(t_i - t_0) \end{pmatrix}$$

Kinetic energy release (KER)

$$E_{KER} = \sum_{i=H,\,CH_3} \frac{|p_i|^2}{2m_i}$$

Asymmetry Parameter

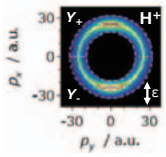

Momentum image

$$A(\Phi) = \frac{Y_+ - Y_-}{Y_+ + Y_-}$$

Energy spectrum

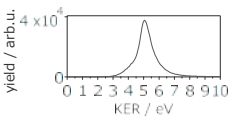

Results and Discussion

(1) $H^+ + CH_3^+$ channel

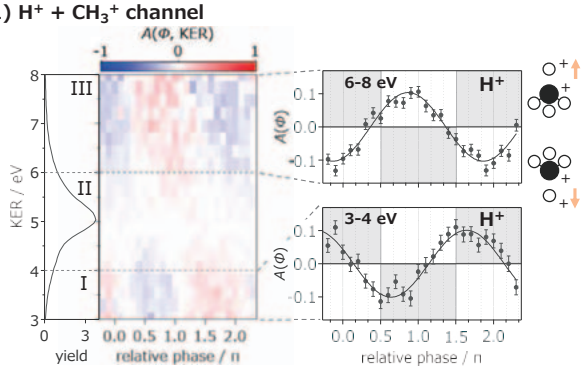

Different relative phase dependence on KER
→ Suggests different dissociation pathways

Fragmentation pathways from CH_4^{2+}

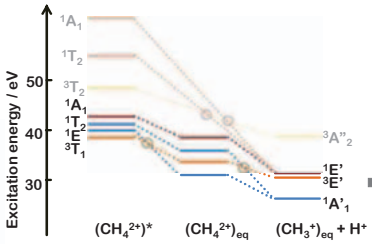

[1] R. Flammini et al., New J. Phys 11, 083006 (2009).

Region III via $^1T_2$ and $^1A_1$
Region I via $^3T_1$ and ^1E

Region I, III : large asymmetry
Direct dissociation from CH_4^{2+} ground and excited states

Region II : small asymmetry
Predissociation from $^3T_1$ to $^1A_1$ → long lifetime[2]

[2]G. Dujardin et al., Phys. Rev. A 31, 5 (1985).

Origin of opposite asymmetry region for I and III

Orientation dependent excitation?
Potential deformation dependent on electronic state?

(2) $H_2^+ + CH_2^+$ channel

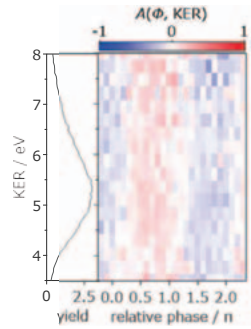

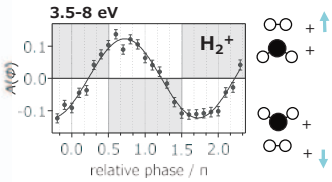

Similar phase dependence to that of Region I of channel (1)

Fragmentation to $H_2^+ + CH_2^+$ via $^1T_2$ state [1]

Summary

Coincidence imaging of Coulomb explosion of CH_4 in phase-locked two-color intense laser fields

(1) $CH_4^{2+} \rightarrow CH_3^+ + H^+$
Different relative phase dependence on KER
→ Suggests different dissociation pathways

(2) $CH_4^{2+} \rightarrow CH_2^+ + H_2^+$
Similar relative phase dependence to that of high KER of (1)

Preparation of Oxide-supported Heterobimetallic Catalysts from Cu-Fe Complex

○Aiko ASAI[1], Satoshi MURATSUGU[1], Mizuki TADA[1,2]

Dept. of Chemistry Nagoya University[1], RCMS and IRCCS, Nagoya University[2], Nagoya, JAPAN

Introduction

Homogeneous catalyst

○Well-defined structure to produce high selectivity

×Aggregation and deactivation

Heterogeneous catalyst

○High activity, isolation and reuse

×Difficult to understand the relationship between active structure and activity due to heterogenity

Supported metal complex catalyst

○One of the preferable heterogeneous systems to understand the relationship between catalytically active structure and reactivity

Ex.) $Ir_2/\gamma\text{-}Al_2O_3$

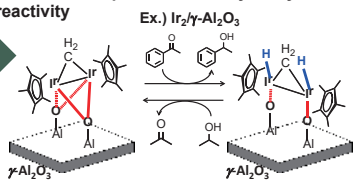

Intermediate structure in the transfer hydrogenation

Homometallic system

S. Muratsugu, et al. *Phys. Chem. Chem. Phys.*, **2012**, *14*, 16023-16031

Purpose

Preparation and catalytic activity of new supported heterobimetalic complex

Ex.) $(NHC)M\text{-}M'Cp(CO)_2$ complex

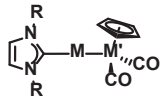

N. P. Mankad, et al. *Organometallics* **2013**, *32*, 3986-3992.

To understand the roles of each metal atom in heterogeneous nature

Preparation of oxide-supported heterobimetallic complex

Bimetallic complex

Ex.) $(IMes)Cu\text{-}FeCp(CO)_2$ (CuFp)

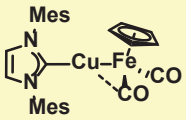

1

- Direct bond between Cu and Fe
- Active for alkyne hydrogenation and benzene borylation

N. P. Mankad, et al. *Organometallics* **2013**, *32*, 3986-3992.

+

Oxide support

Ex.) SiO_2

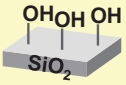

SiO_2, $\gamma\text{-}Al_2O_3$, TiO_2, MgO, $SiO_2\text{-}Al_2O_3$, $K\text{-}Al_2O_3$ (Used after calcination)

- Coordination to metal center

Impregnation

Toluene, r.t. 30 min

Under N_2

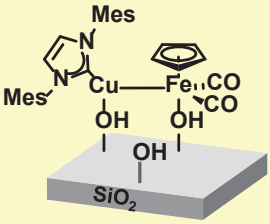

2_SiO_2 (Expected structure)

Characterization of oxide-supported heterobimetallic complex

FT-IR

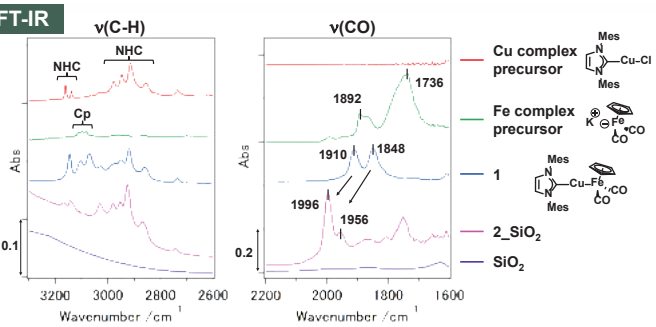

Fe K-edge XANES

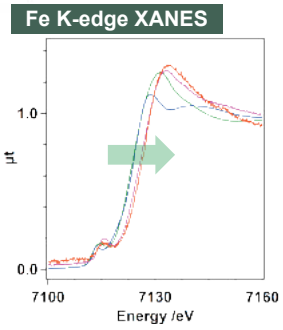

- Fe complex
- 1
- 2_SiO_2
- $2\_K\text{-}Al_2O_3$

After the attachment

(1) NHC was maintained and bridged CO was disappeared. (FT-IR)

(2) Fe was more oxidized than 1. (XANES)

Catalytic reactions on oxide-supported heterobimetallic complex

Diphenylacetylene hydrogenation

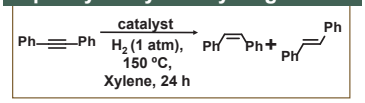

Catalyst	Conv. /%
1	28
2_SiO_2	4
2_TiO_2	0
$2\_\gamma\text{-}Al_2O_3$	20
2_MgO	24
$2\_SiO_2\text{-}Al_2O_3$	69
blank	~ 0

Reaction conditions: Fe(Cu) = 5.0 x 10^{-6} mol, 150 °C, H_2 1 atm, Fe(Cu)/diphenylacetylene = 1/200, 24 h, xylene 5 mL.

Benzene borylation

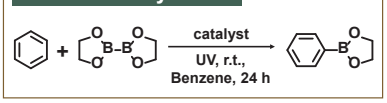

Catalyst	Conv. /%
1	45
2_SiO_2	13
2_TiO_2	30
$2\_\gamma\text{-}Al_2O_3$	26
2_MgO	33
$2\_SiO_2\text{-}Al_2O_3$	0
blank	0

Reaction conditions: Fe(Cu) = 5.0 x 10^{-6} mol, r.t., N_2 1 atm, Fe(Cu)/bis(pinacolato)diboron= 1/25, 24 h, UV: 365 nm, benzene 2 mL.

Xanthene oxidation

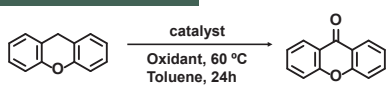

Catalyst	Oxidant	Conv. /%
1	TBHP	40
$2\_K\text{-}Al_2O_3$	TBHP	49
$K\text{-}Al_2O_3$	TBHP	14
blank	TBHP	~ 0
1	H_2O_2	4
$2\_K\text{-}Al_2O_3$	H_2O_2	14
blank	H_2O_2	0

Catalyst	Oxidant	Conv. /%
1	PhIO	~ 0
2_SiO_2	PhIO	6
$2\_K\text{-}Al_2O_3$	PhIO	7
blank	PhIO	~ 0

Reaction conditions: Fe(Cu) = 5.0 x 10^{-6} mol, 60 °C, Fe(Cu)/xanthene/oxidant= 1/50/25, 24 h, Toluene 5 mL.

Summary

- Supported heterobimetallic complex catalysts were prepared by the impregnation of $(IMes)Cu\text{-}FeCp(CO)_2$ (CuFp, 1) on several oxide supports (SiO_2, $\gamma\text{-}Al_2O_3$, TiO_2, $SiO_2\text{-}Al_2O_3$, MgO, $K\text{-}Al_2O_3$).
- After the attachment of 1 on SiO_2 (2_SiO_2), it was suggested that NHC ligand was maintained and bridged CO was disappeared from FT-IR, and that Fe was oxidized from Fe K-edge XANES.
- Catalytic performances (diphenylacetylene hydrogenation, benzene borylation, and xanthene oxidation) on the prepared supported heterobimetallic complexes (2_support) were investigated.

Preparation and Catalytic Oxidation Performance of Rutile Type IrO_2 Nanoparticles

○Takatoshi SUDOH[1], Satoru IKEMOTO[1], Satoshi MURATSUGU[1,2], Mizuki TADA[1,3]
Dept. of Chemistry Nagoya University[1], JST PRESTO[2], RCMS and IRCCS, Nagoya University[3], Nagoya, JAPAN

Introduction and Purpose

Rutile type Iridium dioxide (IrO_2)

(110) surface of rutile type IrO_2:
C-H bond activation at very low temperature
Methane oxidation (-172 °C) [1], [2]
Cyclohexane oxidation (-88 °C) [3]
Oxidation of nitric oxide (NO) (r.t.) [4]

Only from surface chemistry[1], [3] and theoretical chemistry[2],[4] fields
No application as real catalysts

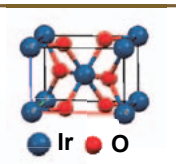

An image for C-H activation on IrO_2(110) surface [2]

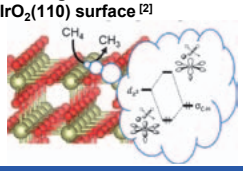

Purpose: Preparation of rutile type IrO_2 nanoparticles with (110) surface and its application as catalysts

[1] Z. Liang. *et al. Science.* **2017**, 356, 299-303. [2] Y. Tsuji. *et al. J. Phys. Chem. C* **2018**, 122, 15359-15381.
[3] Martin, R. et al. *Phys. Chem. Chem. Phys.* **2018**, 20, 29264. [4] Yuan, H. et al. *ACS Catal.* **2018**, 8, 10864−10870.

Preparation of IrO_2 nanoparticle

$Ir(CH_3COO)_3$ + carboxylic acid
↓ H_2O, stirred
↓ calcination
IrO_2 nanoparticle

Characterization of IrO_2 nanoparticle

XRD

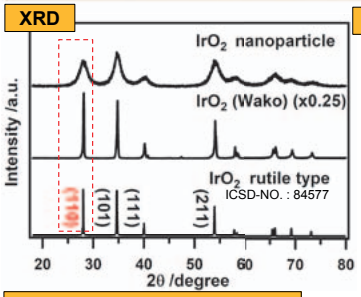

TEM

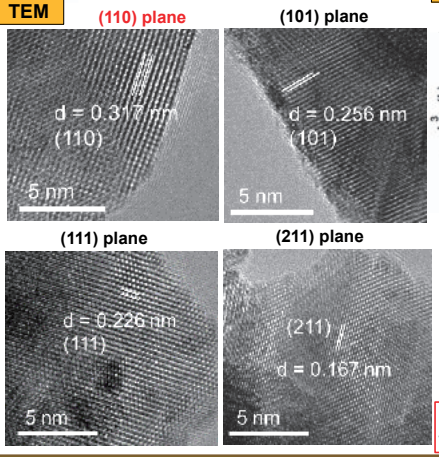

Ir L_{III}-edge EXAFS

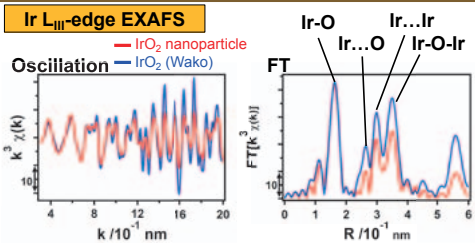

BET and estimated particle size

	Specific surface area (m^2g^{-1})	Particle size (nm)
IrO_2 nanoparticle	21.5	24
IrO_2 (Wako)	0.02	2.6×10^5

XRD: pure rutile type structure and broad peak pattern
particle size : 27 nm from Scherrer's equation
TEM: confirmation of (110) plane
average size: ~20 nm
BET: specific surface area: 21.5 m^2g^{-1}
estimated average particle size: 24 nm
Ir L_{III}-edge EXAFS: smaller Ir…O, Ir…Ir, and Ir-O-Ir contributions
→ smaller size than bulk IrO_2

▪ Rutile type IrO_2 nanoparticles with (110) surface were successfully prepared and characterized.

Catalytic reactions of rutile type IrO_2 nanoparticle

Methane oxidation with O_2

$$CH_4 + 2O_2 \xrightarrow{IrO_2} CO_2 + 2H_2O \quad (\Delta H_{298} = -802\ kJmol^{-1})$$
$$CH_4 + 1/2O_2 \longrightarrow CO + 2H_2 \quad (\Delta H_{298} = -36\ kJmol^{-1})$$

Pretreatment conditions
- Flow gas : He = 100 mL min^{-1}
- Pretreatment temp. : 1) 25-300 °C, 5 °C min^{-1}, 2) 300 °C, 2 h

Reaction conditions
- Reaction gas : $CH_4/O_2/N_2/He$ = 20/10/3/67 (total flow rate = 100 mL min^{-1})
- Reaction temp. : 1) 25-700 °C, 5 °C min^{-1}, 2) 200, 300 °C, 30 min, 3) 500, 700 °C, 10 min
- Amount of Catalyst : 200 mg

Schematic image for flow reactor

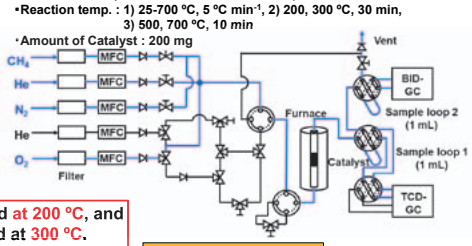

Catalytic activity on IrO_2 nanoparticle

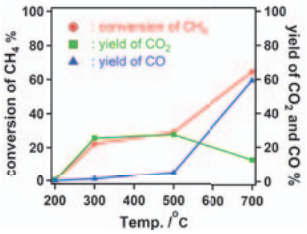

Comparison with bulk IrO_2 (Wako)

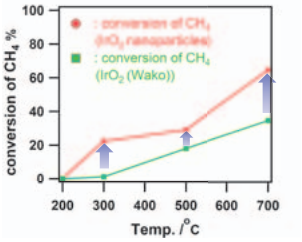

- CO_2 was formed at 200 °C, and CO was emerged at 300 °C.
- IrO_2 nanoparticles showed higher activity than bulk IrO_2 (Wako).

Xanthene oxidation with O_2

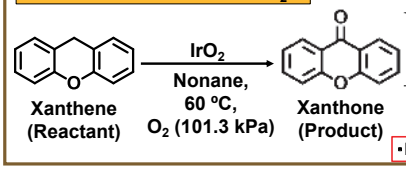

Catalyst	Conversion %	Selectivity %	Mass balance
IrO_2 nanoparticle	82.3	100	0.98
IrO_2 (Wako)	4.8	100	0.98
Blank	4.8	100	1.00

Reaction conditions: IrO_2 (75 mg (0.34 mmol)), Xanthene (0.375 mmol), nonane (1.5 mL), IrO_2/xanthene/dodecane (IS) = 1/25/12.5 (molar ratio), 60 °C, 101.3 kPa of O_2, 24 h.

Conversion-Time plot

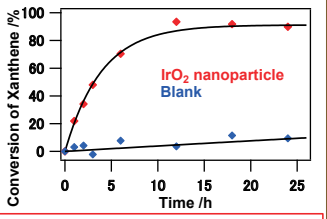

▪ IrO_2 nanoparticles also exhibited higher activity on the xanthene oxidation with O_2 than bulk IrO_2 (Wako).

Conclusions

▪ We succeeded in preparing pure rutile type IrO_2 nanoparticles with (110) planes (ca. 20 nm), which were characterized by XRD, TEM, BET, and Ir L_{III}-edge EXAFS.
▪ The prepared IrO_2 nanoparticles exhibited higher catalytic activity to methane oxidation in gas phase and xanthene oxidation in liquid phase with O_2 than bulk IrO_2.

N_2 Activation by the Fe Sites of Cubane-type $[Mo_3S_4Fe]$ Clusters Supported by Cp Ligands

(Nagoya Univ,[1] Daido Univ,[2] Hawaii Univ[3])
○Kenichiro. Munakata,[1] Keisuke. Uchida,[1] Ryota. Hara,[1] Mami. Kachi,[1] Mizuki. Tada,[1]
Tsutomu. Takayama,[2] Yoichi. Sakai,[2] Roger. E. Cramer,[3] Yasuhiro. Ohki[1]

Introduction

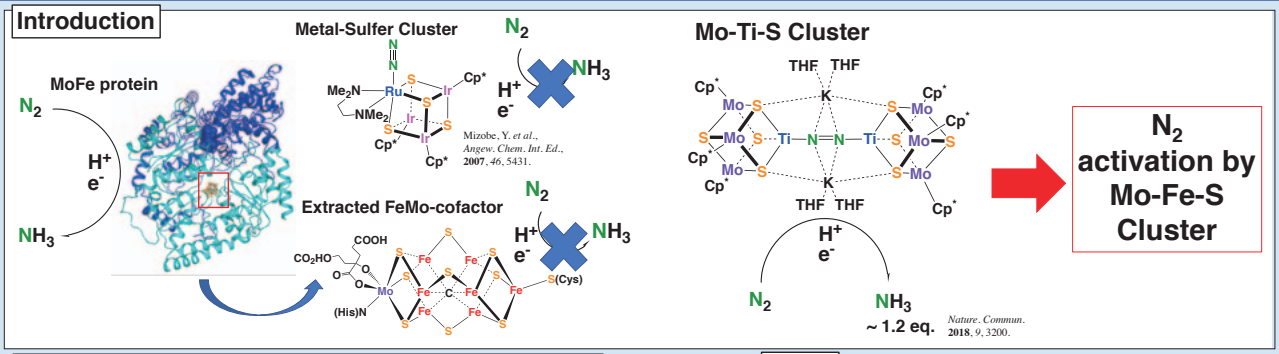

Synthesis and Characterization of Mo-Fe-S clusters

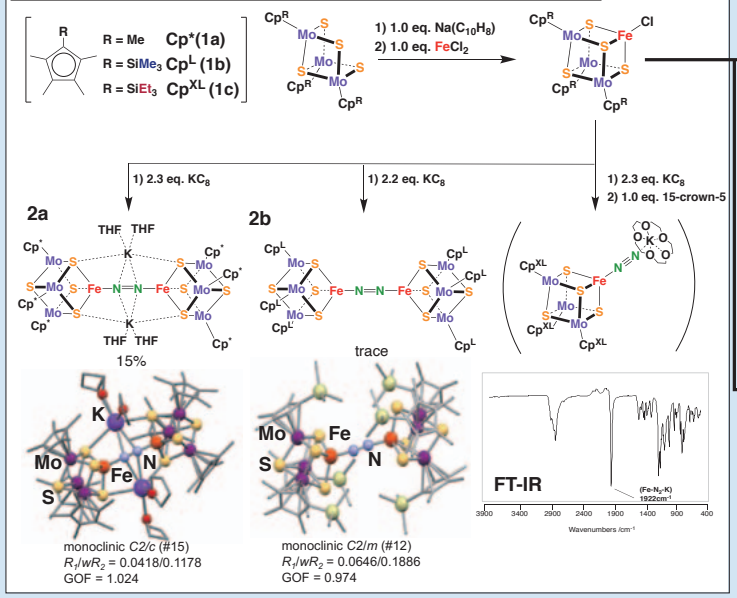

X-ray

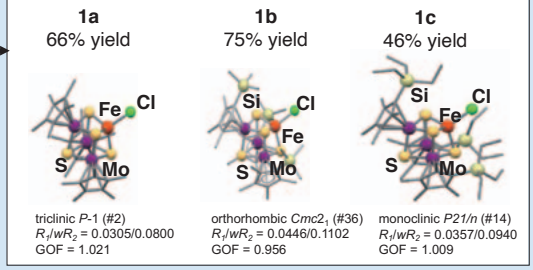

Cyclic Voltammetry

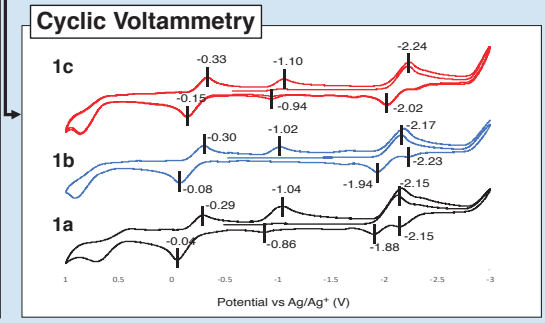

Catalytic Silylation of N_2 by Mo-Fe-S clusters

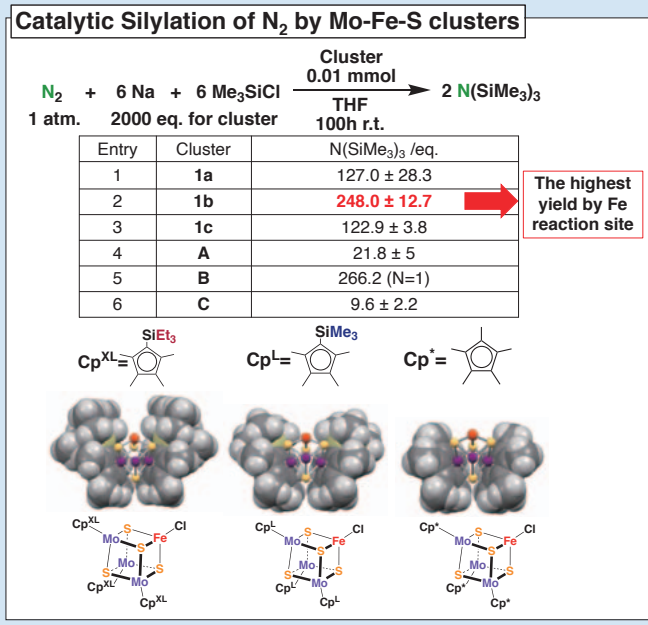

Entry	Cluster	$N(SiMe_3)_3$ /eq.
1	1a	127.0 ± 28.3
2	1b	248.0 ± 12.7
3	1c	122.9 ± 3.8
4	A	21.8 ± 5
5	B	266.2 (N=1)
6	C	9.6 ± 2.2

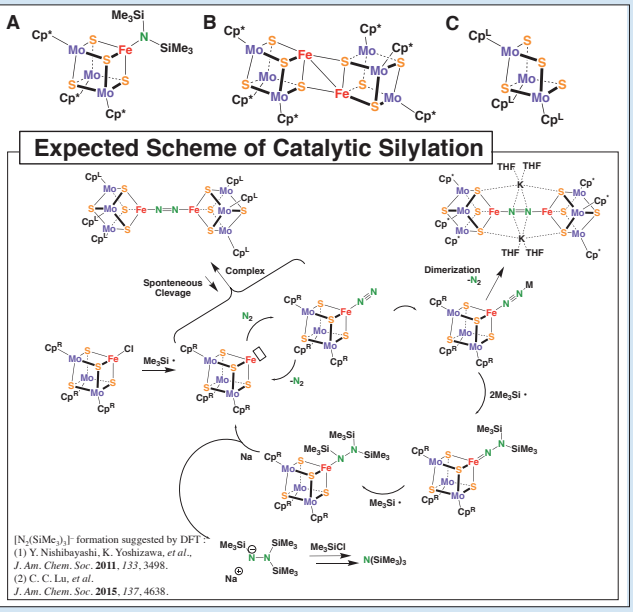

Direct monitoring of gas coordination-adsorption on MOFs with an in situ XAFS system

Hirotoshi Sakamoto, Akihiro Hori, Hirosuke Matsui, Ryotaro Matsuda, Mizuki Tada

Research Center for Materials Science, Nagoya University, Nagoya 464-8602, Japan
Graduate School of Science, Nagoya University, Nagoya 464-8602, Japan
Graduate School of Engineering, Nagoya University, Nagoya 464-8603, Japan

E-mail: sakamotoh@nagoya-u.jp

Backgrounds

MOF for Gas Separation

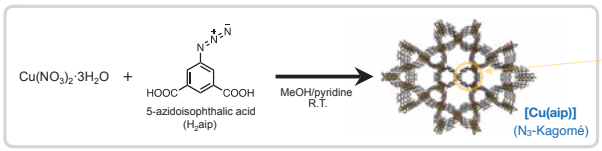

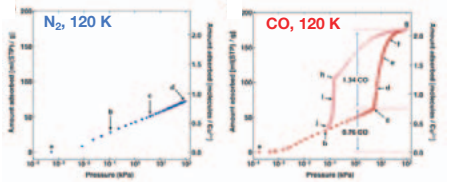

Selective Adsorption of CO over N_2

H. Sato, R. Matsuda, S. Kitagawa *et al. Science*, **2014**, *343*, 167-170

Self-Accelerating Adsorption Process

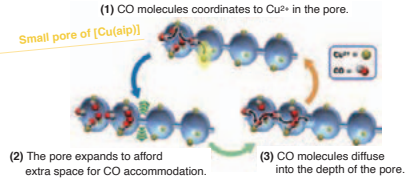

Coordination Environment of Cu^{2+}

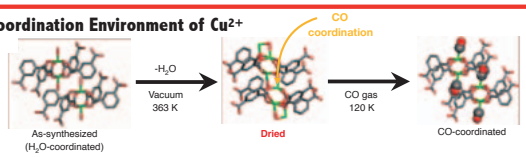

Direct information about the chemical state of Cu in [Cu(aip)]: ***Unavailable***

Objective: In-situ Monitoring of Cu^{2+} Coordination Environment during the Gas Adsorption Process by XAFS

Construction of an In-situ Gas Adsorption-XAFS Measurement System

Cell Design

- *Path for gas*
- *Heating*
- *Attached to the cold head*

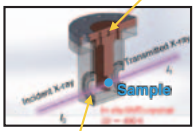

- *X-ray-transparent window*
- *Inside: gas tight for pressure control*

Prototype Cell

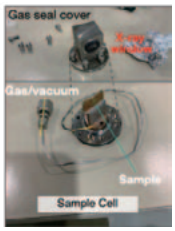

Attached on a Cryostat

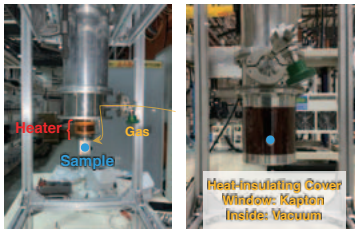

Whole System Setup

(at BL11S2/AichiSR: Hard X-ray XAFS)

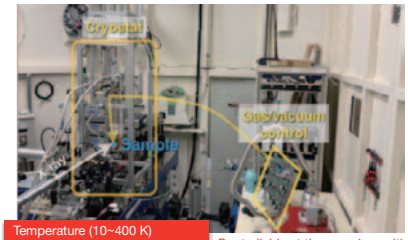

Temperature (10~400 K)
Gas pressure (vacuum~100 kPa)

Controllable at the sample position

Experiments, Results and Discussion

Dehydration Process (Temp. control)

[Cu(aip)(H_2O)] as-synthesized
298 K —Vacuum→ 373 K —Vacuum→ 298 K —Vacuum→ 130 K

CO Gas Introduction (Gas pressure control)

[Cu(aip)] dehydrated
130 K → CO 100 kPa, 120 K → CO 100 kPa, 82 K → CO 100 kPa, 130 K

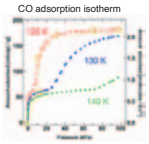

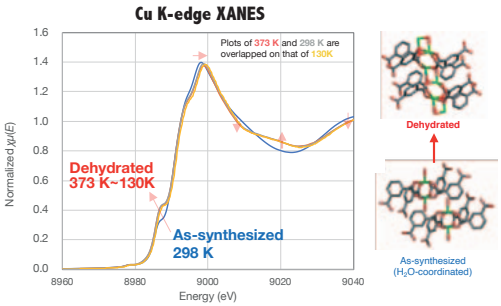

Distinct changes due to the change of the coordination mode of Cu^{2+} in [Cu(aip)]

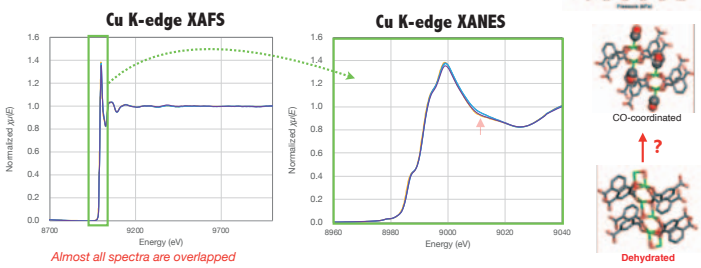

Almost all spectra are overlapped

Much smaller changes than those of the dehydration process

- *Small difference of chemical state between Cu…(CO) and Cu…(O of COO^-)?*
  ➡ EXAFS analysis, Theoretical calculation
- *CO molecules have not diffuse into the pore sufficiently?*
  ➡ In-situ XRD, Machine accuracy improvement

Ligand-promoted PtNi Nanoparticles in Hollow Porous Carbon Spheres as Highly Active and Stable Oxygen Reduction Reaction Catalysts

○ Gabor Samjeské §, Xian-Kai Wan §, Satoshi Muratsugu §, Hirosuke Matsui §, Mizuki Tada §

§ Department of Chemistry, Graduate School of Science, Nagoya University

Objective

- ❑ Pt-based electro-catalysts for the oxygen reduction reaction (ORR) as cathode catalysts in polymer electrolyte fuel cells (PEFC) are still hampered by
  - Sluggish reaction kinetics
  - Low durability
  - High cost
- ❑ Ultra-fine, homogeneously distributed Pt-alloys in the form of ultrafine nano-particles (NP) or wires are the most promising approach to overcome those key-issues
  - Improved catalyst – support interaction → Increased stability
  - Maximum surface to bulk atom ratio → Increased Pt utilization
  - Alloying with 3d-transition metals → Increased catalytic activity
- ❑ Ligand-protection to achieve mono-dispersity but NP agglomeration unavoidable
- ❑ Second, additional protection mechanism: Pore-confinement in hollow porous carbon spheres (HPCS) as carbon support material

Synthesis

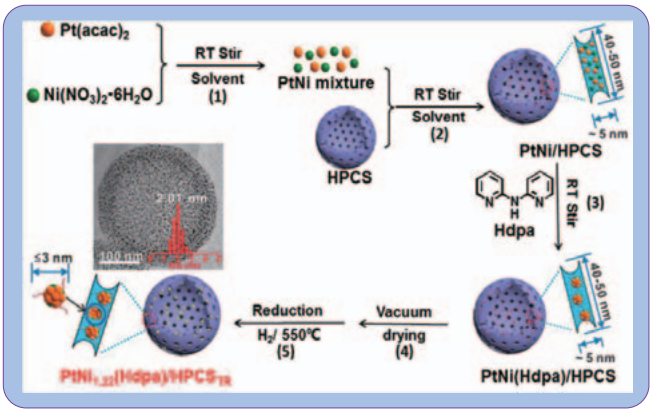

Electrochemical Characterization

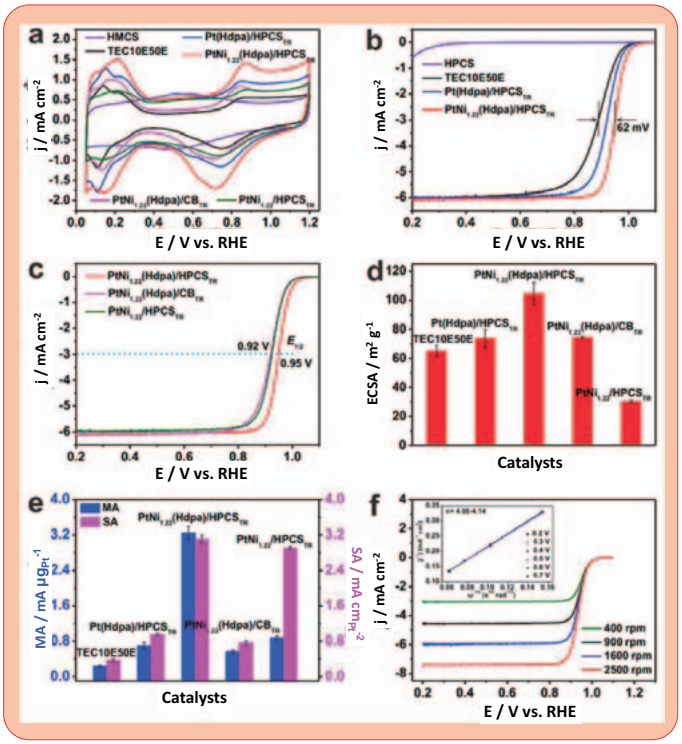

Structure

a) TEM b) HAADF-STEM images of $PtNi_{1.22}$(Hdpa)/HPCS) c) XRD

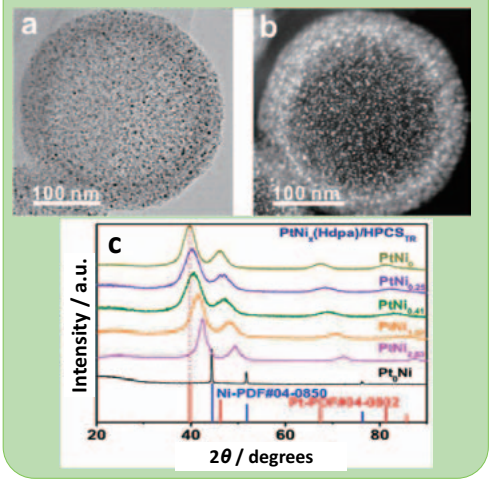

ORR activity for different catalysts

Catalysts	ECSA (m^2/g_{Pt})	I_k(0.9V) (mA/cm^2)	MA ($mA/\mu g_{Pt}$)	SA (mA/cm^2_{Pt})
TEC10E50E	65.19 ± 3.64	4.48 ± 0.00	0.24 ± 0.02	0.37 ± 0.03
Pt(Hdpa)/$HPCS_{TR}$	73.58 ± 6.21	14.62 ± 1.66	0.70 ± 0.08	0.95 ± 0.03
$PtNi_{1.22}$(Hdpa)/$HPCS_{TR}$	104.65 ± 7.81	59.27 ± 2.65	3.25 ± 0.14	3.11 ± 0.09
$PtNi_{1.22}$(Hdpa)/CB_{TR}	74.42 ± 0.52	10.60 ± 0.73	0.57 ± 0.03	0.76 ± 0.05
$PtNi_{1.22}$/$HPCS_{TR}$	30.31 ± 1.19	17.56 ± 0.85	0.88 ± 0.04	2.91 ± 0.03

Durability (Accelerated Durability Test)

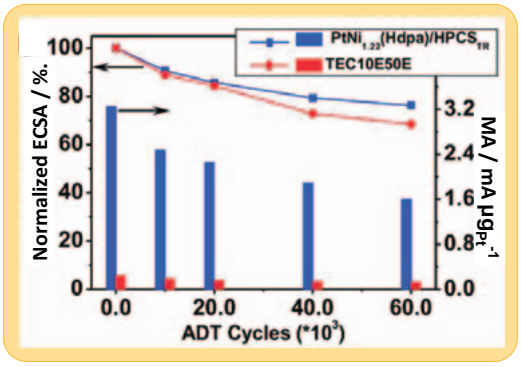

Conclusions

- ✓ *Combining ligand-protection with hollow porous carbon spheres lead to homogeneously distributed ultra-fine PtNi NP with high catalytic activity and stability*
- ✓ *Maximum activity was found for $PtNi_{1.22}$(Hdpa)/HPCS with one magnitude higher mass activity than reference Pt/C (TEC10E50E)*
- ✓ *The similar 13 times higher mass activity as also larger ECSA was observed after 60000 ADT cycles indicating very good durability of $PtNi_{1.22}$(Hdpa)/HPCS*

Topological molecular nanocarbons: all-benzene catenane and trefoil knot

Motonobu Kuwayama[1], Yasutomo Segawa[1,2,*], Yuh Hijikata[2,3,4], Masako Fushimi[1,2], Taishi Nishihara[1,2,5], Jenny Pirillo[3,4], Junya Shirasaki[1], Natsumi Kubota[2], Kenichiro Itami[1,2,3,*]

[1] JST-ERATO, Itami Molecular Nanocarbon Project, Chikusa, Nagoya 464-8602, Japan.
[2] Graduate School of Science, Nagoya University, Chikusa, Nagoya 464-8602, Japan.
[3] Institute of Transformative Bio-Molecules (WPI-ITbM), Nagoya University, Chikusa, Nagoya 464-8602, Japan.
[4] Institute for Chemical Reaction Design and Discovery (WPI-ICReDD), Hokkaido University, Sapporo, Hokkaido 001-0021, Japan
[5] Institute of Advanced Energy, Kyoto University, Uji, Kyoto 611-0011, Japan

ABSTRACT

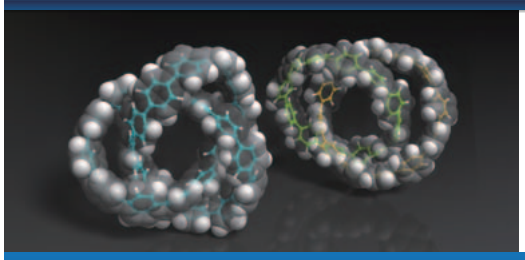

The generation of topologically complex nanocarbons can spur developments in science and technology. However, conventional synthetic routes to interlocked molecules require heteroatoms. We report the synthesis of catenanes and a molecular trefoil knot consisting solely of *para*-connected benzene rings. Characteristic fluorescence of a heterocatenane associated with fast energy transfer between two rings was observed, and the topological chirality of the all-benzene knot was confirmed by enantiomer separation and circular dichroism spectroscopy. The seemingly rigid all-benzene knot has rapid vortex-like motion in solution even at –95 °C, resulting in averaged nuclear magnetic resonance signals for all hydrogen atoms. This interesting dynamic behavior of the knot was theoretically predicted and could stimulate deeper understanding and applications of these previously untapped classes of topological molecular nanocarbons.

Y. Segawa, M. Kuwayama, Y. Hijikata, M. Fushimi, T. Nishihara, J. Pirillo, J. Shirasaki, N. Kubota, K. Itami, *Science* **2019**, *365*, 272-276.

RESULTS and DISCUSSION

1. Topological molecular nanocarbons

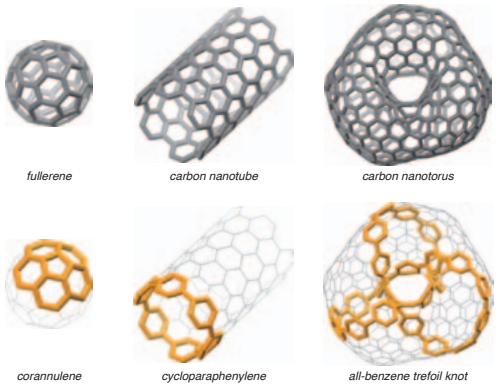

2. Conventional synthesis of catenanes

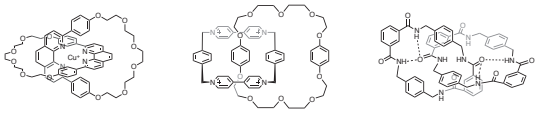

C. J. Bruns, J. F. Stoddart, *The Nature of the Mechanical Bond: From Molecules to Machines*, *Wiley-VCH, Weinheim*, **2016**.

Synthesis of catenanes requires coordinating / polar functional groups.

3. Synthetic strategy for all-benzene catenane and knot

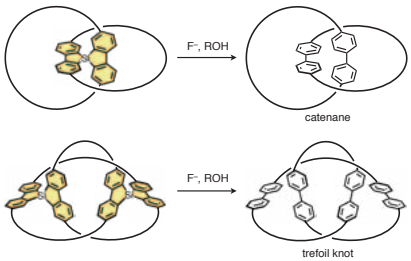

Lenormand, H.; Goddard, J.; Fensterbank, L. *Org. Lett.* **2013**, *15*, 748.

4. Synthesis of all-benzene catenane and knot

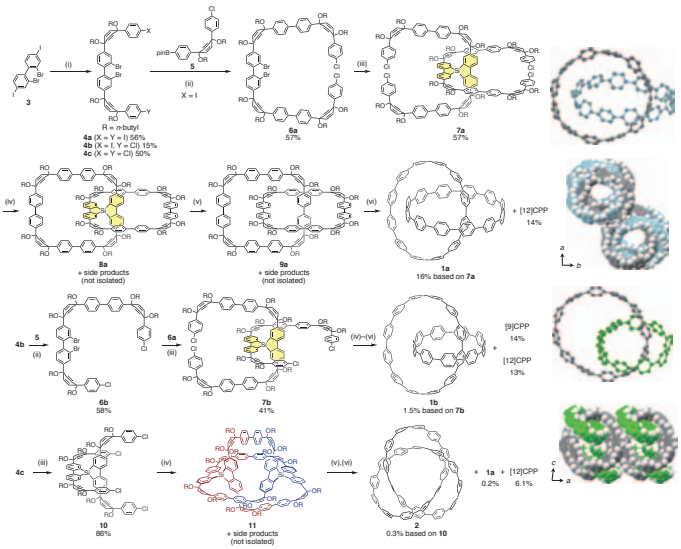

(i) 4 steps. (ii) catalytic $Pd(PPh_3)_4$, K_2CO_3, toluene/EtOH/water or THF/DMF/water, reflux. (iii) *n*-BuLi; then TMEDA, $SiHCl_3$, THF/Et_2O. (iv) $Ni(cod)_2$, 2,2'-bipyridyl, DMF. (v) *n*-Bu_4NF, THF/EtOH. (vi) Sodium naphthalenide, THF; then I_2. Abbreviations: THF = tetrahydrofuran, cod = 1,5-cyclooctadiene, DMF = *N,N*-dimethylformamide, TMEDA = *N,N,N',N'*-tetramethylethylenediamine, Bpin = 4,4,5,5-tetramethyl-1,3,2-dioxaborolan-2-yl.

5. Properties of all-benzene knot

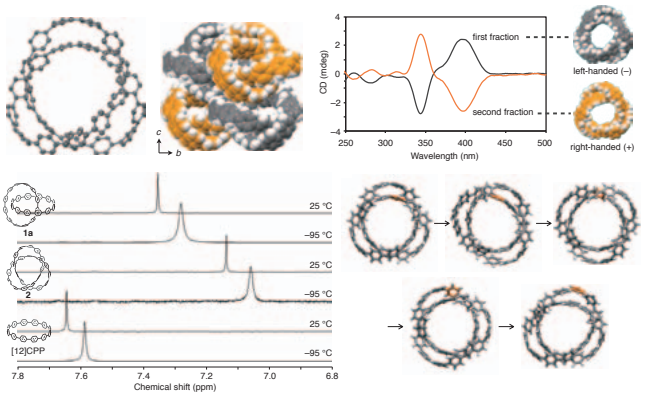

Synthesis of a Zigzag Type Carbon Nanobelt

Kwan Yin Cheung[1] Yasutomo Segawa[2,3,*], Kenichiro Itami[1,2,3,*]

[1] Institute of Transformative Bio-Molecules (WPI-ITbM), Nagoya University, Chikusa, Nagoya 464-8602, Japan.
[2] JST-ERATO, Itami Molecular Nanocarbon Project, Chikusa, Nagoya 464-8602, Japan.
[3] Graduate School of Science, Nagoya University, Chikusa, Nagoya 464-8602, Japan.

INTRODUCTION

Carbon nanobelts, the fully fused polyaromatic hydrocarbons resembling sidewall segment of carbon nanotubes, are gaining much attention recently since the synthesis of the first carbon nanobelt in 2017.[1] Similar to carbon nanotube, carbon nanobelt can be classified into three classes such as armchair, chiral, and zigzag types according to their sidewall structures. Until now, only armchair[2] and chiral[3] type carbon nanobelts were reported while zigzag type carbon nanobelt remains a challenging synthetic target.[4]

Herein we report the synthesis of the first zigzag type carbon nanobelt. The synthesis involves an iterative Diels–Alder reaction sequence followed by reductive aromatization reactions. Being a benzannulated [18]cyclacene with fully benzenoid structure, this zigzag nanobelt is isolated as a stable compound, in stark contrast to the still elusive parent cyclacenes. The structure of this nanobelt is fully characterized by X-ray crystallography and its photophysical properties elucidated by UV-vis absorption and fluorescence spectroscopy.

RESULTS and DISCUSSION

- ***Structures of different types of carbon nanobelts and their synthetic strategies***

Reported:

(a) armchair carbon nanobelt (2017)

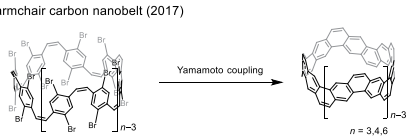

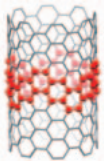

Armchair Carbon Nanotube

(b) chiral carbon nanobelt (2019)

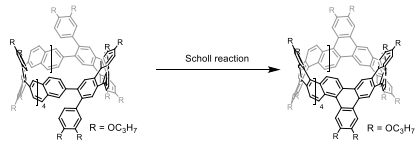

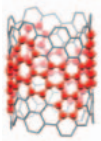

Chiral Carbon Nanotube

This work:

zigzag carbon nanobelt

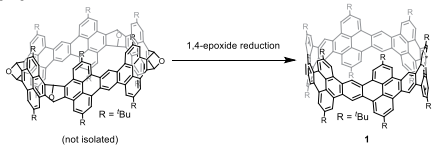

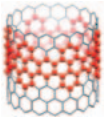

Zigzag Carbon Nanotube

- ***Molecular design of the target zigzag-type nanobelt***

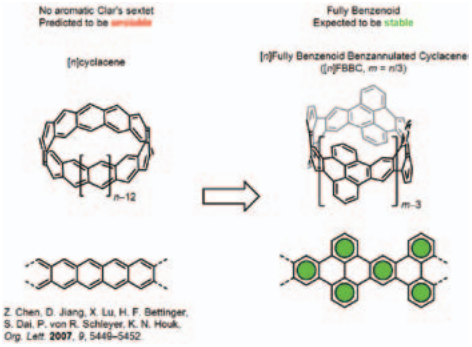

- ***Photophysical Properties***

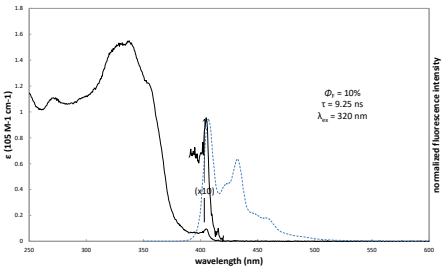

- ***Synthesis and crystal structure***

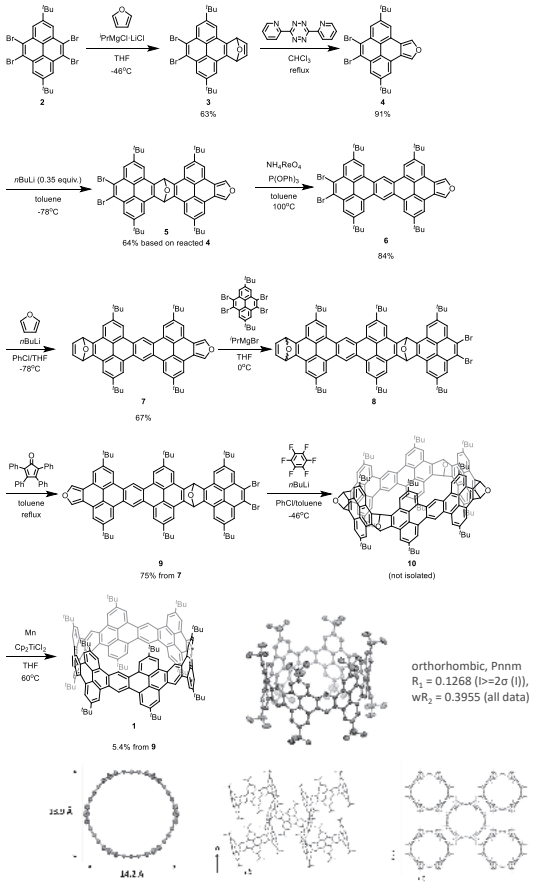

orthorhombic, Pnnm
R_1 = 0.1268 (I>=2σ (I)),
wR_2 = 0.3955 (all data)

- ***Structural analysis***

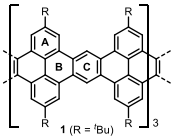

1 (R = tBu)
[18]FBBC (R = H)

	NICS(0) (calculated for [18]FBBC)	HOMA (x-ray)
ring A:	-7.54	0.92
ring B:	0.99	0.23
ring C	-7.44	0.87

- Aromaticity analysis supports a fully benzenoid structure

- ***Reference***

(1) G. Povie, Y. Segawa, T. Nishihara, Y. Miyauchi, K. Itami, *Science* **2017**, *356*, 172.
(2) G. Povie, Y. Segawa, T. Nishihara, Y. Miyauchi, K. Itami, *J. Am. Chem. Soc.* **2018**, *140*, 10054.
(3) K. Y. Cheung, S. Gui, C. Deng, H. Liang, Z. Xia, Z. Liu, L. Chi, Q. Miao, *Chem* **2019**, *5*, 838.
(4) R. Gleiter, B. Esser, S. C. Kornmayer, *Acc. Chem. Res.* **2009**, *42*, 1108.

Synthesis of cycloiptycenes from carbon nanobelt

Hiroki Shudo,[1] Motonobu Kuwayama,[2,3] Yasutomo Segawa,[1,2] Kenichiro Itami[1,2,3]

[1]Graduate School of Science, Nagoya University, Japan
[2]JST-ERATO, Itami Molecular Nanocarbon Project, Nagoya University, Japan
[3]Institute of Transformative Bio-Molecules (WPI-ITbM), Nagoya University, Japan

ABSTRACT

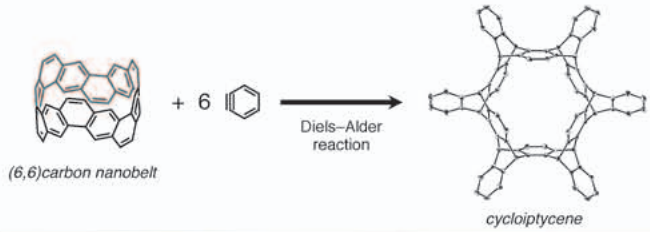

(6,6)Carbon nanobelt ((6,6)CNB), the fully fused belt-shaped aromatic hydrocarbon, can be considered as the precursor for novel carbon nanostructures. Herein we report the first synthesis of pristine cycloiptycene via the Diels–Alder reaction of (6,6)CNB with arynes. The structures of thus-formed cycloiptycenes were confirmed by X-ray crystallography. DFT calculation indicated that gradual releasing of the strain energy of CNB promotes the Diels-Alder reaction.

DISCUSSION

1. Background: Iptycenes

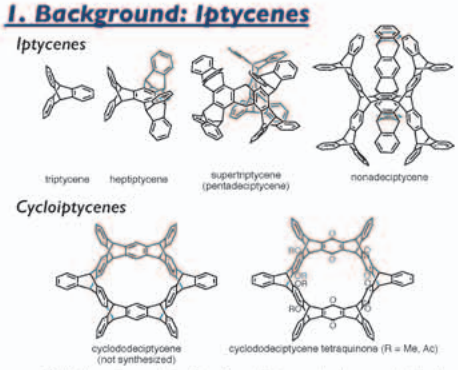

Only the quinone derivative of cycloiptycene has been synthesized.

Review of iptycenes: Y.-X. Ma, Z. Meng, C.-F. Chen, *Synlett* **2015**, *26*, 6.
Cycloiptycene: K. Lou, A. M. Prior, B. Wiredu, J. Desper, D. H. Hua, *J. Am. Chem. Soc.* **2010**, *132*, 17635.

2. Synthetic strategy of cycloiptycene

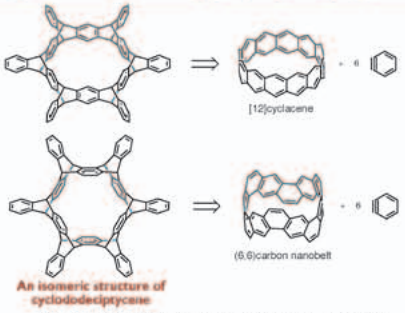

Carbon nanobelt is a potential precursor of cyclopitycenes

(6,6)Carbon nanobelt: G. Povie, Y. Segawa, T. Nishihara, Y. Miyauchi, K. Itami, *Science* **2017**, *356*, 172.

3. Diels–Alder Reaction

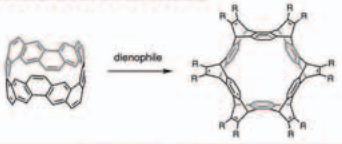

dienophile	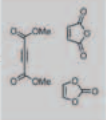			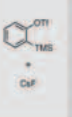	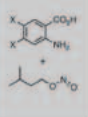
conditions	neat 200 °C 3 days	o-dichlorobenzene 180 °C 5 days	neat 200 °C 3 days	$MeCN/C_2H_4Cl_2$ 100 °C 7 days	$THF/C_2H_4Cl_2$ 85 °C 7 days
result	not detected	n = 1,2 adducts detected	27%	11%	X = H: 13% X = OMe: 18%

4. X-ray crystal structures of cycloiptycenes

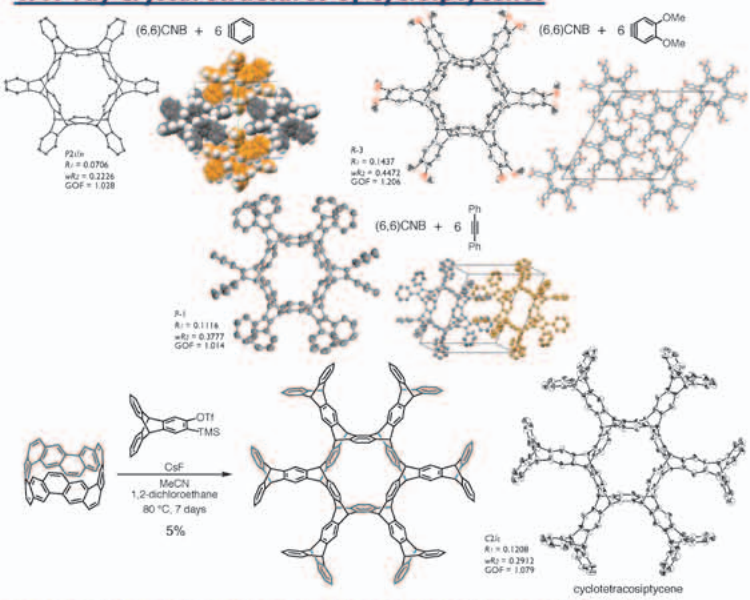

5. Analysis of reaction pathways by DFT calculation

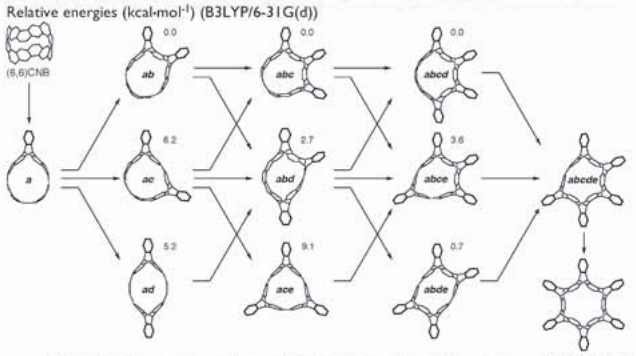

Relationship between reaction position and the number of Clar sextets

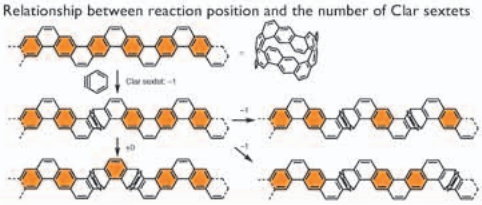

Synthesis of negatively curved polyaromatics by octagon-forming annulative coupling

Satoshi Matsubara,[1] Yoshito Koga,[1] Kei Murakami[1,2] and Kenichiro Itami[1,2,3]
[1]Graduate School of Science, Nagoya University, Chikusa, Nagoya 464-8602, Japan.
[2]Institute of Transformative Bio-Molecules (WPI-ITbM), Nagoya University
[3]JST, ERATO, Itami Molecular Nanocarbon Project, Nagoya University

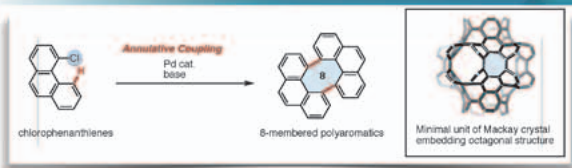

Development of new synthetic methodology for connecting aromatics has been regarded as an important issue in order to pursue functions of polyaromatics depending on their structure. Herein, we report the synthesis of Mackay crystal subunit via palladium-catalyzed annulative coupling *bay*-chlorinated polyaromatics.

Discussions

1) Concept

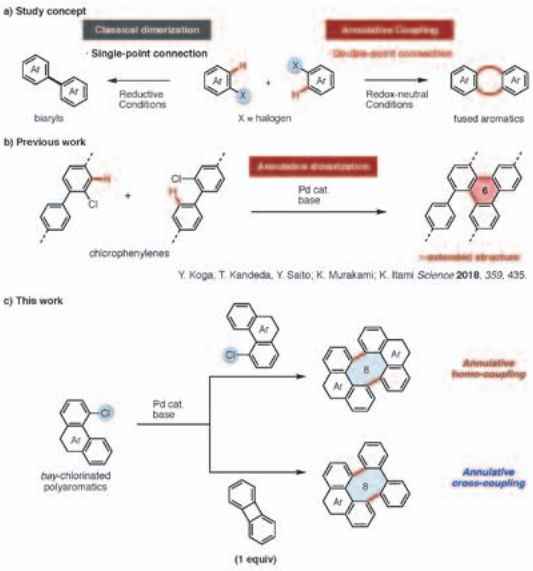

2) Annulative homo-coupling

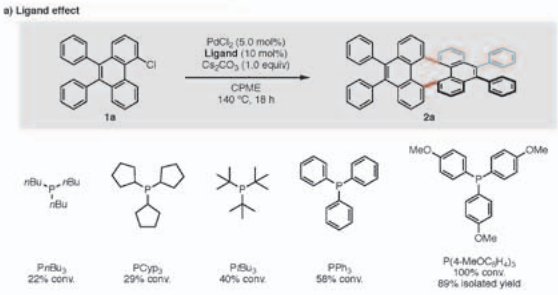

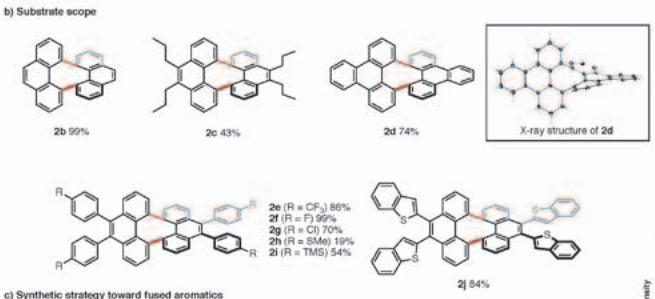

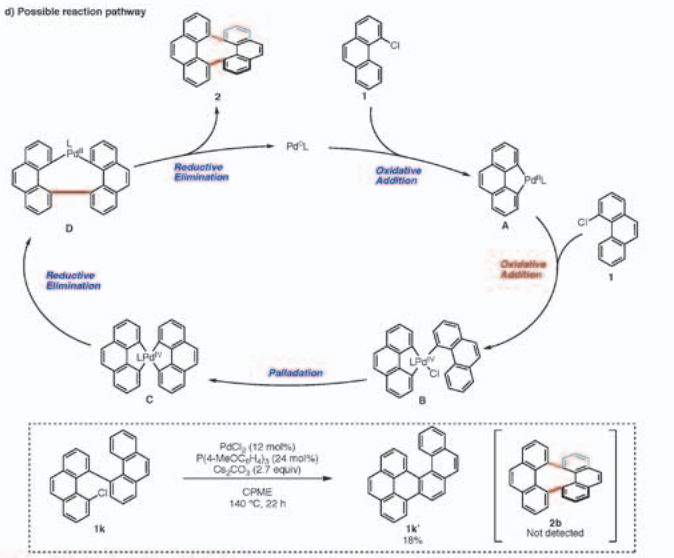

3) Annulative cross-coupling

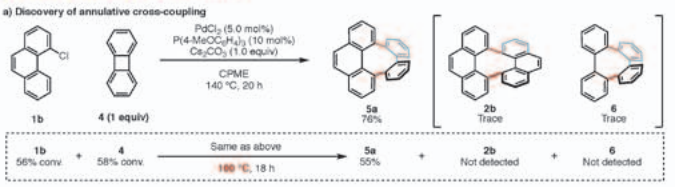

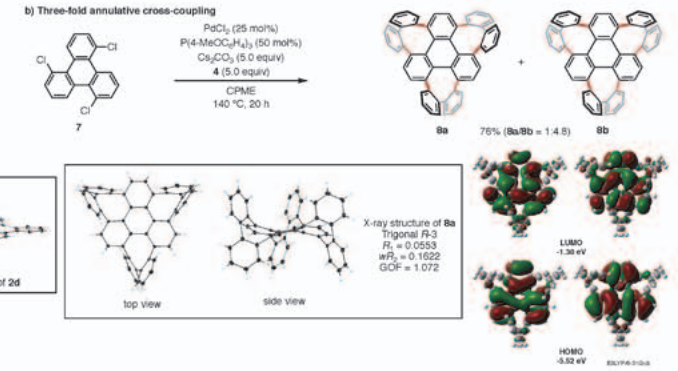

Photoinduced C–H arylation of arylamine

Bumpei Maeda[1], Genki Mori[2], Yota Sakakibara[1], Akiko Yagi[1,3], Kei Murakami[1,3], Kenichiro Itami[1,3,4]
[1]Graduate School of Science, Nagoya University, Chikusa, Nagoya 464-8602, Japan.
[2]Central Pharmaceutical Research Institute, Japan Tobacco Inc.
[3]Institute of Transformative Bio-Molecules (WPI-ITbM), Nagoya University
[4]JST, ERATO, Itami Molecular Nanocarbon Project, Nagoya University

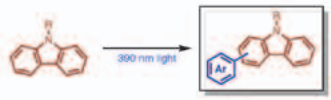

- Direct arylation
- No catalyst
- Mild condition

Arylamine is an important structure in pigments and semiconductor materials. To date, many photoinduced arylations of arylamine have been developed. However, no report on direct sp² C–H bonds arylation of carbazole derivatives has been reported. Herein, we report photoinduced direct sp² C–H bonds arylation of carbazole.

Discussion

1. Arylation of carbazole

General method

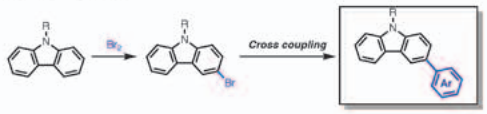

- Multistep synthesis
- Only 3 arylation

2013 Wu[1]

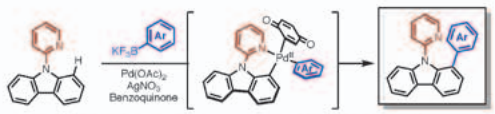

- Directing group
- Only 1 arylation

2. Photoinduced arylation of Arylamine

2017 König[2]

This work: arylation of carbazole

- Direct arylation
- No catalyst
- Mild condition

Facile synthesis of 2, 4 arylated carbazole

3. Optimize reaction conditions

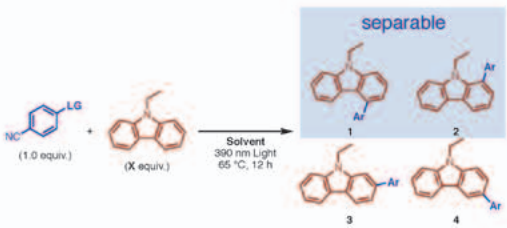

Entry	X	Solvent	LG	Yield (1/2)
1	3.0	MeCN	Br	22% (1/1.2)
2	5.0	MeCN	Br	27% (1/1.3)
3	5.0	MeCN/H_2O = 10:1	Br	29% (1/1.3)
4	**5.0**	**MeCN/H_2O = 10:1**	**N_2^+**	**45% (1/1.6)**

4. Substrate scope

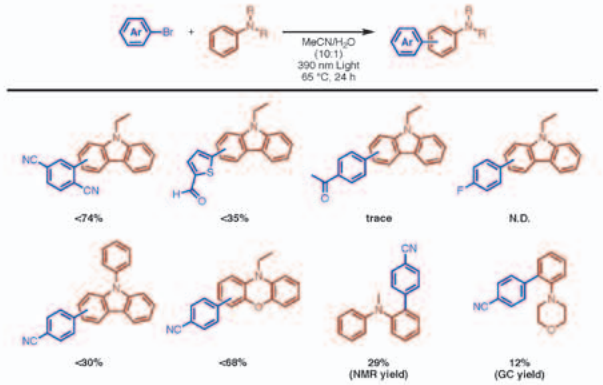

5. sp³ arylation

1980 Tsujimoto[3]

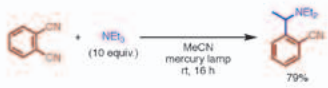

sp³ arylation of carbazole

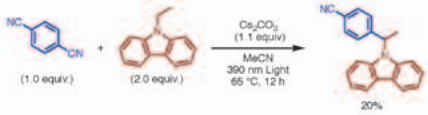

6. Proposed mechanism

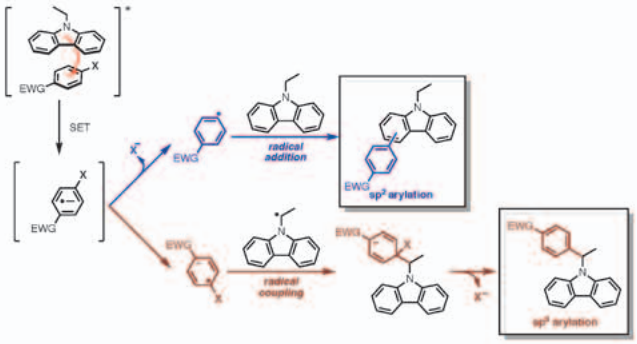

Reference

[1] Wu, M.-J. *et al. Organometallics* **2013**, *32*, 272.

[2] König, B. *et al. Org. Lett.* **2017**, *19*, 5976.

[3] Tsujimoto, K. *et al. Bull. Chem. Soc. Jpn.* **1980**, *53*, 1683.

Photoredox-catalyzed decarboxylative cross-coupling of aryl halides and glycine

Jaehyun Jung[1], Yota Sakakibara[1], Kei Murakami[1,2], Kenichiro Itami[1,2,3]
[1]Graduate School of Science, Nagoya University, Chikusa, Nagoya 464-8602, Japan.
[2]Institute of Transformative Bio-Molecules (WPI-ITbM), Nagoya University
[3]JST, ERATO, Itami Molecular Nanocarbon Project, Nagoya University

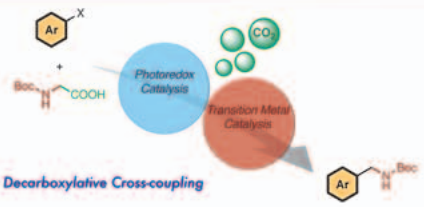

Benzylamine is an important scaffold in bioactive compounds, especially pharmaceuticals. Recently, the synthesis of benzylamine derivatives by photoredox-catalyzed aminoalkylation toward aryl halide have been developed, however, the straightforward synthesis of primary benzylamines remains an important task. Herein, we report nickel- and photoredox-catalyzed synthesis of primary benzylamines, which generated from glycine derivatives. Notably, this reaction can introduce non-substituted aminomethyl group into haloarenes through deprotection.

Discussion

1. Synthesis of Benzylamine

(a) Approach to Primary benzylamine

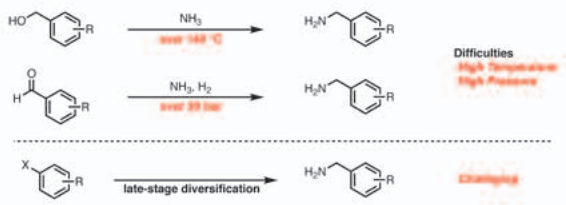

(b) Related Work: Decarboxylative Synthesis

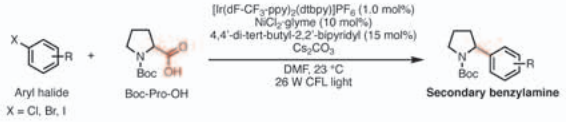

MacMillan, D.W.C. *et al. Science*, **2014**, *345*, 437.

(c) This Work: Late-stage Direct Aminomethylation

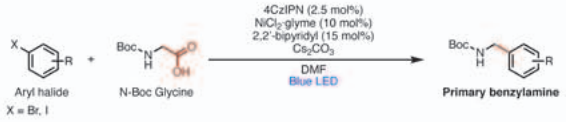

2. Optimization

(a) Ligand (Solvent = DMF)

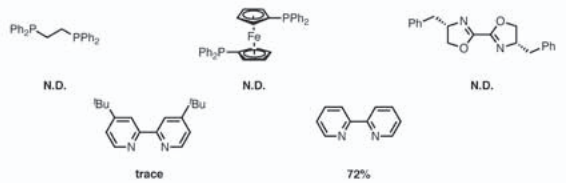

(b) Solvent (Ligand = 2,2'-bpy)

DMF	DMA	DMSO	MeCN
72%	77%	trace	23%

3. Scope

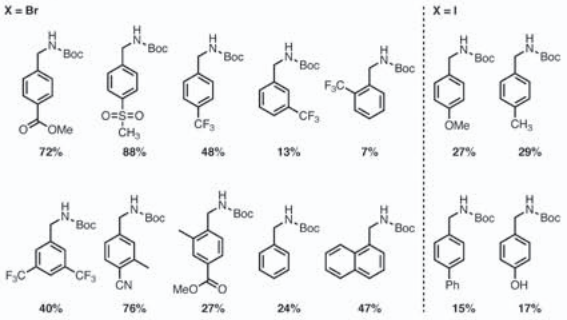

4. Challenge: Multi-aminomethylation

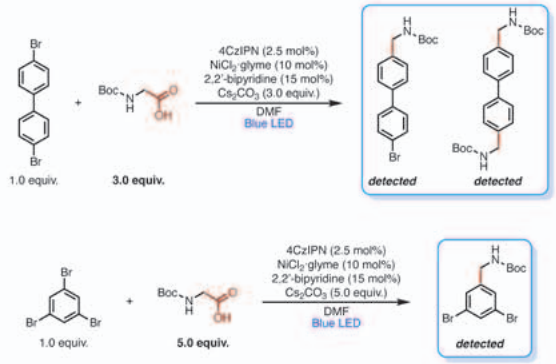

5. Proposed Mechanism

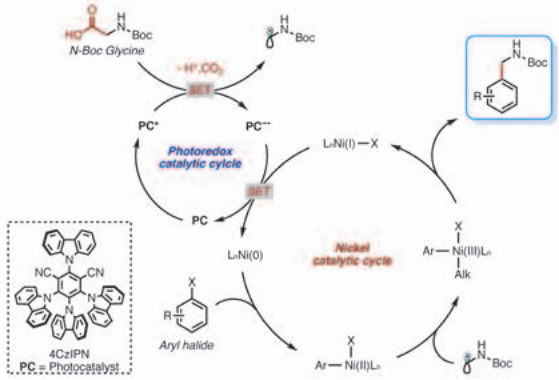

Synthesis of Various Polycyclic Aromatic Hydrocarbons by Annulative π-Extension Reactions

○Keigo Yamada,[1] Wataru Matsuoka,[1] Maciej Krzeszewski,[1] Hideto Ito[1,2] and Kenichiro Itami[1,2,3]

(1) Department of Chemistry, Graduate School of Science, Nagoya Univ. (2) Institute of Transformative Bio-Molecules (WPI-ITbM), Nagoya Univ. (3) JST-ERATO, Itami Molecular Nanocarbon Project. E-mail: itami@chem.nagoya-u.ac.jp

Annulative π-extension (APEX) reaction

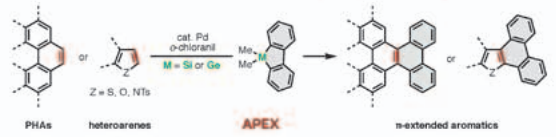

Ozaki, K.; Kawasumi, K.; Shibata, M.; Ito, H.; Itami, K. *Nature commun.* **2015**, *6*, 6251.
Kitano, H.; Matsuoka, W.; Ito, H.; Itami, K. *Chem. Sci.* **2018**, *9*, 7556.

Successive APEX reaction

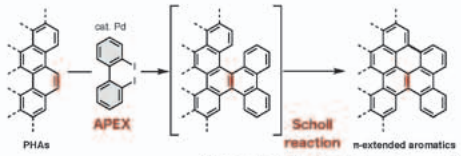

Matsuoka, W.; Ito, H.; Itami, K. *Angew. Chem., Int. Ed.* **2017**, *56*, 12224.

Fused aromatics gather great attentions in the field of materials science, especially in optoelectronics. Therefore, there is a huge demand for the development of efficient synthetic methods for various fused aromatics. Recently, we have proposed annulative π-extension (APEX) as one of the ideal synthetic methods for fused aromatics. APEX refers to a π-extension that constructs one or more new aromatic ring using an unfunctionalized aromatic compound as a template. Herein, we report a reaction that causes the APEX reaction and the Scholl reaction continuously.

Substrates scope

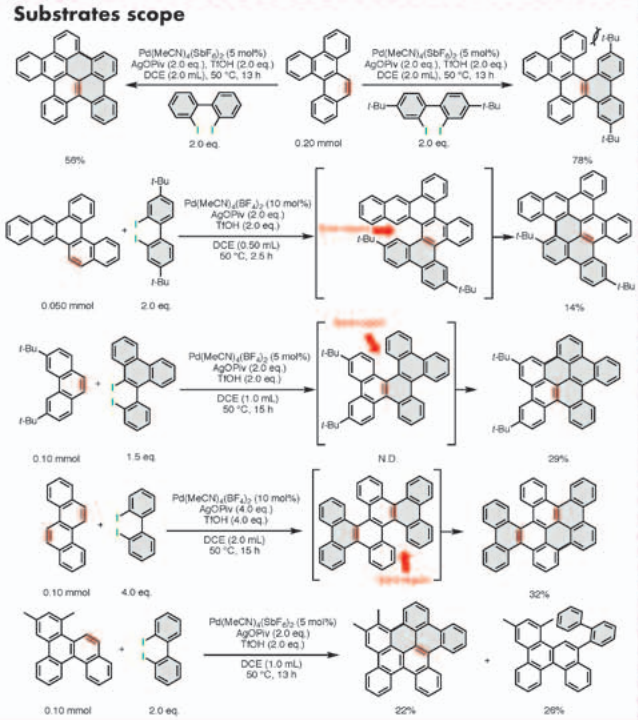

X-ray crystallographic structure

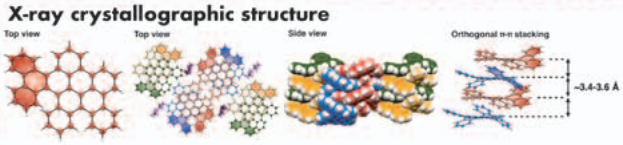

Physical properties

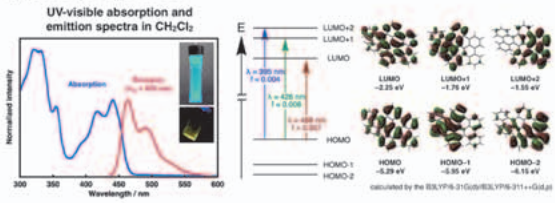

Plausible mechanism

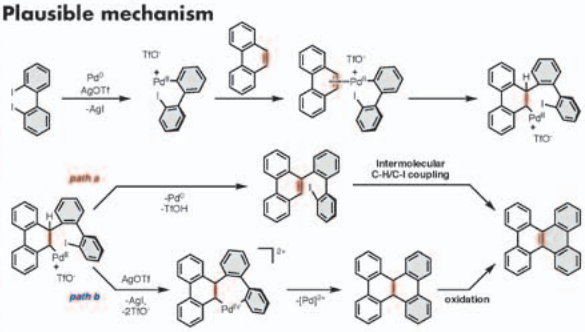

Synthesis of non-hexagonal nanocarbon

Synthetic strategy

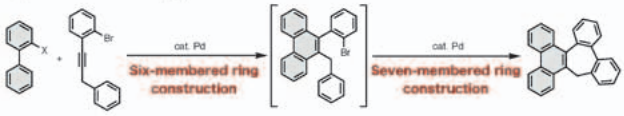

Nanocarbons containing seven-membered ring often exhibit different physical properties from nanocarbons containing only six-membered rings, due to the curved structures. However, there are very few synthetic examples of nanocarbons containing seven-membered ring. We herein report a new synthetic method for aromatic compounds containing seven-membered ring.

References

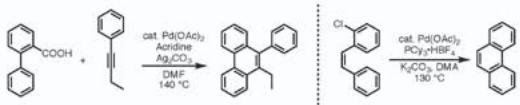

Glorius, F. *et al. J. Am. Chem. Soc.* **2010**, *132*, 14006.

Fagnou, K. *et al. J. Am. Chem. Soc.* **2006**, *128*, 581.

Construction of six-membered ring

Entry	X	Ligand	Base	NMR yield
1	$B(OH)_2$	$PMe(t\text{-}Bu)_2\cdot HBF_4$	KOAc	0%
2	$B(OH)_2$	Acridine	KOAc	0%
3	$B(OH)_2$	Acridine	AgOAc	3%
4	$B(OH)_2$	Acridine	AgOPiv	<1%
5	$B(OH)_2$	Acridine	Ag_2CO_3	9%
6	COOH	Acridine	Ag_2CO_3	12%
7[a]	COOH	Acridine	Ag_2CO_3	18%[c]
8[a,b]	COOH	Acridine	Ag_2CO_3 + KOAc	0%

[a] 0.50 mmol scale. Ligand 50 mol%. [b] Ag_2CO_3 3.0 eq. KOAc 3.0 eq. [c] isolated yield

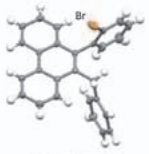

Monoclinic P21/C
R_1 = 0.0469
wR_2 = 0.1409
GOF = 0.903

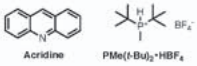

Acridine $PMe(t\text{-}Bu)_2\cdot HBF_4$

Construction of seven-membered ring

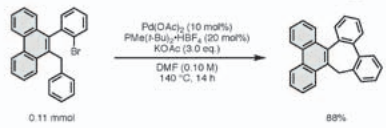

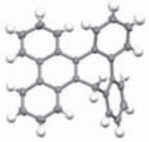

Monoclinic C2/C
R_1 = 0.0578
wR_2 = 0.1971
GOF = 1.023

The Renaissance of 4,5-Diphenylphenanthrene

Yuanming Li,[a,b] Akiko Yagi,[a,b] and Kenichiro Itami[a,b,c]

[a]Institute of Transformative Bio-Molecules (WPI-ITbM), Nagoya University, Japan;

[b]Graduate School of Science, Nagoya University, Japan; [c]JST-ERATO, Itami Molecular Nanocarbon Project, Nagoya University, Japan.

Abstract: The synthesis of nonplanar aromatics *via* the introduction of a three-dimensional (3D) building block as the core of the organic materials into the structure is a useful strategy. We introduce 4,5-diarylphenanthrene as a novel axially chiral, nonplanar, 3D building block for the synthesis of a family of highly twisted and chiral macrocycles.

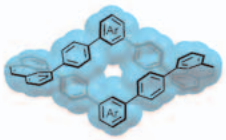

Twisted, nonplanar aromatic macrocycles

- *Modular synthesis of 10 different macrocycles*
- *Conformationally restricted chiral structures*
- *High solubility and unique crystal packing*
- *Aggregation-induced emission*
- *Solvatofluorochromism*

1. Introduction: Representative 3D Building Blocks

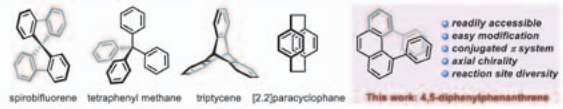

2. Synthesis of Twisted Macrocycles

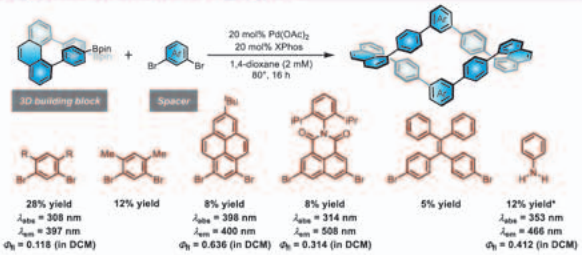

* 4,5-Bis(4-bromophenyl)phenanthrene was used *via* **Buchwald-Hartwig amination**.

3. X-ray Crystal Structures

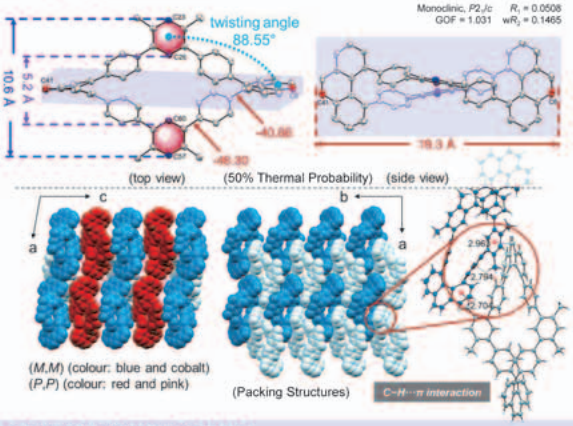

4. Frontier Molecular Orbitals

Calculated at B3LYP/6-31G(d)

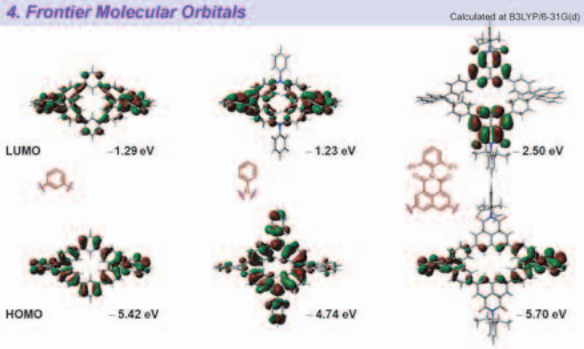

* The Synthesis of 4,5-Diarylphenanthrene

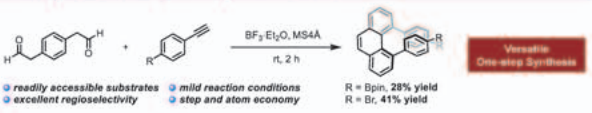

Reference: [1] Li, Y.; Yagi, A.; Itami, K. *Chem. Sci.* **2019**, *10*, 5470. [2] Li, Y.; Yagi, A.; Itami, K. *J. Am. Chem. Soc.* Accepted.

5. Homodesmotic Reaction to Calculate Strain Energy

Calculated at B3LYP/6-31G(d)

Strain energy corresponds to the distortion caused by macrocycle formation.

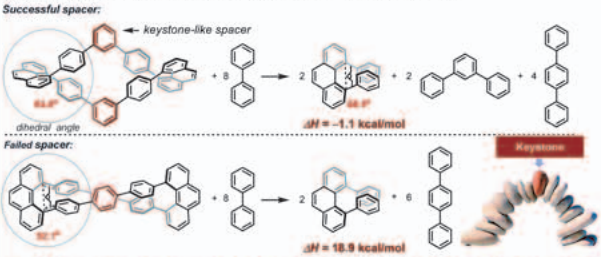

6. Which Kind of Properties Arose Due to the Twisted Structure?

6.1 Racemization Process Between (P,P) and (M,M)

Enhanced Stability!

Calculated at M06-2X/6-31G(d)

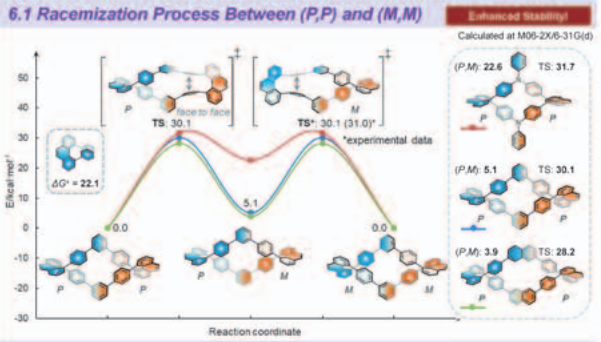

6.2 Circular Dichroism Spectra

Enhanced CD intensities!

Calculated at M06-2X/6-31G(d)

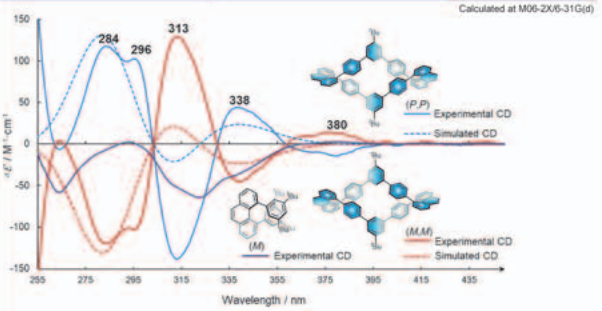

6.3 Photophysical Properties

Remarkable Solvatofluorochromism!

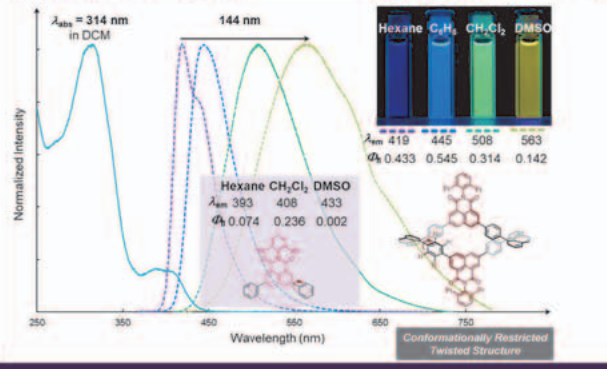

Catalytic C-H Arylation of Cubane toward Synthesis of Novel 3D Molecules

Ryo Okude[1], Genki Mori[1], Akiko Yagi[1,2], and Kenichiro Itami[1, 2, 3]

1) Graduate School of Science, Nagoya University, Chikusa, Nagoya 464-8602, Japan.
2) JST, ERATO, Itami Molecular Nanocarbon Project, Nagoya University , Japan
3) Institute of Transformative Bio-Molecules (WPI-ITbM), Nagoya University, Japan

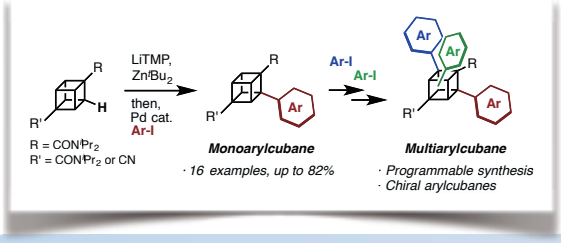

Cubane, which is a cubic alkane first synthesized by Eaton in 1964, has been widely utilized as a unique 3D building block. Despite high potential utility of cubane derivatives, the synthesis has mainly relied on the transformation of the carboxyl or halogeno groups on cubane. To create novel 3D molecules based on cubane, we envisioned to establish a universal method for functionalization of cubane. In this work, identified arylcubane as the first and high value target, a catalytic C–H arylation of cubane was developed. This arylation allowed to install a wide variety of aryl groups and realized the synthesis of multiarylcubanes as well.

Okude, R.; Mori, G.; Yagi, A.; Itami, K. *manuscript preparation*

1. Background

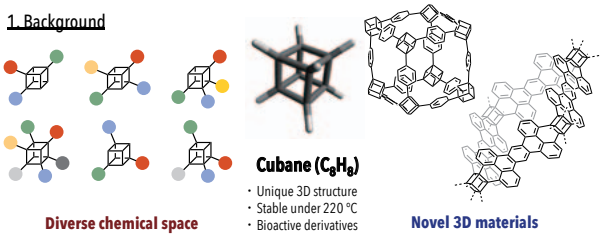

Synthesis of arylcubane: A cubane derivative promising as a unique material

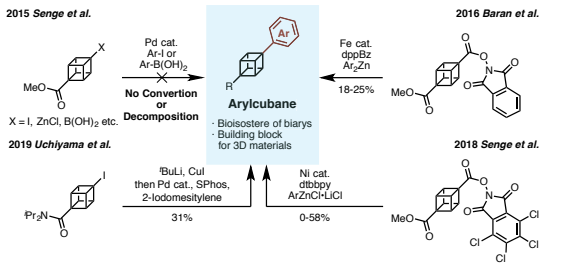

Senge, M. O. *et al. Organometallics* **2015**, *34*, 1408. Baran, P. S. *et al. J. Am. Chem. Soc.* **2016**, *138*, 11132.
Senge, M. O. *et al. Chem. Eur. J.* **2018**, *24*, 1026. Uchiyama, M. *et al. Chem. Sci* **2019**, *10*, 6107.

C–H phenylation of cubane

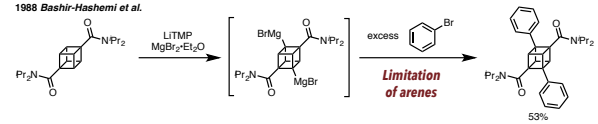

Bashir-Hashemi, A. *J. Am. Chem. Soc.* **1988**, *110*, 7234.

C–H arylation of arene *via* directed *ortho*-metalation

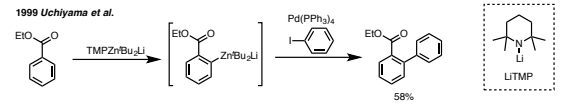

Uchiyama, M. *et al. J. Am. Chem. Soc.* **1999**, *121*, 3539.

2. Development of C–H Arylation of Cubanediamide

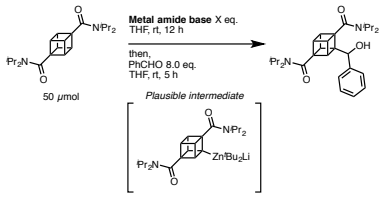

entry	Metal amide base	X	^{1}H NMR yield
1	^{t}Bu$_3$Al(TMP)Li	5.0	N.D.
2	MeCu(TMP)(CN)Li$_2$	5.0	N.D.
3	^{t}Bu$_2$ZnTMPLi	5.0	96%
4	^{t}Bu$_2$ZnTMPLi	2.0	92%
5	^{i}Bu$_2$ZnTMPLi	2.0	98%
6	LiTMP + ZnCl$_2$	2.0	N.D.

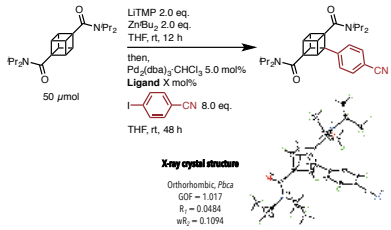

entry	Ligand	X	^{1}H NMR yield
1	PPh$_3$	40	28%
2	P(2-furyl)$_3$	40	N.D.
3	dppe	20	2%
4	dppp	20	13%
5	P(O-C$_6$H$_4$-CF$_3$)$_3$	40	<1%
6	P(OEt)$_3$	40	1%
7	P(OPh)$_3$	40	58%
8[a]	P(OPh)$_3$	80	84%

[a] Pd$_2$(dba)$_3$·CHCl$_3$ 10mol%

3. Scope of Aryl Groups for Monoarylcubane

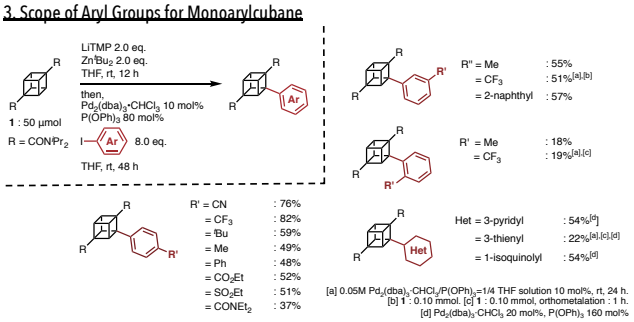

[a] 0.05M Pd$_2$(dba)$_3$·CHCl$_3$/P(OPh)$_3$=1/4 THF solution 10 mol%, rt, 24 h.
[b] **1** : 0.10 mmol. [c] **1** : 0.10 mmol, orthometalation : 1 h.
[d] Pd$_2$(dba)$_3$·CHCl$_3$ 20 mol%, P(OPh)$_3$ 160 mol%

4. Synthesis of Diarylcubanes

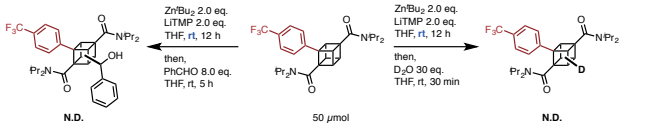

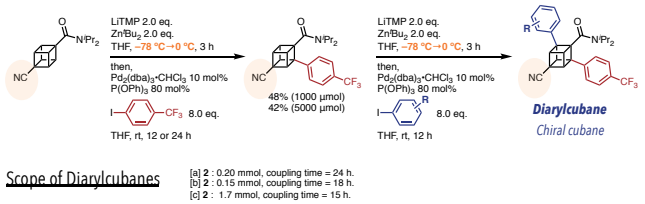

Scope of Diarylcubanes

[a] **2** : 0.20 mmol, coupling time = 24 h.
[b] **2** : 0.15 mmol, coupling time = 18 h.
[c] **2** : 1.7 mmol, coupling time = 15 h.

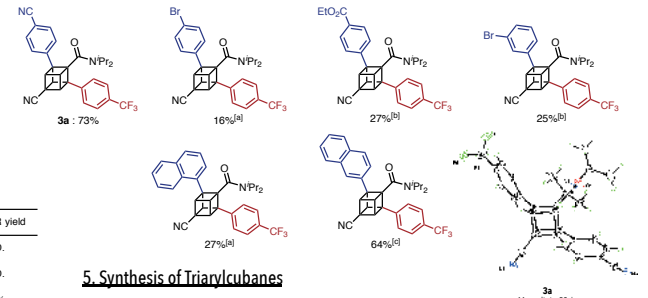

5. Synthesis of Triarylcubanes

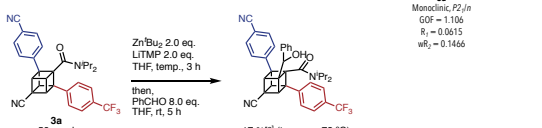

[a] ^{1}H NMR yield

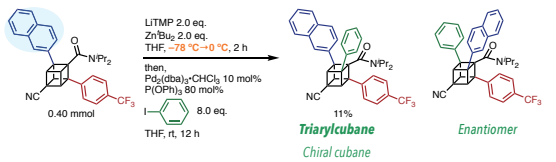

Development of a Synthetic Method for Unsubstituted Nanocarbons

Shusei Fujiki,[a] Akiko Yagi,[ab] Kenichiro Itami[abc]

[a]Graduate School of Science, Nagoya University, Japan
[b]JST, ERATO, Itami Molecular Nanocarbon Project, Nagoya University, Japan
[c]Institute of Transformative Bio-Molecules (WPI-ITbM), Nagoya University, Japan

ITAMI GROUP
RGANIC CHEMISTRY

Solubility Problem

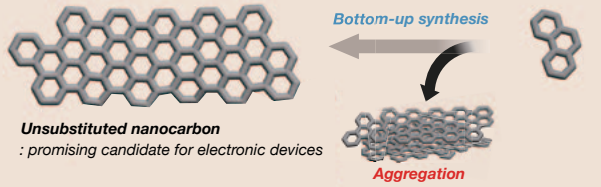

Nanocarbons are promising candidates for electronic devices. Because of their strong intermolecular interaction, nanocarbons easily form the aggregates. In order to suppress the aggregation, long alkyl or alkoxy chains are often installed as substituents in the synthesis of nanocarbons. Since the substituents cause the change of physical properties, a synthetic method for unsubstituted nanocarbons is highly demanded. Herein, we report new synthetic methodologies circumventing this problem. Unsubstituted nanocarbons was successfully synthesized with the aid of cross-linked polystyrene or sterically demanding dendrimer-like molecule. The result implies that strong aggregation of nanocarbons are effectively hampered by this strategy.

Strategies toward Unsubstituted Nanocarbons

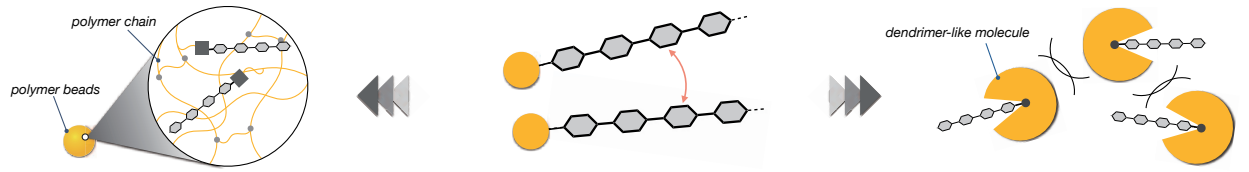

Segregation by cross-linked polymer | Segregation of easy-to-aggregate nanocarbons | Segregation by dendrimer-like molecule

Solid-phase Synthesis

Solid-phase Synthesis

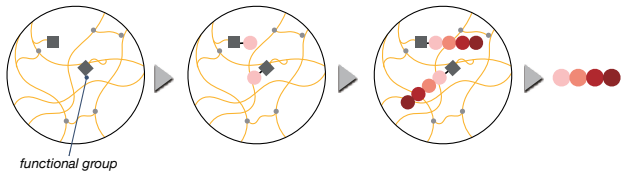

Synthetic Strategy toward Poly(p-phenylene)

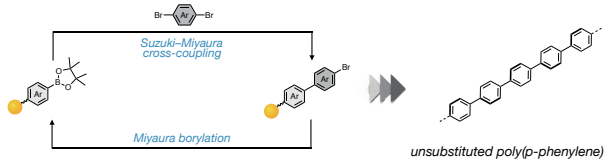

Solid-phase Synthesis of Poly(p-phenylene)

Reaction condition of Miyaura borylation

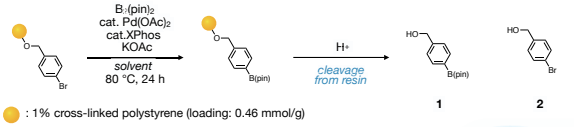

: 1% cross-linked polystyrene (loading: 0.46 mmol/g)

solvent	result[a]
THF	**1**
DME	**1** : **2** = 10 : 1
CPME	**2**

a : Result was determined by H NMR.

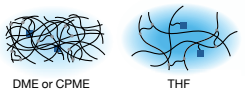

Elongation of phenylene chain

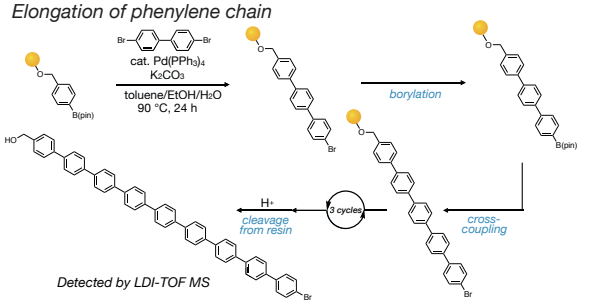

Dendrimer-supported Synthesis

Conventional Liquid-phase Synthesis

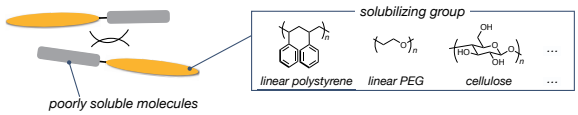

This Work : *Developement of solubilizing group optimazed for nanocarbon synthesis*

Synthesis of Dendrimer-like Support

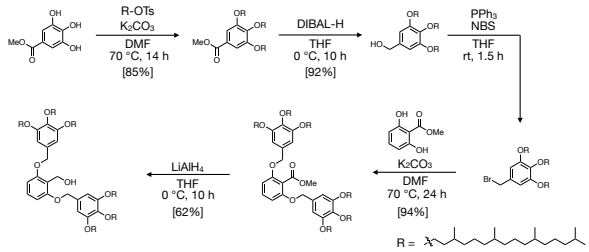

Dendrimer-supported Synthesis of Polythiophene

Choi (2018)

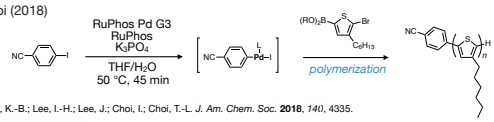

Seo, K.-B.; Lee, I.-H.; Lee, J.; Choi, I.; Choi, T.-L. *J. Am. Chem. Soc.* **2018**, *140*, 4335.

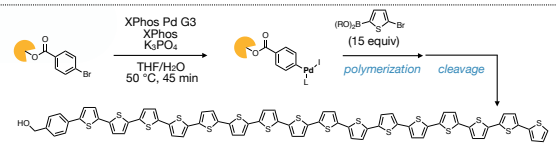

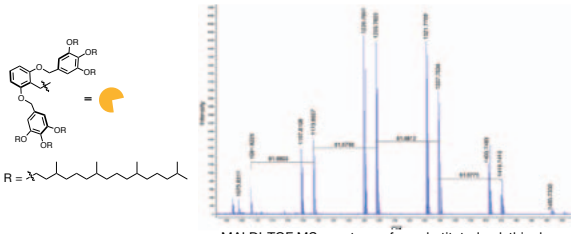

MALDI-TOF MS spectrum of unsubstituted polythiophene

Direct C–H Borylation of Pristine Hexabenzocoronene

Mai Nagase,[a] Kenta Kato,[a] Akiko Yagi,[a] Yasutomo Segawa,[a,b] Kenichiro Itami,[a,b,c]

[a]Graduate School of Science, Nagoya University, Japan
[b]JST, ERATO, Itami Molecular Nanocarbon Project, Nagoya University, Japan
[c]Institute of Transformative Bio-Molecules (WPI-ITbM), Nagoya University, Japan

The physical and electronic properties of polycyclic aromatic hydrocarbons (PAHs), fused arenes that consist of sp^2-hybridized carbon atoms, depend strongly on their structure. In spite of the strong demand of concise and practical methods for the functionalization of PAHs, there have been few reports on the direct functionalization of large PAHs.

In this study, we have established conditions for Ir-catalyzed six-fold C–H borylation of pristine hexabenzocoronene (HBC).

Acknowledgement: Prof. Dr. Tsuyohiko Fujigaya for fruitful discussion.

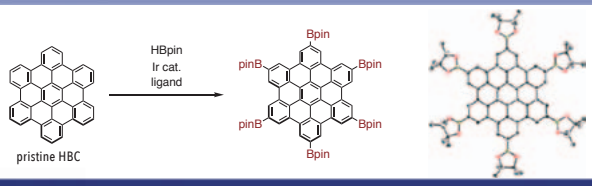

RESULTS

1. Functionalization of pristine PAHs

- Planar PAHs

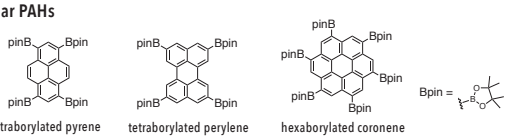

(1) Coventry, D. N.; Batsanov, A. S.; Goeta, A. E.; Howard, J. A. K.; Marder, T. B.; Perutz R. N. *Chem. Commun.* **2005**, *41*, 2172.
(2) Eliseeva, M. N.; Scott, L. T. *J. Am. Chem. Soc.* **2012**, *134*, 15169.

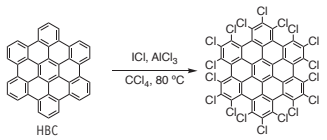

Tan, Y.-Z.; Yang, B.; Parvez, K.; Narita, A.; Osella, S.; Beljonne, D.; Feng, X.; Müllen, K. *Nat. Commun.* **2013**, *4*, 2646.

- Nonplanar PAHs

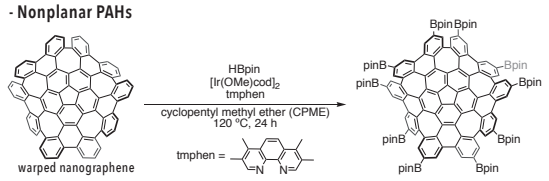

Nonplanar structure increases the solubility of PAHs

Kato, K.; Lin, H. -A.; Kuwayama, M.; Nagase, M.; Segawa, Y.; Scott, L. T.; Itami, K. *Chem. Sci.* **2019**, 10, 9038.

2. Heteroatom-substituted HBCs

- Halogenated HBCs

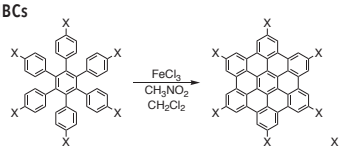

(1) Kikuzawa, Y.; Mori, T.; Takeuchi, H. *Org. Lett.* **2007**, *9*, 4817.
(2) Wu, J.; Fechtenkötter, A.; Gauss, J.; Watson, M. D.; Kastler, M.; Fechtenkötter, C.; Wagner, M.; Müllen, K. *J. Am. Chem. Soc.* **2004**, *126*, 11311.

- Borylated HBCs

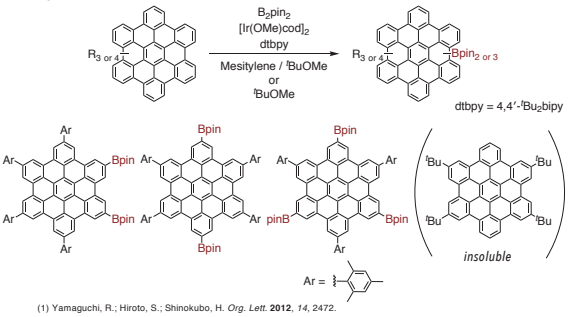

(1) Yamaguchi, R.; Hiroto, S.; Shinokubo, H. *Org. Lett.* **2012**, *14*, 2472.
(2) Ryuichi Yamaguchi, *Ph.D. thesis*, **2014**, *Nagoya University*.

Unexpected rearrangement caused by Scholl reaction

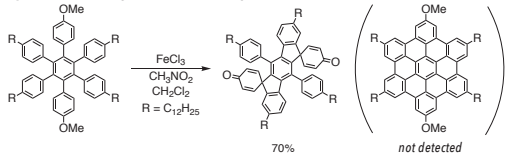

Dou, X.; Yang, X.; Bodwell, G. J.; Wagner, M.; Enkelmann, V.; Müllen, K. *Org. Lett.* **2007**, *9*, 2485.

3. NMP as a magic solvent for nanocarbons

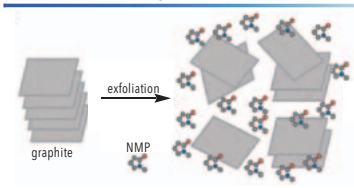

(1) Bottari, G.; M. Á. Herranz, Wibmer, L.; Volland, M.; Rodríguez-Pérez; L.; Guldi, D. M.; Hirsch, A.; Martín, N.; D'Souza, F.; Torres, T. *Chem. Soc. Rev.* **2017**, *46*, 4464.
(2) Bergin, S. D.; Nicolosi, V.; Streich, P. V. ; Giordani, S. ; Sun, Z.; Windle, A. H.; Ryan, P.; Niraj, N. P. P.; Wang, Z.-T. T.; Carpenter, L. ;Blau, W. J.; Boland, J. J.; Hamilton, J. P.; Coleman, J. N. *Adv. Mater.* **2008**, *20*, 1876.

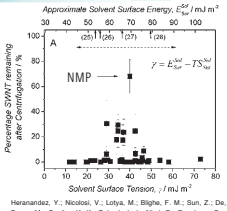

SWNT: single-walled carbon nanotube

Heranandez, Y.; Nicolosi, V.; Lotya, M.; Blighe, F. M.; Sun, Z.; De, S.; McGovern, I. T.; Holland, B.; Byrne, M.; Gun'ko, Y. K.; Boland, J. J.; Niraj, P.; Duesberg, G.; Krishnamurthy, S.; Goodhue, R.; Hutchison, J. Scardaci, V.; Ferrari, A. C.; Colemen, J. N. *Nat. Nanotechnol.* **2008**, *3*, 563.

NMP = *N*-methylpyrrolidone

– Absorption spectra of HBC at 60 °C

Temperature variable UV/vis spectrometer

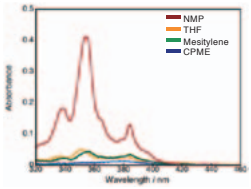

NMP is a good solvent also for HBC

Solubility of HBC at r.t.: Hughes, J. M.; Hernandez, Y.; Aherne, D.; Doessel, L.; Müllen, K.; Moreton, B.; White, T. W.; Partridge, C.; Costantini, G.; Shmeliov, A.; Shannon, M.; Nicolosi, V.; Coleman, J. N. *J. Am. Chem. Soc.* **2012**, *134*, 12168.

4. Direct C–H borylation of pristine HBC

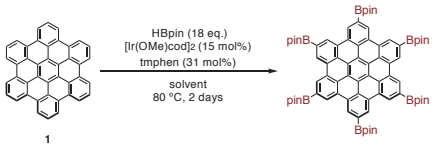

entry	solvent	^{1}H NMR yield
1	CPME	28%
2	THF	5.0%
3	NMP	13%

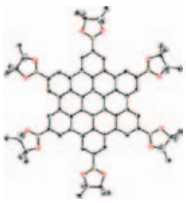

Top view

cubic, *Pa*-3
GOF = 1.063
$R1$ = 0.0705,
$wR2$ = 0.2192

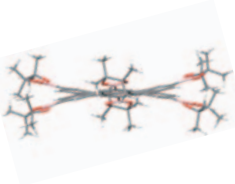

Side view

Slightly distorted to have S_6 symmetry

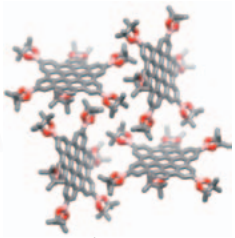

Packing structure

No π–π stacking is observed.

– UV/vis absorption and fluorescence spectra of hexaborylated HBC

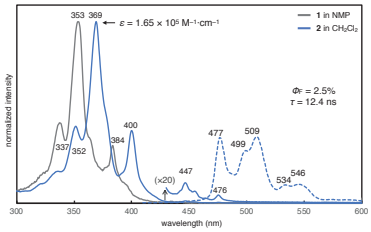

Red-shifted from HBC because of the σ-donation of boryl groups

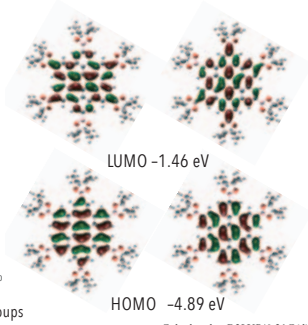

Calculated at B3LYP/6-31G(d)

Stereoselective benzylic hydroxylation catalyzed by cytochrome P450BM3 with Decoy Molecules

Kazuto Suzuki,[a] Joshua Kyle Stanfield,[a] Sota Yanagisawa,[a] Hiroshi Sugimoto,[b,c] Yoshihito Watanabe,[d] Osami Shoji[a,b]

[a] Dept. of Chem., Grad. Sch. of Sci., Nagoya Univ., [b] CREST, Japan Science and Technology Agency, [c] RIKEN SPring-8, Harima Inst., [d] Reserch Center for Materials Science, Nagoya Univ.

Background

Cytochrome P450BM3

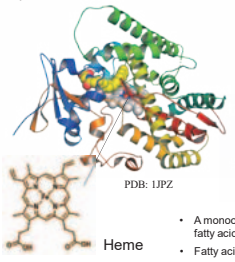

Native reaction: fatty acid hydroxylation

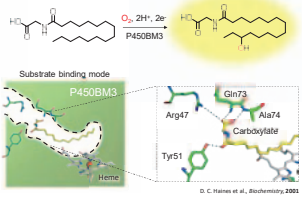

- A monooxygenase, which catalyzes the hydroxylation of long-chain fatty acids at the sub-terminus
- Fatty acid is bound to P450BM3 through hydrogen-bonding interactions.

Catalytic Cycle

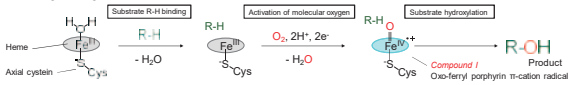

Non-Native Substrate Hydroxylation by Substrate-Misrecognition System

P450BM3's stringent substrate-specificity for fatty acids have prevented the application of the enzyme to an oxidative catalyst bearing substrate generality.

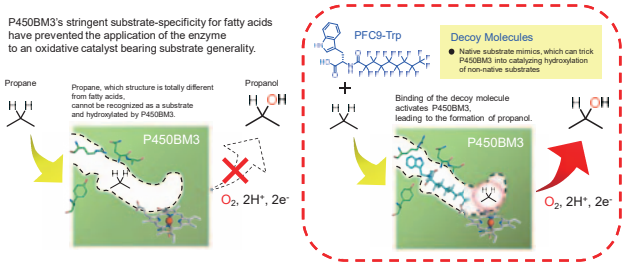

In the presence of the decoy molecules, P450BM3 can catalyze hydroxylation of non-native substrates such as propane and benzene.
Recent studies have demonstrated the potential as decoy molecules of various carboxylic acids with structural diversity.

Fluorinated Decoy Molecules (Perfluorinated Carboxylic Acids, PFC)

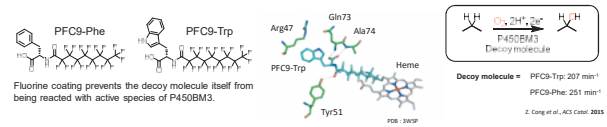

Fluorine coating prevents the decoy molecule itself from being reacted with active species of P450BM3.

Decoy molecule = PFC9-Trp: 207 min^{-1} PFC9-Phe: 251 min^{-1}

Z. Cong et al., ACS Catal. 2015

Non-fluorinated Decoy Molecules

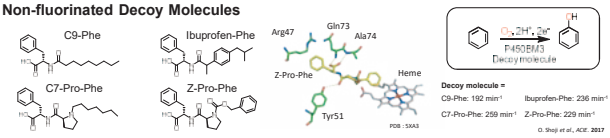

Decoy molecule =
C9-Phe: 192 min^{-1} Ibuprofen-Phe: 236 min^{-1}
C7-Pro-Phe: 259 min^{-1} Z-Pro-Phe: 229 min^{-1}

O. Shoji et al., ACIE. 2017

Aim

Controlling Stereoselectivity of hydroxylation using Decoy Molecules

Direct, yet enantioselective C-H bond functionalization is highly attractive for organic chemists since it promises substantially streamlined synthetic routes. In this study, we aimed to control stereoselectivity of C-H bond hydroxylations of non-native substrates catalyzed by P450BM3 using decoy molecules.

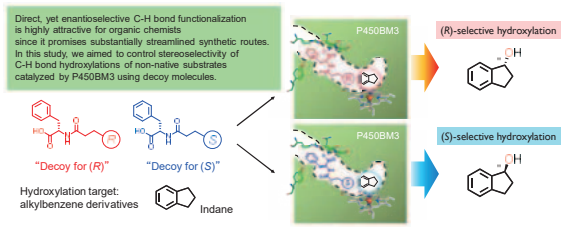

Results

Structures of decoy molecules employed

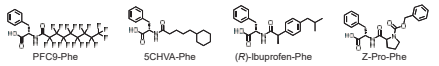

Benzylic Hydroxylation by P450BM3 with Decoy Molecules

Indane Hydroxylation

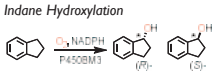

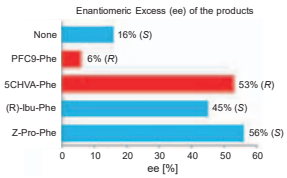

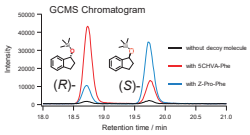

Decoy molecule	Rate [min^{-1}]	ee [%] (R/S)	CE [%]
None	36 ± 2	16 (S)	8
PFC9-Phe	216 ± 8	6 (R)	24
5CHVA-Phe	435 ± 27	53 (R)	44
(R)-Ibu-Phe	314 ± 5	45 (S)	39
Z-Pro-Phe	302 ± 10	56 (S)	43

Ethylbenzene Hydroxylation

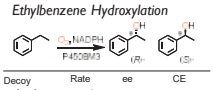

Decoy molecule	Rate [min^{-1}]	ee [%] (R/S)	CE [%]
None	147 ± 11	45 (R)	23
PFC9-Phe	373 ± 46	52 (R)	31
5CHVA-Phe	447 ± 13	85 (R)	47
(R)-Ibu-Phe	321 ± 5	7 (S)	35
Z-Pro-Phe	324 ± 9	4 (S)	43

Tatralin Hydroxylation

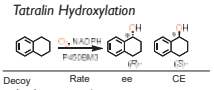

Decoy molecule	Rate [min^{-1}]	ee [%] (R/S)	CE [%]
None	20 ± 1	55 (S)	7
PFC9-Phe	212 ± 16	69 (S)	17
5CHVA-Phe	320 ± 31	13 (S)	49
(R)-Ibu-Phe	332 ± 40	89 (S)	66
Z-Pro-Phe	260 ± 15	96 (S)	82

✓ **Stereoselectivity of benzylic hydroxylation was improved or inverted depending upon decoy molecule displayed above.**

◆ 5CHVA-Phe improved (R)-selectivity.

◆ Z-Pro-Phe improved (S)-selectivity.

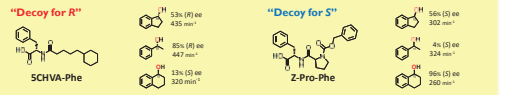

Experimental Procedure

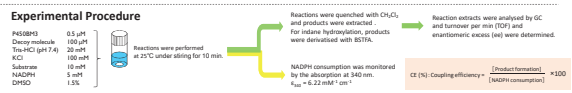

Crystal Structure & Computational Analysis

Crystal Structures of P450BM3 Bound to Decoy Molecules

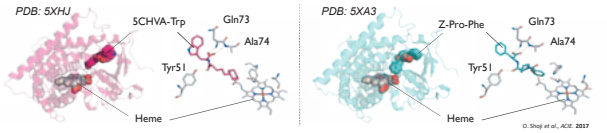

✓ The crystal structures of P450BM3 bound to 5CHVA-Trp and Z-Pro-Phe were successfully solved.

Conformational Change of P450BM3 Induced by Decoy Molecules

P450BM3 with **5CHVA-Trp** → **Closed** conformation
P450BM3 with **Z-Pro-Phe** → **Opened** conformation

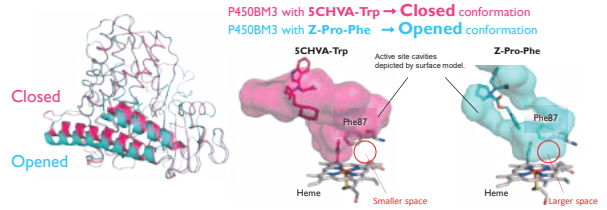

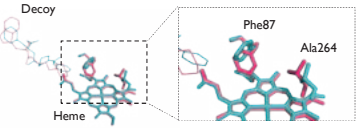

✓ 5CHVA-Trp induced closed conformation while Z-Pro-Phe induced open conformation.

✓ The shapes of active site cavity are different between the two structures.

✓ Phe87 and Ala264, residues near the active site, are displaced by the binding of the decoy molecules.

Docking Simulation of Indane to Decoy-bound P450BM3

Software: AutoDockFR (*PLoS Comput. Biol.*, 2015, **11**, e1004586.)

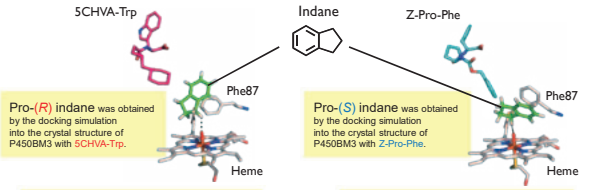

Pro-(R) indane was obtained by the docking simulation into the crystal structure of P450BM3 with 5CHVA-Trp.

Pro-(S) indane was obtained by the docking simulation into the crystal structure of P450BM3 with Z-Pro-Phe.

Experimental: (R)-selectivity (41% (R) ee)

Experimental: (S)-selectivity (56% (S) ee)

✓ The results of each docking simulation were consistent with the experimental stereoselectivity.

Sequence-selective recognition of double-stranded DNA by peptide nucleic acid

○Masanari Shibata, Masaki Hibino, Yuichiro Aiba*, Osami Shoji*
(Department of Chemistry, Graduate School of Science, Nagoya University)

Introduction

▪ Peptide Nucleic Acid (PNA)

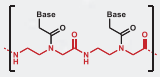

- Electrostatically-neutral backbone
- PNA forms a stable duplex with DNA.
- High resistance to enzymatic digestion

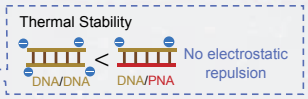

Double-duplex invasion

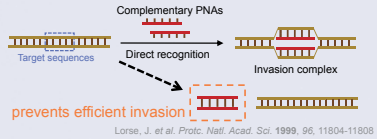

Lorse, J. *et al. Proc. Natl. Acad. Sci.* **1999**, *96*, 11804-11808

➡ PNA invasion is applicable to the DNA recognition *in cellulo* or *in vivo*.
- Gene expression control
- Genome editing

Chemically-modified nucleobase
Pseudo-complementary PNA (pcPNA)

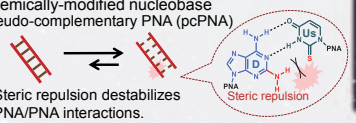

Steric repulsion destabilizes PNA/PNA interactions.
➡ Invasion proceeds efficiently.

D : 2,6-diaminopurine, Us : 2-thiouracil

However **Problems of pcPNA**
- Effective pcPNA monomers are only available for AT pair.
  ➡ **Limitations in recognition sequences**
- Boc synthesis (not applicable to automatic synthesizers, limited to manual synthesis)
  ➡ **Time consuming and laborious**

Summary

- **We have succeeded in developing a novel PNA invasion method.**
- **Parallel invasion does not require any chemical modification of nucleobase.**
- **We will optimize invasion conditions for *in cellulo* and *in vivo* applications.**

Research Aim

Development of a novel invasion method w/o chemical modification of nucleobase

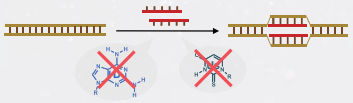

✓Targeting any sequences
✓Fast and automated synthesis of PNA
➡ **Useful for molecular biology applications**

Strategy

- Binding property of nucleic acid

Structure of DNA

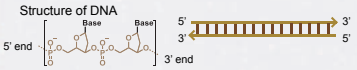

DNA duplex exists stably in anti-parallel orientation.

Thermal stability of PNA/PNA duplex is lower in parallel orientation.

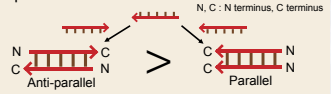

Wittung, P. *et al. Nature* **1994**, *368*, 561-563

Invasion does not proceed when using unmodified PNAs.

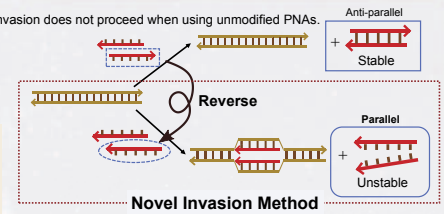

Novel Invasion Method

Reversing the orientation of a PNA inhibits the formation of PNA/PNA duplex.

Results and Discussion

▪ Invasion Experiment

[DNA (119 bp)] = 100 nM
[Each of PNAs] = 100 -1000 nM
[HEPES (pH = 7.0)] = 5 mM

Incubation
50 °C for 1 h

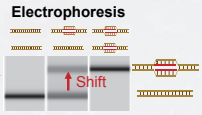

▪ Invasion Efficiency - Electrophoretic Mobility Shift Assay

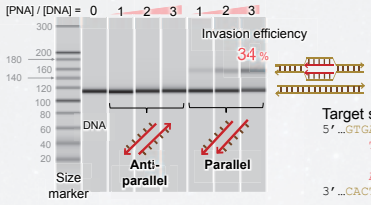

Target sequence
5′...GTGACTACTCTTAGTCATGGT...3′
TGATGAGAATCAGTA
ACTACTCTTAGTCAT
3′...CACTGATGAGAATCAGTACCA...5′

This result is the first achievement of PNA invasion w/o any chemical modification.

▪ Thermal Stability - T_m measurement

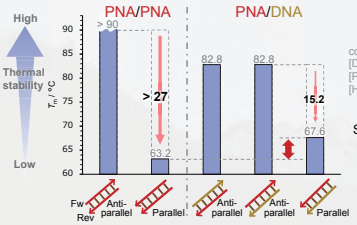

conditions
[DNA (15 mer)] = 1 μM
[PNA (15 mer)] = 1 μM
[HEPES (pH 7.0)] = 5 mM

Sequence of PNA and DNA (15 mer)
Fw: ACTACTCTTAGTCAT
Rev: TGATGAGAATCAGTA

- The thermal stability of parallel PNA/PNA duplexes was very low.
- PNA/DNA duplex was more stable than parallel PNA/PNA duplex.

The results of T_m measurement supported that of the invasion experiment.

▪ Mismatch Sequence Discrimination

Single mismatch was introduced in the center of the target sequence.

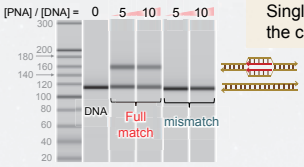

Target sequence (single mismatch)
5′...GTGACTACTCTTAGTCATGGT...3′
TGATGAGAATCAGTA
ACTACTCTTAGTCAT
3′...CACTGATGAGAATCAGTACCA...5′

The single base mismatch prevented the formation of invasion complex.
➡ **Parallel invasion showed high sequence selectivity.**

▪ Investigation of Applicable PNA Length

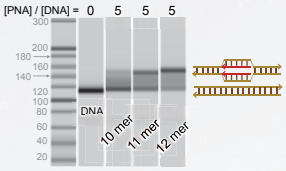

PNA length (10, 11, 12 mer)
5′...GTGACTACTCTTAGTCAT...3′
TGATGAGAATCA
10 mer
11 mer
ACTACTCTTAGT
3′...CACTGATGAGAATCAGTA...5′

The longer PNAs formed invasion complex more efficiently.

▪ Application to other sequence

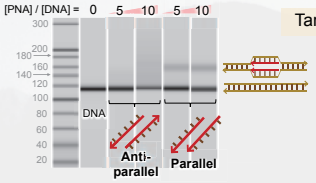

Target : GC-rich sequences

GC content 33% ➡ **67%**

Target sequence (GC rich)
5′...AGTGCTTCAGCCGCTACCCCG...3′
CGAAGTCGGCGATGG
GCTTCAGCCGCTACC
3′...TCACGAAGTCGGCGATGGGGC...5′

Invasion complex was formed even with GC-rich target sequence.
➡ **This result suggested that parallel invasion method covers extensive target sequences.**

Aqueous Two-phase Extraction of Semiconducting SIngle-wall Carbon Nanotubes with Isomaltodextrin and Thin-film Transistor Applications

Haruka Omachi[1,2], Tomohiko Komuro[1], Kaisei Matsumoto[1], Minako Nakajima[2], Hikaru Watanabe[3], Jun Hirotani[4], Yutaka Ohno[4,5] and Hisanori Shinohara[1]

[1] Department of Chemistry, Graduate School of Science, [2] Research Center for Materials Science, Nagoya University, Nagoya J464-8602, Japan
[3] Department of Electronics, Graduate School of Engineering, [4] Institute of Materials and Systems for Sustainability, Nagoya University, Nagoya 464-8601, Japan
[5] R&D Division, Hayashibara Co., Ltd., 675-1 Fujisaki, Naka-ku, Okayama 702-8006, Japan
E-mail: omachi@chem.nagoya-u.ac.jp

Abstract

Semiconducting single-wall carbon nanotubes (s-SWCNTs) are promising materials with potential applications in thin-film transistors (TFTs). However, separation techniques are required to obtain highly enriched s-SWCNTs since conventional as-grown SWCNTs are a mixture of 70% semiconducting and 30% metallic SWCNTs. Here, we developed a rapid single-step aqueous two-phase extraction of high-purity s-SWCNTs using isomaltodextrin, which is a cost-effective polysaccharide that contains a large amount of α-1,6-glucosidic linkages. We also succeeded in fabricating high-density uniform films directly from the high-purity s-SWCNT extract. Fabricated TFTs exhibited an excellent on/off ratio, carrier mobility, and on-current density.

Omachi, H.*; Komuro, T.; Matsumoto, K.; Nakajima, M.; Watanabe, H.; Hirotani, J.; Ohno, Y.; Shinohara, H.* *Appl. Phys. Express* **2019**, *12*, 097003.
Most Read Article, Highlighted in NIKKEI Business Daily, 日刊工業新聞, and 化学工業日報

Single-wall Carbon Nanotubes (SWCNTs)

Electronic-type base on Chirality (n,m)

Semiconducting $n - m \neq 3a$ (a: integer)

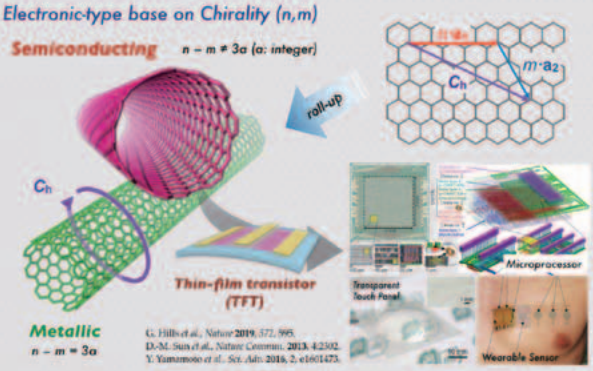

Metallic $n - m = 3a$

G. Hills *et al.*, *Nature* **2019**, *572*, 995.
D.-M. Sun *et al.*, *Nature Commun.* **2013**, *4*:2302.
Y. Yamamoto *et al.*, *Sci. Adv.* **2016**, *2*, e1601473.

Aqueous Two-Phase (ATP) Extraction

Two separated phases composed of water and non volatile components

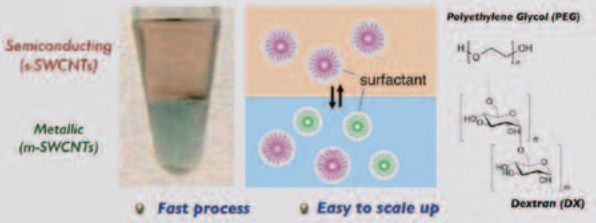

- Fast process
- Easy to scale up

C. Y. Khripin *et al.*, *J. Am. Chem. Soc.* **2013**, *135*, 6822.

Expensive DX polymer is required for SWCNT purification

Inspired by Chemical Structure

Isomaltodextrin (IMD)

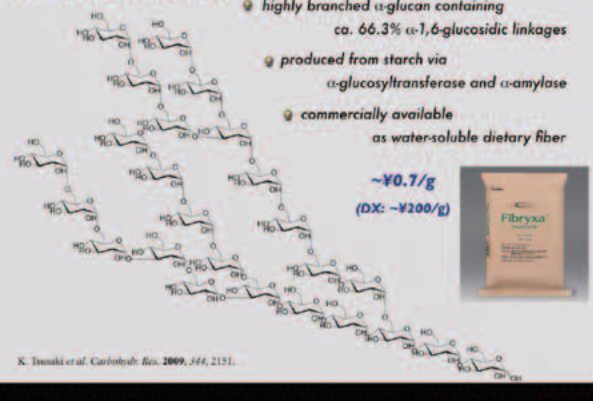

- highly branched α-glucan containing ca. 66.3% α-1,6-glucosidic linkages
- produced from starch via α-glucosyltransferase and α-amylase
- commercially available as water-soluble dietary fiber

~¥0.7/g
(DX: ~¥200/g)

K. Tsuaki *et al.* *Carbohydr. Res.* **2009**, *344*, 2151.

Purity Evaluation

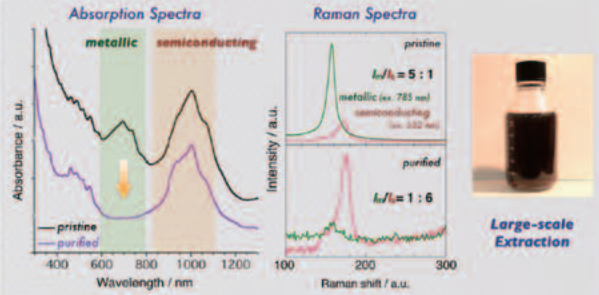

Semiconducting SWCNTs were extracted in 98.4% purity

Thin-film Transistor (TFT) Fabrication

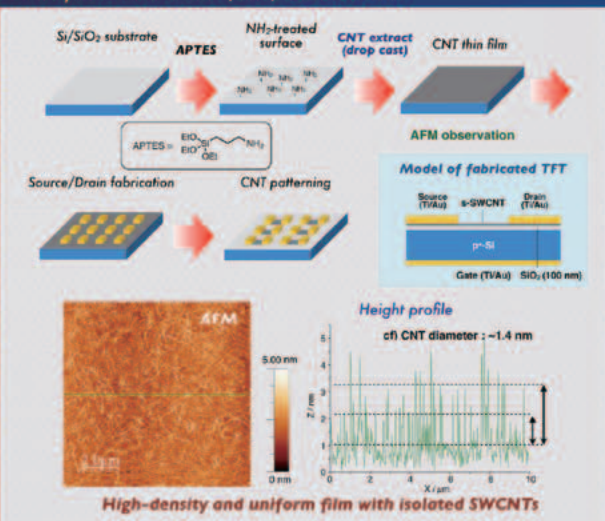

High-density and uniform film with isolated SWCNTs

TFT Measurement

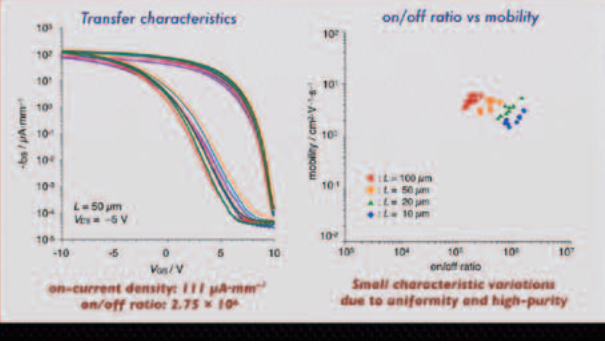

on-current density: 111 μA·mm⁻¹
on/off ratio: 2.75 × 10⁶

Small characteristic variations due to uniformity and high-purity

Fabrication of the Carbon Nanotube Thin Film using the Cross-linking Amine Polymer for Flexible Transistor Applications

Kaisei Matsumoto[1], Kazuki Ueno[1], Jun Hirotani[2], Yutaka Ohno[2,3], Haruka Omachi[1,4]*

[1] Department of Chemistry, Graduate School of Science, [2] Department of Electronics, Graduate School of Engineering, [3] Institute of Materials and Systems for Sustainability, [4] Research Center for Materials Science, Nagoya University, Nagoya, Japan

E-mail: omachi@chem.nagoya-u.ac.jp

Abstract

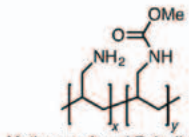

Methoxycarbonyl Polyallylamine (Moc-PAA)

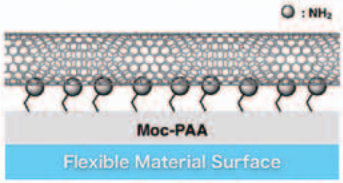

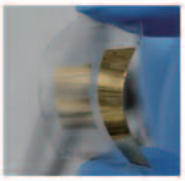

Owing to their remarkable properties, single-walled carbon nanotube thin film transistors (SWCNT-TFTs) are expected to be used in various flexible electronics applications. To fabricate SWCNT channel layers for TFTs, solution-based film formation on a self-assembled monolayer (SAM) covered with amino groups is commonly used. However, this method uses highly oxidized surfaces, which is not suitable for flexible polymeric substrates. Herein, we report a solution-based SWCNT film fabrication using methoxycarbonyl polyallylamine (Moc-PAA). The NH_2-terminated surface of the cross-linked Moc-PAA layer enables the formation of highly dense and uniform SWCNT networks on both rigid and flexible substrates. TFTs that use the fabricated SWCNT thin film exhibited excellent performance with small variations. The presented simple method to access SWCNT thin film accelerates the realization of flexible nanoelectronics.

K. Matsumoto, K. Ueno, J. Hirotani, Y. Ohno, H. Omachi, *submitted*.

Background

General Method for the fabrication of SWCNT film

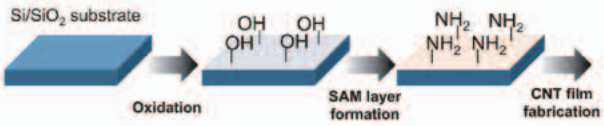

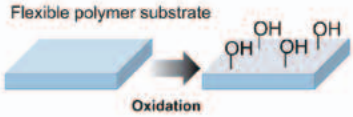

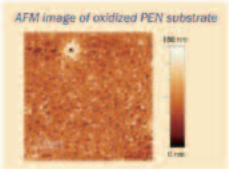

This method damages the surface of flexible polymer substrate

Experiment

Fabricating SWCNTs film

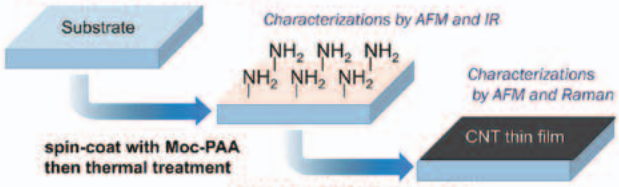

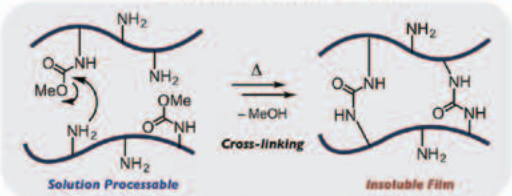

Adhesive layer for SWCNT film fabrication without oxidation

Characterization of Moc-PAA

AFM Observation

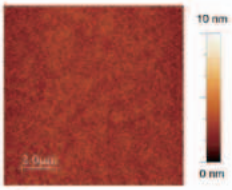

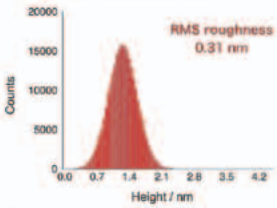

Smooth surface was confirmed

IR Spectra

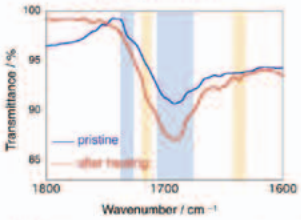

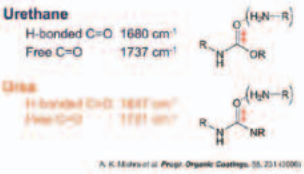

Urea bonds were formed

Characterization of Moc-PAA

Raman spectra

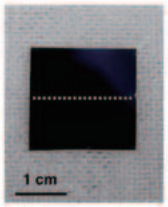

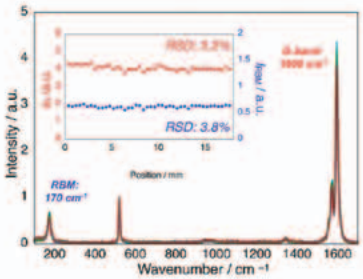

AFM observation

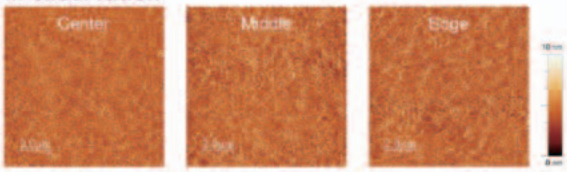

Highly dense and uniform SWCNT networks

Transistor performance

Si/SiO_2 substrate

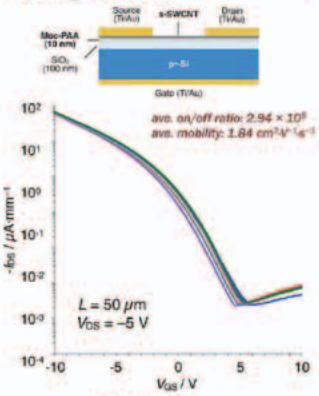

Exposure of s-SWCNTs to air

PEN substrate

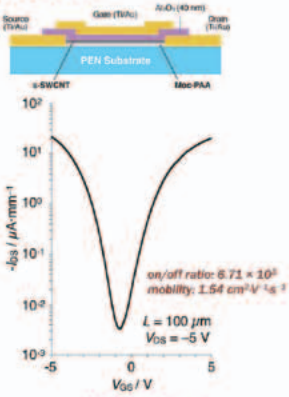

Passivation of s-SWCNTs with Al_2O_3

Gelation of polysaccharides for semiconducting SWCNT separation

Yuki Matsunaga[1], Haruka Omachi[1,2]

[1]Department of Chemistry, Graduate School of Science, Nagoya University, Nagoya, 464-8602, Japan
[2]Research Center for Materials Science, Nagoya University, Nagoya, 464-8602, Japan
E-mail: omachi@chem.nagoya-u.ac.jp

Introduction

Single-wall carbon nanotube (SWCNT)

- ✓ Chemically stable and mechanically robust
- ✓ High carrier mobility
- ✓ Flexibility

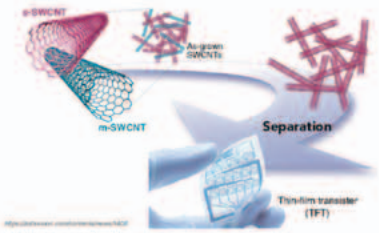

High purity s-SWCNT are strongly required

Gel Filtration Method

Separation method using the difference of affinity

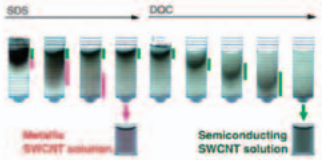

Dextran - conventional polysaccharides gel

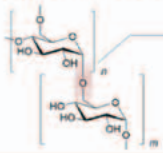

- *Excellent separability*
- *High cost for synthesis*

Aqueous Two-Phase Extraction

Isomaltodextrin(IMD)

- *Commercially available*
- *Low cost*
- *α-1,6-glycosidic bond rich*

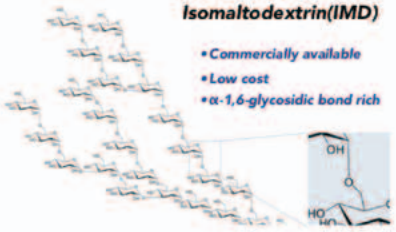

Methods

IMD gel synthesis

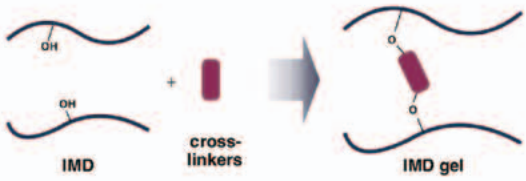

Crosslinking reaction

Separation methods

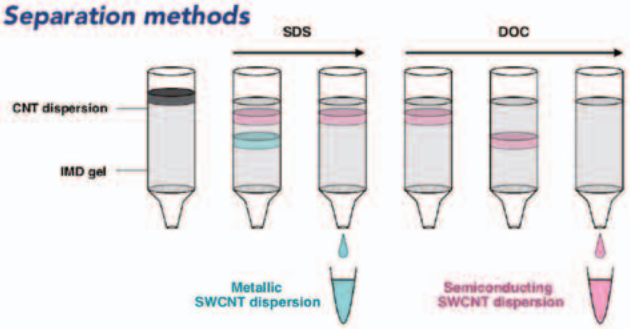

Results

Optimization of gel formation

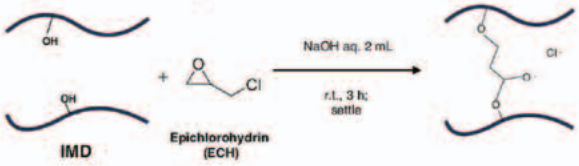

Effect of IMD content[a]

The amount of IMD	Results
400 mg	Not gelation
550 mg	Gelation, but too soft for column separation
560 mg	Gelation
600 mg	Gelation
650 mg	Gelation

[a] 2.5 M NaOH aq. was used.

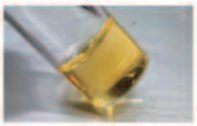

Effect of NaOH concentration[b]

The concentration of NaOH aq	Results
1.0 – 1.5 M	Not gelation
2.0 M	Gelation
2.5 M	Gelation
3.0 M	Gelation, but too soft for column separation
3.5 – 5.0 M	Not gelation

[b] 600 mg of IMD was used.

Column Preparation

1. Wash and crush
2. IMD gel and Sephadex G-100 were mixed (Volume rate = 1 : 1)
3. Pack to a syringe (2 mL)
4. Equilibration of the column with 6 mL of 1% SDS

Gel filtration with synthesized IMD gels

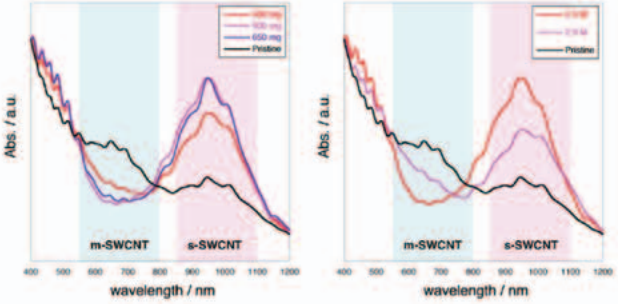

m-SWCNTs were efficiently removed with optimized gel

Summary

- IMD gel was synthesized by cross-linking reaction with ECH
- Efficiently s-SWCNT separation was achieved with the synthesized IMD gel

Transfer Hydration of Dinitriles to Dicarboxamides

Asuka Naraoka[1] and Hiroshi Naka[2]

[1]Graduate School of Science, Nagoya University; [2]RCMS, Nagoya University

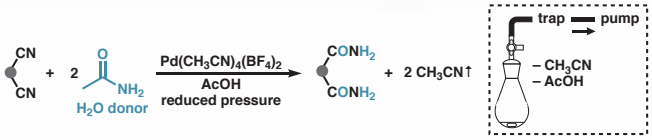

Abstract: We report a robust method for double transfer hydration of dinitriles. The transfer hydration of 1,*n*-dinitriles (*n* = 1–6) proceeds smoothly in the presence of a palladium(II) catalyst with acetamide as a water donor, affording the corresponding diamides in high yields without involving significant side reactions. The equilibrium was shifted in the forward direction by removing coproduced acetonitrile under reduced pressure.

Naraoka, A.; Naka, H. *Synlett* **2019**, *30*, 1977–1980 (Invited Cluster).

1. Background

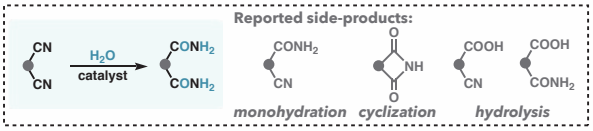

Homogeneous catalysts | **Heterogeneous**

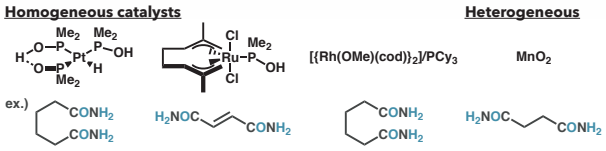

97%	74%	99%	99%
[0.2 mol %, 95 °C, 8 h]	[1 mol %, 60 °C, 1 h]	[2 mol %, 25 °C, 48 h]	[100 °C, 30 min]
Parkins, A. W. *et al.* *J. Mol. Catal. A: Chemical* **2000**, *160*, 249.	Cadierno, V. *et al.* *Dalton Trans.* **2016**, *45*, 13590.	Saito, S. *et al.* *Angew. Chem. Int. Ed.* **2008**, *47*, 3607.	Ley, S. V. *et al.* *Org. Lett.* **2014**, *16*, 1060.

- **Efficient route to 1,*n*-diamides**
- **The substrate scope for 1,3-dinitriles remains limited**

2. Transfer Hydration

This Work: Transfer Hydration of Dinitriles

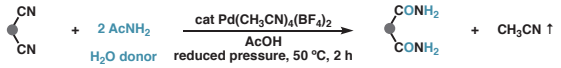

Previous Work: Rapid Transfer Hydration of Cyanohydrins

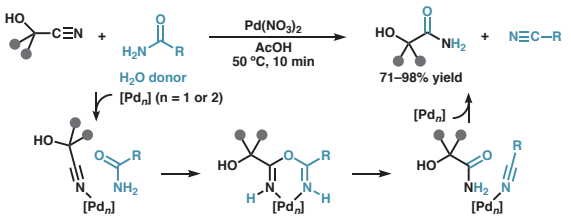

R = CH_3, alkyl

Kanda, T.; Naraoka, A.; Naka, H. *J. Am. Chem. Soc.* **2019**, *141*, 825.

Cf. Pd-Catalyzed Reversible Dehydration of Amides

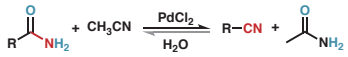

Maffioli, S. I. *et al. Org. Lett.* **2005**, *7*, 5237.
Dai, M. *et al. Org. Biomol. Chem.* **2014**, *12*, 9109.
Ebright, R. H. *et al. Cell* **2017**, *169*, 1240.
Singh, A. K. *et al. Dalton Trans.* **2017**, *46*, 13065.
Croatt, M. P. *Org. Lett.* **2018**, *20*, 6046.

3. Control Experiment

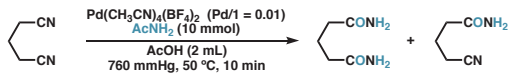

Changes from the above scheme	yield of 2 (%)[a]	yield of 3 (%)[a]
none	73	25
1/$AcNH_2$ = 1:2	29	58
without $AcNH_2$	<1	<1
H_2O instead of $AcNH_2$, 1/H_2O = 1:10	<1	15
without $Pd(CH_3CN)_4(BF_4)_2$	<1	<1
reduced pressure (0.8–1.2 mmHg)	81	17
1 (10 mmol), reduced pressure, 1 h[b]	>99	<1
1 (10 mmol), Pd/1 = 0.001, reduced pressure, 1 h[b]	99	1

[a]Determined by ^{1}H NMR analysis (internal standard = mesitylene).
[b]AcOH (20 mL), 0.8–1.2 mmHg.

4. Pressure Dependence

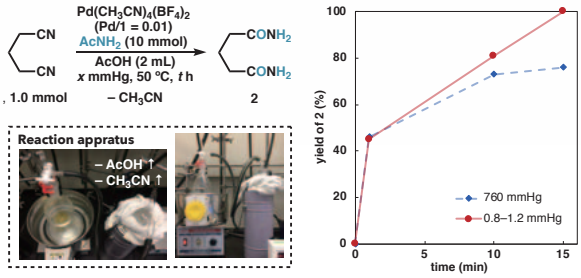

The removal of the coproduct (CH_3CN) and the solvent (AcOH) under reduced pressure is highly effective

5. Substrate Scope

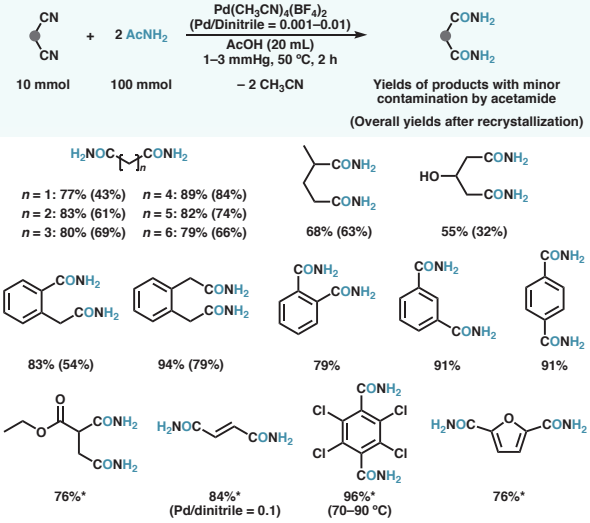

*Dinitrile (0.7 mmol), $AcNH_2$ (7 mmol), AcOH (1.4 mL), 6–30 min.

6. Decagram-Scale Hydration

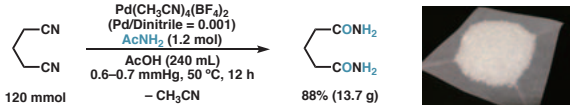

7. Ongoing Project w/ Profs. Uchiyama and Kamigaito

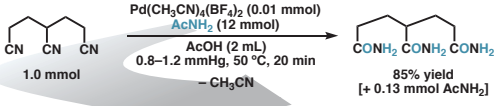

Hydration of Polyacrylonitrile

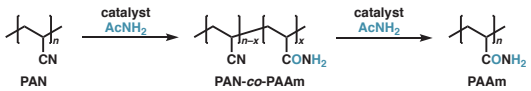

Acknowledgements: We are grateful to support from Profs. M. Uchiyama, M. Kamigaito, R. Noyori and S. Saito. We thank Nagoya Univ. (the MEXT's diversity program) for financial support.

Photocatalytic N-Methylation of Amino Acids with Methanol

Ivven Huang, Yuna Morioka, Susumu Saito, Hiroshi Naka (Grad. Sch. of Sci., & RCMS, Nagoya Univ.)

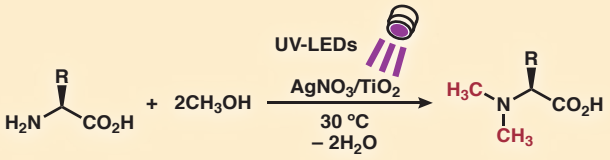

Abstract: A silver-loaded titanium dioxide ($AgNO_3/TiO_2$) photocatalyst promotes N-methylation of amino acids with methanol at ambient temperature under UV light irradiation. Scope and limitation of this method on proteogenic amino acids have been clarified.

1. Introduction

■ Conventional Methods

Bowman, *JCS* 1950, 1342.

HCHO, $NaBH_4$, CF_3CH_2OH, rfx, 24 h

+ Well-established
– Hazardrous reagents

■ CH_3OH as Methylating Reagent

Huang, *CC* 2010, *46*, 7834.

CH_3OH, H_2, Pd/C, rt, 80 h

+ Atom-economical
– Unclear scope

■ Previous Work: Photocatalytic Methylation of Amines with Ag/TiO_2

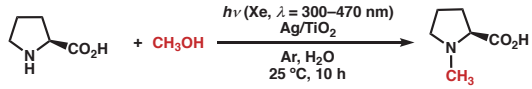

Pro, *S*:*R* = 98:2 — 88%, *S*:*R* = 97:3

Tsarev, Morioka, Caner, Wang, Ushimaru, Kudo, Naka, Saito, *OL* 2015, *17*, 2530.

Scope on other proteogenic amino acids remains unclear.

■ This Work: Photocatalytic Methylation of Amino Acids with $AgNO_3/TiO_2$

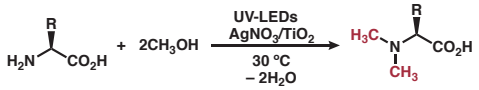

2. Method

■ Photocatalyst Preparation

$AgNO_3/TiO_2$ Impregnation of $AgNO_3$ on TiO_2 (P25)

Ag/TiO_2 Reduction of $AgNO_3/TiO_2$ with $NaBH_4$

■ Photocatalytic Reactions

UV-LEDs 16Wx2 (CCS Ltd.)

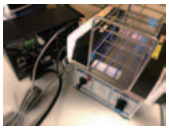

3. Result and Discussion

3.1 Reaction Parameters

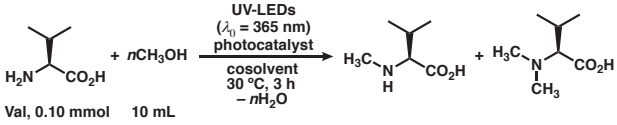

Val, 0.10 mmol — 10 mL

photocatalyst	cosolvent	yield (Me-Val)	yield (diMe-Val)
Ag/TiO_2	none	45%	33%
Ag/TiO_2	H_2O	13%	<1%
$AgNO_3/TiO_2$	none	45%	36%
$AgNO_3/TiO_2$	H_2O	23%	2%

3.2 Scope and Limitations: Proteogenic Amino Acids

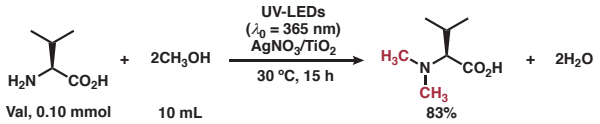

Val, 0.10 mmol — 10 mL — 83%

product, isolated yield, dr:

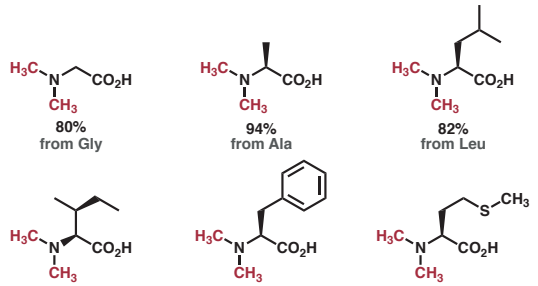

80% from Gly; 94% from Ala; 82% from Leu; 92%, dr >98:2 from Ile; 75% from Phe; 81% from Met

■ Complex mixture with: Ser, Thr, Tyr, Asp, Asn, Glu, Gln, Arg, His, Trp.

■ Cys: Thiazolidine formation and N-methylation

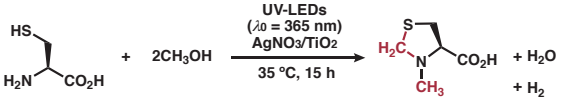

Cys, 0.10 mmol — 10 mL — 70%

■ Pro: monomethylation

Pro, 0.10 mmol — 10 mL — 83%

3.3 Supposed Reaction Mechanism

■ generation of silver nanoparticles ■ generation of Ag-H and HCHO

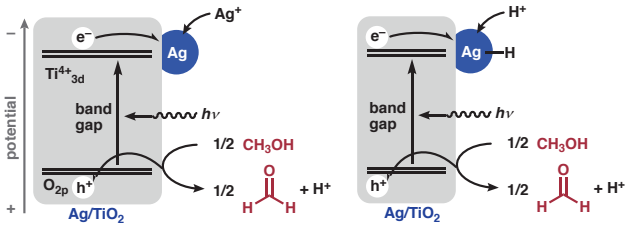

■ first methylation

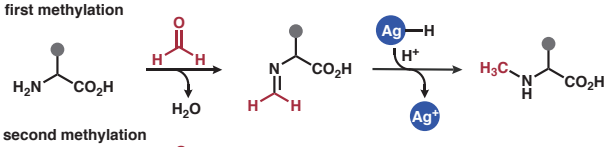

■ second methylation

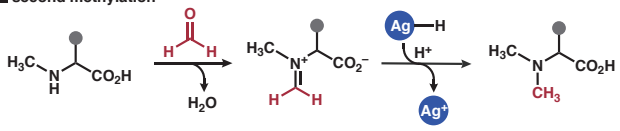

Acknowledgements

Profs. R. Noyori (Nagoya Univ.) for supports; Prof. A. Kudo (Tokyo Univ. of Sci.) for helpful comments.
¥ from JSPS KAKENHI / Iwatani foundation

Synthesis of α-Amino Amides by Transfer Hydration of Nitriles

○Tomoyo Tamura, Taimeng Liang, Ryoji Noyori, and Hiroshi Naka

Graduate School of Science and Research Center for Materials Science, Nagoya University, JAPAN

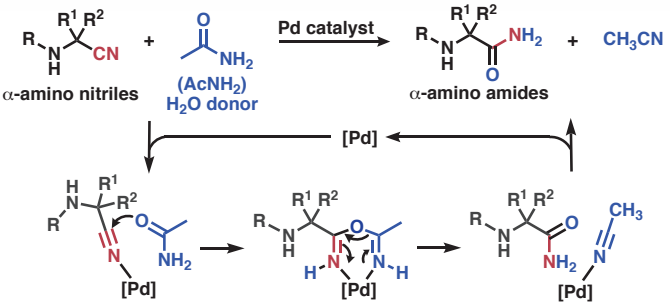

We have recently reported Pd^{II}-catalyzed transfer hydration of cyanohydrins with amide-based water donors (*J. Am. Chem. Soc.* **2019**, *141*, 825–830.). Here we extended this method to the catalytic transfer hydration of α-amino nitriles for the rapid synthesis of α-amino amides. This method enables rapid conversion of various protected amino nitriles to afford α-mono- and α,α-disubstituted-α-aminoamides under mild conditions.

1. Background: Catalytic Hydration of Amino Nitriles

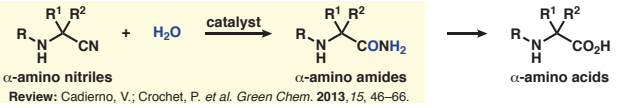

Review: Cadierno, V.; Crochet, P. *et al. Green Chem.* **2013**, *15*, 46–66.

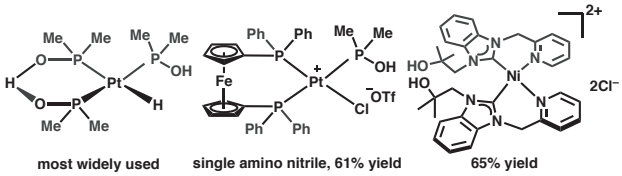

most widely used ester hydrolysis as side reactions	single amino nitrile, 61% yield 0.1 mol %, 40 °C, 12 h TOF = 51 h^{-1}	65% yield 10 mol%, 100 °C, 24 h TOF = 0.27 h^{-1}
Ghaffar, T.; Parkins, A. W. *Tetrahedron Lett.* **1995**, *36*, 8657–8660.	Grubbs, R. H.; Virgil, S. C. *et al. J. Am. Chem. Soc.* **2018**, *140*, 17782–17789.	Bera, J. K. *et al. Chem. Eur. J.* **2017**, *23*, 7761–7771.

Issues: Limited substrate scope and long reaction time

2. This Work: Catalytic Transfer Hydration

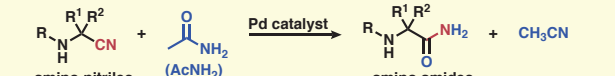

Applicable to acid-/base-sensitive nitriles

Applicable to highly congested nitriles

Pioneering work

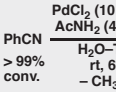

Maffioli, S. I.; Marzorati, E.; Marazzi, A. *Org. Lett.* **2005**, *7*, 5237–5239.

Our previous work

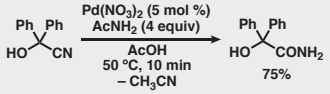

Kanda, T.; Naraoka, A.; Naka, H. *J. Am. Chem. Soc.* **2019**, *141*, 825–830.

3. Result and Discussion

3.1 Effect of Parameters

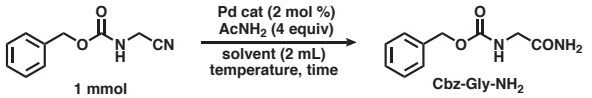

Pd cat	solvent	temperature, time	NMR conv. (%)	NMR yield (%)
$Pd(NO_3)_2$	AcOH	50 °C, 10 min	> 99	> 99
$Pd(NO_3)_2$	CH_3CN/H_2O (3:1)	50 °C, 10 min	54	60
$Pd(NO_3)_2$	CH_3CN	50 °C, 10 min	44	36
$Pd(NO_3)_2$	AcOH	30 °C, 5 min	64	54
$Pd(NO_3)_2$	CH_3OH	30 °C, 5 min	31	22
$Pd(CH_3CN)_4(BF_4)_2$	AcOH	30 °C, 5 min	83	69
$Pd(O_2CCF_3)_2$	AcOH	30 °C, 5 min	55	46
$Pd(CH_3CN)_2Cl_2$	AcOH	30 °C, 5 min	37	25
$Pd(CH_3CN)_4(BF_4)_2$[a]	AcOH	50 °C, 10 min	> 99	92[b]

a) $AcNH_2$ (1 equiv) was used. b) Average of 4 times

3.2 Substrate Scope

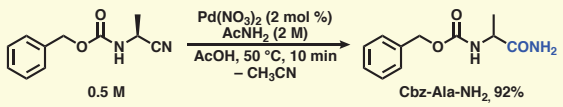

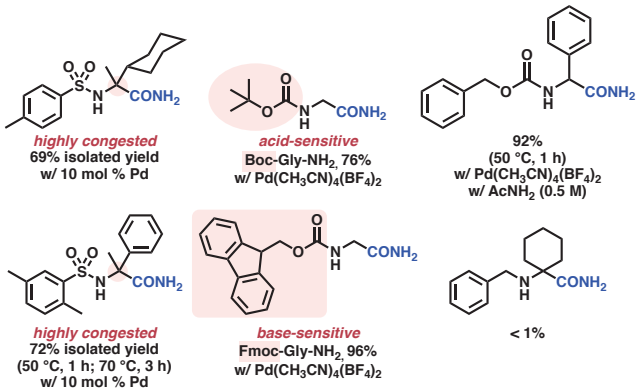

highly congested	acid-sensitive	
69% isolated yield w/ 10 mol % Pd	Boc-Gly-NH_2, 76% w/ $Pd(CH_3CN)_4(BF_4)_2$	92% (50 °C, 1 h) w/ $Pd(CH_3CN)_4(BF_4)_2$ w/ $AcNH_2$ (0.5 M)
highly congested 72% isolated yield (50 °C, 1 h; 70 °C, 3 h) w/ 10 mol % Pd	base-sensitive Fmoc-Gly-NH_2, 96% w/ $Pd(CH_3CN)_4(BF_4)_2$	< 1%

3.3 Conversion to Amino Acid

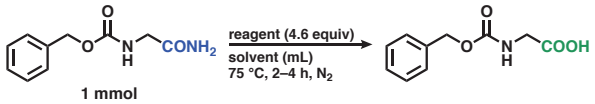

reagent	solvent (mL)	time (h)	NMR conv. (%)	NMR yield (%)	vessel
TBN	AcOH (3 mL)	2	> 99	5	A
TBN	$AcOH/H_2O$ (9:1, 3 mL)	2	87	39	A
TBN	AcOH/TFA (2:1, 3 mL)	2	79	30	A
TBN	AcOH/MeOH (9:1, 3 mL)	2	14	3	A
TBN	AcOH (3 mL)	4	> 99	14	A
TBN	AcOH (2 mL)	2	> 99	9	A
isoamyl nitrite	AcOH (3 mL)	2	80	7	A
hexyl nitrite	AcOH (3 mL)	2	83	4	A
TBN (5 equiv)	AcOH (2 mL)	3	> 99	86	B
TBN (5 equiv)[a]	AcOH (2 mL)	3	> 99	91	B

a) Under air

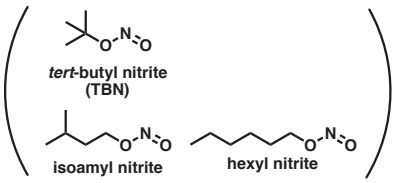

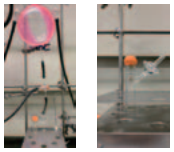

Cf. Kandasamy, J. *et al. Green Chem.* **2016**, *18*, 2323–2330.

Acknowledgements: Prof. S. Saito for fruitful discussion. Prof. T. Ooi, K. Ohmatsu and T. Ohkuma for providing several aminonitriles. Prof. T. Ohshima and H. Morimoto for providing method for synthesis of substrates. ¥ from JSPS KAKENHI 15KT0141 & 17K05859 / Toyota Riken / IQCE

Direct α-C(sp³)–H arylation of amides by TiO_2/Ni complex cooperative catalysts

Masaki Nomura,[1] Shogo Mori,[1] Susumu Saito[1,2]
[1]Graduate School of Science, [2]Research Center of Materials Science, Nagoya University
NAGOYA UNIVERSITY
The Noyori Laboratory

Abstract

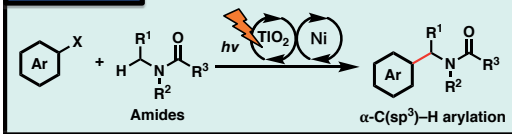

The photocatalyzed direct α-C(sp³)–H arylation of amides with aryl halides is an attractive synthetic strategy to access to complex molecules. Our group has developed this transformation using TiO_2/Ni complex cooperative catalysts, where TiO_2, an inexpensive and easily removable heterogeneous photocatalyst provided a practical synthetic protocol.

1. Introduction

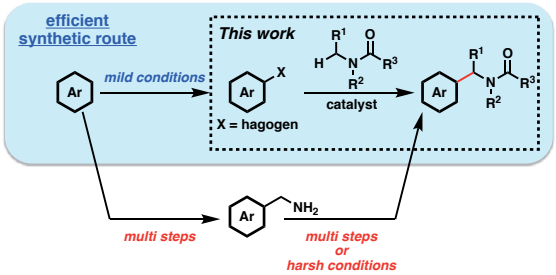

Photocatalyzed direct α-C(sp³)–H arylation provides a short synthetic route to complex amides. Readily accessible starting material, mild reaction conditions, and high selectivity make this strategy attractive for the synthesis of drugs, bioactive molecules and so on.

2. Previous reports

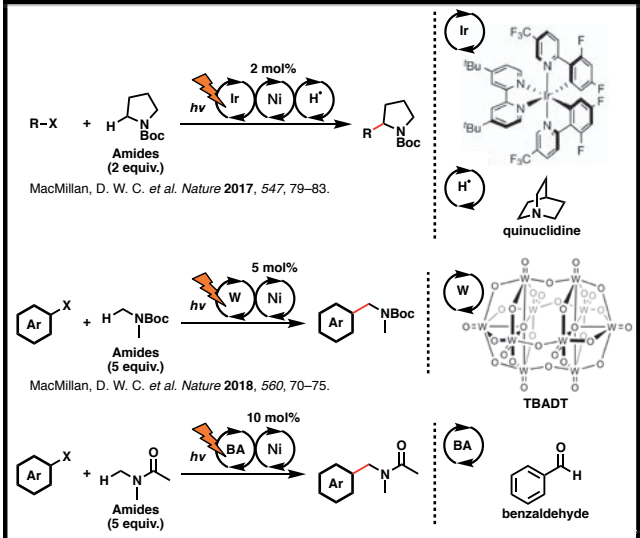

MacMillan, D. W. C. *et al. Nature* **2017**, *547*, 79–83.

MacMillan, D. W. C. *et al. Nature* **2018**, *560*, 70–75.

Hashmi, A. S. K. *et al. Org.Lett.* **2019**, *21*, 6329–6332.

Recently, direct α-C(sp³)–H alkylation/arylation methods with homogeneous photocatalysts and Ni complexes were reported.

3. Our previous system

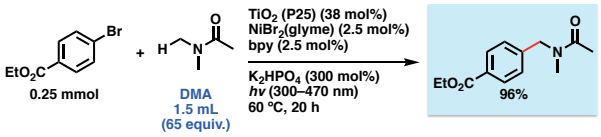

✔ An inexpensive and easily removable heterogeneous photocatalyst

✔ A rare example where simple carboxylic acid amides can be used

DMA as solvent ➡ Limited substrate scope

4. Solvent effect

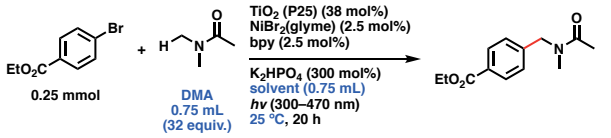

Solvent	Yield (%)	Solvent	Yield (%)
DMA	24	EtOAc	23
THF	55	ethyl formate	71
1,4-dioxane	43	butyl formate	68
MTHP	23	cyclohexane	5
Et_2O	6	toluene	7
$^iPr_2O$	13	acetone	9
^tBuOMe	25	CH_2Cl_2	8
MeOH	9	DMSO	2
^tBuOH	18	H_2O	0
MeCN	17		

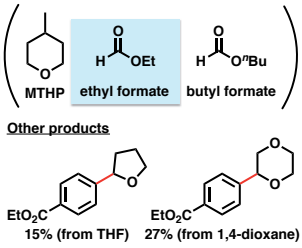

5. Ligand effect

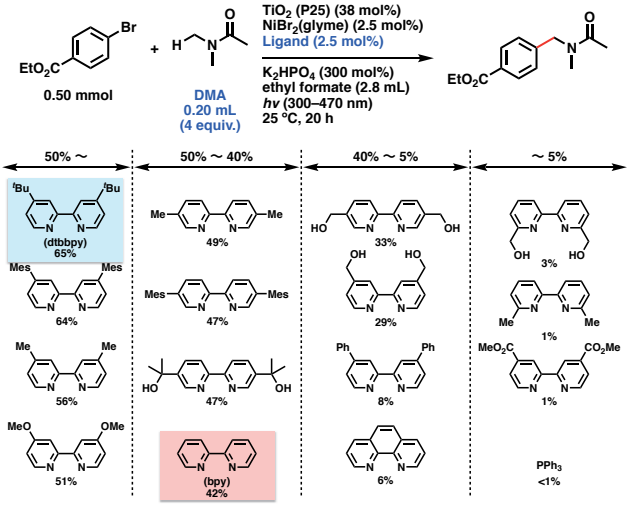

6. Addition pattern of Ni complex

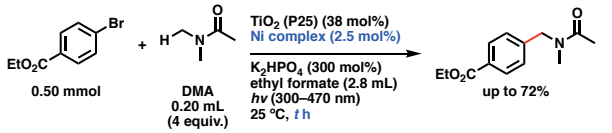

Addition pattern	Yield (%)
$NiBr_2$(glyme) + dtbbpy	65[a]
pre-synthesized $NiBr_2$(dtbbpy)	72[b]

[a] 20 h [b] 24 h

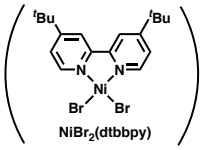

Ethyl formate and pre-synthesized $NiBr_2$(dtbbpy) resulted in efficient α-C(sp³)–H arylation with a small amount of DMA (4 equiv.) at room temperature.

Photocatalytic CO_2 Reduction Using Base Metal Complexes Bearing PNNP-type Tetradentate Ligand

NAGOYA UNIVERSITY

Taku Wakabayashi[1], Kenji Kamada[1], Jieun Jung[1], Susumu Saito*[,1,2]

[1]Graduate School of Science, [2]Research Center for Materials Science, Nagoya University

The Noyori Laboratory

Abstract

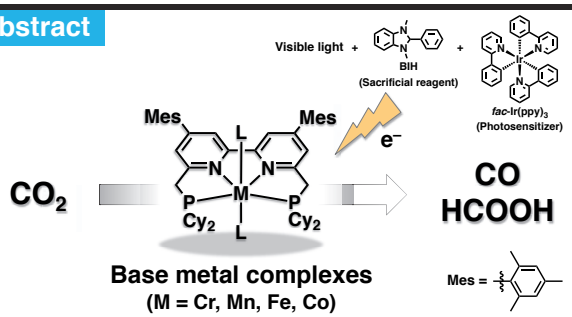

We have developed new base metal complexes which can catalyze CO_2 photoreduction. These catalysts consist of earth-abundant base metals and PNNP-type tetradentate ligands, showing the ability for reducing CO_2 under visible light irradiation to generate CO and HCOOH.

1. Introduction

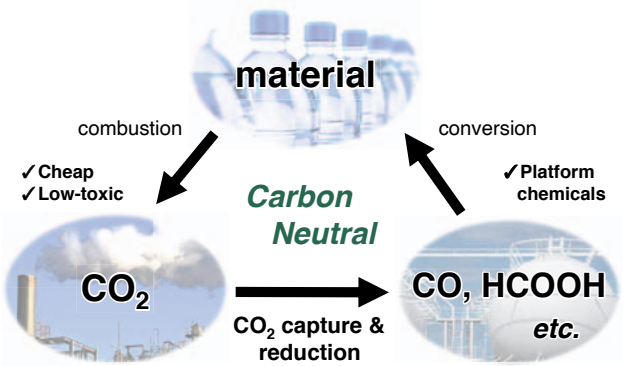

CO_2 reduction can realize sustainable society.

2. Strategy

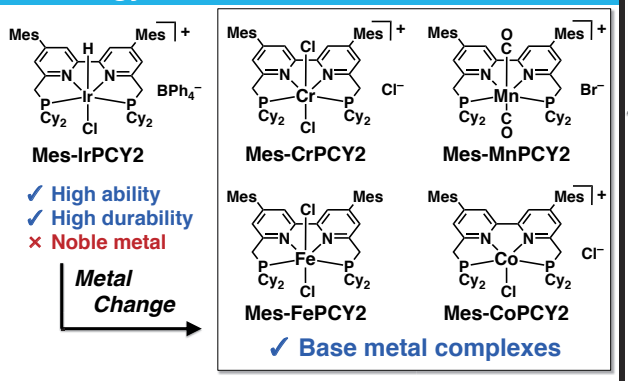

3. Synthesis

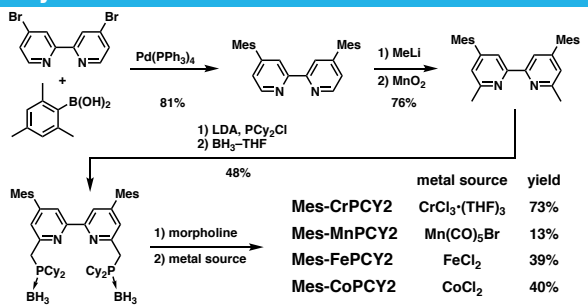

	metal source	yield
Mes-CrPCY2	$CrCl_3 \cdot (THF)_3$	73%
Mes-MnPCY2	$Mn(CO)_5Br$	13%
Mes-FePCY2	$FeCl_2$	39%
Mes-CoPCY2	$CoCl_2$	40%

4. Electrochemical study

Cyclic voltammetry measurement

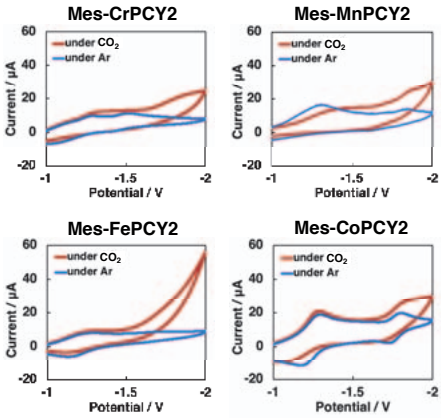

Conditions:
Complex (0.1 mM) in DMA solution containing 0.1 M NEt_4BF_4 as a supporting electrolyte.
Scan rate: 0.1 V/s.

Catalytic current were increased under CO_2 atmosphere.

CO_2 reduction would be occurred.

All complexes have catalytic ability for CO_2 reduction.

5. Results of CO_2 photoreduction

Effect of metal center

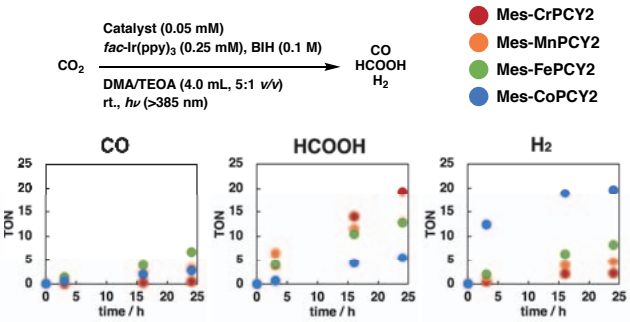

Mes-FePCY2 and Mes-CrPCY2 are suitable for CO and HCOOH production respectively.

Additive effect

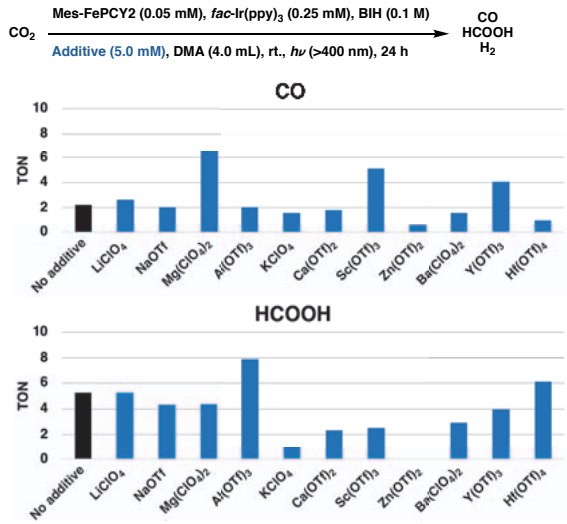

Mg and Al salts can improve CO and HCOOH production respectively.

Ir-catalyzed transformation of bio-renewable even-numbered carboxylic acids into odd-numbered carbon chain

Kazuki Teramoto,[1] Shota Yoshioka,[1] Susumu Saito*,[1,2]

[1]Graduate School of Science, [2]Research Center for Materials Science, Nagoya University

The Noyori Laboratory

Abstract

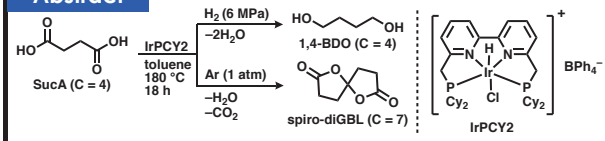

Recently, we have developed multifunctional Ir pre-catalyst, IrPCY2 for hydrogenation of 1,4-dicarboxylic acids (1,4-diCAs) via *in-situ* formation of corresponding anhydrides and lactones. In survey of reaction pathway of the hydrogenation, IrPCY2 was found to convert SucA into spiro-diGBL under Ar atmosphere as shown the scheme. Aming for the application of this reaction toward transformation of diCAs or fatty acids to odd numbered carbon chain, we investigate herein the optimization of left reaction conditions.

1. Introduction

❑ Decarboxylation

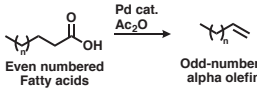

Vider, J. *ACS Catal.* 2016, *6*, 7784–7789

❑ Hydrogenation

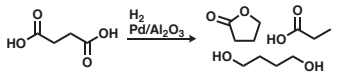

Antoine,B; Ceri, H. *ACS Sustainable Chem.* 2018, *6*, 16341–16351

Ex.) Bio-renewable CAs

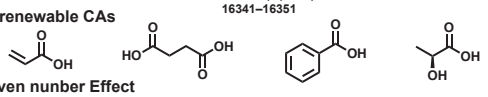

❑ Odd-Even nunber Effect

ex.) Correlation between melting point and crystal density

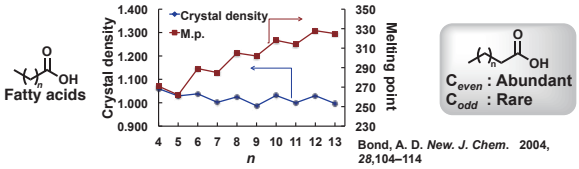

Bond, A. D. *New. J. Chem.* 2004, *28*,104–114

2. This Work

❑ Background

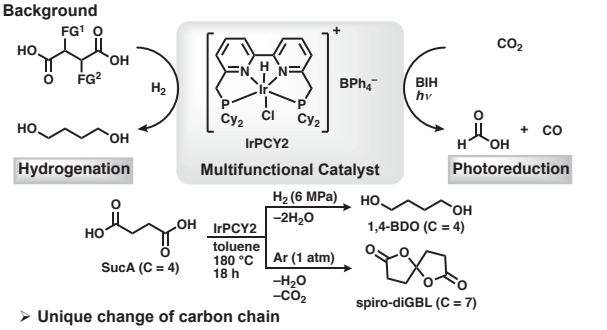

➢ Unique change of carbon chain

❑ Future target

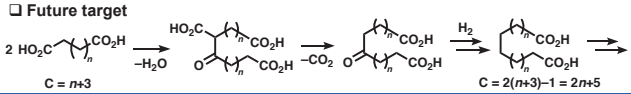

3. Synthesis of Ir precatalyst

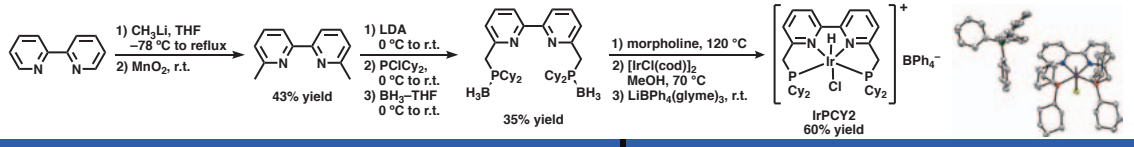

triclinic, P-1, R_1 = 0.0684, wR_2 = 0.1754, GOF = 1.092
H atoms except hydride were omitted for clarity.

4. Screening of the amount of IrPCY2

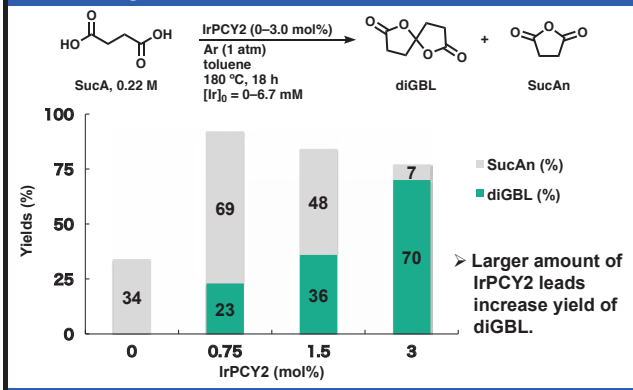

➢ Larger amount of IrPCY2 leads increase yield of diGBL.

5. Effect of different amount of NaH

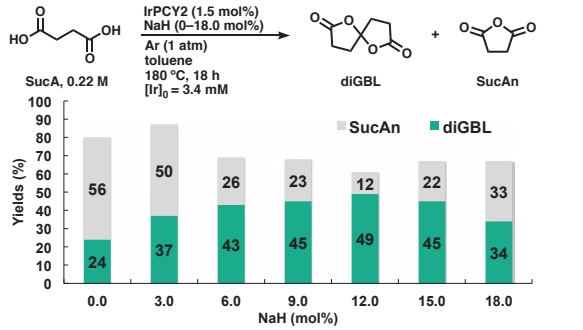

➢ The formation of diGBL might be promoted by NaH.
➢ The propotion (IrPCY2 : NaH = 1.5 : 12.0) is better.

6. Reaction time and Pathway

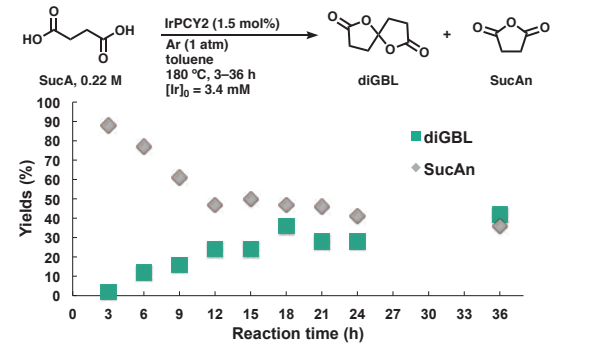

➢ The formation of SucAn might be occurred at first.

Hypothesis

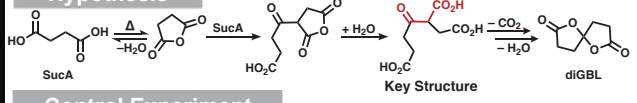

Control Experiment

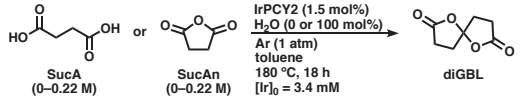

Substrate (mmol)	H_2O (mol%)	conv. (%)	yield of diGBL (%)
SucA (0.67)	0	>99	36
SucAn (0.67)	0	47	26
	100	19	16
SucA (0.335) + SucAn (0.335)	0	>99	28
	100	85	8

Development of Fluoro-phosphoroamidate prodrug for Nucleotide Analogs

Zheng Ti, Yuki Yoshida, Hirotaka Murase, Yasuaki Kimura, Hiroshi Abe
Research Centre for Materials Science, Nagoya University

Introduction

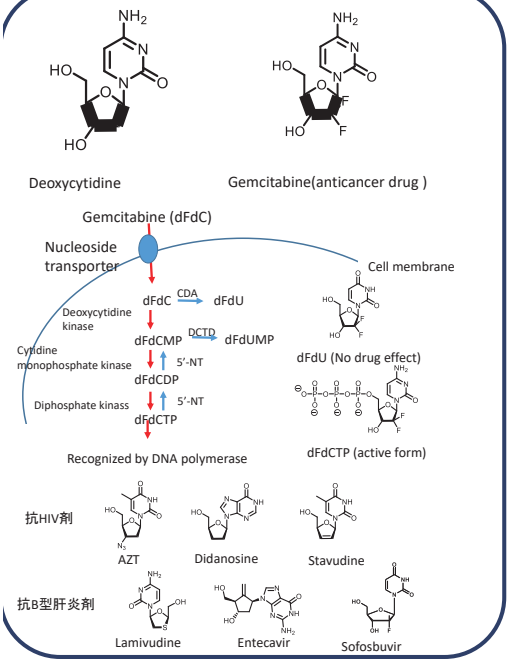

Design

The problem of nucleoside analogue : Time of phosphorylation is too long → long time results in drug convert into inactive form

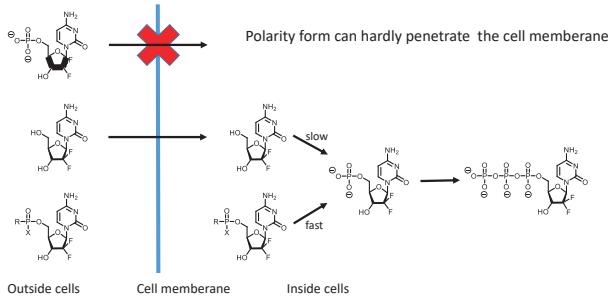

Hydroxyl group connect to phosphoric acid lead to elevation of hydrophobicity → improvement of cell permeability
After being taken up by cells, the reaction to monophosphate by enzyme is fast→increase of efficiency by eliminating detoxified step

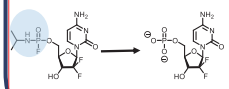

Development of fluoride type phosphate prodrugs
Advantages :
The use of fluoride group leads to decrease of molecular weight
Side reaction is hard to occur due to the stability of P-F bond

Experimental Results

1. Synthesis of phosphate prodrugs

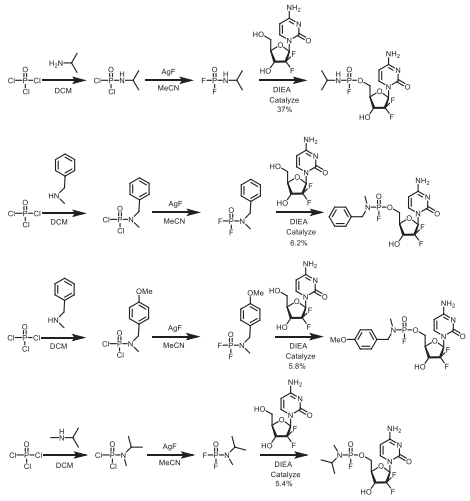

2. 殺がん細胞活性評価

HeLa: Cervical cancer cell line

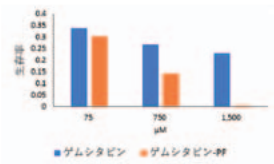

H1299:Lung cancer cell line

3. Synthesis of anti-hepatitis prodrugs

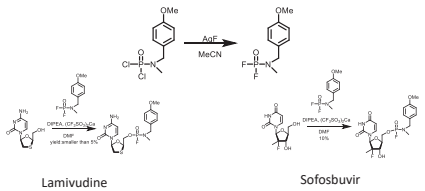

- Selectively react with 5'- hydroxyl group
- In addition to Gemcitabine, other nucleoside analogs can also be synthesized under the same reaction condition.

Conclusion & Prospect

Conclusions

- We developed a new type of Fluoride type phosphate prodrug and established a synthesis scheme.
- Cell assay shows that it is effective to cancer cells
- The synthesis method is also applicable to other nucleotide analogs

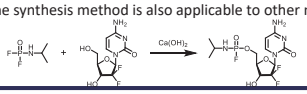

Prospects

- Make sure that the prodrug itself is not toxic.
- Evaluate anti-hepatitis effect of prodrugs

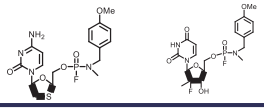

IRCCS 統合物質創製化学研究推進機構

阿波賀邦夫　**エネルギー・資源研究プラットホーム**
〒464-8602　名古屋市千種区不老町 名古屋大学大学院理学研究科
TEL 052-789-2291　FAX 052-789-5947

中野　環　**新反応・新触媒研究プラットホーム**
〒001-0021　北海道札幌市北区北 21 条西 10 丁目 北海道大学触媒科学研究所
TEL 011-706-9155　FAX 011-706-9156

島川祐一　**マテリアル研究プラットホーム**
〒611-0011　京都府宇治市五ヶ庄 京都大学化学研究所附属元素科学国際研究センター
TEL 0774-38-3110　FAX 0774-38-3118

吉澤一成　**ケムバイオ研究プラットホーム**
〒819-0395　福岡市西区元岡 744 九州大学先導物質化学研究所
TEL 092-802-2529　FAX 092-802-2528

機構事務室
〒464-8602　名古屋市千種区不老町 名古屋大学物質科学国際研究センター
TEL 052-789-5907　FAX 052-789-5900

IRCCS, Integrated Research Consortium on Chemical Sciences